The Dissertation Committee for Kevin Martin Befus certifies that this is the approved version of the following dissertation:

Groundwater flow controls on coastal water quality and global groundwater ages

Committee:

M. Bayani Cardenas, Supervisor

Thomas P. Gleeson

Marc A. Hesse

Jeffrey G. Paine

John M. Sharp

Groundwater flow controls on coastal water quality and global groundwater ages

by

Kevin Martin Befus, B.S.; M.S.

Dissertation

Presented to the Faculty of the Graduate School of

The University of Texas at Austin

in Partial Fulfillment

of the Requirements

for the Degree of

Doctor of Philosophy

The University of Texas at Austin

May 2015

Acknowledgements

My dissertation is comprised of chapters resulting from collaborations that made my research possible. At the beginning of each chapter, I provide the reference for the corresponding publication and provide a summary of the contributions from each co-author. Beyond the specific contributions to the papers, my collaborators on the projects were examples of academic excellence and rigor that I hope to emulate.

I have benefited immensely from the interactions, shared research goals, and friendships within the Cardenas research group. From the beginning, my academic elder siblings, Audrey Sawyer and Kuldeep Chaudhary, encouraged me and gave constructive advice. Travis Swanson and John Nowinski provided humorous hydrologic and more random discussion outlets. Peter Zamora and Lichun Wang were my academic brothers, starting and ending our Ph.D.'s at the same time as me. As such, I grew with them through courses, our individual research projects, field endeavors, and hundreds of lunch conversations. My Ph.D. would have been a lonelier time without them. More recent additions to and graduates from the Cardenas group have also contributed to both my academic and social happiness, including Mike Kanarek, Alyse Briody, Raquel Flinker, Jeff Watson, Lizhi Zheng, Michael O'Connor, Eric Guiltinan, and Matt Kaufman.

Kenny Befus has been a lifelong role model, and during my Ph.D. this was no different. His example as a diligent and hypothesis-driven scientist impressed and inspired me to spend the long hours tackling the shallow and deep questions that arose. Kenny encouraged me through the highs and lows of my graduate career, and I am extremely grateful.

Outside of my advising committee, a number of professors invested in my professional development. Isaac Santos mentored me beyond our collaborative work in Rarotonga and sets the standard of scientific excellence extremely high. Luc Lavier gave me opportunities to develop my teaching style as both a teaching assistant and assistant instructor with him. Much of my future mentoring will reflect the conversations I had with Luc during our empty office hours. Jay Banner and the Environmental Science Institute's Scientist in Residence program taught me to be a better science communicator, and I had a blast working with Trevor Hance at Laurel Mountain Elementary school. Trevor never fails to bring the excitement and has continued to be a solid mentor to me in teaching and in science.

I thank my advising committee for years of guidance and mentorship. Jack Sharp and Marc Hesse taught many of my hydrogeology courses and significantly conditioned my perspective on hydrologic science. Jeff Paine was and is my geophysical role model. Tom Gleeson inspired me to think big about problems related to water and reiterated the value applying creative and patient brainstorming on developing research goals. I thank Bayani Cardenas most of all for entraining in me the desire to tackle fundamental hydrologic problems and for shepherding my development as an academic.

My Ph.D. work would not have been possible without a number of funding opportunities. The Geology Foundation at The University of Texas at Austin funded a year of my Ph.D. through a fellowship as well as numerous other field and conference-related trips. Funding outside of UT came from the Geological Society of America's Graduate Research Grant, the Ozarka Every Drop Counts Fellowship, and the American Geophysical Union's Horton Research Grant.

Groundwater flow controls on coastal water quality and global groundwater ages

Kevin Martin Befus, Ph.D.

The University of Texas at Austin, 2015

Supervisor: M. Bayani Cardenas

Humanity relies on groundwater. But, current consumption may be outpacing groundwater renewal rates, and anthropogenic activities are altering its quality. This dissertation advances the state of knowledge of how local and regional groundwater dynamics affect its quality and quantity. First, I investigate groundwater discharge patterns and fluxes in three lakes in the Nebraska Sand Hills region and on the island of Rarotonga, Cook Islands, to understand the hydrologic connection between groundwater and surface water in these lacustrine and coastal settings. In Nebraska, I use electrical geophysical methods to characterize the spatial signature of groundwater recharge and discharge to and from the lakes using groundwater salinity patterns. On Rarotonga, a detailed field study of groundwater flow at the intertidal zone shows how groundwater flow influences the thermal regimes of nearshore environments, affecting the biota that live and chemical processes that occur near and below this dynamic interface. Next, a dense network of geophysical surveys across the coastal plain and into the lagoon on Rarotonga constrains multiple features of the larger-scale hydrologic system that are primarily controlled by the local carbonate and volcanic geology on the island. Finally, I give the first estimate of the global storage and spatial distribution of groundwater with a mean age since recharge of less than fifty years. I use several thousand two-dimensional groundwater flow and age-as-

mass transport simulations parameterized by the best available hydrologic and geologic datasets. This global analysis suggests that ~6% of the groundwater stored in the upper 2 km of the Earth's crust is younger than 50 years. Comparing this young groundwater storage to current groundwater depletion rates indicates that more than half of the irrigated areas depending significantly on groundwater could have already used up all of the young groundwater and are using groundwater more quickly than the storage is replenished. Together, these studies advance how to quantify groundwater as a renewable resource through the global estimation of groundwater storage associated with certain timespans and by analyzing the implications of groundwater flow on water quantity and quality in field settings.

Table of Contents

List of Tables ..... **xii**

List of Figures ..... **xiii**

Chapter 1:
Introduction **1**

1.1. Water 1

1.2. Motivating questions 3

1.3. A groundwater mass balance framework 4

Chapter 2:
Classification and delineation of groundwater–lake interactions in the Nebraska Sand Hills (USA) using electrical resistivity patterns **6**

Abstract 6

2.1. Introduction 7

2.2. Hydrology and hydrogeology of the Nebraska Sand Hills 8

2.3. Methods 10

2.3.1. Continuous Resistivity Profiling (CRP) 12

2.3.2. Inversion and post-processing 13

2.4. Results and Discussion 22

2.4.1. Wilson Lake 22

2.4.2. Alkali Lake 28

2.4.3. Gimlet Lake 30

2.5. Summary and Conclusion 33

Chapter 3:
Heat transport dynamics at a sandy intertidal zone **35**

Abstract 35

3.1. Introduction and background 36

3.2. Study site and Methods 40

3.2.1. Study site 40

3.2.2. Data collection and analysis 41

3.3. Results 45

3.3.1. Water level measurements 45
3.3.2. Electrical resistivity tomograms 48
3.3.3. Measured temperature distributions....50
3.4. Discussion 59
3.4.1. Potential sources of error and other limitations 59
3.4.2. Hydrodynamic processes 61
3.4.3. Heat transport regime....65
3.4.4. Synthesis of hydraulic, thermal, and geophysical results 68
3.4.5. Ecological and biogeochemical implications....71
3.5. Conclusions....72

Chapter 4:
Geoelectrical signals of geologic and hydrologic processes in a fringing reef lagoon setting 74
Abstract 74
4.1. Introduction....75
4.2. Study site....78
4.3. Electrical resistivity (ER) methods 80
4.3.1. Field ER surveys 82
4.3.2. ER inversion....83
4.3.3. ER forward modeling....84
4.4. Results....85
4.4.1. Onshore ERT surveys 87
4.4.2. Seafloor ERT surveys 89
4.4.3. Lagoon ERT transects....89
4.4.4. Forward model simulations....92
4.5. Discussion 96
4.5.1. Forward model discussion 96
4.5.2. Field ERT interpretation 97
4.5.3. Implications for groundwater flow 104
4. Summary and conclusions 110

Chapter 5:
Quantifying global renewable groundwater.....113
Abstract.....113
5.1. Introduction.....114
5.2. Quantitative Analysis of Groundwater Age.....118
5.2.1. Hydrologic datasets.....118
5.2.2. Binning hydrologic datasets for modeling.....119
5.2.3. Numerical simulation: groundwater flow and age transport....120
5.2.4. Effective depth and the renewable groundwater equivalent....126
5.2.5. Modeled renewable metrics to watersheds globally.....130
5.2.6. Renewable groundwater comparison for thirty aquifers.....130
5.3. Results.....134
5.3.1. Comparison of aquifer geochemical and modeling results.....134
5.3.2. Global distribution of renewable groundwater.....140
5.3.3. Volume of renewable groundwater.....146
5.3.4. Volumes of Holocene-aged groundwater storage.....149
5.4. Discussion.....150
5.4.1. Model simplifications.....150
5.4.2. Groundwater recharge in the numerical simulations.....154
5.4.3. Lifespan and vulnerability of renewable groundwater.....163
5.5. Conclusions.....168

Chapter 6:
Conclusion.....171
6.1. Dissertation Summary.....171
6.2. Future Research.....175
6.2.1. Groundwater age and groundwater renewal.....175
6.2.2. Groundwater-surface water interactions.....176
6.3. Broader dissertation significance.....177
6.4. Concluding Remarks.....178

References.....183

List of Tables

Table 2.1. ER Inversion settings 15

Table 2.2. Overview of lake properties and CRP data. 27

Table 5.1. Aquifer comparison of young groundwater metrics 138

Table 5.2. Previous global hydrologic flux estimates 156

Table 5.3. Groundwater recharge and renewal rate estimates 161

List of Figures

Figure 2.1. Location map, Nebraska Sand Hills....11
Figure 2.2. Wilson Lake example section....16
Figure 2.3. Alkali Lake example section....17
Figure 2.4. Gimlet Lake example section....18
Figure 2.5. Recorded lake water temperatures....20
Figure 2.6. ER profiles in Wilson Lake and Alkali Lake....24
Figure 2.7. ER depth sections for all lakes....26
Figure 2.8. ER profiles in Gimlet Lake....31
Figure 3.1. Rarotonga location and study site map....42
Figure 3.2. Groundwater head and flux data....46
Figure 3.3. Tidal ER surveys....49
Figure 3.4. Temperature time series....52
Figure 3.5. Temperature distributions....54
Figure 3.6. Temperature mean and range....55
Figure 3.7. Vertical heat flux and net transport....58
Figure 3.8. Intertidal conceptual model....70
Figure 4.1. Rarotonga geology and site map....79
Figure 4.2. Forward ER model setup....86
Figure 4.3. Inland ER surveys....88
Figure 4.4. Parengaru Creek ER surveys....90
Figure 4.5. Taakoka passage ER surveys....91
Figure 4.6. Muri Lagoon ER surveys....93
Figure 4.7. Forward model ER comparison....95

Figure 4.8. Hydrostratigraphy of Muri Lagoon.....107

Figure 5.1. Hydrologic parameter histograms.....121

Figure 5.2. Groundwtaer simulation setup.....123

Figure 5.3. Conceptual model of $d_{effective}$ and $d_{equivalent}$.....128

Figure 5.4. Example groundwater age distributions.....131

Figure 5.5. Aquifer $R_{renewable,3H}$ profiles.....136

Figure 5.6. Aquifer-model $d_{effective}$ comparison.....137

Figure 5.7. Aquifer-model renewable storage comparison.....139

Figure 5.8. Global map of$d_{effective}$.....141

Figure 5.9. Global map of $d_{equivalent}$.....142

Figure 5.10. Histograms of global $d_{effective}$ and $d_{equivalent}$.....143

Figure 5.11. Global map of the range in $d_{equivalent}$.....144

Figure 5.12. Distributions of the range of $d_{effective}$ and $d_{equivalent}$.....145

Figure 5.13. Global map of$V_{renewable}$.....147

Figure 5.14. $V_{renewable}$ map of Texas.....148

Figure 5.15. Distribution of groundwater storage to 9,500 years.....151

Figure 5.16. Global map of poorly constrained areas.....162

Figure 5.17. Global map of the lifespan of renewable groundwater.....165

Figure 5.18. Global map of areas with heavy groundwater use.....166

Chapter 1:

Introduction

Water, water, every where,
Nor any drop to drink.
- from "The Rime of the Ancyent Marinere"
by *Samuel Taylor Coleridge* [1798]

1.1. WATER

Water is an irreplaceable necessity. Water supports life on Earth as a medium for exchange as well as storage, distributing both energy and mass from one place and time to another. The spatiotemporal patterns of water on Earth threaten life in times of extreme excess or scarcity, but otherwise sustain life. Water can spread unwanted chemicals or act as the dilution agent for other solutions. The many roles and manifestations of water in the natural and engineered worlds are important for mindfully managing present-day and future water resources and the natural and human systems that rely on water.

The hydrologic cycle on Earth circulates water through natural purification stages, distillation through evapotranspiration and filtration through sediment, that define water as a renewable resource [*Oki and Kanae*, 2006]. But is all water similarly renewable and pure?

Groundwater comprises the underground portion of Earth's water cycle and more strictly refers to interstitial water at and below a water table. As part of the water cycle, groundwater is replenished by precipitation that infiltrates through the ground to the water table (i.e., groundwater recharge) as well as through water inputs from surface water bodies and, in the modern era, through agricultural irrigation and water transportation systems. Once part of groundwater, the water flows in the subsurface (i.e., aquifers and water-bearing layers) at widely varying rates and pathways to flow back eventually to the Earth's surface (i.e., groundwater discharge). The dynamics of groundwater flow control how

quickly groundwater and its chemical constituents travel through the subsurface. Therefore, any investigation of either groundwater quantity or groundwater quality inherently requires some understanding of groundwater flow. However, groundwater dynamics result from an incredibly diverse integration of spatiotemporally distributed lithologic properties and hydrologic forcings, whereby the quantification or even qualification of groundwater in many environments remains limited. My dissertation focuses first on measuring and describing groundwater dynamics and their effects on other physical processes in the field. I constrain groundwater flowpaths and interactions with surface water to unravel the control groundwater flow has on thermal and chemical transport in coastal settings.

With the fundamental understanding of groundwater flowpaths and the hydrogeologic features controlling them, the next step is to understand how the timing of groundwater flow contributes to its quality and availability. Groundwater flow inherently incorporates a temporal aspect, where the rates of groundwater flow are controlled by a multitude of environmental factors that together determine how long water takes to traverse a hydrogeologic system. However, the residence time of groundwater for groundwater systems are mostly unconstrained, and the duration that a water molecule resides as groundwater also varies widely, ranging from timescales of minutes in hyporheic exchange [*Cardenas*, 2008; *Cardenas et al.*, 2008; *Gomez et al.*, 2012] to millions of years [*Phillips et al.*, 1986; *Sturchio et al.*, 2004]. These groundwater residence times affect the potential for groundwater-rock interactions and can lead to changing water quality along even a single flowpath [*Chebotarev*, 1955]. Beyond quality, the magnitude and patterns of groundwater flow also control how quickly water flushes through a groundwater system, setting the renewal timescale of that system. Thus, the renewability of groundwater depends upon the hydrologic conditions and subsurface properties, with a range of relevant

timescales of groundwater flow within a single groundwater system. My dissertation will explore what renewability means physically for groundwater and estimate how much groundwater is physically renewed over various timescales with numerical models.

1.2. MOTIVATING QUESTIONS

My dissertation is focused around questions of how the dynamics of groundwater flow affect its availability from both quantity and quality perspectives: How do groundwater-surface water interactions change groundwater flow and thus the delivery of groundwater and its constituents in natural settings, and how does groundwater flow control its availability? Important to these questions are how to integrate multiple physical processes and properties over the relevant spatiotemporal scales.

My dissertation starts by addressing the questions of how do groundwater flow regimes interact with surface waters and how do these interactions affect water quality? I show how groundwater, solute, and energy fluxes in discharge zones result from groundwater-surface water interactions and field-scale hydrologic heterogeneity, ultimately controlling the groundwater quality at each field site. With these studies, I address the following questions:

1. How do groundwater-lake interactions alter groundwater discharge and recharge patterns and contribute to the local water quality?
2. How do groundwater dynamics in the subsurface intertidal zone affect the delivery of freshwater to the coast, alter the subsurface salinity distribution, and control the temperature dynamics?
3. How do geologic heterogeneities control how groundwater flows in coastal areas and into coastal waters?

Next, I explore the question of how groundwater flow controls renewal timescales at the global scale and its implications for groundwater quantity motivated by the following questions:

1. How much groundwater is renewed on a 50 year timescale?
2. How sustainable are current groundwater extractions based on a renewal timescale of 50 years?
3. What are the dominant timescales of groundwater flow on Earth?

My dissertation advances the understanding of how groundwater dynamics control the quality and quantity of groundwater. The ultimate purpose of my dissertation is to quantify the relevant timescales and characteristics of groundwater flow from the continental interior to coastal environments. The quantitative analyses can then provide insight into how groundwater processes affect and are affected by global and local issues of groundwater availability.

1.3. A GROUNDWATER MASS BALANCE FRAMEWORK

A groundwater mass balance integrates groundwater dynamics with groundwater storage, where recharge and discharge fluxes control changes in storage. Therefore, I structure my dissertation to first present my contributions towards better understanding and constraining groundwater flow at recharge and discharge features and their implications on groundwater quality. Then, building off of this foundation of quantified groundwater flow, I develop a quantitative framework for assessing groundwater renewability.

My first three chapters develop three field-based case studies that delineate how groundwater flow and hydrogeologic conditions contribute to other physical processes. In Chapter 2, I use electrical resistivity surveys in three lakes in the Nebraska Sand Hills to constrain groundwater-surface water interactions and the complexity of groundwater

recharge and discharge zonation throughout the lakes, transporting and controlling the distribution of salinity. Next, in Chapter 3, I investigate groundwater flow and heat transport below and through an intertidal zone, where groundwater controls the subsurface thermal and chemical regimes. Then, I discover and assess the impacts of larger-scale geologic spatial heterogeneity on the potential for groundwater flow and delivery of fresh water into a reef lagoon in Chapter 4. Finally, in Chapter 5, I use numerical simulations of groundwater age to estimate the stored volume of groundwater on Earth renewed in less than fifty years, while introducing a novel framework for quantifying physical groundwater renewability that integrates the temporal component of groundwater flow.

Chapter 2:

Classification and delineation of groundwater–lake interactions in the Nebraska Sand Hills (USA) using electrical resistivity patterns[1]

We have no waters to delight
Our broad and brookless vales—
Only the dewpond on the height
Unfed, that never fails—

- from "Sussex" by *Rudyard Kipling* [1902]

ABSTRACT

Lake-groundwater interactions exhibit a complex three-dimensional (3D) structure that is seldom studied. The utility of waterborne electrical resistivity (ER) surveys is explored for characterization of 3D groundwater flow and solute transport patterns for three lakes in the Nebraska Sand Hills, USA. Waterborne ER surveys, using contrasts between lake and groundwater solutes as natural tracers, are useful for inferring 3D patterns of groundwater flow and solute transport as well as classifying groundwater-lake interactions. Three unique groundwater flow systems are interpreted under each lake from dense networks of two-dimensional (2D) waterborne ER surveys. A lateral transition from high to low ER values beneath the saline Wilson Lake expresses its flow-through regime, where groundwater salinity indicates changes from groundwater inflow to outflow. Alkali Lake ER profiles reveal a prevalent ER increase with depth over the lakebed area that is characteristic of groundwater discharge lakes. ER profiles beneath Gimlet Lake are the most resistive and indicate pockets of high ER related to fresh groundwater discharge into the lake, supporting a flow-through regime with a short flushing time. These ER patterns correctly classify groundwater–lake interactions and

[1]Befus, K. M., M. B. Cardenas, J. B. Ong, and V. A. Zlotnik (2012), Classification and delineation of groundwater–lake interactions in the Nebraska Sand Hills (USA) using electrical resistivity patterns, *Hydrogeol. J.*, doi: 10.1007/s10040-012-0891-x.

All of the authors participated in the data collection and conceptual development of the project. I was responsible for the quantitative analysis of the data, preparation of the article.

provide high spatial resolution of mixing patterns for systems with varying water salinity. This chapter was published as part of a collaborative project [*Befus et al.*, 2012].

2.1. INTRODUCTION

Lakes fed by groundwater with no surface water inputs or outputs mark a unique hydrologic interface between terrestrial, aquatic, and atmospheric systems. Groundwater flow and precipitation into these lakes are only balanced by evaporative losses and any return seepage of lake water through the lakebed. Present and paleoclimatic conditions strongly control the solute concentrations and water balances of such lakes. In order to understand the physical, chemical, and biological dynamics of these lakes, knowledge of the spatial distributions of solute concentrations and fluxes around and underneath the lakes is needed.

Groundwater-lake interactions and their classification have been studied quantitatively and extensively with numerical and analytical models [e.g. *Winter and Pfannkuch*, 1984; *Townley and Trefry*, 2000; *Zlotnik et al.*, 2009; *Zlotnik et al.*, 2010]. In field studies [e.g. *Winter*, 1977; *Schneider et al.*, 2005; *Turner and Townley*, 2006; *Ong and Zlotnik*, 2011], estimation of groundwater fluxes in lakes is typically accomplished using lake water budgets, and/or monitoring the head gradients and solute concentrations in limited numbers of piezometers installed in lakebed and shore sediments [*Rosenberry et al.*, 2010]. More direct flux measurements are also possible with seepage meters but are often restricted to near or along the shore, and instrument installation is challenging in lakebed sediments which are typically fine-grained, easily disturbed from their natural state, and prone to clogging piezometer screens [*Rosenberry et al.*, 2010]. In addition, a few point measurements fail to characterize a substantial portion of the lake, which may lead to oversimplified conceptualization of groundwater-lake interactions and potentially inaccurate lake water budgets. Therefore, the delineation of groundwater flow and transport

beneath lakes and classifying the lake-groundwater connections remain important problems in hydrogeology and limnology.

Differences in electrical resistivity (ER) between surface water and groundwater can provide excellent tracers and targets for electrical and electromagnetic geophysical surveys [e.g. *Bauer et al.*, 2006; *Ong et al.*, 2010; *Cardenas and Markowski*, 2011]. ER imaging has the potential to noninvasively capture the configuration and various characteristics of groundwater flow systems beneath lakes and wetlands [*Day-Lewis et al.*, 2006; *Mansoor and Slater*, 2007; *Nyquist et al.*, 2009; *Toran et al.*, 2010]. While previous studies have utilized both natural and anthropogenic tracers in various settings, ER surveys have not been used for classifying lakes as groundwater 'discharge' or 'flow-through' lakes.

To analyze the differences in groundwater-lake interactions among various lakes, continuous resistivity profiles (CRP) were conducted across several kilometers within three small lakes (< 0.5 km^2) in the Nebraska Sand Hills (NSH), USA. A series of 2D profiles, organized in networks in each lake, elucidate the 3D ER patterns of lake-groundwater fluxes; however, the survey density was not sufficient for 3D inversion of the data. Interpretation of these surveys guide the classification of the lake-groundwater hydrologic system and delineate the potential spatial distributions of groundwater discharge and recharge zones within the lakes. This study also reveals the utility of waterborne CRP as a rapid, noninvasive, and robust method for determining 3D groundwater flow and solute distribution under lakes, especially in difficult settings.

2.2. HYDROLOGY AND HYDROGEOLOGY OF THE NEBRASKA SAND HILLS

The NSH are the largest vegetated dune field in the western hemisphere, covering an area of 58,000 km^2. The NSH experiences continental climate with an annual rainfall of

533 mm and a mean temperature of about 10 °C [*Szilagyi et al.*, 2011]. It hosts thousands of perennial and ephemeral lakes typically found in interdune areas. Pronounced geochemical variability among these lakes has been hypothesized to be primarily controlled by how the lakes interact with groundwater [*Labaugh*, 1986; *Gosselin et al.*, 1994; *Bennett et al.*, 2007]. Lake water total dissolved solids (TDS) in the region ranges more than three orders of magnitude (0.32-122 g/L) whereas the groundwater remains much fresher with two orders of magnitude less TDS than the lakes (0.13-1.7 g/L) [*Ong et al.*, 2010].

According to Loope et al. [1995] and references therein, the dunes of the NSH overlie between 150 and 300 m of late Cenozoic coarse clastic deposits that are part of the Ogallala or High Plains aquifer. Unconsolidated Quaternary fluvial sands, eolian sand sheets, and Pliocene fluvial sand and gravel separate the Quaternary dune sand from the underlying Miocene Ogallala Group. The eolian dunes comprise about 80% of the total sediment volume of the NSH. The thickness of Quaternary eolian sand ranges from <10 m, below interdune surfaces, to up to 20 m. In general, lakebed stratigraphy in the NSH is composed of < 2 m of lacustrine mud (gyttja), sometimes contains peat layers of variable thickness, and is underlain by eolian sand [*Loope et al.*, 1995]. This stratigraphy varies spatially within individual lakes depending on depositional and hydrologic lake history [*Loope et al.*, 1995; *Ong and Zlotnik*, 2011].

There is little runoff in the NSH due to high soil hydraulic conductivity [*Wang et al.*, 2009] which promotes infiltration. The area is therefore considered an important recharge area for the High Plains aquifer [*Szilagyi et al.*, 2011], where regional groundwater flow is generally towards the east or southeast (Figure 2.1). The productive, conductive, and regionally extensive aquifer system interacts with diverse dune and lake morphology to result in a variety of groundwater-lake exchange regimes [*Winter*, 1986;

Ong et al., 2010]. As the highly variable lake chemistry suggests, significant local hydraulic gradients near lakes alter local groundwater flowpaths [*Zlotnik et al.*, 2009]. The NSH is therefore an ideal site for investigating groundwater-lake interactions and testing approaches for doing these studies.

While there have been numerous hydrogeologic, geochemical, and geophysical studies conducted in the vicinity of the lakes in the NSH [*Labaugh*, 1986; *Winter*, 1986; *Gosselin et al.*, 1994; *Bennett et al.*, 2007; *Ong et al.*, 2010; *Ong and Zlotnik*, 2011; *Zlotnik et al.*, 2012], especially in recent years, a three-dimensional understanding of the groundwater flow and transport regime directly underneath the lakes is lacking due to the difficulty of conducting observations within the lakes. Detailed understanding at such scales is recognized as a critical gap in groundwater-surface water interaction studies [*Sophocleous*, 2002]. This report expands on and complements the past hydrogeologic studies in the NSH while helping fill a broader knowledge gap.

2.3. METHODS

Exploiting the electrical properties supplied by the TDS contrast between lake water and groundwater, three groundwater-fed lakes with different flow regimes were investigated (Figure 2.1) [*Ong et al.*, 2010]: Wilson Lake is a saline, groundwater flow-through lake; Alkali Lake is a saline, groundwater discharge lake; and Gimlet Lake is a freshwater flow-through lake. Shallow subsurface materials are eolian sands, silts, and clays with predominantly sands forming the dunes and finer materials settling to the lakebeds [*Loope et al.*, 1995]. The lakebed stratigraphy in the dune environment may vary across individual lakebeds with interbedded deposits of paleo-lacustrine and eolian sediment [*Loope et al.*, 1995; *Ong and Zlotnik*, 2011]. This potential stratigraphic

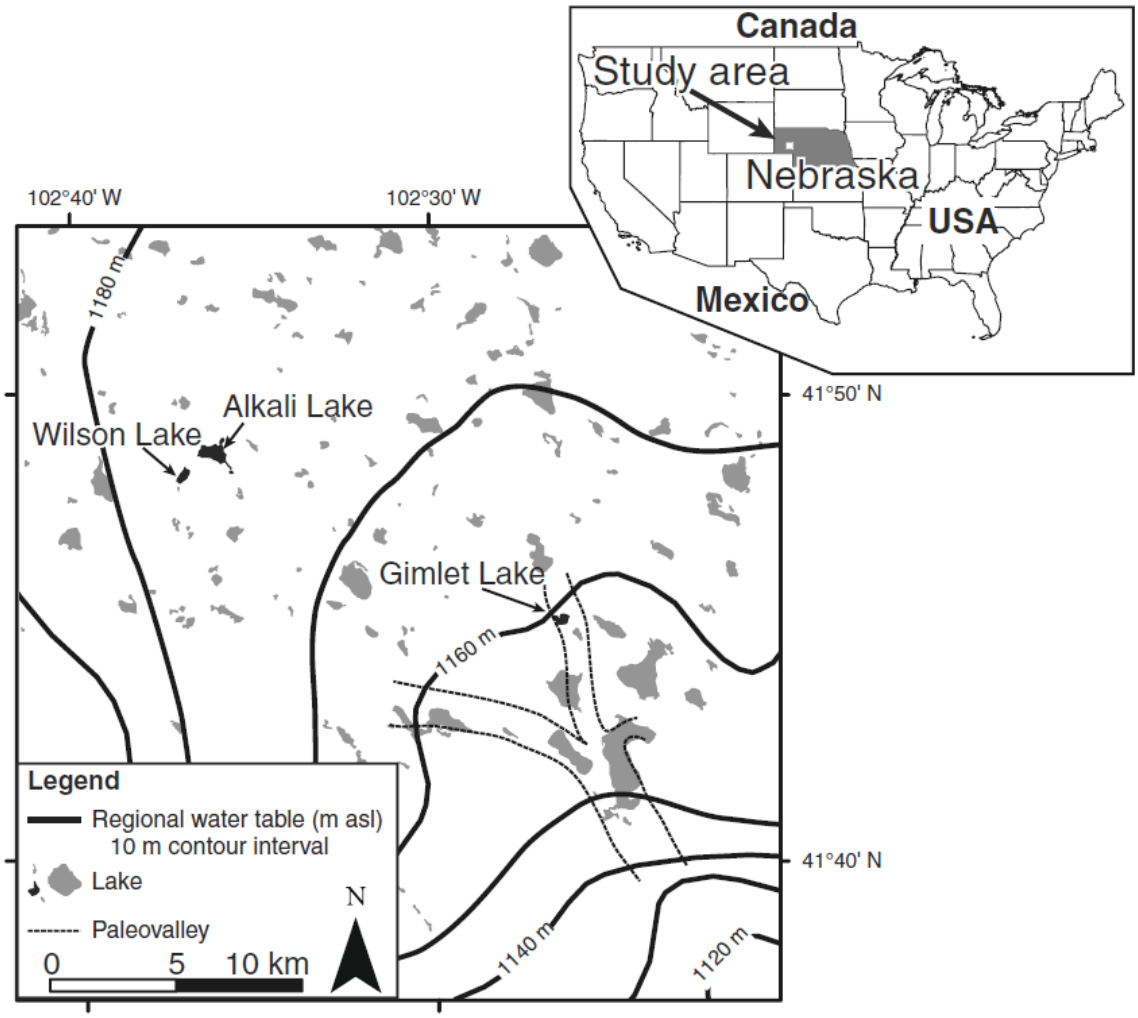

Figure 2.1. Location of Wilson, Alkali, and Gimlet Lakes, and water table map of the Western Nebraska Sand Hills (modified after *Ong et al.* [2010]). The regional groundwater flows towards the southeast. A hypothesized paleovalley in the study area also influences groundwater flow [*Loope et al.*, 1995].

complexity contributes to the electrical signal measured with CRP, requiring careful interpretation of hydrologic phenomena from the ER profiles. In locations with high fluid conductivity, the fluid may govern the bulk resistivity and overcome the influences of sediment ER variability [*Zarroca et al.*, 2011]. High lake water conductivity in Wilson and Alkali Lakes suggests most variations in ER were due to porewater TDS, rather than to variability of lakebed sediment composition and texture. The fresher Gimlet Lake requires consideration of spatial variations in lakebed sediment composition.

2.3.1. Continuous Resistivity Profiling (CRP)

The CRP surveys were recorded with the Advanced Geosciences, Inc. (AGI) Marine SuperSting R8 eight-channel ER system. Details of the method can be found in Day-Lewis et al. [2006] and Rucker et al. [2011]. Surveys were conducted using a floating cable with eleven electrodes at 5 m spacing. Two graphite electrodes transmit electrical current while the remaining stainless steel electrodes are paired into eight dipoles which measure the potential field. The electrode array was towed behind a boat moving with a speed less than 2 km/hr and following a marching dipole-dipole configuration. As the electrode array is translated, an integrated GPS device and sonar recorded position and water depth; the sonar transducer also simultaneously measured lake water temperature.

CRP surveys were conducted in May 2010 when the lakes were full enough to use a 3-m boat with a trolling motor; this was an opportunity that very seldom occurs in Alkali and Wilson Lakes. During data collection, water depths in the three lakes ranged from 0.3 to 1.7 m along the survey lines. Strong winds, sometimes above 7 m/s, at times interfered with data collection by pushing the boat off course or by stopping forward motion. The wind occasionally created slack or multiple bends in the CRP cable that alter the electrode

configuration and break the 2D inversion assumption of aligned quadripoles, leading to ER artifacts in the inverted sections. These portions of the CRP data were not included in the inverted datasets.

Several limitations of CRP require consideration when choosing the inversion procedure and then later when interpreting the results. By towing the resistivity array, repeat and reciprocal measurements that are common for ensuring data quality in land-based ER surveys cannot be collected easily. Slow towing speeds allow some repeat measurements with the danger of wind, waves, or currents deforming the array, introducing geometrical errors. Other measurement errors may arise from high boat speeds causing electrode cavitations, vegetation getting tangled on electrodes, or damaged cables with internal shorts [*Day-Lewis et al.*, 2006]. Prior to inversion, errors associated with random noise and other sources must be eliminated. If left in the inverted dataset, these errors could bias the resulting tomogram towards extreme values. To counter the effects of errors and to represent subsurface electrical fields more faithfully, ER inversion solves for a smoothly varying ER profile, where the amount of smoothing is specified in the inversion settings. Even for clean datasets, the inversion process will smooth the final ER profile to varying degrees and introduce correlation error [*Day-Lewis et al.*, 2005]. Thus small ER features in the subsurface with very different ER values from the background material will appear as broader anomalies with lower magnitude ER values in the inverted section [*Day-Lewis et al.*, 2006].

2.3.2. Inversion and post-processing

Post-processing involved: (1) manual separation of the surveyed lines into straight sections, (2) incorporation of water depth data, and (3) piecewise, 2D data inversion using the CRP module of the AGI EarthImager software with a 65% overlap of consecutive sub-

sections. A smooth model inversion method was used with data quality and inversion settings listed in Table 2.1. Convergence of ER sub-sections took 4 to 6 iterations with final RMS values from 3% to 9%.

The 5 m spacing dipole-dipole array used for the CRP surveys has a maximum investigation depth of ~12 m from the air-water interface but also depends on the electrical conductivity of the water and subsurface sediments. The high lake water conductivity and the fine-grained bed sediments at the lake bottom (~1-2 m) caused low inverse model sensitivity in some areas of Wilson and Alkali Lakes (Figures 2.2-4).

Lower relative model sensitivity indicates the observed data have less control over the inverted ER value. Inversion of ER data requires an electrical potential forward modeling step that pads the inversion domain with additional grid cells. These grid cells extend beyond the CRP data but can affect the final CRP ER section. Thus the sides and bottom of an inverted CRP section may contain incorrect values discernible only with the model sensitivity analyses. Alkali and Wilson Lakes data exhibit favorable model sensitivity magnitude ($> 1x10^{-3}$) to 4-6 m depth below the air-water interface, and the fresher Gimlet Lake keeps these values to depths of 10-12 m (Figures 2.2b-4b). However, the shallow water depth in Alkali and Wilson Lakes (0.3-0.7 m) resulted in sufficient magnitude of electrical fields to be measured by the furthest dipoles (Figures 2.2-4), so the reduced depth penetration is a function of the ER structure and is not an artifact of noise; the noise in the transfer resistance remained low (< 5%) and was consistent when compared to a low-pass filtered version of the data (Figures 2.2a-4a) [*Rucker et al.*, 2011].

The measured resistance values also provide insight into the quality of CRP data by displaying anomalously high and low resistances for a dipole that indicate bends in the cable either from turning the boat or from slack in the CRP cable. The measured resistance in both Wilson and Gimlet Lake show the effects of including a portion of the data that

Table 2.1. Settings for the smooth model inversion in AGI EarthImager 2D.

Data Quality	**Forward Modeling**
Min voltage: 0.02 mV	Method: Finite element
Max repeat error: 3%	Equation solver: Cholesky decomposition
Min app res: 0.03 Ωm	Boundary condition: Dirichlet
Max app res: 1000 Ωm	# Mesh divisions: 1
Remove spikes: Yes	Thickness incremental factor: 1.1
Remove negative resistivity:Yes	Depth factor: 1.1

Resistivity Inversion
Stop Criteria: 8 iterations, 3% max RMS error, or L2 Norm
CG iterations: 6
Starting iteration of Quasi-Newton method: 20
Smoothness factor: 100
Damping factor: 100
Starting model: Average apparent resistivity
Min ER: 0.1 Ωm
Max ER: 1000 Ωm
Horizontal to vertical roughness ratio: 0.1
CRP Module > Number of electrodes per section: 250
CRP Module > Overlap: 60% (150 electrodes)
CRP Module > Fix water resistivity: No

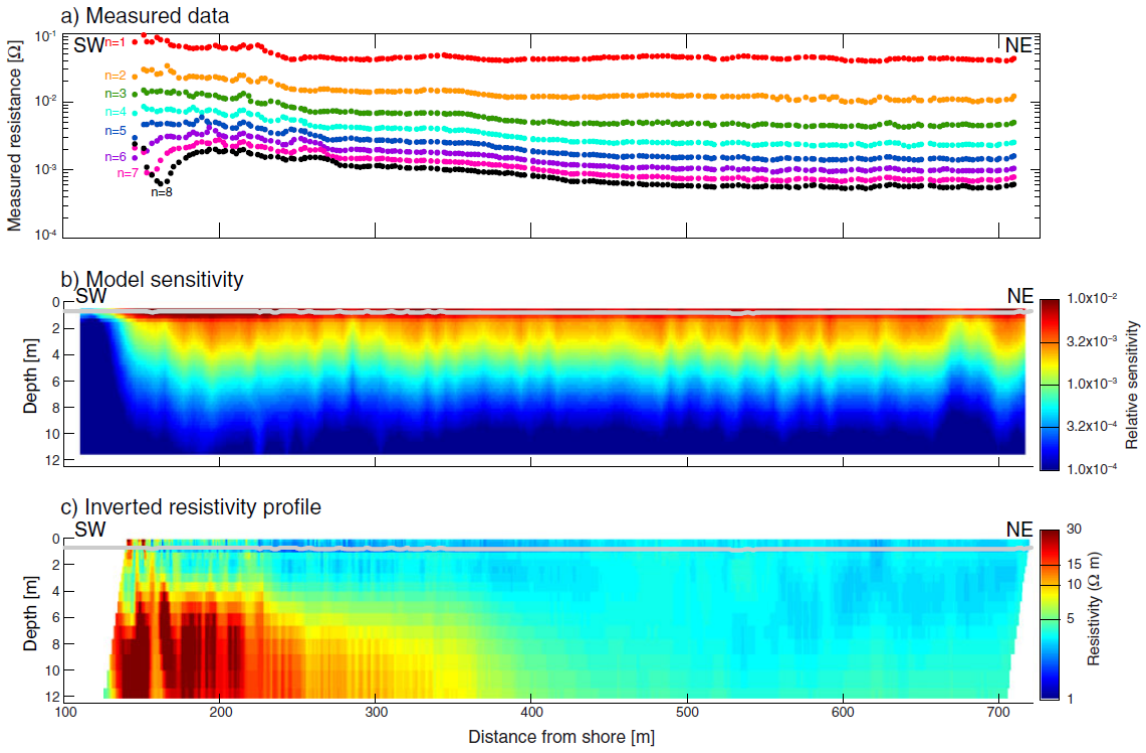

Figure 2.2. Wilson Lake example section: a) recorded transfer resistance data for each potential dipole as a function of distance from the southeast shore (location of origin marked in Figure 2.5a); b) inverse model sensitivity giving a relative confidence of data control over model values; c) inverted ER profile that has been adjusted to a 20°C standard temperature. The grey line marks the sediment-water interface recorded during CRP collection.

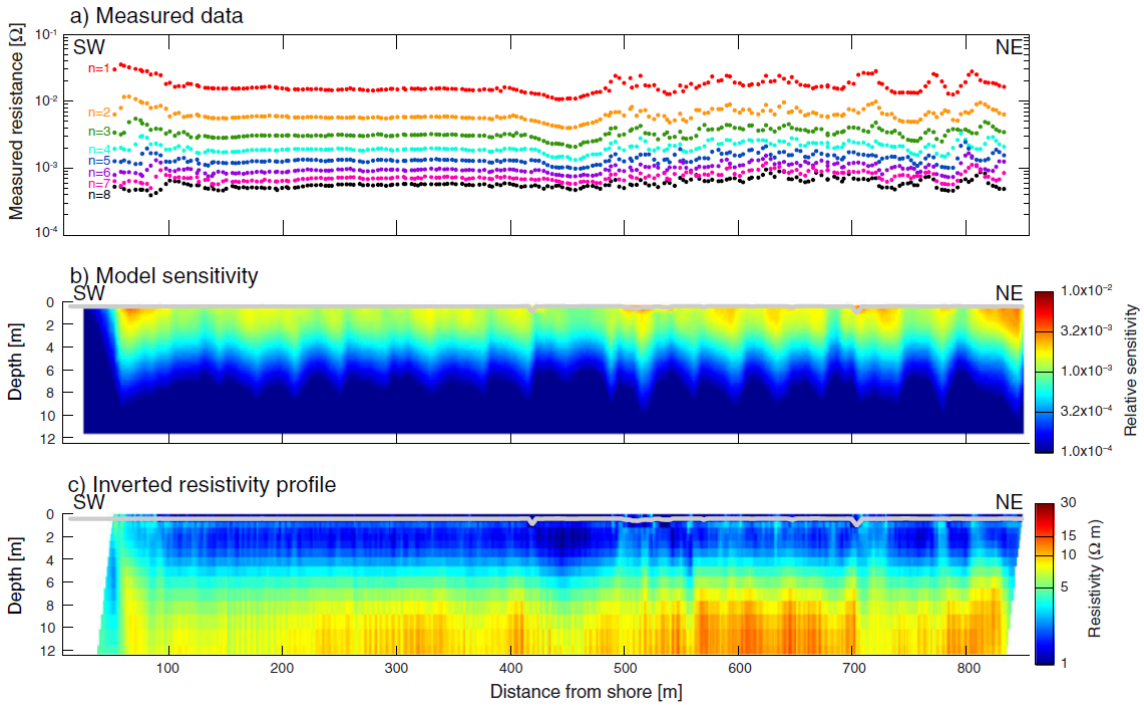

Figure 2.3. Alkali Lake example section: a) recorded transfer resistance data for each potential dipole as a function of distance from the southeast shore (location of origin marked in Figure 2.5b); b) inverse model sensitivity giving a relative confidence of data control over model values; c) inverted ER profile that has been adjusted to a 20°C standard temperature. The grey line marks the sediment-water interface recorded during CRP collection.

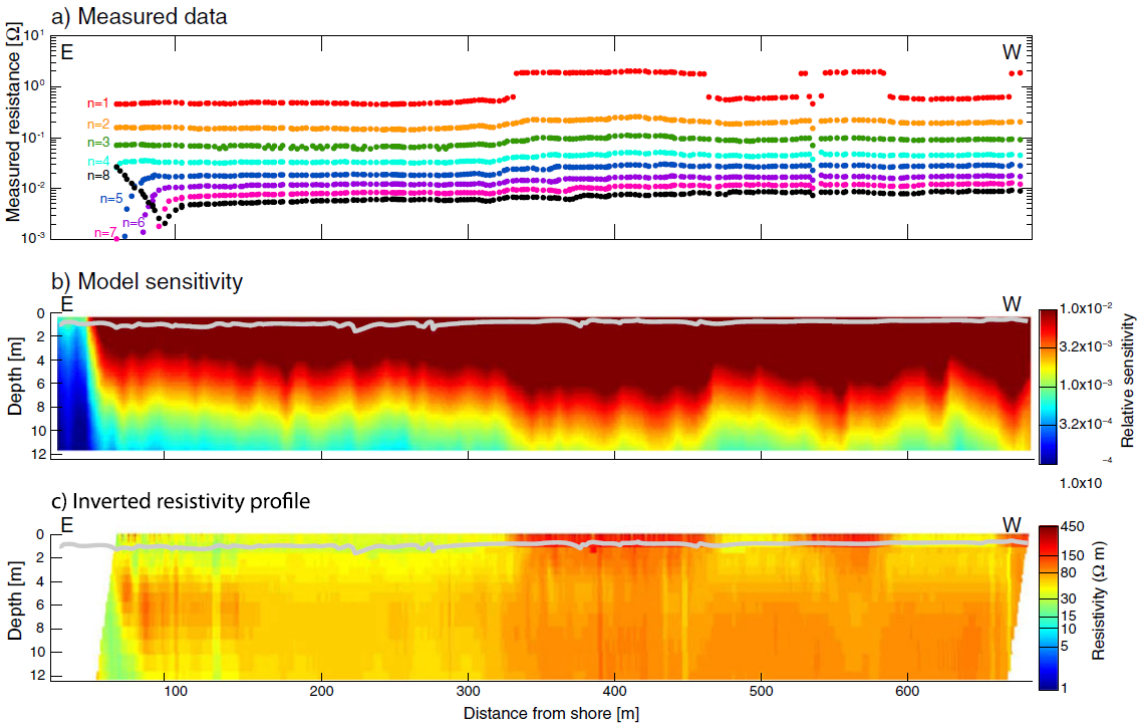

Figure 2.4. Gimlet Lake example section: a) recorded transfer resistance data for each potential dipole as a function of distance from the southeast shore (location of origin marked in Figure 2.5c); b) inverse model sensitivity giving a relative confidence of data control over model values; c) inverted ER profile that has been adjusted to a 20°C standard temperature. The grey line marks the sediment-water interface recorded during CRP collection.

was collected just after the boat turned (Figures 2.2a and 4a). In this case, the unaligned dipoles are closer to the current injection, leading to lower resistance values. When inverted, these erroneous values create false conductivity regions (e.g. 50-80 m in Figure 2.4c).

Good quality raw data and reasonable inversion results did not require further data removal or repeated inversions; data with marginally higher misfits after inversion were removed for different profiles and inverted without significant decreases in data misfit or changes to the resulting inverted ER profile. A single lake water electrical conductivity measurement was recorded in each lake with a YSI-3000 T-L-C meter. This single measurement is a reasonable representation of an average lake water column resistivity due to strong winds mixing the lake water and a very low groundwater seepage rate [*Ong*, 2010]. At the time of recording, the lakes fit the physical characteristics of well-mixed lakes, which were assumed would require only one lake water conductivity sample. In the inversion, water ER was not constrained or set to a constant value to allow for salinity variations imposed by groundwater-lake water exchanges evident in the recorded temperature and raw ER data.

Detectable but subtle changes in lake water temperature across the lakes were found in spite of strong winds and shallow water depths (Figure 2.5). Both Wilson and Gimlet Lakes were surveyed in a single day and less than 4 hours each. Unlike salinity, temperature distribution is more variable, especially laterally as was found in similar lakes [*Tcherepanov et al.*, 2005]. Wilson and Gimlet Lake temperature patterns show 0.5-1.0°C decreases in surface water temperature towards the northeast and southeast, respectively. Alkali Lake surveys were collected over three mornings to exploit calmer lake conditions. Variability in air temperature on these three days dominates the lake water temperature patterns recorded in Alkali Lake and cannot be used to interpret lake-groundwater

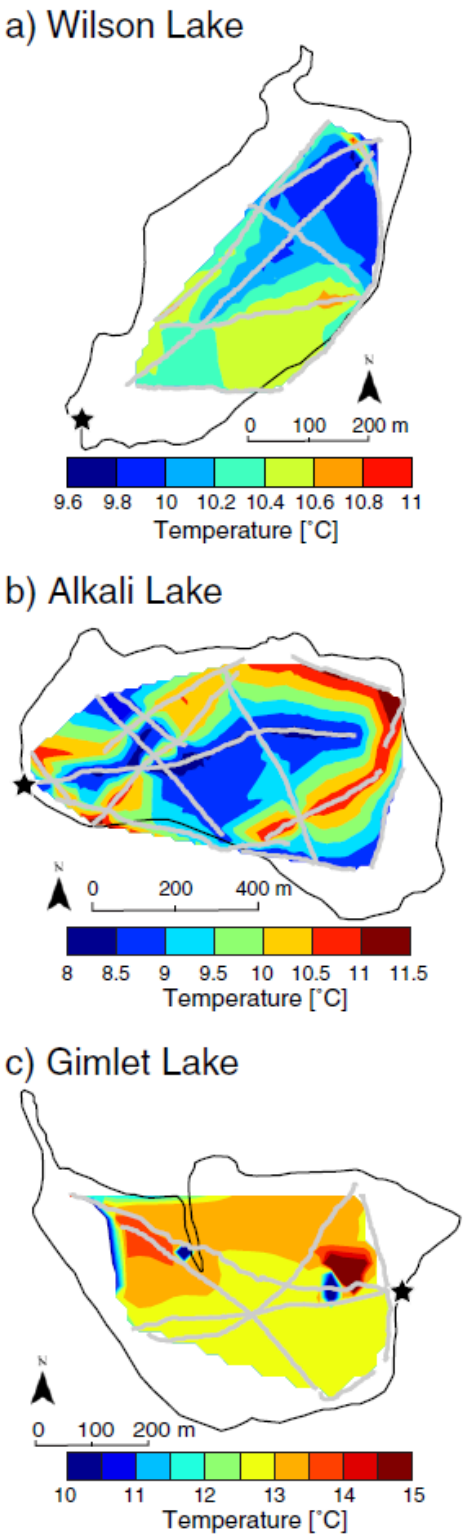

Figure 2.5. Recorded lake water temperatures during CRP data collection in a) Wilson Lake, b) Alkali Lake, and c) Gimlet Lake linearly interpolated between survey lines (grey). Stars mark the origin for the individual profiles in Figures 2.2-2.4.

interactions (Figure 2.5b). Since ER is also a function of temperature, measured ER values were corrected to 20°C based on the geo-referenced lake water temperature measurements using [*Keller and Frischknect,* 1966]:

$$\rho_0 = \rho_T [1+\alpha(T-T_0)] \quad (2.1)$$

where ρ_T is the ER at ambient temperature T [°C], ρ_0 is the ER at a reference temperature T_0, and α describes how ER changes with temperature and ranges between 0.017-0.023 [$°C^{-1}$] [*Revil et al.*, 1998; *Hayashi*, 2004; *Hayley et al.*, 2007]. A conservative estimate for sand and clay mixtures is α=0.018$°C^{-1}$ [*Hayley et al.*, 2007]. For the profiles, larger α values increase the contrast between the high and low ER values in the CRP data; high ER areas correspond to higher temperatures and low ER areas occur where lower lake water temperatures were recorded. Reasonable values of α applied to the ER data result in a maximum amplitude error of 3 Ωm for all recorded ER values. Vertical thermal variations were not used to adjust ER values because subsurface temperatures were not recorded. Thus, the temperature correction was applied uniformly to vertical ER data slices based on the lake water temperature recorded by the sonar transducer.

Since the lakes were very shallow, sonar data were sparse and did not provide adequate resolution to be used for water resistivity corrections. These sparse data and erroneous depth readings led to prominent artifacts in the inversions when constraining water resistivity values. Although assigning lake water depth and a water resistivity value may improve the ER model resolution and more accurately describe the true resistivity distribution below the sediment-water interface [*Day-Lewis et al.*, 2006], unconstrained inversions can still adequately describe water column resistivity changes and yield similar resistivity results to the constrained inversion [*Amidu and Dunbar*, 2008].

Assigning the depth of the transition zone between fresher groundwater and saltier lake water requires the application of a petrophysical model to distinguish between ER signals from porewater chemistry and sediment conductivity. Porewater resistivity values can be calculated with Archie's Law [*Archie*, 1942], which describes the relationship between bulk and fluid resistivity and sediment porosity:

$$F = \rho_b / \rho_f = \alpha\, n^{-q}\, S^{-\kappa} \qquad (2.2)$$

where the formation factor (F) is the ratio of the bulk resistivity (ρ_b) to the fluid resistivity (ρ_f) and is related to the effective electrical tortuosity (α), porosity (n), a cementation factor (q), fluid saturation (S), and a saturation factor (κ). Local lakebed sediment have an estimated n=0.3 [*Zlotnik et al.*, 2010]. Sediment under the lakes are assumed to be saturated (S=1). In general $\alpha \approx 1$ [*Ewing and Hunt*, 2006], especially if the pores are electrically well-connected as expected for n=0.3 in unconsolidated material with conductive porewater. Without experimental data, q remains a fitting parameter for assigning an appropriate petrophysical model. For unconsolidated sediment $q \approx 2$ [*Ewing and Hunt*, 2006], and the ER data are interpreted considering a range of q from 1.8-2.2. With these parameters, F=8.7-14.1. Inherent to these parameter estimations is an assumption that they represent the characteristic properties of the subsurface, integrating and averaging the effects of any heterogeneity in the subsurface.

2.4. Results and Discussion

2.4.1. Wilson Lake

Eight straight segments of 2D CRP profiles with total a length of 2.7 km were extracted from 3.0 km of raw data collected at Wilson Lake (Figures 2.5 and 2.6c). Mean water depth was 0.7 m and did not exceed 1.0 m, while the adjusted lake water ER was

1.35 Ωm, collected off the northeastern shore. The ER depth of investigation extends at least 7 m into the lakebed sediments, but resolution decreases with depth (Figure 2.2b). An overview of lake properties during the survey period and CRP results is given in Table 2.2.

Based on the measured Wilson Lake water ER, the expected ρ_b for materials containing only lake water is between 11.8-19.0 Ωm. Applying Archie's Law to the Wilson Lake ER results, values greater than ~15 Ωm describe pore fluids that are fresher than the measured lake water. Resistivity values above this threshold are observed mainly in the southwest portion of Wilson Lake with resistivities below 15 Ωm towards the northeast. The resistivity values > 15 Ωm occur from 3 m below the water level in the southwest, and this transition zone becomes gradually deeper towards the middle of the lake (Figures 2.2c and 2.6c). These values extend 250-350 m into the lake from the southwest shore before the bulk sediments become more conductive (Figures 2.2c and 2.7a).

TDS is inversely related to ER, and the TDS of the groundwater in the NSH in general is much lower than that of lake water. The lower ER values correspond to areas with higher TDS and indicate the lake water as its source, while higher ER and the lower TDS indicate the deeper, fresh groundwater as a source. As a broad, shallow (<0.5 m) lake under normal conditions, groundwater flowing into Wilson Lake would evaporate and concentrate ions in the lake water, increasing the salinity and lowering the ER of the original groundwater discharged into the lake over time. The more saline lake water is driven by advection into the subsurface and mixes with fresher groundwater following theoretical models by *Townley and Trefry* [2000] and *Zlotnik et al.* [2009]. This lake clearly indicates a transition that separates a lakebed section with upward fluxes from a zone that releases solutes back to the aquifer; this is often called a "hinge" line (see Figure 1 in *Ong et al.* [2010] for illustration of the conceptual flow model). The transition from high to low

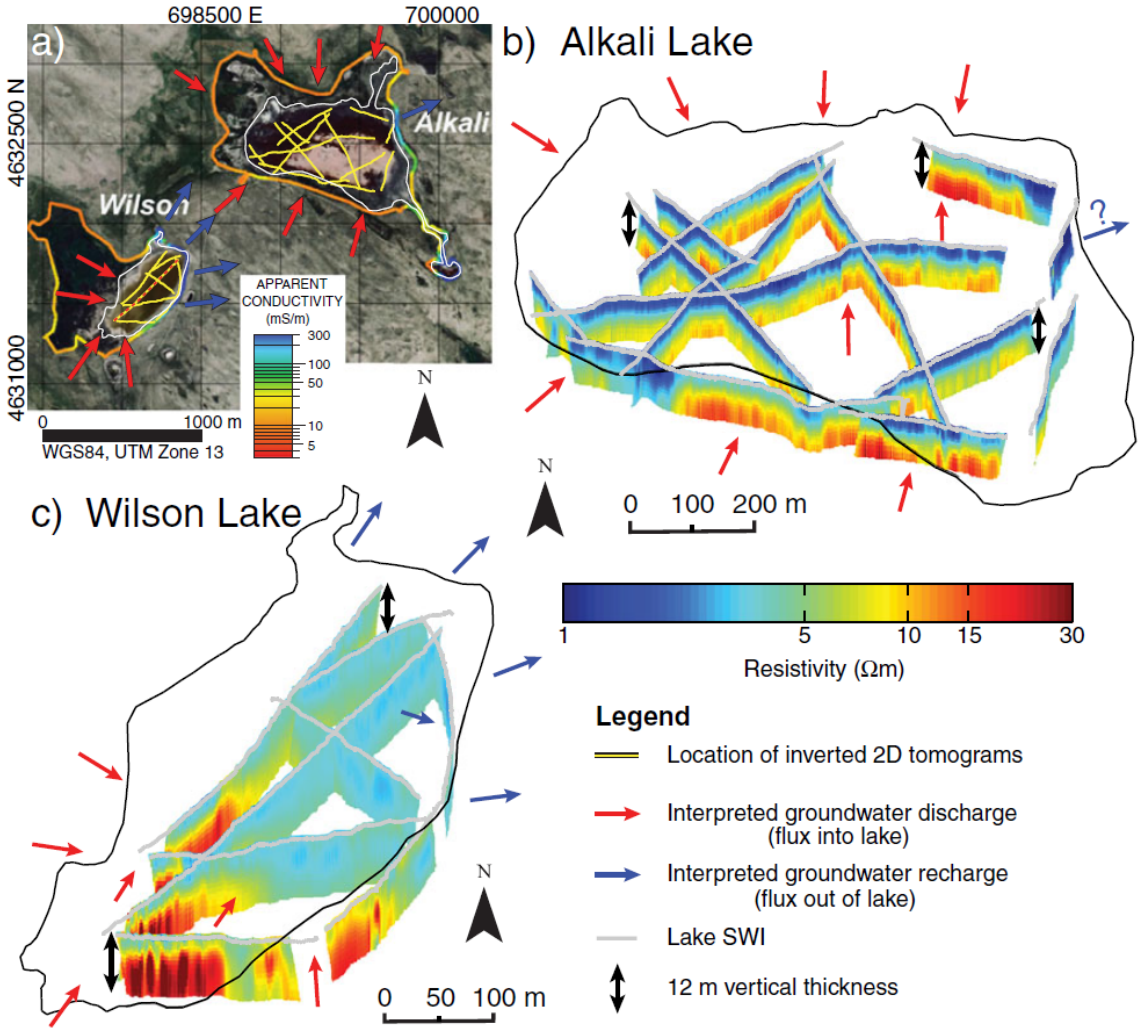

Figure 2.6. ER profiles within Wilson Lake and Alkali Lake image patterns of fresh groundwater and saline lake water fluxes around and beneath the lakes: a) groundwater flow directions interpreted using EM and ER surveys around the lakes and CRP results, modified after *Ong et al.* [2010] (note units for apparent electrical conductivity); b) increasing resistivity with depth in Alkali Lake (0.3-1.0 m lake depth; 0.5 m mean) is an indicator of a groundwater discharge lake; c) transition from higher ER values at the southwest area to significantly lower ER values at the northeast subsurface of Wilson Lake (0.4-1.0 m lake depth; 0.7 m mean), indicating the inflow of fresh groundwater below the lake in the southwest and outflow of saltier lake water to the aquifer in the north. Note exaggeration of vertical scales.

resistivity values from the southwest to northeast of Wilson Lake indicates fresher groundwater below the lake changes to more conductive groundwater, interpreted as lake water that recharged the aquifer, with a hinge line trending roughly southeast-northwest. The CRP lake water temperature data (Figure 2.5) also show a similar pattern that becomes cooler towards the northeast, where groundwater is ~10°C and the air temperature during surveying was 5-8°C. These transitional ER and temperature patterns verify the flow-through groundwater regime of Wilson Lake and give an indication of local groundwater flow. The fresher groundwater seeps upward from the underlying aquifer into the southwestern third of Wilson Lake. Groundwater underneath the lake becomes more saline towards the middle of the lake as the saltier lake water infiltrates and mixes with the fresh groundwater. Eventually, further towards the northeast shore, the CRP lines suggest saline lake water is recharging into the lakebed and flowing into the aquifer. Note that the Wilson lakebed is very sandy [Ong and Zlotnik, 2011]. For the transition of ER to be dominated by sediments, over 7 m of gyttja would be required in the northeast portion of Wilson Lake that quickly transitions quickly to < 1 m along the southeast shoreline.

These observations of lake-groundwater interactions extend similar results from previous land-based electromagnetic (EM) surveys along the shoreline and ER surveys at the northeast shore of Wilson Lake (Figure 2.5a here and Figure 5 in *Ong et al.* [2010]). With the CRP data, the signature of the groundwater flow under the lake demonstrates the groundwater-surface water mixing zones both laterally and with depth (Figure 2.7). The interpreted northeast-trending groundwater flow is inconsistent with the southeast-trending regional hydraulic gradient (Figure 2.1), suggesting a local hydraulic gradient set by lake-lake or lake-groundwater interactions. Around the southern shoreline, high ER values persist further north than in the center of the lake, where local recharge from nearby dunes may sustain shallow flow paths that are directed opposite the regional flow. Evaporative

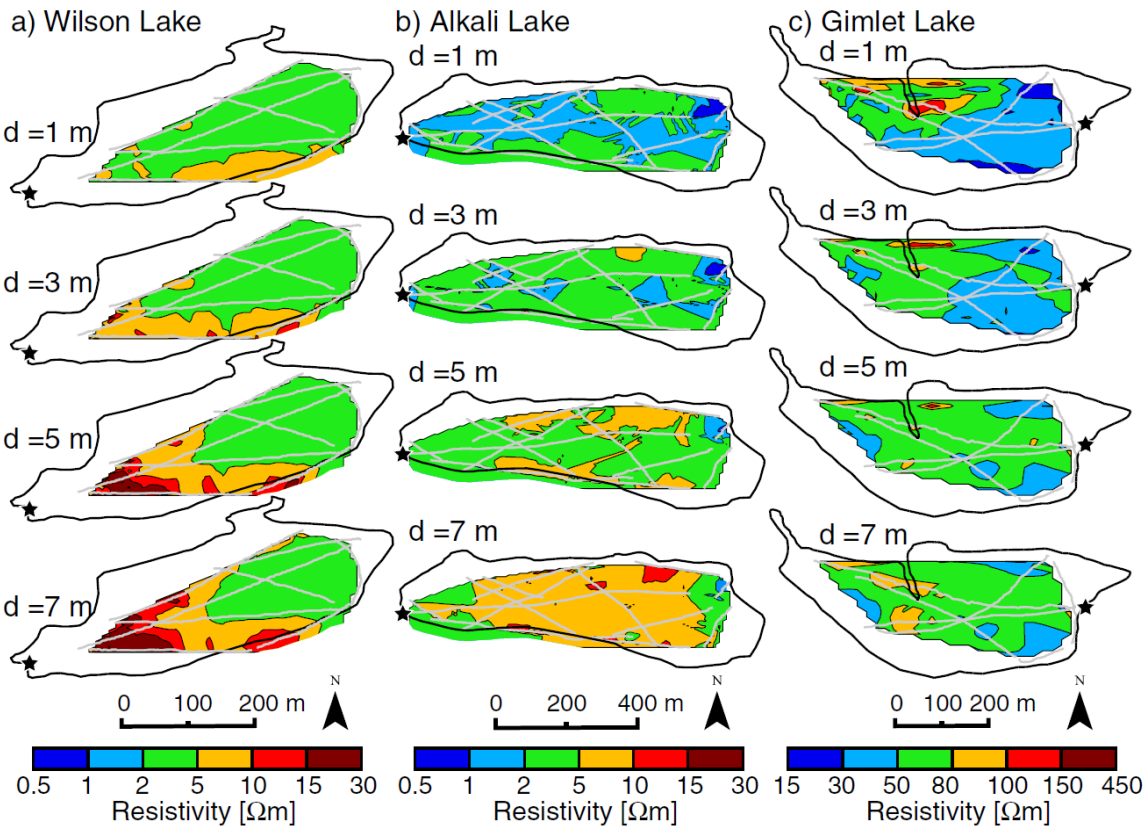

Figure 2.7. ER depth sections for a) Wilson Lake, b) Alkali Lake, and c) Gimlet Lake taken at depths of 1 m, 3 m, 5 m, and 7 m below the air-water interface. ER values between transects were linearly interpolated to create the depth section. Three-dimensional inversion of CRP data requires much closer spacing of survey lines but yields a more accurate estimate of the ER structure than interpolating between 2D sections. The grey CRP survey tracks represent the highest confidence in the depth section estimates. Beyond the survey tracks, the depth section accuracy decreases, especially in areas not bounded by a survey line (e.g. northern edge of Gimlet Lake depth sections). These depth sections provide insight into the subsurface 3D ER structure, but a much denser network of CRP surveys would be required to fully capture the true ER structure under the lakes. Stars mark the origin for the individual profiles in Figures 2.2-2.4.

Table 2.2. Overview of lake properties and CRP data.

Lake water properties	Wilson Lake	Alkali Lake	Gimlet Lake
Surface area[1] [ha]	19.2	50.3	24.5
Flow classification[2]	through	discharge	through
Temperature [°C]	9.6	7.5	14.2
Electrical conductivity [mS/cm]	6	30	0.62
Electrical resistivity [Ωm]	1.67	0.33	16.26
Temperature corrected ER [Ωm]	1.35	0.26	14.56
ER range in subsurface [Ωm]	11.8-19.0	2.3-3.7	78.1-119
CRP data			
CRP length (total) [km]	2.7 (3.0)	5.3 (9.0)	2.6 (2.8)
Lake depth range [m]	0.3-1.0	0.3-1.0	0.5-1.7
Lake depth mean [m]	0.7	0.5	0.9
Temperature range [°C]	9.7-11.3	8.2-11.6	13.0-14.4
Temperature mean [°C]	10.2	9.7	13.3
CRP ER range[Ωm]	1.5-567	0.2-29.2	9.2-334.7
CRP ER mean [Ωm]	6.5	4.1	67.8

[1]after *Ong et al.* [2010]
[2]following classification by *Born et al.* [1979]

losses from neighboring Alkali Lake may sustain a sufficient local gradient to overprint the regional flow system. This is discussed further with additional evidence from Alkali Lake CRP data in *Section 2.4.2*.

ER data cannot give estimates of seepage rates, but these data can guide the installation of seepage meters to capture the distribution of groundwater fluxes across the lake [*Toran et al.,* 2010]. To my knowledge, this is the first example of using ER for classifying a shallow groundwater-fed lake in a semi-arid environment.

2.4.2. Alkali Lake

Survey data with a total length of 5.3 km comprising thirteen 2D CRP sections were selected and processed from 9.0 km of raw data from Alkali Lake (Figures 2.3 and 6b, Table 2.2). Water depth ranged from 0.3 to 1.0 m with a mean of 0.5 m. Lake water ER was 0.26 Ωm. The lowest ER values of the three lakes were observed in Alkali Lake profiles (0.2-29.2 Ωm) and reached the resistivity of sea water (0.2 Ωm). At depths > 4 m, the ER profiles mostly show ER values above 4 Ωm, where any value over 2.3-3.7 Ωm suggests a groundwater component for the pore fluids. This supports the model by Zlotnik et al. [2010] where the deeper, fresher groundwater flows upwards throughout most of the lakebed, resulting in vertically increasing solute concentration towards the lake surface. The majority of Alkali Lake CRP data show a spatially uniform increase in ER with depth (Figure 2.7b). This may mean the saline and denser lake water has not initiated free convection at a resolution that CRP can capture, which is likely prevented and counteracted by the upward flowing fresher groundwater [*Ong and Zlotnik,* 2011]. Also, the wet months and greater fluxes of fresh groundwater into the lake preceding the survey allowed boat navigation but diluted the lake water. These combined freshening effects would further

lower the potential for free convection that may exist during long term average climate conditions.

Thus, the ER data suggest Alkali Lake is predominantly a groundwater discharge lake which is consistent with observations of upward seepage at five more or less evenly spaced areas along the banks of the lake (see Figure 2 in *Ong and Zlotnik* [2011]). In a small area towards the northeast corner of Alkali Lake, low ER values occur at depth. This area, where *Ong et al.* [2010] observed high electrical conductivity along the shore, suggests a small zone where saline water from Alkali Lake may seep into the lakebed and sink. However, seepage fluxes (or head gradients) have not been quantified where there is evidence for saline discharge from Alkali Lake, so downward fluxes due to density gradients or very local hydraulic gradients causing outflow or inflow of lake water cannot be ruled out completely. Finer lakebed sediments could explain low ER values at depth, but this portion of Alkali Lake contains sandy material at least along the shore to depths of 1 m [*Ong and Zlotnik*, 2011] and deeper as shown by lakebed coring [*Ong*, 2010]. Therefore, the high salinity of the lake water suggests the ER values are more likely related to porewater chemistry and not due to more electrically conductive fine-grained sediment. Moreover, ER transects near this zone but further away from the bank show a conductive area which may be part of the groundwater plume sourced from the lake (see Figure 5b in *Ong et al.* [2010]).

In the southwest corner of Alkali Lake, CRP transects show another area of low ER values (< 5 Ωm) that persists beyond depths > 5 m. These values correspond to ER values from the northeastern portion of Wilson Lake that were interpreted as saline water recharging the lakebed and aquifer (Figure 2.7). Together, these similar ER values may outline a series of groundwater flowpaths starting from Wilson Lake and then discharging salty groundwater into Alkali Lake, 640 m away. In order for groundwater to flow from

Wilson Lake to Alkali Lake, a northeast trending hydraulic gradient is required; however, the regional gradient is east to southeast. Therefore, local dune topography and significant evaporative flux from Alkali Lake appear to create a sufficient hydraulic gradient to maintain flow nearly perpendicular to the regional gradient.

Local hydraulic gradients towards discharge lakes may allow for significant solute fluxes that could intensify lake salinization. Thus, the low ER pocket in the northeast of Alkali Lake may also arise from saline groundwater inputs recharged by lakes 200-400 m to the northeast, and saline groundwater was previously found up-gradient from Alkali Lake in this area [*Ong et al.*, 2010]. However, a deficit of solutes is observed for Alkali Lake when considering advective and diffusive fluxes over the past 700 years [*Zlotnik et al.*, 2010; *Zlotnik et al.*, 2012]. Saline groundwater discharge into Alkali Lake would require additional solute losses, most likely from eolian deflation, reduced solute influxes in the Holocene, and free convection [*Zlotnik et al.*, 2010].

2.4.3. Gimlet Lake

Six 2D CRP profiles with total length 2.6 km were extracted from 2.8 km of raw data in Gimlet Lake (Figure 2.8 and Table 2.2). Lake water depth varied between 0.5 and 1.7 m with a mean of 0.9 m. The lake water ER was 14.56 Ωm. The profile resistivity range was 8.8-261.1 Ωm, but most values exceeded 30 Ωm for the majority of the profiles. Across the lake, ER values remain generally between 30-80 Ωm, where the range for sediment saturated with only lake water is 127-206 Ωm using the values discussed above. However, since Gimlet Lake is a groundwater-fed lake, a freshening of the lake water relative to the already fresh groundwater would require significant precipitation. Thus, the lower ER values from the CRP transects may describe a lake freshening due to heavy precipitation or the parameters used in the calculation of Archie's Law may not capture the subsurface

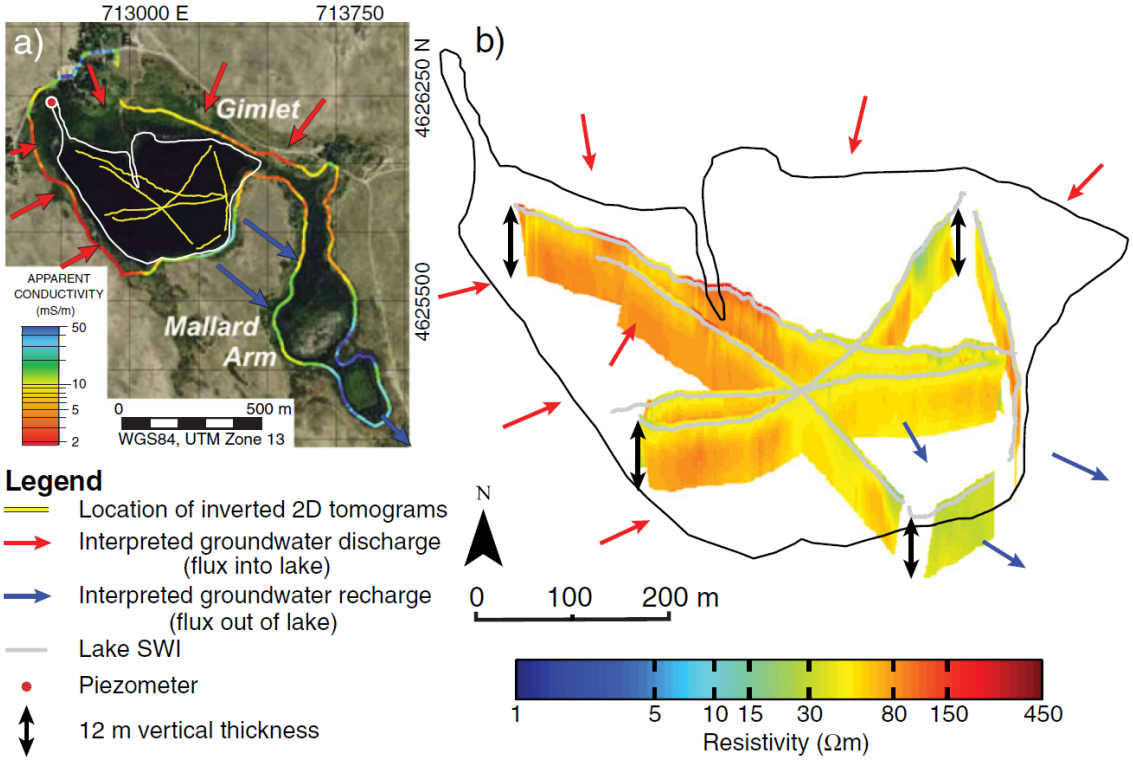

Figure 2.8. ER profiles for freshwater Gimlet Lake: a) EM observations taken along the lake shore show a decrease in conductivity to the southeast (modified after *Ong et al.* [2010]), b) ER profiles under Gimlet Lake with 0.5-1.7 m lake depth; 0.9 m mean (note larger ER range in legend compared to Figure 2.6). Very resistive areas may represent locations of fresh groundwater seepage into the lake but are likely composed of more resistive sediment as well.

properties for all three lakes. Since Gimlet lake is 15 km southeast of Wilson and Alkali Lakes and is located within the hypothesized paleo-valley (Figure 2.1), the same Archie parameters likely do not apply, related to the potential for fluvial depositional processes changing sediment type and packing. Instead, n=0.35 and q=1.6-2.0 are used, giving an ER range for lake water saturated sediment of 78.1-119 Ωm. With these values, the majority of subsurface material beneath Gimlet Lake may be saturated with lake water. However, the groundwater ER is likely within the same ER range and indistinguishable from lake water, or lake water has not evolved significantly from its groundwater source. For salinity to remain similar to groundwater, lake water must be flushed quickly through Gimlet Lake because it experiences a similar evaporative potential as Alkali Lake, albeit Gimlet Lake is on average twice as deep.

Despite the similarly and relatively fresh lake water and groundwater in Gimlet Lake, ER still varied spatially. Near the surface of the lakebed, high ER (50-150 Ωm, 320-460 m in Figure 2.4c) values transition to lower values (<50 Ωm) that may describe fresh groundwater fluxes into the lake in the northwest and a hinge line with slightly more conductive water recharging the aquifer in the southeast (Figure 2.7c). This is consistent with EM and ER observations taken along the shore (see Figure 6 in *Ong et al.* [2010]). Available airborne EM data also show high ER values in the shallow subsurface on the western side of the lake, but this quickly transitions to lower values to the east, halfway through the lake [*Smith et al.,* 2010]. The high ER (> 80 Ωm) pockets in the center of the lake at both shallow (1 m) and deeper (7 m) ER depth slices may mark discrete fresh groundwater springs and/or an area comprised of more resistive matrix materials (Figure 2.7c). A 26-m deep, flowing piezometer discharging fresh water on the northwest corner of the lake had a hydraulic head of 1.4 m above the lake level (Figure 2.8a), which supports the existence of upward flow and the possibility for diffuse or discrete groundwater

discharge into the lake. Although lower resistivities persist in the northeast and southeast portions of the lake, they never reach the low ER values found in Wilson and Alkali Lakes. Lake perimeter EM and ER data reveal low ER values along the southeastern shore of Gimlet Lake but not to the northeast (Figure 2.8a) [*Ong et al.*, 2010].

Gimlet Lake is likely embedded within the eastern branch of the Pleistocene-aged, southeastward trending Blue Creek paleo-valley [*Loope et al.*, 1995]. Therefore, discharge of water from the lake interpreted from low ER values underneath Gimlet Lake may be controlled by the regional hydraulic gradient towards the permeable fluvial deposits in the paleo-valley (Figure 2.1). Even so, the CRP results suggest Gimlet Lake is dominated by fresh groundwater inputs and intensively flushed, preventing the buildup of solutes in the lakebed and underlying deeper sediments that decreases ER, unlike in the other two lakes.

2.5. SUMMARY AND CONCLUSION

This study reveals the ability to determine and classify the groundwater flow regimes within and beneath groundwater-dominated lakes in the Nebraska Sand Hills by exploiting differences between solute concentrations of groundwater and surface water. Additionally, CRP surveys mapped 3D variations in ER of lakebed materials saturated with waters of contrasting salinity. This study complements and corroborates results from other studies which have not been able to show the three-dimensional character of groundwater-lake interactions directly underneath the lakes. In Wilson Lake, a clear transition from high to low bulk ER in the lakebed suggests a flow-through system where fresh groundwater enters the lake from the southwest, and more saline lake water infiltrates into the lakebed and recharges the aquifer in the lake's northeast portion. A kilometer away, the resistivity distribution beneath Alkali Lake shows a systematic and prevalent increase in ER with depth. This leads to the interpretation that fresh groundwater entering the lake from beneath

is trapped in the lake; evaporation results in the accumulation of solutes in the lake and lakebed. More conductive profiles in the northeast corner of Alkali Lake may suggest a zone of local downward vertical flux of low resistivity water. Nonetheless, Alkali Lake is mainly a groundwater discharge lake with a possible small groundwater recharge area in the northeast. The apparent flow pattern of groundwater under Wilson Lake towards Alkali Lake and similar ER values under the neighboring portions of each lake elucidated a hydraulic connection between them, where the flow direction is perpendicular to the regional hydraulic gradient. ER profiles in Gimlet Lake show much fresher groundwater underlying the lakebed than in the two other lakes. A stronger flushing capacity of the flow-through Gimlet Lake explains the weak solute accumulation in contrast to that observed in Wilson and Alkali Lakes. The lakebed ER pattern indicates fresh inputs both from the east and west with outflow most likely towards the southeast where the shallow subsurface becomes less resistive. The surveys also show the possibility of freshwater springs. A flowing well on the northwest shore of Gimlet Lake suggests favorable hydrogeologic conditions for spring activity under the lake. In general, the surveys provide the spatial distribution of flux direction across the lake-aquifer interface.

Among various applications of waterborne ER surveys, this study is the first to apply ER for classification of shallow, groundwater-fed lakes in a semi-arid environment. These lakes are widespread in semi-arid to arid areas on several continents. Such surveys can rapidly provide critical information regarding the pattern of groundwater flow under lakes; these noninvasive surveys can be performed in a short amount of time even in environments where direct instrumentation of the lakebed is difficult or impossible.

Chapter 3:

Heat transport dynamics at a sandy intertidal zone[2]

The shore has a dual nature, changing with the swing of the tides, belonging now to the land, now to the sea. On the ebb tide it knows the harsh extremes of the land world, being exposed to heat and cold, to wind, to rain and drying sun. On the flood tide it is a water world, returning briefly to the relative stability of the open sea.

-from "The Marginal World" in *The Edge of the Sea*
by Rachel Carson [1955]

ABSTRACT

Intertidal zones are spatially complex and temporally dynamic environments. Coastal groundwater discharge, including submarine groundwater discharge, may provide stabilizing conditions for intertidal zone permeable sediments. In this study, I integrated detailed time series temperature observations, porewater pressure measurements, and two-dimensional electrical resistivity tomography profiles to understand the coupled hydraulic-thermal regime of a tropical sandy intertidal zone in a fringing coral reef lagoon (Rarotonga, Cook Islands). I found three heating patterns across the 15 m study transect over tidal and diel periods: (1) a highly variable thermal regime dominated by swash infiltration and changes in saturation state in the upper foreshore with net heat import into the sediment, (2) a groundwater-supported underground stable, cool region just seaward of the intertidal slope break also importing heat into the subsurface, and (3) a zone of seawater recirculation that sustained consistently warm subsurface temperatures that exported heat across the sediment-water interface. Simple calculations suggested thermal conduction as the main heat transport mechanism for the shallow intertidal sediment, but deeper and/or multi-dimensional groundwater flow was required to explain

[2] Befus, K. M., M. B. Cardenas, D. V. Erler, I. R. Santos, and B. D. Eyre (2013), Heat transport dynamics at a sandy intertidal zone, *Water Resour. Res.*, 49, 1-17, doi: 10.1002/wrcr.20325.

Befus and Cardenas collected the field data with the assistance of Erler and Santos. Erler and Eyre funded the field expedition. Befus analyzed the data and prepared the manuscript under the supervision and guidance of the co-authors.

temperature patterns beyond 20 cm depth. Temperature differences between the distinct hydrodynamic zones of the foreshore site resulted in significant thermal gradients that persisted beyond tidal and diel periods. The thermal buffering of intertidal zones by coastal groundwater systems, both at surface seeps and in the shallow subsurface, can be responsible for thermal refugia for some coastal organisms and hotspots for biogeochemical reactions. This chapter arose through collaborative work and has been published [*Befus et al.*, 2013].

3.1. INTRODUCTION AND BACKGROUND

Intertidal zones represent the interface over which physical, chemical, and biological processes of terrestrial and marine systems interact. Together, these systems support dynamic mass and energy transfers, intimately tied to the competition of terrestrial surface and groundwater forcing versus tidal and wave processes. Heat transport dynamics within intertidal sediment specifically contribute to ecosystem stability and sustainability by moderating thermal regimes [*Dale and Miller*, 2007] and biogeochemical activity [*Jickells*, 1998].

Coastal geology and morphology interact with marine forcings that control the physical and hydrologic properties of an intertidal zone. Broad coastal shelves and sediment-mantled coastlines dissipate wave energy, leading to gently sloping foreshores with fine-grained sediment [*Wright and Short*, 1984]. Reflective coastlines are steeper and more likely to be rocky than dissipative or intermediate conditions [*Wright and Short*, 1984; *McLachlan and Turner*, 1994;]. As coastlines evolve through erosive (e.g. storms) or depositional (e.g. river or current sediment delivery) events, the intertidal zone exists in a transient state controlled by timescales on the order of seconds (e.g. waves) to millennia (e.g. eustatic sea level change). In turn, the coastal topography and geologic framework determine the hydrologic properties and hydrodynamic boundary conditions controlling

interactions between terrestrial groundwater and the marine system [*McLachlan and Turner,* 1994; *Robinson et al.*, 2006].

Terrestrial groundwater systems may serve as both sources and sinks of mass and energy in intertidal zones. Coastal groundwater generally flows towards the sea but may be diverted by geologic heterogeneity, discharge into rivers, lakes, or marshes, and affected by human exploits. Even under these circumstances, terrestrially-sourced groundwater discharges beyond the shore in a multitude of coastal conditions worldwide and has led to the active study of submarine groundwater discharge (SGD) [*Burnett et al.*, 2003; *Santos et al.*, 2012c]. Intertidal groundwater flow is a component of SGD, occurring in a domain of transient and dynamic mixing of marine and terrestrial waters that has been described and referred to as a subterranean estuary (STE) [*Moore,* 1999]. Intertidal porewater flow is induced both by tidal and wave action as well as by terrestrial hydraulic head gradients, creating a dynamic, spatially heterogeneous flow system [*McLachlan and Turner*, 1994; *Robinson et al.*, 2006; *Robinson et al.*, 2007a; *Maji and Smith*, 2009; *Xin et al.*, 2010]. While STE mixing occurs across a broad range of scales [*Bratton*, 2010], the intertidal zone acts as both a transient upper boundary condition and outlet for the shallowest expression of the STE, producing dynamic environmental conditions in the foreshore forced by terrestrial and marine processes.

Intertidal zones are ideal for studying how aquatic communities and processes respond to chemical and thermal variability, orchestrated in part by intertidal hydrodynamics. Abundant intertidal biological communities have evolved to survive the transition between aquatic and subaerial existence dictated by tides and waves [*McLachlan*, 1983]. Groundwater seeps in the intertidal and subtidal ecosystems add both benefits and challenges for these communities. Salinity changes occur both spatially and temporally, creating osmotic gradients that may stress organisms [*Miller and Ullman*, 2004; *Mitbavkar*

and Anil, 2005; *Dale and Miller*, 2008]. Groundwater seeps in the foreshore may also support species that prefer lower salinities [*Zipperle and Reise*, 2005; *Dale and Miller*, 2008]. Additionally, nutrient-enriched terrestrial groundwater may reach some intertidal and littoral zones and support large communities of specific nearshore organisms [*Ullman et al.*, 2003; *Miller and Ullman*, 2004; *Zipperle and Reise*, 2005; *Waska and Kim*, 2010], sustain significant microbial decomposition of organic matter [*Jickells*, 1998], and feed microbial mats that change the flow conditions in intertidal sediment and alter the chemical environment [*Decho*, 2000]. Where groundwater inputs are minimal or heterogeneous, steep chemical gradients may develop as microbial communities consume available organic matter through various oxidation-reduction reactions [*Fenchel and Riedl*, 1970; *Jickells*, 1998; *Windom and Niencheski*, 2003; *Anschutz et al.*, 2009]. Finally, groundwater seeps may thus provide more stable temperature envelopes for thermally sensitive organisms and influence community dynamics [*Miller and Ullman*, 2004; *Dale and Miller*, 2007; *Morelissen and Harley*, 2007]. In turn, the organisms can alter and shape the hydrodynamics and thermal regimes of the foreshore environment [*Piccolo et al.*, 1993; *Dale and Miller*, 2008]. Spatial and temporal differences of intertidal biota behavior and activity over short spatial and timescales created by intertidal dynamics offer insight into how communities may respond to future climate-related biological stresses or ecosystem shifts [*Sanford*, 1999; *Helmuth and Hofmann*, 2001; *Harley and Helmuth*, 2003].

Previous studies of intertidal zone porewater temperature dynamics capture tidal, diel, and seasonal cyclicity as well as spatial and temporal variability across multiple scales [*Leland and Hummon*, 1971; *Wilson*, 1983; *Harrison and Morrison*, 1993; *Smith*, 2002; *Dale*, 2006; *Birt and Tibbetts*, 2007; *Dale and Miller*, 2007; *Vandenbohede and Lebbe*, 2011; *Ricklefs and Vanselow*, 2012]. In a beach without active fresh groundwater seeps, shallow (10 cm) temperatures are buffered by infiltrated seawater from the swash zone and

experience diel solar radiation fluctuations that decay quickly with depth in the sediment [*Wilson,* 1983; *Harrison and Phizacklea,* 1987; *Piccolo et al.*, 1993; *Cho et al.*, 2005; *Ricklefs and Vanselow,* 2012]. Mixing groundwater and surface water in the foreshore create decimeter scale heterogeneity in flow conditions and temperature patterns and may follow local hydraulic conductivity patterns [*Dale*, 2006; *Dale and Miller*, 2007]. Broader thermal regime shifts may be imposed by seasonal groundwater and marine temperature changes that affect entire coastal aquifers [*Vandenbohede and Lebbe,* 2011]. In turn, intertidal temperature gradients can induce density-driven convection and alter fluid flow dynamics on short timescales [*Rocha,* 2000]. In this study, I advance the understanding of coupled hydrodynamic and thermal regimes in the interstitial intertidal zone with detailed spatial and temporal hydraulic and temperature measurements.

I focus on temperature dynamics in a sandy tidal flat, where groundwater flow influences the thermal regime. Extreme temperature fluctuations in rocky intertidal areas have been shown to affect organism activity, competition, and mortality [*Sanford*, 1999; *Helmuth and Hofmann*, 2001; *Morelissen and Harley*, 2007]. More moderate temperature fluctuations occur in sandy intertidal zones where perched tidal pools are rare, but these sand communities may still be stressed or otherwise influenced by changes in the thermal regime [*Grant*, 1986; *Miller and Ullman*, 2004; *Dale*, 2006;]. Heat dynamics in sandy intertidal zones also influence local biogeochemical activity, where temperature increases in intertidal porewater have been shown to accelerate microbial degradation of organic matter through multiple redox reactions [*Grant*, 1986; *Al-Raei et al.*, 2009; *Sanz-Lázaro et al.*, 2011]. I investigate the heat transport dynamics of a sandy intertidal zone to determine the potential effect of groundwater-seawater mixing on energy availability to intertidal biogeochemical and biological processes. I hypothesize that the hydrodynamics of the STE control the intertidal zone thermal regime and regulate its thermal budget. Next, I

hypothesize tidal fluctuations impose the dominant transience of intertidal zone STE temperatures by controlling both the thermal and hydrologic boundary conditions. Additionally, I hypothesize that the terrestrial groundwater buffers the diel solar radiation effects and semi-diel tidally-induced subsurface temperatures. I synthesize detailed temperature time series, water level measurements, and electrical resistivity (ER) tomography results to elucidate the complex thermal regime within an intertidal sandflat on Rarotonga, Cook Islands. I find that surface temperature signals penetrate to different depths related to groundwater-surface water interactions and heat conduction along a 15 m shore-perpendicular profile, instrumented with 52 temperature sensors (thermistors). Upward and seaward groundwater flow in the intertidal STE reveal a predominance of terrestrial gradients in this intertidal zone that are reflected in a high resistivity 'tube' where cooler and more stable temperatures were recorded.

3.2. STUDY SITE AND METHODS

3.2.1. Study site

Rarotonga (21.2°S 159.8°W) is a high volcanic island 1450 km east of the Tonga Trench in the south-central Pacific Ocean with a well-developed fringing reef (Figure 3.1) [*Hein et al.*, 2004]. Rugged mountains cover the majority of Rarotonga's 67 km^2 area, but volcaniclastic and coastal sediment surround the volcanic interior, providing a 0.3-1.2 km wide strip of developable land for the 13,000 inhabitants [*Wood and Hay*, 1970]. Two seasons define the tropical island: wet summers with potential cyclone activity (October to April) and drier winters (May to September). The highest temperatures are expected between January and February, and the mean annual temperature is ~24°C [*Hein et al.*, 2004]. Annual rainfall averages 2100 mm. There are only two perennial streams that originate in the island interior that reach the coast, but many smaller ephemeral streams

drain the peripheral slopes [*Waterhouse et al.*, 1986; *Hein et al.*, 2004]. Wetlands lie between the alluvium and storm-related beach-ridge deposits, and most of the smaller streams discharge into these wetlands, not reaching the coast via surface pathways [*Hein et al.*, 2004; *Waterhouse et al.*, 1986]. Anecdotally reported shoreline and underwater reef-crest springs are postulated to be related to groundwater recharge in the high elevation alluvial terraces, coastal marshes, and fracture networks in the volcanic rocks [*Waterhouse et al.*, 1986]. Rarotonga tides are microtidal, ranging 0.8 m during spring conditions and 0.4 m during neap conditions [*Waterhouse et al.*, 1986].

The study site is located adjacent to Parengaru Stream in Muri on the southeast corner of Rarotonga. Parengaru Stream is a first-order stream that has formed a deltaic sandflat (~1700 m^2) and is tidally-affected until crossing the main road, about 100 m onshore of the high tide mark (Figure 3.1b). At Muri, a broad reef lagoon is protected by a reef crest ~700 m from the main shoreline. Significant SGD occurs in the lagoon and is estimated to range from 0.2-1.9 cm day^{-1} [*Tait et al.*, 2013]. The permeable coastal sediment at the study site consists of predominantly bioclastic, calcareous sand over 3 m thick with sporadic lenses of coarser reef and shell detritus related to storm events [*Leslie*, 1980]. Nearby beaches in Muri have exposed or slightly buried (< 0.5 m) beach rock but was not encountered near Parengaru Stream.

3.2.2. Data collection and analysis

In February 2011, I installed a 15 m-long shore-perpendicular transect of piezometers beginning at the highest obvious expression of the swash zone (Figure 3.1c-d). Thirteen piezometers (T1-T13) were constructed from 2.5 cm diameter, 2 mm thick steel tubing and installed 50 cm into the intertidal sandflat. The piezometers were screened from 40-50 cm below the sediment-water interface (SWI) to allow water into the

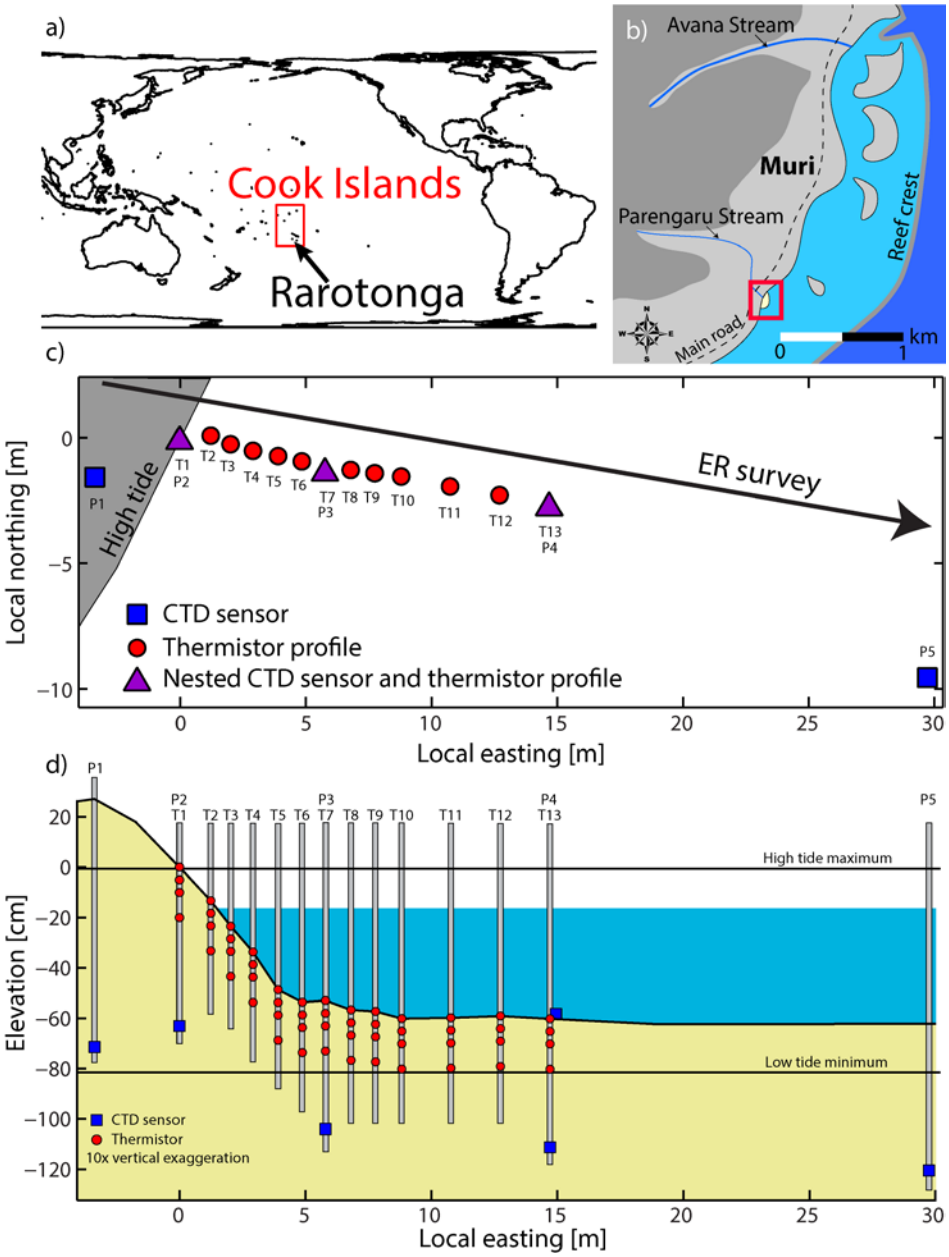

Figure 3.1. Location and study site map. a) Rarotonga is located in the southern Cook Islands. b) The study site was located on an intertidal sandflat created by Parengaru Stream. c) Map view and d) profile view of the piezometer transect, consisting of piezometers with conductivity, temperature, and depth (CTD) sensors (P) and temperature sensor arrays (T).

piezometer to dampen the effect of air temperature fluctuations and approximate the thermal properties of the saturated, porous sediment. The first ten piezometers, starting from the land, were spaced 1 m apart, and the final three in the sandflat were spaced 2 m apart. Within each piezometer, I inserted four thermistors attached to a steel rod for careful placement at 0 cm (i.e. intertidal sediment surface), 5 cm, 10 cm, and 20 cm below the surface. Each thermistor was thermally isolated from the internal steel rod by electrical tape. No effort was made to isolate individual thermistors within the vertical arrays (e.g. packers were not used). The implications of the piezometer design on the results are explored in the discussion section. Using this configuration, I deployed a total of 52 HOBO TMC20-HD thermistors attached to HOBO U12 four-channel data loggers, which have a measurement accuracy of ± 0.25°C and resolution of 0.03°C.

Five additional piezometers (P1-P5) were installed along and beyond the thermistor piezometers for measuring interstitial hydraulic heads, ranging from 4 m landward of the first thermistor piezometer and 15 m seaward of the last thermistor piezometer. Five In-Situ Inc. vented Aqua Troll 200 conductivity, temperature, and depth (CTD) probes were installed in these piezometers and recorded water level (< 1 cm accuracy and < 5 mm resolution) and temperature (± 0.1°C accuracy and 0.01°C resolution). One additional Aqua Troll 200 was secured at the base of the most seaward thermistor piezometer to record tide level and temperature at the sediment surface. Two In-Situ Inc. MiniTroll Pro pressure sensors were installed at thermal endmember locations. One recorded water levels 300 m into the lagoon to measure lagoon water temperature and lagoon water level during low tides exposing the entire sandflat. The other was installed in a 3 m deep piezometer 100 m inland from the thermistor transect to measure groundwater temperature and level. Piezometer locations and casing elevations were measured with a Leica TCR407 total station, and sensor deployment depths were measured with a tape measure.

Temperature and water level data were recorded every 5 minutes over three days and five tidal cycles in February 2011 during the transition from neap to spring tides. Data measurement from the piezometers began two hours after installation to allow the sediment return to an undisturbed state. Piezometer casing diameter introduces <10 minutes of lag in the temperature signal for the piezometers used, where five minute recording interval will fully sample external temperature changes without under-sampling [*Cardenas*, 2010].

I performed time-lapse ER surveys to capture larger scale porewater mixing dynamics in the intertidal zone. In direct current ER methods, an electrical current is injected into the ground through metal stakes (electrodes), and the resulting electrical field is measured with a separate pair of electrodes [see *Telford et al.*, 1990; *Dimova et al.*, 2012]. Both sediment and water electrical properties contribute to measured ER values. Shoreline groundwater salinity and discharge patterns have been inferred from subsurface ER patterns by multiple studies [*Swarzenski et al.*, 2006; *Swarzenski and Izbicki*, 2009; *Henderson et al.*, 2010; *Nakada et al.*, 2011; *Dimova et al.*, 2012].

I conducted the ER surveys simultaneously with the temperature measurements on an 82.5 m-long transect running parallel to the thermistor transect, offset by 5 m. The ER cable consisted of 56 graphite electrodes spaced 1.5 m apart. The first eight electrodes were connected to stainless-steel stakes and driven 10-20 cm into the sediment. Electrodes within the intertidal zone were buried with seawater-saturated sand multiple times during the surveying. Subtidal electrodes were placed on the seafloor and secured with large rocks. The total station was used to locate each electrode and provide topographic information for data inversion. ER data were collected using an Advanced Geosciences, Inc. (AGI) SuperSting R8 multi-channel resistivity system. ER surveys using the Schlumberger array were recorded approximately every half hour during the final 24 hours of temperature measurements. Each ER dataset was inverted individually with AGI EarthImager2D using

a smooth model constraint [see *Toran et al.*, 2010; *Dimova et al.*, 2012]. Time-lapse inversion of these data was not possible with the available software while still including critical topographic and tide level data in the inversion. Water depths were assigned using the offshore pressure sensor to set the water level elevation. Water resistivity was constrained to be 0.21 Ωm, the mean recorded in the lagoon during the data collection. All time steps converged to models with < 10% root-mean-square error in four iterations.

3.3. RESULTS

3.3.1. Water level measurements

Hydraulic heads decreased between piezometers in the seaward direction for the majority of the time series (Figure 3.2). The tide water level remained below all of the head elevations in the piezometers, except for a few measurements related to individual waves. Pressure data were recorded every 5 minutes with no real-time averaging, so the sensor measured instantaneous pressure waves in the piezometers created by the surface waves. P1 and P2 heads continued to decrease during low tide but quickly increased with incoming floods. P3 and P4 heads decreased slightly over low tides. Low tide hydraulic heads at P5 began to decay slowly, and then, ~1.5 hrs after mean tide, the heads started to more closely follow the tide stage. Head data were obscured for P2 between 06:50-08:00 on 2/17 by pumping and for P2 and P3 between 11:20-14:40 on 2/17 by a push-pull tracer test in nearby boreholes that significantly affected the water levels in the piezometers (Figure 3.2a).

Based on the instantaneous head measurements (h) in the piezometers and of the tide water level, horizontal (q_h) and vertical (q_v) groundwater fluxes were calculated following Darcy's Law:

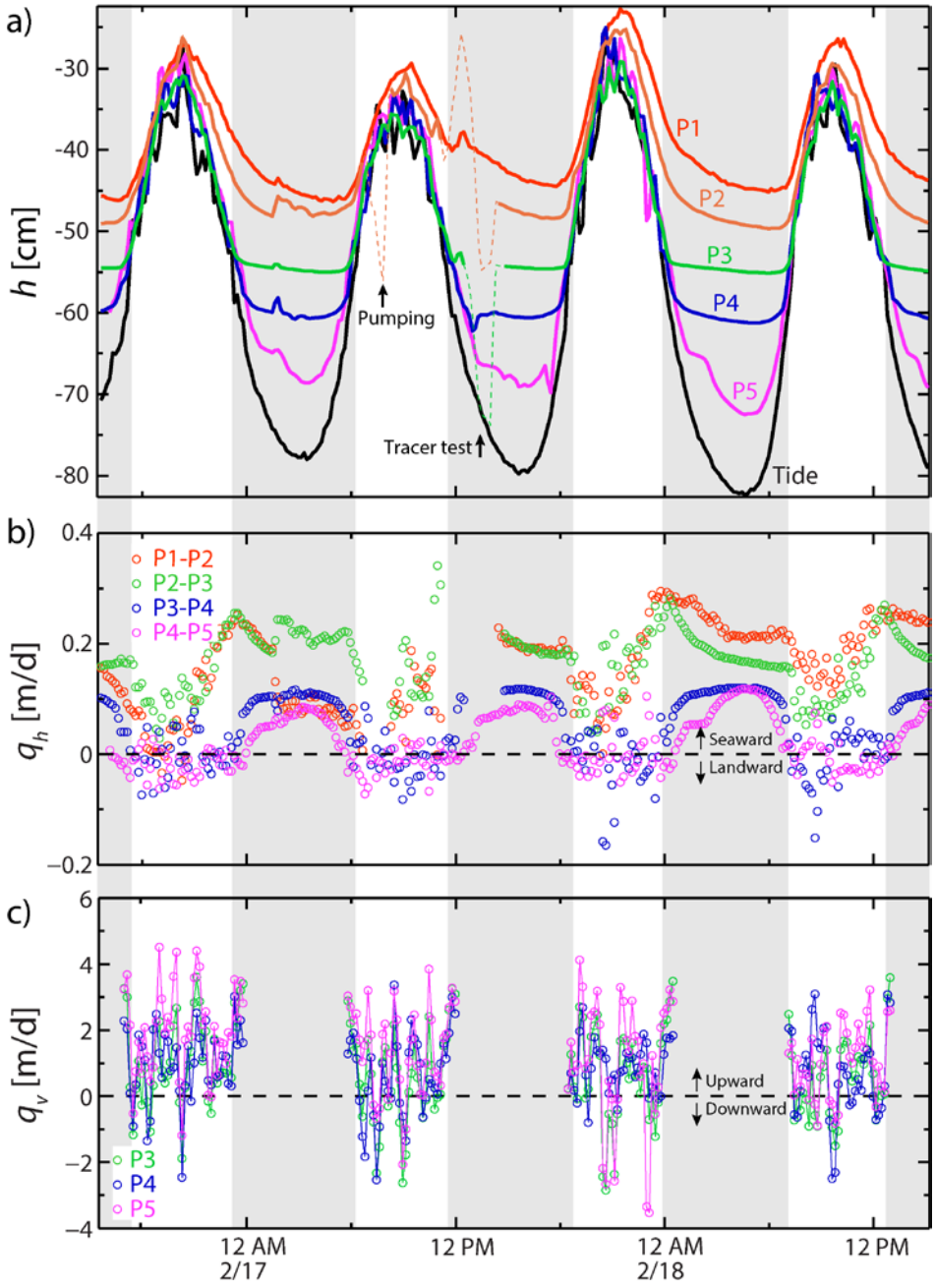

Figure 3.2. a) Calculated hydraulic head time series, b) horizontal groundwater flux (q_h), and c) vertical groundwater flux (q_v). Positive q_h and q_v represent seaward and upward water fluxes, respectively. The gaps in the q_v time series mark when the lagoon water level was below the SWI at the piezometers (see Section 3.3.1 for additional discussion).

$$q_h(t) = -K_{sat} \cdot \frac{dh_{p-p}(t)}{d\ell} \quad (3.1a)$$

$$q_v(t) = -K_{sat} \cdot \frac{dh_{p-t}(t)}{dz} \quad (3.1b)$$

where K_{sat} is the saturated hydraulic conductivity. Horizontal gradients were calculated using the head data from two piezometers, $dh_{p\text{-}p}(t)$, and the distance between the piezometers ($d\ell$) derived from the total station survey. Vertical gradients were comprised of the difference between piezometer head and the water level of the tide, $dh_{p\text{-}t}(t)$, divided by the depth from the SWI to the middle of the screen (dz). Thus, a vertical flux could only be calculated when the tide water level exceeded the elevation of the intertidal sediment at the piezometers. The fluxes were calculated so that positive q_h indicated a seaward flux and positive q_v indicated an upward flux. For the beach, I adopted a single K_{sat} value, implying that the sediment is homogeneous and isotropic and, thus, simplifying the stratigraphy of the shallow foreshore sediment. The K_{sat} was estimated with multiple in-situ slug tests in two piezometers and with laboratory constant head permeameter tests using samples from the site. Based on these analyses, K_{sat} for the Muri sands was $4.1 \times 10^{-4} \pm 4 \times 10^{-5}$ m/s and $1.89 \times 10^{-4} \pm 4 \times 10^{-5}$ m/s for the permeameter and slug tests, respectively. $K_{sat} = 2 \times 10^{-4}$ m/s was used for the flux calculations, putting more confidence on the in-situ and less disturbed conditions of the slug tests.

Horizontal fluxes between neighboring piezometers ranged from -0.2-0.3 m/d with seaward (positive) groundwater flow for the majority of the study duration. On average, q_h was 0.1 m/d. Seaward, q_h decreased in magnitude during most tidal conditions, so the most landward piezometer pair (P1-P2) typically measured the largest fluxes. As the tide rose, q_h decreased across the intertidal zone. Seaward of P3, the deeper lagoon water forced landward groundwater fluxes with nearly the same magnitude as the seaward fluxes at

lower lagoon stages. The most landward piezometer pair (P1-P2) suggested some landward fluxes during peak tide heights, whereas P2-P3 always yielded a seaward flux.

Between the upper and lower foreshore, the horizontal fluxes responded differently to ebb and flood transitions. In the two landward pairs of piezometers (P1-P3), horizontal fluxes decreased quickly as the tide began to exceed the mean water level. These piezometers also recorded a high seaward flux ~3 hrs after the peak tide that decayed throughout low tide. Piezometers further seaward (P3-P5) indicated horizontal fluxes that inversely followed the tide stage smoothly and without time lags.

Vertical fluxes calculated using the three most seaward piezometers (P3-P5) ranged from -3.5-4.5 m/d. On average, upward (positive) fluxes were measured to be 1.0 m/d, but individual events related to quick pressure changes measured in the piezometers created a broad range of instantaneous vertical fluxes. P3 and P4 each averaged an upwards flux of 0.8 m/d, and P5 had a mean of 1.5 m/d with the largest range.

3.3.2. Electrical resistivity tomograms

A total of 24 ER surveys were conducted between 2/17 11:15 and 2/18 11:30 (Figure 3.3 and electronic supplement Figure 1 in *Befus et al.* [2013]). First, I performed a depth of investigation analysis to quantify the robustness of the ER results, which relied on the output model sensitivity matrix from the inversion of the ER observations; this provides relative information on the extent to which the observations determined the final inverted section [*Ward et al.*, 2010; *Cardenas and Markowski*, 2011; *Befus et al.*, 2012]. In general, the inverted sections were less controlled by the data with increasing depth. Low resolution values reached near the SWI (4 m) under the seaward half of the transect, where there was a thicker layer of overlying seawater. On the landward portion of the surveys, no more than the upper 8 m of the transect was sufficiently controlled by the data.

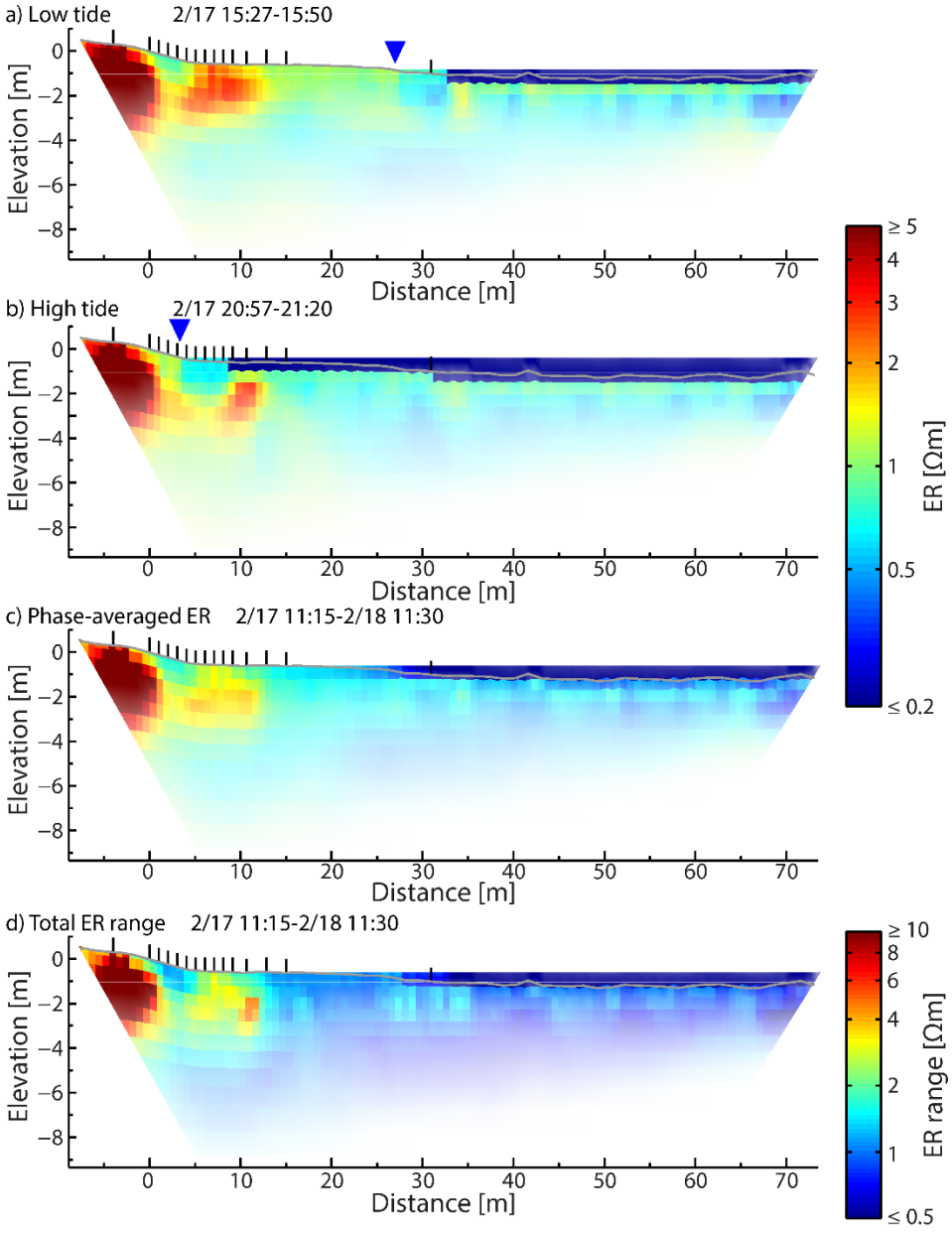

Figure 3.3. Characteristic ER profiles for a) low tide and b) high tide conditions. c) Phase-averaged ER values in each cell show the mean ER conditions of the intertidal zone. d) The total ER range per inversion cell reveals subsurface areas with dynamic ER signals over 24 hours. Mean tide location during the surveys is marked by a blue triangle. The sediment surface is shown as a grey line. Piezometer locations are indicated by vertical black lines. See electronic supplement for *Befus et al.* [2013] for an animated version showing all 24 ER tomograms.

The ER time series revealed dynamic subsurface patterns. The majority of the ER changes occurred in the first 21 m (-8-13 m) of the ER transect (Figure 3.3). A high ER (30-50 Ωm) feature was imaged from the start of the line to 0 m that extended to 4 m depth in all inverted sections, corresponding to the supratidal portion of the cable. Next, a dynamic pocket of low ER values (< 2 Ωm) that ranged between 0.5-2.5 m thick was located at -2-4 m along the survey. During high tide, this pocket reached its maximum size (from -2-8 m) and its minimum values (0.5 Ωm), approaching that of seawater (Figure 3.3b). A ubiquitous area of higher ER values (1-3 Ωm) extended below and beyond the more conductive pocket in all inverted sections that also grew and shrank with the tide (Figure 3.3a-c). Except during the highest tide stages, the high ER area stretched from 3-14 m and spread over the upper 4 m of the profile (Figure 3.3c). With high tides, this high ER feature collapsed into an arm that was ~1 m thick at 3 m depth, below the low ER pocket, and then may have curved towards the surface between 8-13 m. However, low ER values at the surface reduce the simulated current that reaches lower model cells and can lead to over-estimated ER values [*Clément et al.*, 2009]. Even so, the high ER feature remained during high tides, but the upper 2 m of the subsurface became less resistive. From 10-35 m, the upper 3 m of the inverted profiles fluctuated between saltwater values and less than 1 Ωm, depending on the tide position (Figure 3.3d). ER changes beyond 35 m were small (<1.5 Ωm), and the low model sensitivity of this portion of the ER line rendered these fluctuations less significant (Figure 3.3d).

3.3.3. Measured temperature distributions

Surface temperatures at the most seaward piezometer ranged between 23.1°C and 32.7°C with a mean of 27.3°C during the survey, incorporating emerged and submerged intertidal conditions. Lagoon water averaged 28.5°C with a 5°C range (26.7-31.9°C) 300

m offshore from the transect, where the water was 0.9 m deep. At the inland piezometer, groundwater averaged 25.8°C with the water table 2 m below the ground surface. Within the temperature piezometers, temperature fluctuations at depth generally followed the pattern at the SWI (Figures 3.4-6). Deeper thermistors recorded damped temperature changes relative to the surface signal with varying degrees of phase lag. Temperatures at 20 cm depth corresponded to temperature shifts at the surface with time lags ranging from nearly instantaneous to almost 16 hours. The time lag at 20 cm depth was less than 30 minutes for most thermistor arrays during the first tidal cycle, increasing to 4-16 hours during the second tidal cycle. Tidal amplitudes remained similar for these two cycles with low tides after midnight and noon, transitioning later over the course of the data collection.

Thermal fronts spread from the surface to different depths across the length of the thermistor transect (Figure 3.4). Temperature changes recorded at the first thermistor piezometer, T1, showed thermal signals reaching 43 cm into the sediment. A majority of the temperature change at the surface attenuates by the second thermistor at 5 cm depth in the sediment, except during periods of prolonged hot surface conditions. Even so, surface temperature signals contributed to a 1.1°C range at 43 cm below the SWI, where the mean was identical to the SWI mean temperature of 27.3°C. Towards the middle of the transect, at T7, temperature variations closely followed surface changes to a depth of 5 cm with little attenuation or lag. At 10 cm in T7, the temperature variability is reduced by 2-3°C, and at 20 cm the temperature range is less than 1.0°C around the mean of 26.8°C. Some periods of the time series for T7 contained highly attenuated temperature signals at 5 cm depth (see 2/17 00:00-05:20 and 2/17 13:20-17:30, local time: GMT-10). Directly adjacent to T7, P3 recorded less than ± 0.2°C around the mean of 26.6°C at 37 cm depth. Only 9 m further seaward, T13 displayed conspicuously different subsurface temperature patterns than T7.

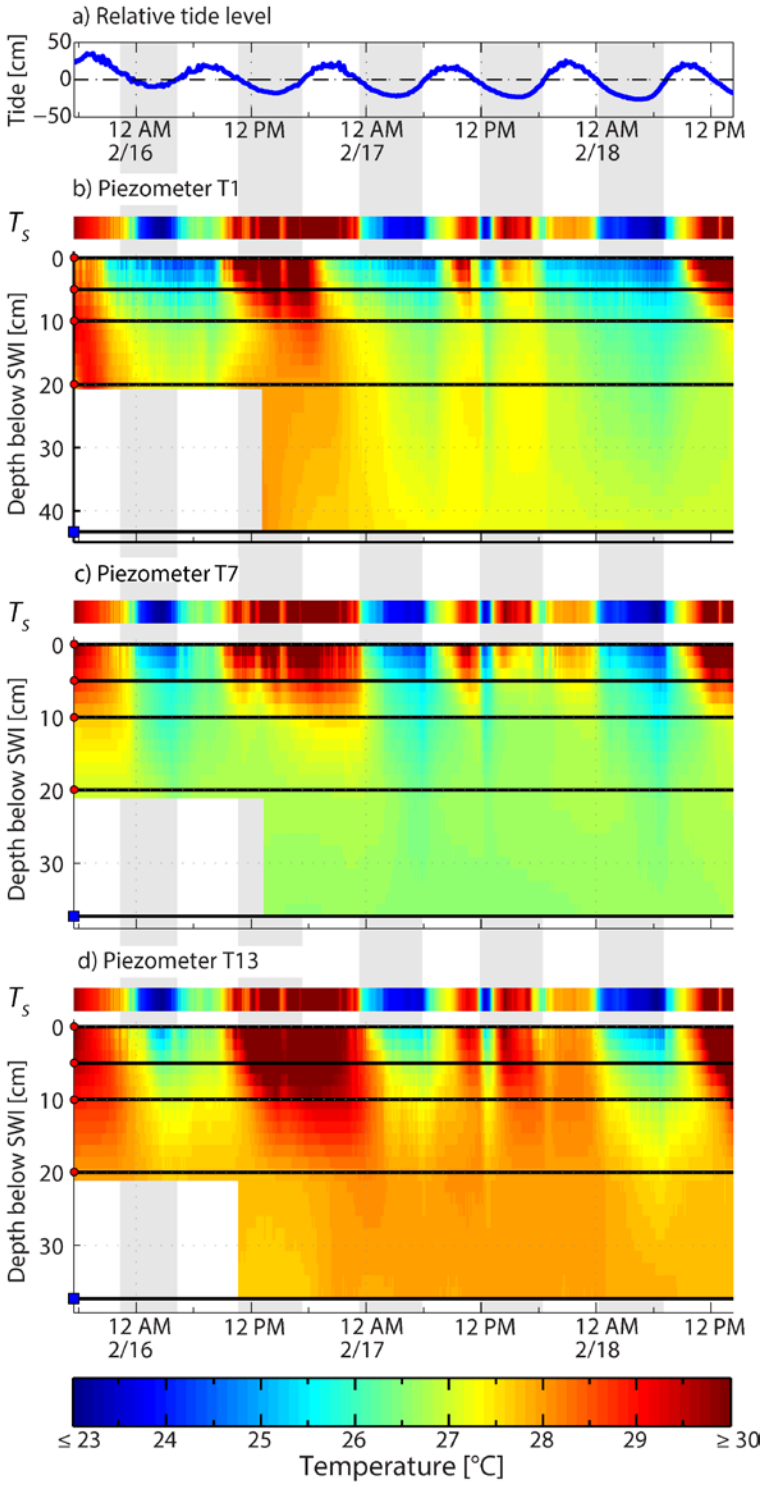

Figure 3.4.

a) Tide level and b-d) temperature array time series over multiple tides for piezometers b) T1, c) T7, and d) T13. Ambient surface temperature measurements (Ts) were recorded outside of T13 at the SWI. Temperature sensor locations are indicated by the solid black lines and symbols from Figure 3.1. Low tide conditions are shaded grey.

Shallow temperature front penetration showed more variability for T13 with some surface temperatures attenuating 2-2.5°C before reaching 5 cm depth (2/17 00:00-05:20) and another thermal front extending to 10 cm with almost no attenuation over a full tide cycle (2/16 10:00-22:30). At 20 cm depth, the thermistor recorded a 0.6°C range and a mean of 27.9°C. Similarly, P4 logged a mean temperature of 27.9°C with a range of 0.4°C at 37 cm depth. In the 9 m span between T7 and T13, a 1.3°C difference persisted at larger depths and was minimally affected by diel temperature changes at the SWI.

The thermal responses observed at the intertidal zone followed three patterns over different tide stage and surface temperatures (Figure 3.5 and electronic supplement Figure 2 from *Befus et al.* [2013]), exemplified by the phase-averaged temperatures and temperature range over the study period (Figure 3.6). Along the upper beachface (T1-T4), surface temperature signals retained more than 1°C amplitudes at 20 cm depth and reached 10 cm in less than 20 minutes. Just beyond the slope break, thermistor arrays T6-T10 experienced small variations (<1°C) at 20 cm depth and remained at a roughly constant temperature, slightly cooler (26.8°C) than the mean surface fluctuations that mainly affected the upper 5 cm. Directly at the break in slope, T5 measured similar changes as T6-T10, but temperature patterns at 20 cm were not recorded due to a faulty thermistor. Thermistor arrays furthest seaward (T11-T13) recorded consistently warmer temperatures than the mean surface temperature and also responded little to surface temperatures beyond 10 cm depth (<1°C). Arrays T3 and T4 showed out-of-phase temperatures with respect to the surface signal at 10 cm and 20 cm throughout most of the survey.

Additional analysis of the heat transport mechanisms explained the prevalence of downward heat transport in the intertidal sediment despite calculated upwards groundwater flow, which suggested net upwards heat advection over the 0.5 m depth range. At smaller

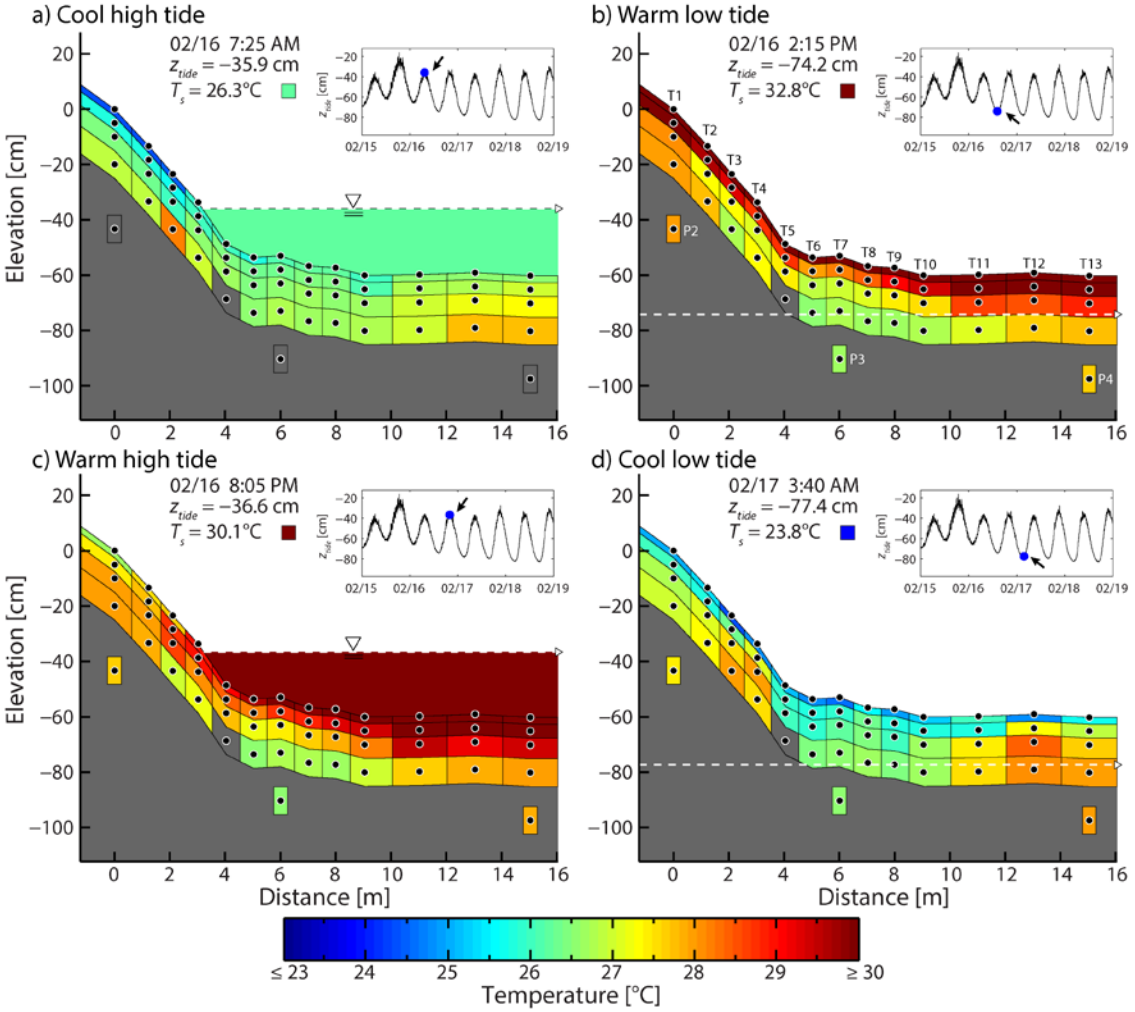

Figure 3.5. Temperature distribution across the study transect at different tide levels and surface temperatures: a) cool high tide, b) warm low tide, c) warm high tide, and d) cool low tide. Tide level inset charts show a blue dot and arrow for the time of the temperature profile. Tide level (z_{tide}) is shown by the dashed line and is not indicative of groundwater level when below the SWI. See electronic supplement from *Befus et al.* [2013] for an animated version of the plots, showing the complete time series.

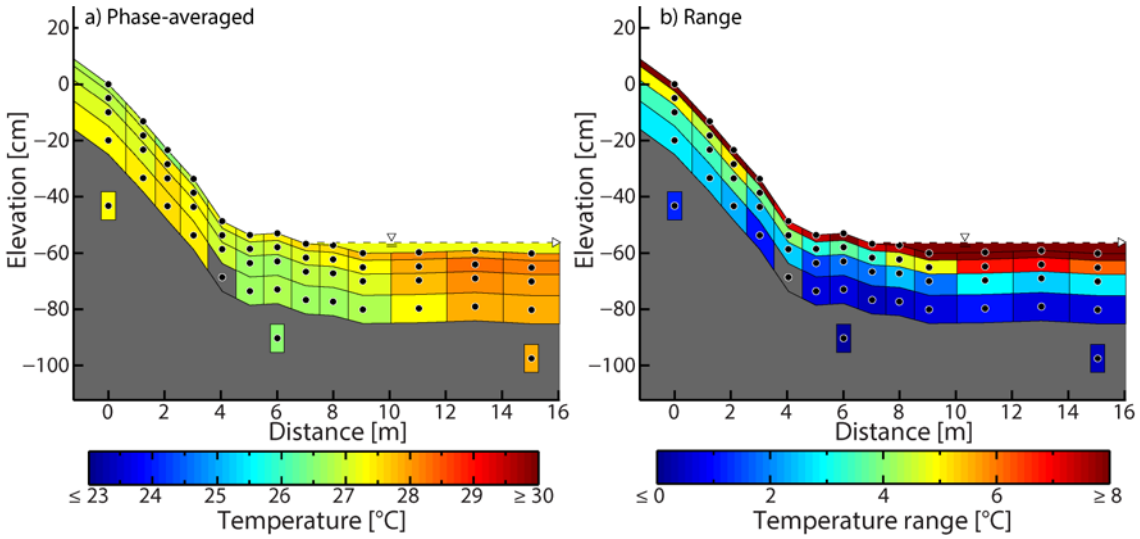

Figure 3.6. a) Phase-averaged temperatures and b) temperature range distribution for the study transect. The dashed line shows the mean tide level, and the fill color corresponds to the phase-averaged temperature and temperature range for the measured surface temperature.

spatial scales, both heat conduction and advection may control sediment temperatures. A characteristic length scale (d_c) over which conduction could be responsible for sinusoidal heat pulses into the sediment in the absence of advection is described by:

$$d_c = \sqrt{\frac{\alpha T}{\pi}} \tag{3.2}$$

where α is the thermal diffusivity, T is the period of the temperature fluctuations, and d_c is the depth where a surface temperature pulse has decayed to ~0.37 (i.e. e-folding length) of the original pulse amplitude. With the 9.6°C temperature range during the study, d_c indicated the depth where sediment temperatures are ~1.8°C different from the temperature at the surface due only to downwards conducting thermal pulses. I measured α of the beach sand using a Decagon KD2 PRO probe and found $\alpha = 3.4 \times 10^{-7} \pm 5 \times 10^{-8}$ m^2/s. Both diel radiation and tidal cycles influenced the thermal patterns in the intertidal zone (Figure 3.4), giving T=12 hrs and T=6 hrs, respectively. Over the diel timescale, d_c =6-8 cm, and d_c = 4-6 cm for the tidal timescale. The penetration of surface temperatures into the studied intertidal zone fit within the calculated range of d_c across a majority of the thermistor transect for most of the study period (Figures 3.4 and 3.6b), indicating heat conduction could explain a majority of the shallow temperature patterns. It is important to note that d_c does not explain the complete extent surface temperature pulses penetrate into the subsurface; temperature pulses continue to penetrate and decay through conduction below d_c, as is visible in the temperature data (Figure 3.4).

Since conduction is an important heat transport mechanism at the studied intertidal zone, I calculated vertical conductive heat fluxes ($q_{v,heat}$) using Fourier's Law:

$$q_{v,heat}(t) = -k_{therm} \cdot \frac{dT(t)}{dz} \quad (3.3)$$

with k_{therm} the bulk thermal conductivity of the sediment-water mixture and T(t) the temperature time series data recorded by the thermistors. I used a constant k_{therm}=0.8 $Wm^{-1}C^{-1}$, the average of the measured KD2 Pro probe values, ignoring any potential heterogeneity of the thermal properties of coastal sediment and the dependence of k_{therm} on water content (e.g., *Ochsner et al.* [2001]). Calculated $q_{v,heat}$ within the intertidal zone varied primarily with the diel solar radiation cycle and not the tide stage (Figure 3.7). Both near the intertidal surface (0-10 cm) and deeper (10-20 cm), $q_{v,heat}$ distribution responded quickly to radiative surface heating. In the middle foreshore, the high $q_{v,heat}$ at the surface persisted, but the cool conditions lower in the sediment reduced the effect of surface heating beyond 10 cm depth. Deeper $q_{v,heat}$ between $T1_{20\ cm}$-P2, $T7_{20\ cm}$ -P3, and $T13_{20\ cm}$ -P4 were over an order of magnitude lower than calculated in the shallower intertidal zone, but these $q_{v,heat}$ rates also responded to the combined signals of tide stage and surface temperature. The relative correlation between surface temperature and $q_{v,heat}$ in the subsurface, however, cannot explain the distinct thermal regimes across the intertidal zone, as revealed by integrating these conductive heat fluxes in time for each thermistor array to give the change in heat storage in intertidal sediment (Figure 3.7e). Within the upper and middle intertidal zone, heat was imported into the subsurface (i.e. heat sink) over the study period, whereas the outer intertidal zone hydrogeologic system exported heat (i.e. heat source). Thus, heat conduction was not the sole heat transport mechanism in the intertidal zone sediment.

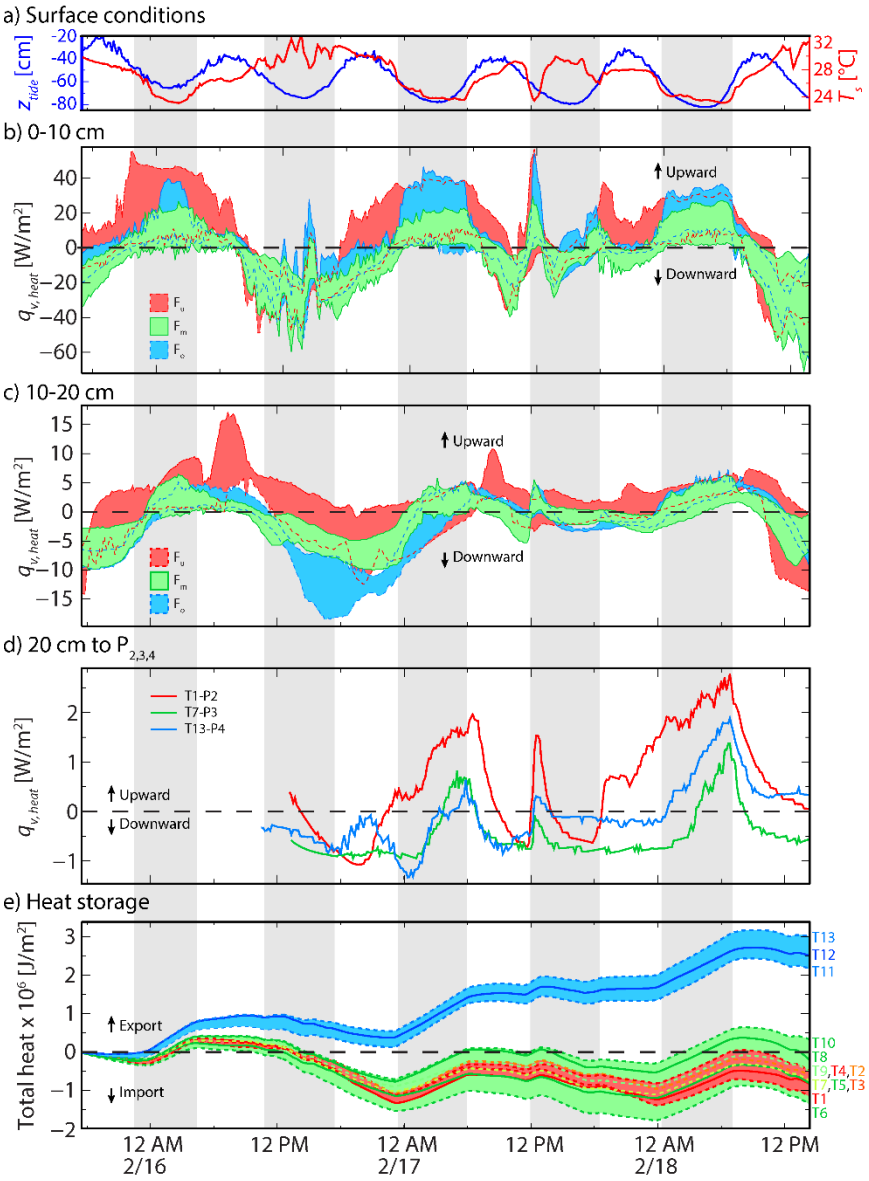

Figure 3.7. a) Tide elevation and surface temperature (T_s). b-d) Vertical heat flux ($q_{v,heat}$) values calculated for different areas and depth ranges of the foreshore: F_u = upper foreshore (T1-T4), F_m = middle foreshore (T5-T10), F_o = outer foreshore (T11-T13). Heat fluxes from 20 cm to $P_{2,3,4}$ includes the three pressure piezometers P2, P3, and P4; the flux was calculated using the nearest thermistors at 20 cm depth: T1, T7, and T13, respectively. An upward heat flux is positive. e) Cumulative heat storage in the intertidal sediment calculated from integrating $q_{v,heat}$ in time for each thermistor array.

3.4. DISCUSSION

3.4.1. Potential sources of error and other limitations

Inaccuracies when installing and surveying the pressure piezometers would impact the calculated hydraulic heads. When installing the pressure sensors, I carefully measured the piezometer dimensions as well as the depths of the sensors. My total station measurements of piezometer locations were accurate to < 1 cm, and tape measurements were recorded to the millimeter. Even so, these measurements were taken in sand, where the vertical dimension could be inaccurately measured by recording from different locations around the base of the piezometer or by allowing the surveying rod to sink inconsistently into the sand. Taken together, these error sources could lead to at least 1 cm inaccuracy in the calculated hydraulic heads. These 1 cm errors would lead to changes of about 50% in the vertical flux measurements and up to 57% for the horizontal fluxes. Thus, small errors in the hydraulic heads contribute significantly to the magnitude of the fluxes. Based on these responses, the vertical flux calculations could indicate erroneous flow directions with an error of 2-3 cm. For the horizontal fluxes, the two landward pairs of piezometers (P1-P2 and P2-P3) were most affected due to shorter distances ($d\ell$) and smaller differences in head ($dh(t)$), and the horizontal fluxes from the last three pairs changed by < 20% with a 1 cm error. Thus, a 2 cm error for the first three piezometers could have led to incorrect calculations for the direction of horizontal fluxes (i.e. landward instead of seaward), where a 5 cm error would be required for the seaward piezometers.

Beyond piezometer construction contributing to uncertainty in the calculated groundwater fluxes, the pressure time series were susceptible to recording water levels uncharacteristic of the overall behavior of the intertidal sediment. Pressure waves would nearly immediately propagate through the porewater and to the piezometer [*Reeves et al.*, 2000; *Cardenas and Jiang*, 2011], where the pressure sensors would record an

instantaneous water level that may have little impact on groundwater motion over the recording interval. These high frequency signals do appear in the water level measurements, and thus in the head and flux data, during higher tides, occasionally reaching a magnitude of 5 cm. The 5-minute sampling frequency generally captured different wave conditions that provided good coverage of mean conditions, as well as the wave variability. As another example of atypical pressure signals, pumping during the experiment near P2 and P3 between 11:20 A.M.-2:40 P.M. on 2/17 led to spurious data and was culled before analysis.

The ER dataset suffered from difficulties encountered in the field as well as from typical geophysical limitations. After culling faulty surveys due to incorrect cable connections and poor contact resistances, 24 ER surveys were inverted and subject to the uncertainty and non-uniqueness of the ER inversion process. Firstly, a conductive water layer at the surface reduces the current density reaching lower, more resistive layers. This effectively shields the lower portion of the profile from being imaged, and the inversion has less direction on what the true resistivity model should be in this area [*Day-Lewis et al.*, 2006; *Henderson et al.*, 2010]. ER inversions also rely on assumptions of relatively smoothly varying ER values in the subsurface to minimize an objective function, which leads to underestimation of ER magnitudes for individual features as well as a general smoothing of geological structure and are collectively termed correlation losses [*Day-Lewis et al.*, 2005]. Thus, both geological formation boundaries and sharp salinity interfaces in the ER surveys could appear more spatially diffuse than reality.

The temperature measurements were temporally restricted by piezometer design. The vertical thermistor arrays required piezometers with at least a 2 cm diameter to fit the sensors, where a smaller diameter tube would have allowed quicker thermal equilibration between the thermistors and the sediment around the piezometer. A 5 minute minimum

sampling interval was dictated by the lag associated with the piezometer design to not oversample, thus integrating shorter duration thermal variations occurring in the sediment. However, these high frequency temperature signals, potentially due to small clouds or wind gusts, would quickly attenuate in the subsurface and compose a minor portion of the thermal budget of the sediment [*Taniguchi et al.*, 1999]. Vertical heat conduction along the steel piezometer to the thermistors is expected to be negligible [*Alexander et al.*, 2005; *Cardenas*, 2010]. Finally, vertical water flow within the piezometers may have artificially allowed thermal signals from the screen location (40-50 cm below the SWI) to extend further towards the surface, restricting the depth to which surface temperature signals would penetrate. Given the <10 min response time of the piezometer in the presence of upwards groundwater flow [*Cardenas*, 2010], this biasing of the internal piezometer temperatures would only matter for interpreting temperature variability on timescales shorter than 10 minutes.

Vertical temperature profile measurements can also be used to independently estimate groundwater velocities [*Hatch et al.*, 2006; *Keery et al.*, 2007]; however, the analytical models typically used for this require steady and one-dimensional groundwater flow, both of which are violated by the multi-dimensional and dynamic hydraulics of the shallow subterranean estuary.

3.4.2. Hydrodynamic processes

The studied intertidal sands contained dynamic groundwater fluxes that result from interactions between the marine and terrestrial geomorphic and hydrologic systems. Calculated horizontal groundwater fluxes indicated that seaward groundwater flow occurred across the foreshore (Figure 3.2b), especially during low tide and between the three most landward pressure piezometers (P1-P3). In this upper foreshore area, seaward

groundwater flux was more responsive to tides than the seaward foreshore. The upper foreshore from -3-4 m was steeper (0.10-0.15 topographic gradient) than the seaward portion of the sandflat (0.002-0.03 topographic gradient). As the tide inundated the sandflat, all of the piezometer heads increased to nearly the same elevation (Figure 3.2a). Only P1 and P2 recorded heads 1-5 cm higher than the others. These higher heads could be from short-lived terrestrial groundwater pulses but were more likely created by tide and wave run-up infiltration into the sediment due to both the timing at high tide and the recurrence interval, as described by high resolution beachface groundwater studies [*Nielsen*, 1990; *Turner and Nielsen*, 1997; *Li et al.*, 2000; *Li et al.*, 2009; *Xin et al.*, 2010; *Heiss*, 2011]. Water levels then remained high despite a falling tide, as the infiltrated seawater traversed a longer lateral distance than the vertical infiltration (topographic gradient $\ll 1$). This asymmetry in hydraulic head time series data has also been observed elsewhere [*Lanyon et al.*, 1982; *Nielsen*, 1990; *Vandenbohede and Lebbe*, 2007; *King et al.*, 2010]. Thus, the upper piezometers were responding to a water table mound associated with both wave and tide infiltration that supported seaward groundwater motion throughout low tides.

Further seaward along the transect, horizontal fluxes were less variable than the upper foreshore because the flatter intertidal interface created more spatially homogeneous infiltration during inundation by the high tide (Figure 3.2b). However, sufficient horizontal hydraulic gradients persisted within the lower sandflat for seaward fluxes to initiate at mean tide stage, potentially supported by seawater recharged during high tide or the seaward extension of the terrestrial phreatic groundwater flow system.

Mean upward fluxes across the SWI existed over high tide conditions, but the experimental design prevented flux calculations during low tide (Figure 3.2c). Thus, the influence of infiltration versus terrestrial groundwater gradients on supporting the upward

fluxes remained ambiguous. Along coastlines with low terrestrial hydraulic gradients, tidally-induced infiltration supports upward fluxes during higher-than-mean tide stages [*Robinson et al.,* 2006]. However, given sufficiently large terrestrial groundwater discharges, a higher tide could offset upward gradients that would otherwise support upward fluxes during low tides [*Robinson et al.*, 2007a]. Upward groundwater flow in the intertidal zone for mean tide conditions is consistent with the conceptual model of converging terrestrial and saline groundwater bodies at the foreshore, as well as with other field studies [*Robinson et al.*, 2006; *Gibbes et al.*, 2008] and numerical models [*Glover*, 1959; *Bear,* 1979; *Jeng et al.*, 2005; *Robinson et al.*, 2007a; *Vandenbohede and Lebbe*, 2007; *Xin et al.*, 2010; *Kuan et al.*, 2012].

The ER tomograms also revealed important STE mixing patterns (Figure 3.3). High ER values as well as high variability over the landward-most 10 m of the ER images indicated fresh groundwater discharging towards the coast with the water table height changing with tide stage (Figure 3.3c-d). The ER tomograms also showed a persistent high ER lens between 1-4 m local depth and over 3-14 m distance of the transect. Since subsurface geology is constant between the time-lapse images, fluid conductivity changes would be the lone reason for ER changes, neglecting artifacts of the inversion process [*Swarzenski and Izbicki*, 2009; *Henderson et al.*, 2010; *Nakada et al.*, 2011; *Dimova et al.*, 2012]. Thus, the high ER tube marked the location of fresher groundwater that expanded and contracted with low and high tide, respectively. Several previous studies have presented models supported by field observations that show nearshore groundwater fluctuations interact with tide stage to affect fluid flow and solute transport as imaged by these ER surveys [*Li et al.*, 1997; *Li and Barry*, 2000; *Teo et al.*, 2003; *Jeng et al.*, 2005; *Robinson et al.*, 2007a; *Xin et al.*, 2010; *Kuan et al.*, 2012].

ER profiles also imaged the dynamics of the so-called upper saline circulation cell throughout the tidal cycle; this is the low-resistivity area at the surface, 0-5 m along the transect, in between the high-resistivity zones (Figure 3.3). Interestingly, fresher groundwater quickly raised ER values along shallow foreshore ~2 hrs after high tide (Figure 3.3a-b). This rapid freshening occurred as terrestrial gradients became dominant over the tidal gradient, and fresh terrestrial groundwater diluted and/or flushed the infiltrated seawater. My ER observations clearly demonstrated the occurrence of a dynamic upper saline plume overlying fresh groundwater and are consistent with high resolution salinity observations in other sandy beaches [*Robinson et al.*, 2007b; *Santos et al.*, 2009]. Tides and waves create this upper saline plume in the foreshore, where infiltrated seawater is recirculated seaward with residence times and spatial extent determined by the magnitude of the surface water oscillations, terrestrial groundwater discharge, and beach slope [*Robinson et al.*, 2007a; *Vandenbohede and Lebbe*, 2007; *King et al.*, 2010; *Xin et al.*, 2010; *Kuan et al.*, 2012]. The importance of tides and waves on controlling foreshore hydrodynamics is determined by the coastal setting, but both can support well-developed upper saline plumes that may extend terrestrial groundwater discharge further seaward and reduce seawater intrusion [*Xin et al.*, 2010; *Kuan et al.*, 2012]. As terrestrial groundwater gradients decrease, tidal fluctuations can induce more seawater intrusion than a similar system with no tidal influences [*Ataie-Ashtiani et al.*, 1999; *Robinson et al.*, 2007a].

The groundwater flow regime for the study site depicts the transience expected within a subterranean estuary. My results are consistent with and further extend the previous observations and model results by describing the thermal regime within the context of the hydrodynamics.

3.4.3. Heat transport regime

This study reveals that the intertidal zone is a thermally diverse interface for heat exchange between marine and terrestrial systems. Across the scale of the intertidal zone, porewater dynamics interact with and respond to surface conditions, creating several distinct thermal regimes. At the sub-meter scale, thermal conduction may become important in areas with low mean groundwater fluxes.

Along the steeper beachface (T1-T4), thermal fronts seemed mainly controlled by changes in saturation due to draining swash waters. As high tide began to ebb and/or as swash began to reach the high tide mark, waves intermittently thermally buffered the upper portion of the intertidal zone (e.g., T1 in Figure 3.4a). Without prolonged inundation by tidal waters, surficial intertidal sediment and porewater cooled by up to 5°C compared to inundated areas of the intertidal transect; this cooling may be due to evaporation, exporting latent heat to the atmosphere. These cooler surface temperatures occurred up to 4 hours earlier than nocturnal cooling at 10 cm below the swash zone during one of the tidal cycles (2/16 7:30-11:30 PM) and completely buffered deeper portions during another warm evening high tide (2/17 7:00-11:00 PM) (Figure 3.4a). As the surface cooled, heat continued to conduct deeper into the sediment from an earlier warm period, creating steep vertical gradients (0.2°C/cm). This phenomenon is driven by the changing hydrodynamic boundary conditions. During low tide, the water table at T1 would fall to 10 cm below the sediment surface, reducing the thermal buffering of the beach above the capillary fringe enough for at least the first two thermistors to record more rapid temperature changes. The deeper, saturated sediment with more thermal inertia would be less sensitive to these air-induced fluctuations, as displayed by the 10 cm thermistor in T1 that showed temperature changes connected to mostly higher tide levels (Figure 3.4a).

Closer to the slope break, T3 and T4 indicate that heat was stored at these locations from previous tidal cycles at 10-20 cm, since the temperature fluctuations were consistently out-of-phase with surface temperatures by up to 7 hrs (Figure 3.5 and electronic supplement Figure 2 from *Befus et al.* [2013]). This apparent thermal storage and inertia may be controlled by infiltrated swash and tidal waters whose hydraulic forcing weakens as the tide ebbs, resulting in deceleration or stagnation of fluid flow [*Staver and Brinsfield*, 1996; *Robinson et al.*, 1998; *Turner and Acworth*, 2004; *Robinson et al.*, 2006a; *Vandenbohede and Lebbe*, 2006]. A relative and short-lived hydraulic stasis would create long residence times for water within the tidal recirculation zone between tides, and the interstitial environment would retain thermal signals from the previous high tide that would change only if local boundary conditions resulted in thermal gradients conducive for heat conduction. Furthermore, models indicate larger tidal range can increase groundwater residence time in the tidal circulation zone [*Robinson et al.*, 2007a]. While tidal amplitudes were small in this study, beach morphology and permeability alter flow patterns and may allow small hydraulic gradients to exist in the tidal circulation zone [*Vandenbohede and Lebbe*, 2006]. The thermal storage I observed in this portion of the foreshore is consistent with the conceptual model of relative hydraulic stasis at specific areas in the intertidal zone.

In the center of the thermistor transect, T5-T10 recorded consistently cooler temperatures and muted and shallow penetration of diel fluctuations compared to areas both landward and seaward in the intertidal sediment (Figures 3.4b, 3.5, 3.6, and electronic supplement Figure 2 from *Befus et al.* [2013]). Since the terrestrial groundwater 100 m from the coast was also much cooler than the lagoon water (25.8 °C vs 28.5 °C, respectively), these thermistors suggested the presence of a cool intertidal groundwater seep that supported thermal gradients of up to 0.7 °C/cm, but this changed with diel and tidal fluctuations. Temperatures recorded by T5-T10 were warmer than the terrestrial

groundwater by 1°C and showed the effects of additional heat diffusing downward from the intertidal surface.

At the most seaward portion of the intertidal zone (T11-T13), warmer, but still stable, temperatures persisted at lower depths, where the temperatures ranged between the average SWI and the lagoon water temperatures (Figures 3.4c, 3.5, 3.6, and electronic supplement Figure 2 from *Befus et al.* [2013]). Hotter average surface conditions prior to the field measurements could explain these subsurface temperatures. This scenario would require heat from before the data collection to have been transferred deeply into the sediment with short-lived temperature fluctuations during the survey that were uncharacteristic of previous conditions. However, tidal pumping seaward of the piezometers followed by landward groundwater flow or during high tides at the piezometers could also advect warm lagoon water down to the lower thermistors. The temperature recorded at the SWI incorporated both inundated and aerially exposed conditions and, thus, did not dictate the potential for heat to enter the subsurface. Instead, the thermal signature of T11-T13 more closely followed the temperature of the warm lagoon water, controlling the heat at depth. Both the higher heat capacity of water compared to air and thermal blanketing by the upper 10 cm of variably-saturated sediment during low tide allowed the deeper intertidal interstitial environment to retain the heat from warm high tides for the duration of the study (Figure 3.6). Then, at depth, some of the heat stored during the day would be conducted out as nighttime cool pulses originated from the surface, and cooler terrestrial groundwater mixed with the intertidal groundwater.

Thermal conditions at the study site lack the drivers for density-driven convection that contribute significantly to porewater dynamics studied elsewhere [*Rocha*, 2000; *Moore and Wilson*, 2005; *Santos et al.*, 2012a]. First, the studied intertidal zone was thermally shielded from cooler ocean waters by the shallow backreef lagoon. Over the 5-

10 day residence time in the Muri lagoon [*Tait et al.*, 2013], solar radiation would heat the lagoon water, reducing the potential temperature gradients that the lagoon water would impose during flood tide at the similarly heated SWI. Cool, less saline groundwater inputs to the studied intertidal zone also create less possibility for thermally-driven convection while introducing the potential for convection based on solute concentration gradients. This study calculated significant, albeit noisy, upward groundwater fluxes over length scales of ~0.5 m, indicating forced convection drove porewater flow (Figure 3.2c); however, free convection initiates at a smaller scale (10 cm) in some intertidal zones [*Rocha*, 2000] and was below the resolution of this study.

The three distinct thermal zones across the studied intertidal zone suggested vertical heat transport controls the spatial distribution of heat more than horizontal heat transport. Heat conduction provides the mechanism for the surface temperature to penetrate vertically into the sediment, but alternate sources of heat transport are required to explain the difference in temperatures beyond 20 cm depth across the intertidal zone (Figure 3.4). Over the duration of the study, the upper and middle foreshore imported heat through the SWI, while the outer foreshore radiated heat across the SWI (Figure 3.7).

3.4.4. Synthesis of hydraulic, thermal, and geophysical results

Despite downward propagation of surface temperature signals into foreshore sediment, groundwater hydraulic head gradients indicated prevalent seaward and upward porewater flow (Figure 3.2). Unknown vertical fluxes during low tides create two opposite but not exclusive scenarios for downward thermal pulses: low tide marked a period of downward advection by porewater that caused heat to reach greater depths, or upward groundwater advection was overcome by downward thermal conduction.

Both temperature measurements and ER tomograms supported the hydrodynamic context suggested by the observed hydraulic heads and are summarized in Figure 3.8. Swash zone saturation changes and minimal thermal buffering by overlying water were interpreted from the very dynamic temperatures in the upper foreshore and in the ER changes of the upper saline plume. Persistent cool temperatures just beyond the break in slope topography, and co-located high ER values, suggested terrestrial groundwater inputs similar to the fresh groundwater discharge plume of *Robinson et al.* [2007b]; local groundwater was 2.7°C cooler on average than the lagoon water. Direct solar radiation on the surface of the sediment and conduction supplied heat to the upper 40 cm of this portion of the foreshore, but the surface heating attenuated quickly (~10 cm) because of upward groundwater flow that equilibrated with the warmer, shallow sediment. Furthest seaward, the subsurface hydrodynamics of the sandflat consisted of circulating lagoon water dependent on tide stage: temperatures reflected surface conditions, and the ER images suggested the presence of mainly saline porewater.

The conductive length scale, d_c, revealed the significance of heat conduction from surface heat pulses into the shallow (< 20 cm) subsurface. Swash infiltration, seaward terrestrial groundwater flow, and seawater circulation also affected the heat transported into and through the intertidal zone but, in this foreshore setting, mainly contributed to the intertidal thermal regime by setting the lower thermal boundary condition in the subsurface (Figure 3.6). The shallow intertidal sediment heat budget was predominantly controlled by diel solar radiation forcing and conductive transfer vertically, but in the outer foreshore net radiative heat loss was calculated (Figure 3.7). Larger tidal ranges and/or waves could increase and alter the groundwater fluxes to more significantly affect heat transport at the study site, potentially undergoing seasonal cycles.

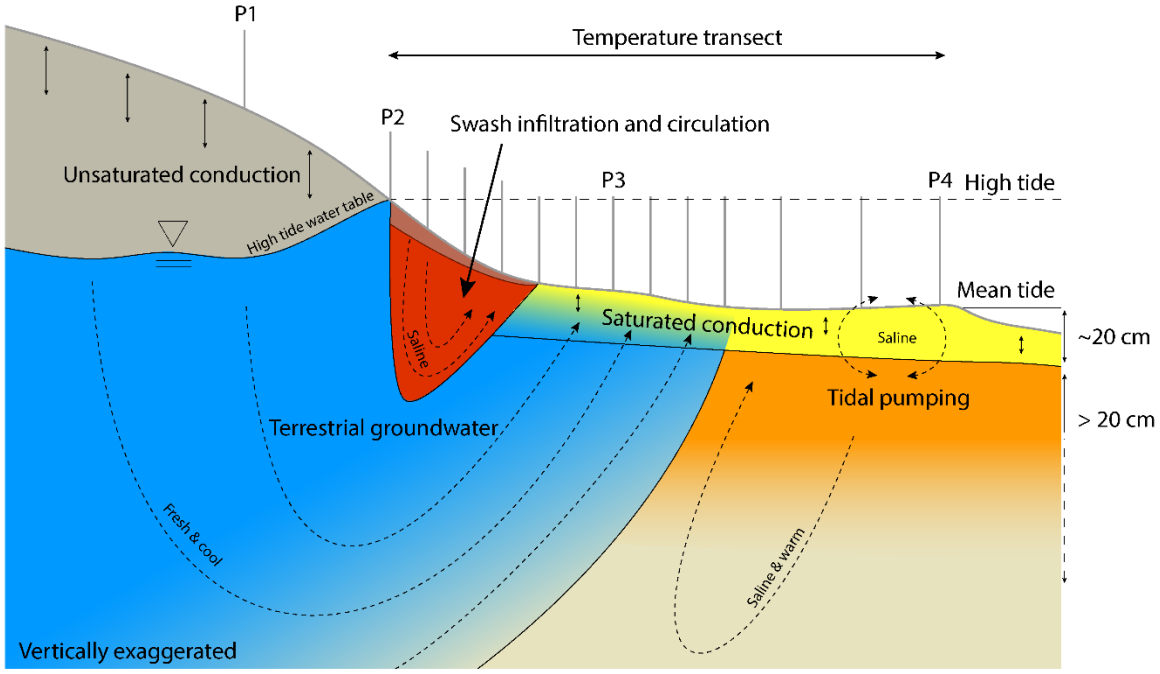

Figure 3.8. Conceptual model of the hydrologic and heat transport setting for the studied intertidal zone. Dashed arrows represent groundwater flowpaths, advecting heat. Solid arrows indicate heat conduction.

3.4.5. Ecological and biogeochemical implications

Stable temperatures in the shallow subsurface of the intertidal zone create refugia for temperature-sensitive fauna. These refugia may have no surface expression, depending upon the beach sediment type, terrestrial groundwater flow system, and the marine energy setting (i.e., waves, tides, and currents). The temperature differences mapped in this study may not represent a significant stress to tropical intertidal species that are well-adapted to larger temperature fluctuations at the surface. However, this study reveals the existence of hydrodynamically-supported thermal refugia that may become critical to certain species in more temperate climates. Multiple studies have already suggested the important role intertidal groundwater seeps have in supporting biological communities through changing nearby sediment and porewater temperatures [*Miller and Ullman*, 2004; *Dale and Miller*, 2007; *Morelissen and Harley*, 2007]. My observations show that organisms would only need to bury themselves 5 cm to escape most diel temperature fluctuations in locations with persistent terrestrial groundwater flow (Figure 3.6b). Different tide, wave, and groundwater hydrodynamics will alter this depth to the thermal refuge.

Within the portion of the intertidal zone where terrestrial groundwater flow significantly mediates the thermal conditions, chemical reaction rates may be significantly more or less favorable than in the adjacent areas of the foreshore. Temperature controls kinetic reaction rates and equilibrium thermodynamics. In nutrient-rich environments, increasing temperature can significantly increase the production of microbial metabolic products [*Sanz-Lázaro et al.*, 2011; *Veraart et al.*, 2011; *Santos et al.*, 2012b]. Thermal variability also affects the photosynthetic capacity of intertidal organisms [*Blanchard et al.*, 1996] and may contribute to the alkalinity budget of the littoral zone [*Cyronak et al.*, 2013]. Additionally, in coastal settings with contaminated groundwater, the potential microbial transformation of contaminants may be regulated by heat transported through the

intertidal sediment, where a significant portion of coastal groundwater contaminants seep into coastal waters through the foreshore [*Westbrook et al.*, 2005; *Maji and Smith*, 2009].

As coastal groundwater systems evolve with increasing coastal water demand due to ongoing development and urbanization and with climate and sea-level change, the properties affecting the fate and transformation of groundwater constituents may also change. Altered terrestrial groundwater gradients may lead to different terrestrial-marine interactions, where saltwater intrusion changes the dynamics between terrestrial groundwater and tidal fluctuations. These changes to the groundwater flow regime may, in turn, affect the intertidal thermal regime and nearshore marine ecosystems therein.

3.5. CONCLUSIONS

Detailed temperature, pressure, and electrical resistivity tomography measurements are combined in this study to explore the importance of coastal hydrodynamics on the thermal regime of a tropical sandy intertidal zone. I confirmed that groundwater-seawater interactions play a critical role in the transport and storage of thermal energy in the shallow portion of intertidal zone sediment. I showed that tide stage can affect the penetration of thermal signals into intertidal sediment as a result of the changing hydrologic boundary conditions, but the diel solar radiation cycle had a larger effect on the transient heating of the intertidal zone than the hydrodynamic transport processes. Even so, areas with terrestrial groundwater discharge sustained cooler temperatures than either swash infiltration or seawater circulation groundwater regimes, highlighting the importance of hydrodynamic boundary conditions on heat transport. When considering only vertical heat transport, conduction explained a majority of the temperature signal propagation, but the measured horizontal groundwater fluxes and temperature patterns $\geq$ 20 cm suggested

alternative flow scenarios that incorporate deeper and multi-dimensional groundwater movement.

The variety in the forcing mechanisms of heat transport in the studied intertidal zone resulted in three unique thermal regimes, collectively characterized by pressure, temperature, and ER measurements. Groundwater hydraulic head gradients indicated the presence of seaward and upward groundwater flow, even during high tide. ER profiles imaged salinity changes that were used to interpret the flow conditions. Within the upper foreshore, variable flooding and swash infiltration created rapid temperature changes during most tide stages leading to net import of heat into sediment, but near a break in topographic slope of the beach, surface temperatures lingered in the saturated subsurface up to 4 hours. Just seaward of the slope break, sediment temperatures beyond depths of 10 cm were stable and 1.3°C cooler than the rest of the intertidal sandflat. This thermal pattern was explained by upward and seaward groundwater flow suggested by both the pressure and ER data and also resulted in a net import of heat into the sediment. The most seaward portion of the study transect recorded stable but warm temperatures in the shallow subsurface with a net export of heat from the sediment, which matched the average surface temperatures. Groundwater movement in this seaward portion of the sandflat may be primarily due to tidal pumping; hence, the temperature range reflects primarily seawater temperatures.

My analysis revealed the potential for subterranean thermal refugia in intertidal zones supported by coastal groundwater systems. In more temperate regions or where larger differences exist between groundwater and seawater temperatures, the thermally moderated portion of intertidal zones may control habitat quality as well as biogeochemical reaction rates.

Chapter 4:

Geoelectrical signals of geologic and hydrologic processes in a fringing reef lagoon setting[3]

Don't you realize that the sea is the home of water? All water is off on a journey unless it's in the sea, and it's homesick, and bound to make its way home someday.

-a quote by Zora Neale Hurston (1891-1960)

ABSTRACT

Coastal groundwater may discharge into nearshore and offshore waters forced by terrestrial fluxes, controlled by local geology, and modulated by the hydrodynamics of littoral water. I investigated the electrical signature of these features with a dense, multiscale network of electrical resistivity tomography (ERT) surveys in the Muri Lagoon of Rarotonga, Cook Islands. The ERT surveys spanned from onshore to 400 m into the lagoon and used standard electrodes on land and across the foreshore, submerged electrodes in the shallow subtidal zone, and floating electrodes towed throughout the reef lagoon by a boat. ERT surveys on land mapped a typical freshwater lens underlain by a saltwater wedge, but with possible deviations in flowpaths and salinity distribution from the classical model due to an adjacent tidal creek. Further inland, ERT surveys imaged a layer of lava flow deposits that is potentially a confining hydrogeologic unit; this unit was used to constrain the expected electrical resistivity of these deposits below the lagoon. ERT surveys across the intertidal zone and into the lagoon indicated fresh groundwater and porewater salinity patterns consistent with previous small-scale studies including the seaward extension of fresh groundwater pathways to the lagoon. Electrical resistivity (ER) variations in the lagoon subsurface highlighted heterogeneities in the lagoon structure that may focus submarine groundwater discharge (SGD) through previously unknown buried lava flow deposits in

[3]Befus, K. M., M. B. Cardenas, D. V. Erler, and D. R. Tait (2014), Geoelectrical signals of geologic and hydrologic processes in a fringing reef lagoon setting, *J. Hydrol*., doi: 10.1016/j.jhydrol.2014.05.070.

All of the authors contributed to the data collection and interpretation of the results. Befus was responsible for the analysis and data collection.

the lagoon. A transition to higher ER values near the reef crest is consistent with the ER signature of porosity reduction due to ongoing differential cementation of reef deposits across the lagoon. The imaged coastal hydrostratigraphic heterogeneity may thus control terrestrial and marine porewater mixing, support SGD, and provide the pathways for groundwater and the materials it transports into the lagoon. This hydrogeophysical investigation highlighted the spatial heterogeneity of submarine coastal geology and its hydrogeologic control in a reef lagoon setting, but is likely to occur in many coastal settings. Ignoring geologic complexity can result in mischaracterization of SGD and other coastal groundwater processes at many spatial scales. This chapter was published as a part of collaborative work [*Befus et al.*, 2014].

4.1. INTRODUCTION

Coastal communities often rely on limited freshwater resources that are vulnerable to changes in groundwater storage and contamination [*White and Falkland*, 2010; *Bailey and Jenson*, 2013]. Coastal groundwater systems respond to these perturbations over multiple timescales controlled in part by aquifer properties [*Michael et al.*, 2005; *Ferguson and Gleeson*, 2012; *Gonneea et al.*, 2013]. Moreover, spatial heterogeneities in permeability and porosity, related to lithology and/or geologic history, can accentuate the effects of climate- or human-induced changes on groundwater availability and residence times for even large aquifers [*Swarzenski et al.*, 2013]. Thus, delineating coastal hydrogeologic structure, or hydrostratigraphy, can improve the characterization of groundwater flow and management of groundwater resources. Additionally, hydrostratigraphic complexities may control how coastal aquifers interact with marine ecosystems, transport solutes to coastal waters, and respond to perturbations such as climate change.

Electrical resistivity (ER) surveys have been used extensively in coastal settings to reveal groundwater dynamics and mixing with seawater [e.g., *Zohdy and Jackson*, 1969;

Manheim et al., 2004; *Breier et al.*, 2005; *Day-Lewis et al.*, 2006; *Swarzenski et al.*, 2006; *Swarzenski and Izbicki*, 2009; *Cardenas et al.*, 2010; *Henderson et al.*, 2010; *Dimova et al.*, 2012; *Befus et al.*, 2013]. Many ER studies rely on assumptions of geologic homogeneity to interpret porewater salinity variations or interpret inconsistent ER anomalies as being caused by heterogeneity in geologic properties. However, subsurface geologic heterogeneity is expected in coastal environments, where structural, volcanic, erosional, and diagenetic processes shape and alter coastal geology [*Moore*, 2001; *Montaggioni and Braithwaite*, 2009; *Evans and Lizarralde*, 2011; *Rankey and Garza-Perez*, 2012; *Ramalho et al.*, 2013]. Time-lapse ER surveys remove some uncertainty when interpreting the results of coastal ER studies as the changes measured in time-lapse ER surveys are predominantly from dynamic porewater salinity rather than changing subsurface geologic materials or their electrical properties [*Ogilvy et al.*, 2009; *Zarroca et al.*, 2011; *Dimova et al.*, 2012; *Befus et al.*, 2013; *Misonou et al.*, 2013]. But, even these surveys suffer from uncertainty associated with both the ER structure and the electrical boundary conditions in or over dynamic salinity water regimes [*Day-Lewis et al.*, 2006; *Henderson et al.*, 2010; *Orlando*, 2013]. Thus, ER surveying always images the subsurface within an integrated geologic and hydrodynamic context, and the relative contributions of each to the measured ER signal must be acknowledged during interpretation.

As the ultimate goal of many coastal ER studies is to elucidate groundwater features, ER surveys are used to develop and test the reliability of groundwater models. However, insights into the hydrodynamic processes involved in submarine groundwater discharge (SGD) and porewater mixing within the subterranean estuary often arise through models that predominantly consider a homogeneous subsurface [e.g., *Robinson et al.*, 2007b; *Vandenbohede and Lebbe*, 2007; *Gibbes et al.*, 2008; *Xin et al.*, 2010; *Konikow et al.*, 2013]. Coastal ER results can compare favorably to shoreline groundwater simulations,

but are typically based on the assumption of homogeneity [*Henderson et al.*, 2010; *Nakada et al.*, 2011]. However, both geologic data [*Moore*, 2001; *Emery and Myers*, 2009; *Ramalho et al.*, 2013] and geophysical surveys [*Zohdy and Jackson*, 1969; *Evans and Lizarralde*, 2011; *Dimova et al.*, 2012; *Misonou et al.*, 2013; *Russoniello et al.*, 2013] document spatial heterogeneity across multiple spatial scales. Indeed, spatial variability in substrate properties and hydrodynamic conditions exist within the subterranean littoral zone and contribute to the magnitude of benthic fluxes [*Santos et al.*, 2012b; *Dose et al.*, 2013; *Sawyer et al.*, 2013]. In this chapter, I characterize coastal geologic heterogeneity with ER surveys in the context of a fringing reef lagoon system. These methods and results can help guide future SGD field studies and coastal groundwater flow models as they evolve to measure and incorporate different scales of heterogeneity.

I investigated the hydrostratigraphic framework of a reef in southeastern Rarotonga with comprehensive onshore and offshore electrical resistivity tomography (ERT) surveys and interpreted the findings within the context of previous geologic and hydrologic studies. First, I briefly revisit related studies on Rarotonga that detected active fresh SGD at the same field site. I next use a petrophysical model and the range of ER values corresponding to fresher porewater from the previous work to identify other areas where fresh groundwater may be present and volumetrically significant in the subsurface with the more extensive ERT network in this study. Next, I discuss the ERT surveys within the context of the local geology to understand the effects of spatial heterogeneity of the lagoon geology on the ERT results. I then explore the sensitivity and uniqueness of these ER results with synthetic simulations (i.e., forward models) to assess the reliability of my data and to guide the interpretations. Finally, I extend these results to elucidate potential heterogeneous geologic controls on groundwater pathways into any nearshore or reef system.

4.2. STUDY SITE

Rarotonga is a 67 km^2 volcanic island with a fringing reef located in the south-central Pacific Ocean (21.2°S 159.8°W) (Figure 4.1a). The island was formed by basaltic eruptions ~2 million years ago (Ma), experienced a brief volcanic hiatus, and then underwent a short period of late-stage volcanism [*Thompson et al.*, 1998]. Eroded and weathered basalts (1.1-2.3 Ma) now shape the rugged, mountainous interior of Rarotonga. A narrow rim (0.3-1.2 km) of alluvium and reef deposits surrounds the exposed volcanic rocks. Within this coastal plain, spring- and stream-fed wetlands form inland of beach-ridge deposits. During average flows, nearly all of the streams terminate in these coastal marshes and do not discharge directly to the coast [*Waterhouse and Petty*, 1986]. The fringing reef crest ranges from 50-900 m offshore and sets the breadth of the shallow (<3 m) reef lagoon.

This study was conducted in the Muri area and Muri Lagoon on the southeast of Rarotonga (Figure 4.1). Muri Lagoon is the widest portion of the lagoon surrounding Rarotonga (500-800 m) and contains the only lagoon islets. Both on and offshore, the local geology at Muri is complicated by the Raemaru phonolite flow deposit (1.1 Ma) that is exposed in the mountainous interior as well as the southernmost islet, Taakoka. The subterranean expression of the Muri Raemaru flow is unknown but may extend into the Muri Lagoon [*Thompson et al.*, 1998]. On land, the surficial geology consists of carbonate sand beach ridges, wetland sediments, and alluvial deposits [*Moriwaki et al.*, 2006], which comprise a shallow aquifer system with groundwater flow towards the coast [*Waterhouse and Petty*, 1986]. An ER sounding in north Muri detected volcanic bedrock at 13.7 m depth, potentially constraining the local thickness of the coastal aquifer [*Ricci and Scott*, 1998]. The geologic framework of the lagoon and near-beach environment addressed in this study has not been investigated before in detail.

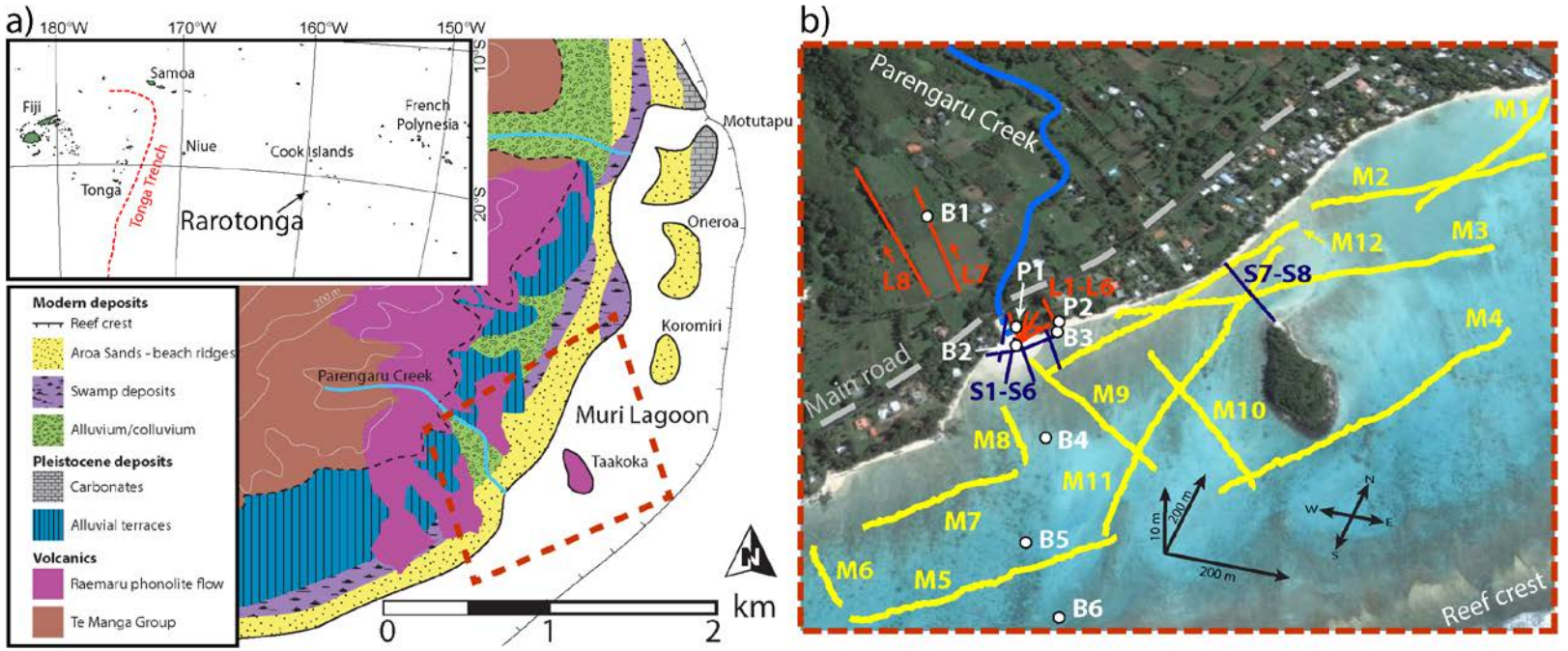

Figure 4.1. a) Surficial geologic map of the southeast corner of Rarotonga with the location of b) outlined in red [after *Wood and Hay*, 1970; *Thompson et al.*, 1998; *Moriwaki et al.*, 2006]. b) The locations of the onshore (red lines), seafloor (blue lines), and marine (yellow lines) ERT surveys. Ground truth measurements were conducted on land and in the lagoon (white dots).

Previous hydrologic studies at Muri provide site-specific evidence of SGD into the reef lagoon. Many of the recent studies focus on the coastal environment near Parengaru Creek, a perennial creek that is tidally-affected until the main coastal road (Figure 4.1b). Porewater sampling at the outlet of Parengaru Creek identified brackish porewater (< 20 practical salinity units, PSU) extending 50 m into the lagoon with fresher porewater (<10 PSU) 10 m seaward of the high tide mark [*Erler et al.*, 2014]. SGD also delivers significant amounts of reactive nitrogen into the lagoon [*Erler et al.*, 2014]. Most of the saturated sediment was anoxic within 3 cm of the water table or sediment-water interface (SWI) [*Cyronak et al.*, 2012]. Along a nearby transect, an ERT survey imaged ER values > 1.5 Ωm over the first 10 m of the intertidal zone, where net groundwater discharge (up to 1 m d^{-1}) was also measured directly with both pressure and temperature measurements [*Befus et al.*, 2013]. Beyond quantifying groundwater dynamics at the coast, significant SGD fluxes (0.2-1.9 cm d^{-1}) into the Muri lagoon were calculated using radiogenic isotopes [*Tait et al.*, 2013]. Thus, the Muri Lagoon actively receives SGD, but the distribution and pathways of this SGD to the lagoon remain poorly constrained.

4.3. ELECTRICAL RESISTIVITY (ER) METHODS

Direct current ER surveys measure the electrical potential field generated by controlled electrical current sources. Earth materials have different electrical resistivity values as a function of chemical composition and porosity, and bulk ER of subsurface materials can be significantly reduced by the low ER of ion-rich interstitial fluids [*Telford et al.*, 1990]. Disentangling the relative contributions of lithology and porewater in a measured ER signal relies upon petrophysical models. In sandy sediment or rock, the bulk ER (ρ_b) of the fluid and the matrix can be described using the empirical relationship [*Archie*, 1942]:

$$\rho_b = \rho_f n^{-m} \tag{4.1}$$

incorporating ER contributions from the fluid resistivity (ρ_f) and the properties of the matrix through the porosity (n) and a cementation factor (m). ERT surveys roughly provide the spatial pattern of this ρ_b once the field data are inverted (see *Loke and Barker* [1996] for an introduction to ERT inversion). Equation (4.1), known as Archie's Law, works well for sandy sediment and sandstones but does not accurately estimate the ρ_b for sediment with clay or other rock types [*Revil et al.*, 1998; *Jackson et al.*, 2002].

A variety of field deployment methods and configurations exist for ERT imaging [*Loke et al.*, 2013]. ERT datasets are collected by combining numerous electrode spacings and positions to image the subsurface both in depth (i.e., soundings) and at least one horizontal direction (i.e., profiling). Direct current ER data incorporate both the configuration of the electrodes and the ability of a medium to transmit current when investigating the subsurface [*Telford et al.*, 1990]. As the arrangement of the source and receiver electrodes are changed, the sensitivity (i.e., the ability to accurately image the subsurface [*Henderson et al.*, 2010]) of the survey to the surrounding medium also changes. ERT surveys are also restricted by the ability to resolve features in the subsurface due to the integrated contributions from individual subsurface components [*Day-Lewis and Lane*, 2004; *Henderson et al.*, 2010].

An inverted ERT section may show ER structure that fails to recover the true ER of individual geological entities, creating an important difference between the inverted (i.e., ρ_b) and true ER ($\rho_{b,\text{true}}$) structure of the subsurface. Together, the effects of different electrode configurations and electrode placements in relation to water would change the results from marine, submerged, and terrestrial ERT surveys investigating the same subsurface areas. Also, the thickness and conductivity of the water column strongly affects ERT results [*Loke and Lane*, 2004; *Day-Lewis et al.*, 2006; *Henderson et al.*, 2010;

Orlando, 2013]. Thicker and more conductive overlying water greatly reduces the sensitivity of ERT to the subsurface, whereby the majority of the injected current remains in the conductive water layer, termed current channeling [*Day-Lewis et al.*, 2006].

Quantitative measures of the sensitivity of the ERT survey can be calculated using components of the inverse problem [*Alumbaugh and Newman*, 2000; *Day-Lewis et al.*, 2004; *Day-Lewis et al.*, 2005]. In this study, I used the model resolution matrix, specifically the diagonal of this matrix calculated using Equation 10 in *Day-Lewis et al.* [2005], to gauge the ability of an ERT survey to describe a prescribed ρ_b structure. A model resolution with a diagonal of unity indicates a perfectly resolved ER feature (i.e, $\rho_{b,\text{true}} = \rho_b$), while lower resolution suggests greater uncertainty in the ρ_b values of the inverted model. The model resolution analysis was performed on the synthetic data to test the ability of the analogous field ERT surveys to image real subsurface features.

4.3.1. Field ER surveys

Two-dimensional ERT surveys were conducted during two field seasons: February 2011 and March 2012. I used a SuperStingR8 resistivity meter (Advanced Geosciences, Inc) to collect ERT data with three configurations: 1) 56 graphite electrodes with a 1.5 m spacing on a stationary waterproof cable deployed on the seafloor, 2) continuous resistivity profiling (CRP) using an 11 electrode boat-towed, floating cable with 5 m spacing, and 3) terrestrial ERT surveys with 1.25-3 m electrode spacing with 56 stainless-steel stakes. During the CRP surveys, two graphite electrodes injected current to create an electrical field that was measured by nine stainless-steel electrodes. The CRP survey used the dipole-dipole array, while the submerged and terrestrial surveys were run as both dipole-dipole and Schlumberger arrays. During the CRP survey, simultaneous differential GPS and sonar measurements recorded position, water temperature, and water depth, while an independent

sonde measured water conductivity. The GPS measurements were used to position the CRP and sonar measurements, using the offset between the sonar, CRP cable, and GPS receiver. Terrestrial and seafloor ERT surveys were referenced with a total station. Select boreholes were drilled with a 41 mm outside diameter portable core drill, and pits were hand dug to characterize sediment type and determine refusal depths.

4.3.2. ER inversion

ERT datasets were inverted using Res2DInv [*Loke and Barker*, 1996] with robust parameter constraints. Dipole-dipole and Schlumberger surveys were merged and inverted together for all terrestrial and submerged datasets collected during the same tide conditions. Up to 10% of the merged datasets were culled to remove poor quality data and improve inversion performance.

Each field survey required configuration-specific constraints within the inversion. Seafloor ERT inversions included seafloor topography, water thickness, and water resistivity information. Terrestrial surveys included topography in their inversions. The CRP survey was cropped into straight segments prior to inversion. Consistent transfer resistances for the CRP raw data indicated all eight dipoles collected data above the noise threshold [*Rucker et al.*, 2011; *Befus et al.*, 2012]. CRP inversions incorporated water depths from the sonar records, and the mean lagoon water resistivity (ρ_f = 0.175±0.001 Ωm) during the survey was prescribed in the inversion. The marine ERT dataset was collected during low tide to maximize the investigation sensitivity, and the water depth ranged from 0.4-2.5 m with an average depth of 1.4 m. Due to the significant current channeling expected in the lagoon water, the ER of the water layer was solved for in the CRP inversion but with the constraint to minimize variability from the prescribed lagoon ρ_f value. Lagoon water temperature was 28.2 ± 0.5°C during the marine surveys. ER is

dependent on temperature, but 0.5°C would introduce ~1% error to the measurements and was less than the expected noise in the data (~3%) [*Hayley et al.*, 2007; *Befus et al.*, 2012]. Thus, no temperature correction was applied to the ERT data.

4.3.3. ER forward modeling

I simulated ERT surveys to test the degree to which the field ERT surveys could image a resistive body and thus constrain the interpretation of resistive features in the inverted field profiles. Simulated ERT measurements using the field survey configurations were modeled with the generic finite-element software Comsol Multiphysics after *Butler and Sinha* [2012]. The electrode spacing, array types, and active quadrapoles from the submerged and marine surveys in the field were used for the electrode configurations in the simulations. The static electrical field for each current dipole was solved in three-dimensional (3D) space with tetrahedral elements:

$$\nabla \cdot \nabla \left(\frac{1}{\rho(x,y,z)} \Phi(x,y,z) \right) = q, \tag{4.2}$$

where $\mathbf{\Phi}(x,y,z)$ is the 3D scalar electrical potential field [V], $\boldsymbol{\rho}(x,y,z)$ is the 3D scalar electrical resistivity field [Ωm], and $\mathbf{q}$ is a vector of the current sources and sinks [A]. Infinite boundary elements surrounded the main domain, except for a Neumann no-flux condition applied to all exterior model surfaces (Figure 4.2) [*Butler and Sinha*, 2012]:

$$\nabla\Phi \cdot n = 0 \text{ , for } z = z_{surf},\ z = -\infty, \text{ and } x = y = \pm\infty, \tag{4.3}$$

with $\mathbf{n}$ the normal vector of each surface and z_{surf} the elevation of the top domain boundary (i.e., land or water surface). An infinite boundary element is mapped or stretched toward infinity, thereby reducing model edge effects by extending the electrical insulation

boundaries (Equation 4.3) infinitely away from the main domain [*Zienkiewicz et al.*, 1983]. I refined elements near all active electrodes to accurately simulate the near-field electrical potentials. Models with > 5×10^4 elements introduced < 2% error to simulated potentials modeled with 10^6 elements. Thus, refining the mesh to > 5×10^4 elements no longer changed the surface electrical potential significantly in the context of modeling field-scale ER signals.

In addition to potential numerical errors introduced by the numerical model to the calculated electrical field (< 2%), normally distributed random noise was added to the simulated raw resistance data with a standard deviation of 5% of the mean modeled resistance value to resemble the noise levels that occur during data collection. Dipole-dipole and Schlumberger array model results were combined prior to the inversion of the seafloor scenario. These forward model outputs were then inverted using the same inversion parameters as the field data.

4.4. RESULTS

A network of 28 ERT surveys was collected during the two field seasons, comprised of 8 terrestrial (L1-L8), 8 seafloor (S1-S8), and 12 CRP (M1-M12) lines (Figure 4.1b). Terrestrial and seafloor ERT surveys are shown for higher than average tides, while the CRP survey was conducted during low tide. Inversion absolute error (E_{abs}) provides a metric for how well an inverted ERT survey reproduced the field data:

$$E_{rel} = \frac{100}{N}\sum\left|\log_{10}(\boldsymbol{\rho}_{\mathbf{a,meas}}) - \log_{10}(\boldsymbol{\rho}_{\mathbf{a,calc}})\right| \tag{4.4}$$

with N data points and the apparent resistivities of the measured data ($\boldsymbol{\rho}_{\mathbf{a,meas}}$) and synthetic data ($\boldsymbol{\rho}_{\mathbf{a,calc}}$) calculated using a forward model based on the ρ_b structure for a given iteration. E_{abs} was below 6% for all but one of the inverted sections (S7, E_{abs}= 9.5%).

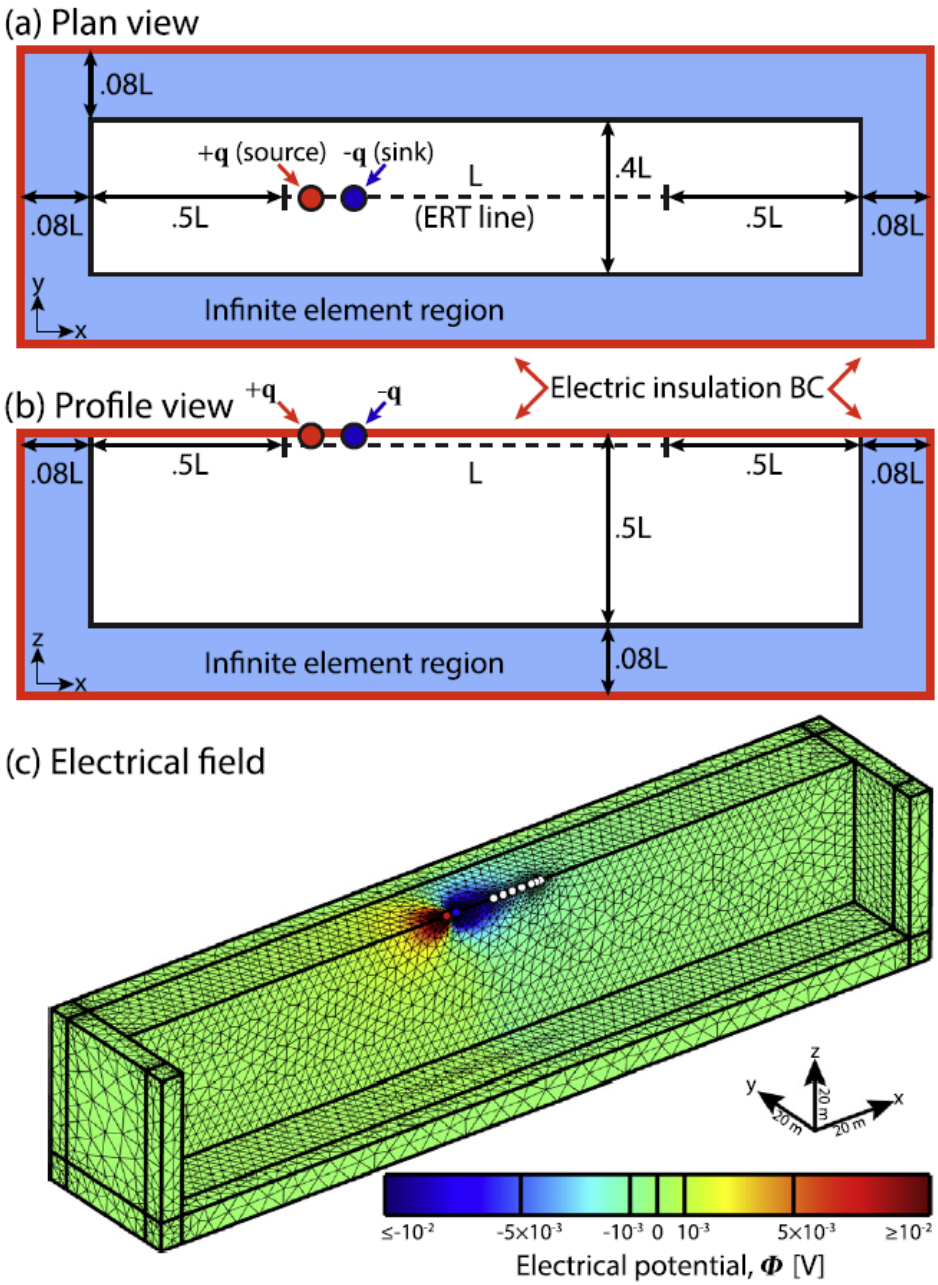

Figure 4.2. Forward model geometry of the static electrical field in a) plan view and b) profile view. The main model domain (white) was surrounded by infinite elements (blue), except for the top insulating boundary. c) The forward model domain with an example electrical potential solution, tetrahedral mesh, current electrodes (red and blue), and potential electrodes (white) for a dipole-dipole array. Half of the main domain and one subdomain in the -y direction are transparent in c).

The inversions converged within four iterations, and additional iterations did not significantly improve E_{abs} values or more accurately resolved ER patterns. All ERT results show the inverted profile after four iterations.

4.4.1. Onshore ERT surveys

Two roll-along ERT surveys (L7-L8) were conducted inland to image the local coastal geology, where porewater salinity effects on the survey results would be minimal (Figure 4.3). In both surveys, 3-5 m of relatively conductive materials (10-70 Ωm) at the surface overlaid a much more resistive layer (≥ 100 Ωm) for the seaward half (L8) and the entirety (L7) of the lines. This resistive layer was 5-10 m thick. Both profiles also became more conductive > 10 m below the land surface.

Near the outlet of Parengaru Creek, six land ERT surveys (L1-L6) and six seafloor surveys (S1-S6) were collected (Figure 4.1b and 4.4a). The upper 0.5-2 m of the terrestrial lines showed a layer of high ρ_b (>100 Ωm). Only along L2 was this resistive layer mostly absent, where the line was within the intertidal zone until 10 m from the northern end. L1, L3, L4, and L6 detected shallow ρ_b anomalies > 50 Ωm at the inland portions of the lines that reached to within ~20 m of the shoreline. Moderate ρ_b values (5-50 Ωm) comprised the majority of the terrestrial ERT surveys. An inland dipping transition to lower ρ_b values (< 5 Ωm) was imaged at the seaward ends of L3 and L4. Running along shore, L2 detected a ~3 m thick lens of ≥ 10 Ωm to 5 m depth overlying more conductive material.

A different ρ_b pattern was imaged approaching Parengaru Creek than in the other terrestrial profiles. The southern 10 m of L6 and the majority of L5 imaged conductive (≤ 10 Ωm) subsurface material further inland than the other terrestrial surveys. Additionally, the upper 5 m of S1 imaged a ~2 m thick layer of conductive material (≤ 10 Ωm) at 3 m depth that became more resistive inland. Thus, the ERT surveys imaged an overall

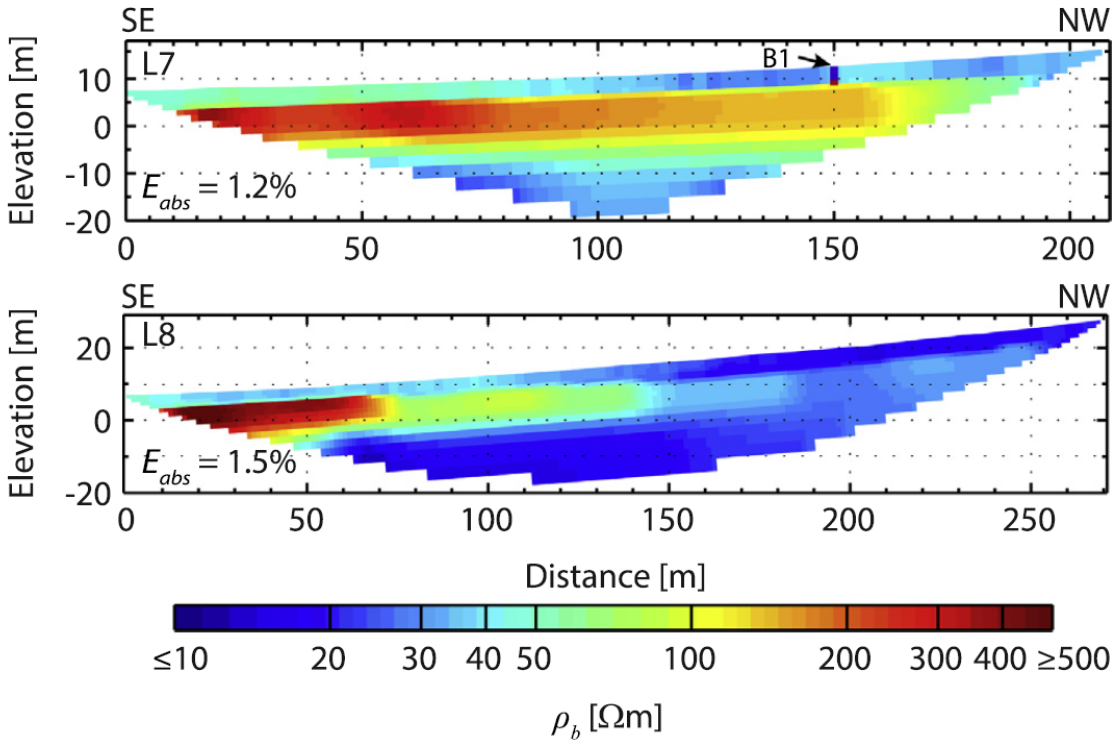

Figure 4.3. Inverted ERT profiles of L7 and L8 running parallel to Parengaru Creek over the Raemaru phonolite flow and alluvial deposits (see Figure 4.1a). Conductive materials at depth may be colluvium or weathering products of older lava flows produced during a volcanic hiatus [*Thompson et al.*, 1998]. Borehole B1 was drilled through 3 m of clay-rich soil (blue layer in B1) before refusal (shown as red in B1).

transition from higher ρ_b (≥ 50 Ωm) to lower ρ_b (≤ 5 Ωm) moving towards the lagoon, and a slightly smaller decrease in ρ_b moving towards Parengaru Creek.

4.4.2. Seafloor ERT surveys

Seafloor ERT surveys (S1-S6) imaged ER anomalies across the intertidal zone and into the proximal, subtidal portion of the lagoon (Figure 4.4a). Across the mouth of Parengaru Creek, S3 detected two moderate ρ_b (≥ 5 Ωm) zones at 5 m depth, matching the ρ_b signal from S1 running along the creek. S2 also imaged the same feature at 5 m depth that extended seaward for 10 m beyond the intersection with S3, thereafter becoming increasingly conductive throughout. Moving north along the beach, S4 imaged an even more resistive ρ_b anomaly than across the mouth of Parengaru Creek, and S5 imaged moderate ρ_b zones 60-80 m into the lagoon. S6 showed a slight ρ_b increase at the seaward end that may be connected to the high ρ_b feature to the north in S5.

At the Taakoka passage, two seafloor surveys (S7 and S8) imaged the top of a resistive anomaly (> 5 Ωm) 3-7 m below the SWI with more conductive overlying material (Figure 4.5). The interface depth of the resistive feature dipped from Taakoka towards mainland Rarotonga and became increasingly less resistive in the 40 m approaching the mainland.

4.4.3. Lagoon ERT transects

Marine ERT surveys from Muri Lagoon (M1-M12) imaged changes in near-surface ρ_b structure over 0.5 km^2 (Figure 4.6a). Every inverted marine ERT line became more resistive with depth, but not uniformly. Within 2 m below the SWI, the ρ_b mainly remained ≤ 0.5 Ωm, where ρ_b values > 0.5 Ωm began at depths of 1.1 m ± 0.9 m. All of the marine surveys detected zones with ρ_b > 0.8 Ωm, and 45% of the profiled subsurface was comprised of ρ_b > 1.5 Ωm (Figure 4.6a). Indeed, large, more resistive features were imaged

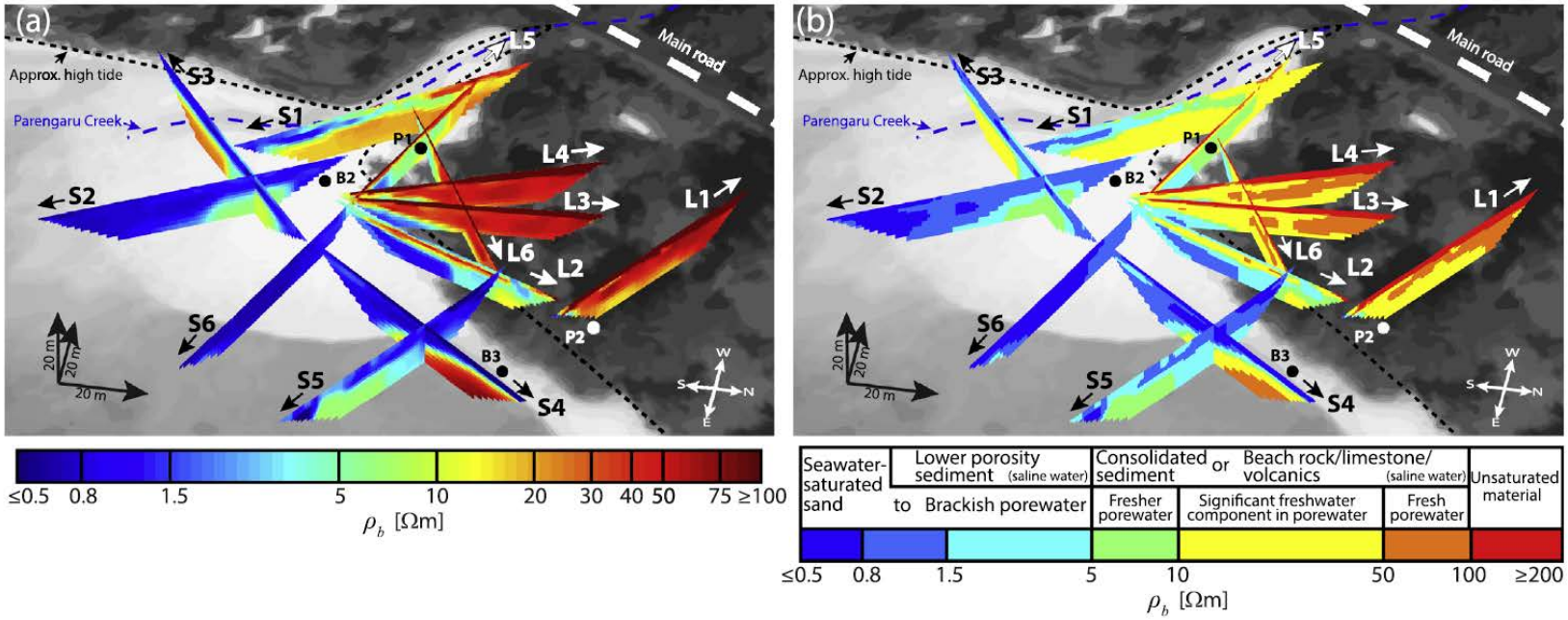

Figure 4.4. a) Inverted ERT results and b) inverted ERT results with contours at interpreted ρ_b values for terrestrial and seafloor ERT surveys at the outlet of Parengaru Creek. Resistive features characteristic of fresh porewater extend into the lagoon under the deltaic sandflat and 50 m north of the creek, indicating potential for active fresh groundwater discharge to the lagoon. Approximate geologic and hydrologic interpretations of the ρ_b values are given in the top and bottom rows of the legend, respectively, incorporating the incorporating analysis with Archie's Law (Equation 4.1), the time-series study in *Befus et al.* [2013], and estimated values of heterogeneous geology after *Telford et al.* [1990].

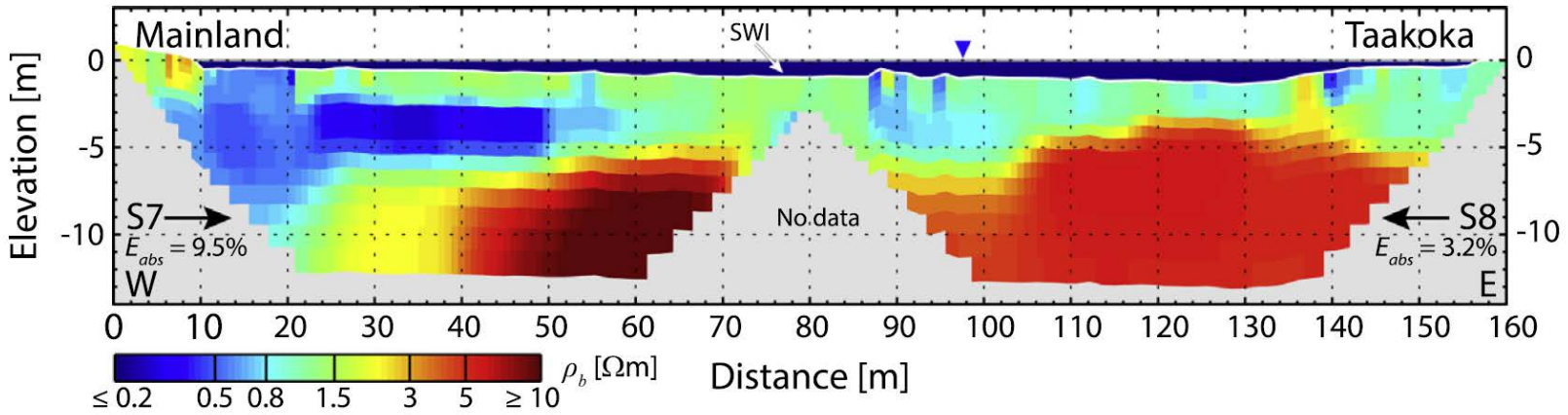

Figure 4.5. The seafloor ERT inverted profiles for S7 and S8, spanning the passage between the Taakoka islet and mainland Rarotonga.

southwest of Taakoka (M11-12) ≥ 5 Ωm and in the surveys running near the reef crest (M4-5) ≥ 3 Ωm. Lower magnitude ρ_b signals (0.8-1.5 Ωm) were broadly distributed in the lagoon subsurface as a hummocky interface (e.g., M9-11) or as individual pockets (M1-3). Near the shore, more resistive water column ρ_f values (≥ 0.5 Ωm) were required by the inversions than the measured ER for lagoon water (0.175 Ωm), predominantly in very shallow (< 1 m) portions of the lines (Figure 4.6a).

4.4.4. Forward model simulations

I simulated ERT surveys with a prescribed $\rho_{b,true}$ structure to test the ability of the marine ERT methods to image resistors despite the overlying conductive lagoon water and seawater-saturated materials. The $\rho_{b,true}$ structure for the forward models consisted of a buried resistive body (500 Ωm, consistent with the resistive layer in L7 and L8) overlain by 2 m of more conductive sediment (ρ_b = 0.431 Ωm with ρ_f =0.175 Ωm, n=0.5, and m=1.3 in Equation 4.1) (Figure 4.7a and f). The resistive body spanned the center 20% of the modeled survey and was bounded on each side by the conductive sediment. In each simulated survey, a 1.4 m layer of very high conductivity (0.175 Ωm, average lagoon ρ_f) was included at the surface, corresponding to the study area average lagoon depth. This $\rho_{b,true}$ structure extended infinitely in the line-perpendicular y-direction. While many combinations of $\rho_{b,true}$ structure and values may be explored, the structure adopted here tested a maximum current channeling scenario, describing the lowest resolution of a resistive body buried below layers of very conductive, shallow water and very porous sediment saturated with the overlying water.

Simulated seafloor and marine field configurations accurately imaged the position of the assigned resistive anomaly, but the individual relative resolutions of the ERT surveys were not sufficient to recover the full magnitude of the high $\rho_{b,true}$ feature (Figure 4.7).

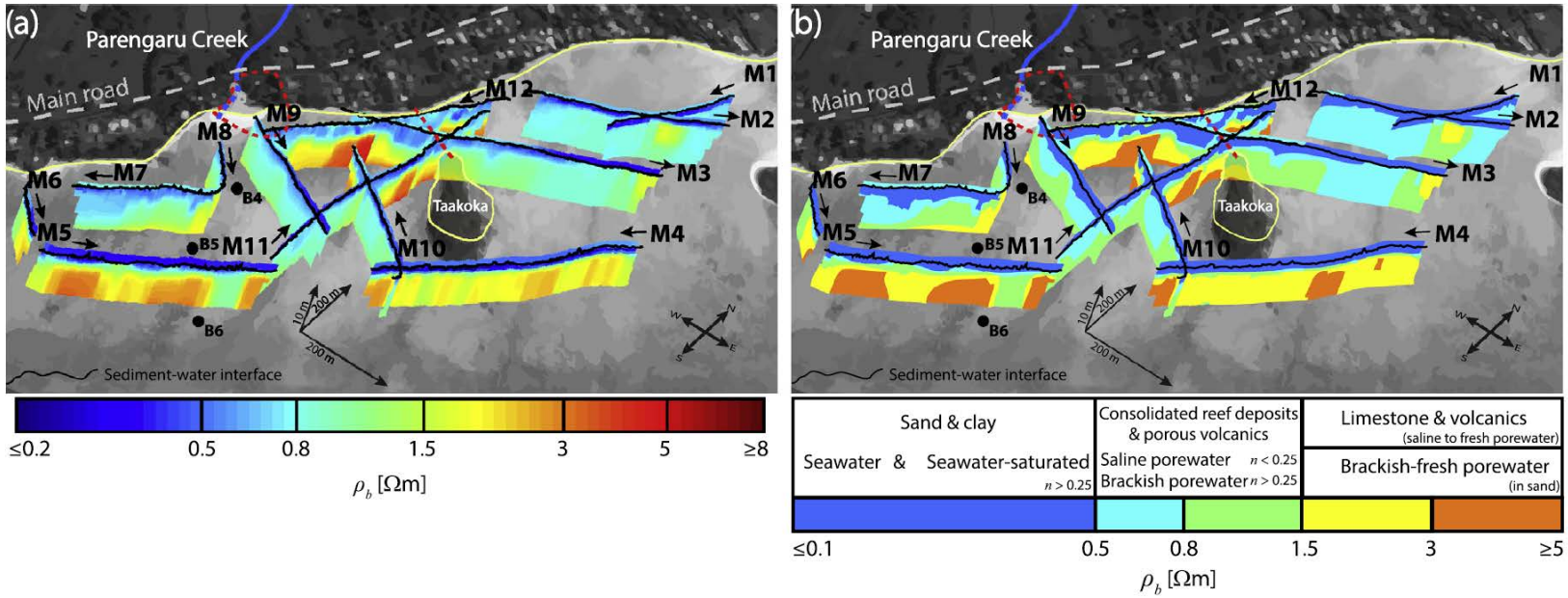

Figure 4.6. a) Inverted marine ERT survey results and b) contours at interpreted ρ_b values from Muri Lagoon (M1-M12). High ρ_b features existed throughout the lagoon. Lithology or porewater salinity changes could explain the ρ_b patterns. The locations of the onshore surveys are outlined in red. Approximate geologic and hydrologic interpretations of the ρ_b values are given in the top and bottom rows of the legend, respectively, incorporating the time-series analysis by *Befus et al.* [2013], Archie's Law (Equation 4.1), and estimated values of seawater-saturated heterogeneous geology developed from the forward models in this study.

While both models included constraints for the water layer, the modeled marine inversion (Figure 4.7g) independently solved for the ρ_f of the water layer. Conversely, the geometry and ρ_f of the water layer in the modeled seafloor survey (Figure 4.7b) were constant during the inversion and were thus perfectly resolved.

Both inverted ERT simulations resolved the conductive layer between the water and resistive body, but the smaller electrode spacing of the seafloor survey (Figure 4.7b) detected the boundary of the resistive body better. Away from the resistive body, both inverted profiles replicated the starting model to within ± 0.25 Ωm for the majority of the domains. Below the SWI, the inverted marine simulation (Figure 4.7g) included excessively conductive values that resulted, in part, from the 5 m electrode spacing not sufficiently resolving this interface. This low ρ_b just below the SWI also occurred in the inverted field CRP sections (e.g., Figure 4.7e), suggesting the field marine inversions (Figure 4.6) also lacked the resolution to accurately model the shallowest sediment.

Within the resistive anomaly, the maximum ρ_b values for the seafloor and marine simulations were 8.1 Ωm and 12.4 Ωm, respectively, returning < 2.5% of the starting model $\rho_{b,true}$ maximum. The marine simulation modeled the edges of the resistive feature accurately to 12 m depth (Figure 4.7g and h). The simulated seafloor survey, instead, only resolved the upper ~5 m of the resistive zone, yielding a resistive structure that disappeared or became more conductive at depth (Figure 4.7b and c). Thus, the maximum electrode spacing (9 m) of the seafloor survey failed to detect the prescribed structure at > 10 m depth, setting a lower limit of interpretation for the field seafloor surveys of ~ 10 m (i.e., depth of investigation). It is important to note that the model resolution is inherently linked to 1) the inversion setup that includes the measurement errors in the data and the regularization or noise dampening used and 2) the ERT data collection that incorporates $\rho_{b,true}$ structure, electrode spacings, amounts of current injected, and electrode

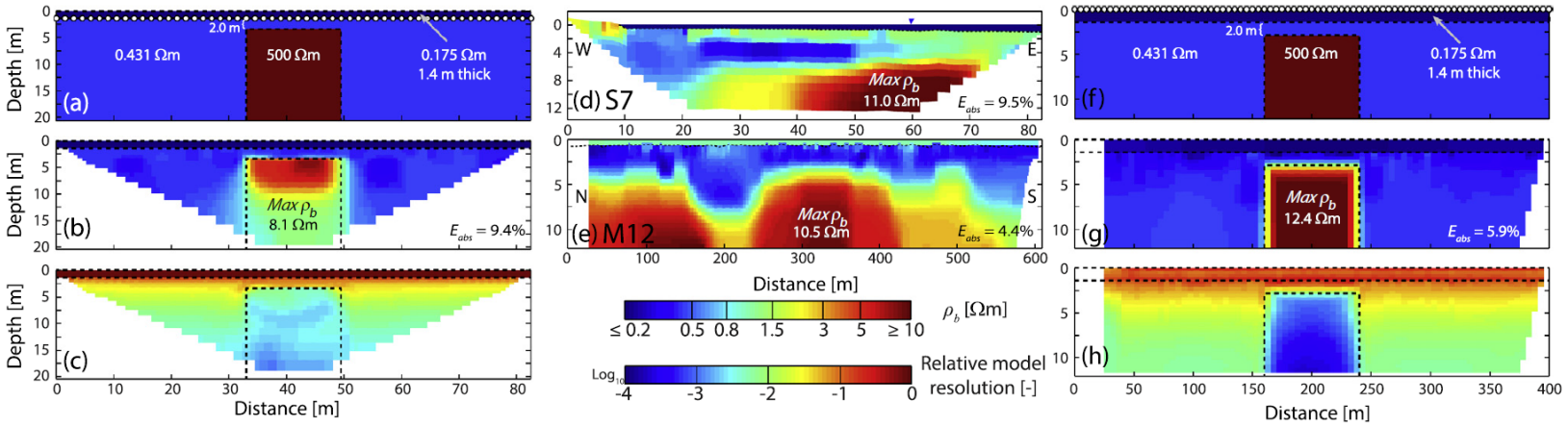

Figure 4.7. Seafloor (a-c) and marine (f-h) simulations and comparison to inverted field profiles of S7 (d) and M12 (e). The $\rho_{b,true}$ structure for the a) seafloor and f) marine forward model included a resistive body over 20% of the total line length. White circles in a) and f) mark the electrode locations for the simulated surveys. Inversions of the simulated surveys (b and g) detected the resistive anomaly but could not recover the $\rho_{b,true}$ magnitude, as indicated by the low relative model resolutions within the anomalies (c and h). The field data (d and e) detected similar ρ_b features to those imaged by the forward models (b and g).

configurations. Changing these parameters would result in different model resolution patterns. Thus, comparing the model resolutions of different surveys quantitatively must account for these variables, or the model resolutions can be used qualitatively through the relative model resolutions as in this analysis (Figure 4.7c and h).

4.5. DISCUSSION

4.5.1. Forward model discussion

Despite a significant reduction in the ρ_b of the resistive anomaly imaged by simulated ERT surveys from $\rho_{b,true}$, both forward models accurately located the 500 Ωm resistive body. This ρ_b decrease resulted from current channeling in the simulated conductive seawater and surrounding sediment.

The simulated analog of the ρ_b structure using the water conductivity and average depth of Muri Lagoon closely resembled the field surveys that detected resistive material below the lagoon. At the Taakoka passage, S7 and S8 imaged a resistive anomaly with $\rho_b \leq 11$ Ωm compared to the 8.1 Ωm of the resistive body in the seafloor simulation. This resistive feature in the field data was imaged shallower than the 10 m investigation depth suggested by the simulation, but the $\rho_{b,true}$ for this anomaly remains unconstrained. The thicker layer (~5 m) of conductive material above the anomaly would also channel current away from this resistive feature more than in the simulation, leading to less ability to detect the resistive body. However, more resistive sub-bottom material across the end of S7 and throughout S8 would have less current channeling and resolve the resistive anomaly better than the synthetic seafloor survey. Therefore, S7 and S8 can and did detect a resistive anomaly with a ρ_b magnitude that is consistent with a $\rho_{b,true} = 500$ Ωm anomaly below 3.4 m of very conductive material.

Similarly, the field CRP surveys, specifically those near the Taakoka passage, could and did image ρ_b anomalies ($\leq$ 10.5 Ωm) with similar magnitude as the simulated CRP survey (ρ_b = 12.4 Ωm). Both synthetic ERT surveys represented a worst-case scenario for high current channeling and low model resolution below the conductive water and sediment layers, and the field CRP surveys would have better detection capabilities than the simulations for an identical $\rho_{b,true}$ structure. Since the simulations could accurately detect conductive materials away from the resistive body, ERT surveys with purely low ρ_b accurately omitted nonexistent resistive features, but much smaller resistive anomalies could exist below the detection limit of the current ERT setup. Similarly, the field CRP surveys would have been able to image a very resistive body (e.g., volcanic rock) within the 12 m depth of investigation, but with potentially less resolvability for resistive bodies deeper than the simulated 3.4 m anomaly. Thus, the resistive ρ_b anomalies in the field CRP data were real geologic features and not inversion artifacts.

4.5.2. Field ERT interpretation

Variations in ρ_b may be due to lithology or porewater salinity or both in the coastal ERT surveys in this study. Therefore, I use the insights from previous studies of the hydrology and geology of Muri to guide the interpretation of the ERT results, where possible, and develop multiple possible hypotheses where I lacked sufficient corroborating data. As is the case for all geophysical surveys, ground truth measurements are critical for interpreting the nonunique results, but this is not always feasible to obtain for every entity detected in field data.

The two inland surveys (L7 and L8) were both conducted on the northern branch of the Raemaru phonolite deposits south of Parengaru Creek (Figure 4.1). At 150 m on L7, I drilled through 3 m of clay-rich soil before refusal on a very coherent rock layer (B1,

Figure 4.3). Therefore, I interpret this high ρ_b layer to represent the Raemaru phonolite flow deposit, but no sample could be recovered. While the layer thickness cannot be exactly extracted from these ERT surveys, mapped lava flows on Rarotonga can be as thick as 5 m with an average of 1-2 m [*Thompson et al.*, 1998], matching the resistive layer thickness detected in both profiles (Figure 4.3). The transition to more conductive materials ($\rho_b \leq 20$ Ωm) at depth may have imaged freshwater-saturated colluvium (ρ_f =1-10 Ωm, n=0.2-0.3, and m=1.3 in Equation 4.1) and/or clay-rich weathering products formed during the hiatus between the mafic and felsic volcanic activity on Rarotonga [*Thompson et al.*, 1998]. Interestingly, L8 only partially imaged the resistor interpreted as Raemaru deposits, matching the contact with Pleistocene alluvial deposits mapped further inland (Figure 4.1a) and visible in a road cut at 250 m on L8. A thicker clay-rich layer would channel more of the injected current, lowering the detectability of the lava flow deposit over the upper portion of L8. These inland surveys did not detect potential recharge zones in the form of discontinuous resistive anomalies, but the ERT surveys imaged the shallow hydrostratigraphy potentially consisting of a thin (3-5 m) layer of conductive clay-rich alluvium overlying the Raemaru phonolite flow deposits that could confine older, but similar, sediment.

At the outlet of Parengaru Creek, ERT profiles potentially detected the water table and the transition from fresh to saline groundwater. Two pits, P1 and P2 (Figure 4.4), dug near the ERT surveys showed a 0.8 m (P1) and 1.5 m (P2) thick layer of unsaturated, unconsolidated sand reaching the water table, and extended 0.4 m below the water table in similar sediment. These unsaturated sediments would explain the high ρ_b (>100 Ωm) of the uppermost layer of the terrestrial surveys (Figure 4.4b). Then, if ρ_b > 100 Ωm marks the extent of the vadose zone, saturated sediment would lie everywhere below this layer in L1-L6, and changes in the inverted ρ_b values would reflect changes in porewater conductivity,

neglecting changes in sediment type or packing. ERT imaged diminishing ρ_b values in the phreatic zone from at least 50 Ωm to at least 10 Ωm near the shoreline, detecting a transition in ρ_f from at least 10-26 Ωm to 2.4-5 Ωm (n=0.3-0.6). This ρ_f corresponds to < 2 PSU [*Perkin and Lewis*, 1980], indicating fresh porewater in the phreatic zone. Below the interpreted fresh groundwater, the ERT results imaged a reduction in ρ_b to ≤ 1.5 Ωm (ρ_f < 0.3-0.8 Ωm, n=0.3-0.6; > 8-20 PSU), suggesting increasingly saline porewater. Together, these ERT surveys clearly delineated the transition from the freshwater lens and underlying saltwater wedge (Figure 4.4b), where L2 running along the high tide mark was conductive throughout, except for a shallow more resistive layer that may be the alongshore expression of the upper saline plume and fresh groundwater discharge patterns imaged at the southern end of L2 [*Befus et al.*, 2013]. Furthermore, tracing the ρ_b-approximated water table in L3 and L4 gave a horizontal hydraulic gradient of ~1.4×10^{-2}, within the spread of gradients measured by pressure sensors < 15 m away [*Befus et al.*, 2013].

Alternatively, the terrestrial hydraulic gradient can be estimated by using the apparent slope of the fresh-salt porewater ρ_b interface with the approximation of sediment homogeneity and hydrostatic conditions [*Ghyben*, 1888; *Herzberg*, 1901]. If ρ_b < 5 Ωm and ρ_b > 5 Ωm are used as the approximate threshold of the fresh-salt porewater interface, the hydraulic gradient required to support such an interface was ~7.6×10^{-3}, which is within the uncertainty introduced by the discretization of the inversion. Together with the homogeneous sediment found in the pits, the potential salinity distribution imaged in the ERT surveys may therefore characterize the shallow (< 8 m) shoreline aquifer as a classic homogeneous flow system with parabolic groundwater pathways [*Badon-Ghyben*, 1888; *Herzberg*, 1901; *Glover*, 1959] and without significant heterogeneities [*Dose et al.*, 2013; *Lu et al.*, 2013] in direct contrast with [*Befus et al.*, 2013].

Importantly, the classic pattern of coastal groundwater discharge through homogeneous material [*Badon-Ghyben*, 1888; *Herzberg*, 1901] did not exist adjacent to nor under Parengaru Creek. Instead, the sharp ρ_b interface imaged in L3 and L4 was much broader (32 m) in L5, with some change imaged in L6 as well (Figure 4.4). In S1, the deepest subsurface detected never reached below 15 Ωm, extending into the lagoon subsurface. Since Parengaru Creek underwent inundation by the tide for the full extent of the ERT surveys, lower ρ_b near the creek may be explained by infiltrating saline seawater. However, the onset of $\rho_b \geq 10$ Ωm materials in S1 at depths > 5 m complicate the interpretation of L5 beyond the simplest explanation of saltwater intrusion from the creek. An indication of transience in ρ_b structure, and thus salinity, was imaged in S1, where an apparent lens of conductive ρ_b values persisted at the surface of the profile near the lagoon that then moved deeper into the section further inland. This may be a dynamic ρ_b feature as different level tides interact with the stream and underlying groundwater during the wet and dry seasons. The apparent dissonance between S1 and L5 may be explained by more active flushing of the sediment below the stream, while the infiltration of saltwater during higher tides diffuses slowly through the neighboring sediment, explaining the gentler gradient in ρ_b imaged by L5. An increase in sediment size and packing provide an alternative explanation for the higher ρ_b under Parengaru Creek, fitting the assumption that the high energy environment of the creek could host larger sediment sizes, but L5 showed more conductive material, requiring deposition of fine sediment (e.g., clay) or less compaction, within close proximity to both S1 and the other terrestrial surveys with similar > 5 m deep ρ_b structure.

Seafloor ERT surveys near the outlet of Parengaru Creek detected more resistive subsurface anomalies than seawater saturated sand (ρ_b =0.4-1.5 Ωm with ρ_f = 0.175-0.2, n=0.2-0.6). Across the mouth of Parengaru Creek, S3 imaged a continuation of ρ_b values

consistent with the interpreted fresh groundwater below the creek in S1 (Figure 4.4b), but this feature becomes more conductive further into the lagoon (S2). Even so, these ρ_b anomalies were well above the cutoff for seawater-saturated sand further into the lagoon than in S6, towards the edge of the deltaic sandflat. Supporting the porewater salinity interpretation of these signals, S6 was the location for the previous time-lapse ERT, hydraulic head, and temperature measurements that described fresh groundwater and net heat discharge into the lagoon [*Befus et al.*, 2013]. Additionally, boreholes B2 and B3 encountered predominantly sandy material to 3 m depth and detected some freshwater component in porewater samples 3 m below the SWI (< 15 PSU). Resistive anomalies (ρ_b > 5 Ωm) in S4 and S5 may also have been related to porewater, but B3 did not extend deep enough to reject a geologic difference as the source of the anomaly. Interestingly, the anomaly in S4 was much more resistive than the other seafloor surveys, potentially detecting a different and/or more consolidated lithologic unit.

ERT surveys across the channel between Taakoka islet and the mainland revealed more resistive material than would be expected for seawater-saturated sediment ($\rho_b \geq 1.5$ Ωm). Given the islet is comprised of Raemaru phonolite deposits [*Thompson et al.*, 1998](Figure 4.1a), this resistive layer could be the continuation of these lava deposits under the lagoon, overlain by 3-5 m of seawater-saturated sediment (Figure 4.5). Previous ER soundings from Rarotonga also imaged interpreted Raemaru deposits ($\rho_b = 5\times10^5$ Ωm) in Muri at 13.7 m depth, north of the current study area [*Ricci and Scott,* 1998]. The ρ_b value of the lava deposits from the ER sounding is many orders of magnitude larger than that imaged in S7 and S8 (5-11 Ωm). Basaltic rocks can be very resistive ($\rho_{b,true} = 10^1$-10^8 Ωm with $n = 0$) [*Telford et al.*, 1990], but saltwater saturation of the volcanic rock and overlying layers would greatly reduce the $\rho_{b,true}$ and the ability to resolve the basalt at depth. No sensitivity testing in *Ricci and Scott* [1998] restricts the reliability of 5×10^5 Ωm to be

the expected value for ρ_b of the Raemaru flow deposits. If instead the 500 Ωm value from L7 and L8 is applied as the ρ_b value for the local Raemaru deposits and considering the low detectability of this feature below conductive material with the synthetic seafloor model results, the resistive materials in S7 and S8 could be the Raemaru deposits. Combining these results with the very high ρ_b imaged nearby in the lagoon, if a 500 Ωm resistor were to exist in the lagoon subsurface, any connected porosity within the geologic entity could be filled with seawater, drastically reducing the ρ_b of the fluid-rock combination. Saturation of geologic materials with conductive water can thus make rock appear orders of magnitude more conductive than a dry, pure sample [*Telford et al.*, 1990].

Difficulties encountered in collecting S7 in the field added other restrictions in interpreting the ρ_b features of the Taakoka passage. The high E_{abs} (9.5%) of S7 may have resulted from high repeat error for several surface electrodes and geometrical problems, both of which are likely related to the ERT cable being draped over multiple coral heads with very irregular geometries. These bad data near the SWI resulted in poorly constrained ρ_b values in the upper portion of S7 (Figure 4.7d). Indeed, the very conductive values centered on 4 m depth from 10-50 m on S7 may not be accurate and also lower the ability to detect features below this conductive layer. Therefore, the apparent termination of the resistive anomaly approaching the mainland may be an artifact of the inversion and does not signify a disconnection between the Raemaru flow deposits on Rarotonga and Taakoka.

The dense network of CRP surveys near the Taakoka passage contribute additional evidence for the existence of Raemaru flow deposits within the lagoon subsurface. South and west of Taakoka, an extensive resistive anomaly ($\rho_b \geq 5$ Ωm) was detected by multiple marine ERT surveys (M3, M10-M12) (Figure 4.6). As suggested by the forward CRP simulation in *Section 4.5.1.*, this high ρ_b was consistent with the CRP signature of a 500 Ωm anomaly buried in conductive sediment. Therefore, if L7 and L8 imaged a layer of the

Raemaru phonolite deposits, then the ρ_b anomaly imaged between Taakoka and the mainland could also result from similar lava flow deposits. Also, the resistive anomaly southwest of Taakoka was disconnected from the resistive feature along the reef crest by ρ_b values characteristic of seawater-saturated sand ($\rho_b < 1.5$ Ωm) and may therefore be a separate anomaly.

Alternatively, I surmise that this resistive feature along the reef crest represents a decrease in the porosity of the lagoon substrate, potentially due to reef diagenesis (e.g., cementation). Overall, the ρ_b values in M4 and M5 ranged from 1.5-5 Ωm, whereas the CRP results near Taakoka reached 10 Ωm. This difference in ρ_b values is not definitive on its own in explaining the uniqueness of the two signals, especially since M4 and M5 were conducted in deeper water (up to 2 m) and may thus suffer from lower resolution. The pervasive $\rho_b > 1.5$ Ωm in the subsurface imaged by M4 and M5 may be volcanic rocks, but a reduction in porosity due to the lithification of the carbonate sediment also provides a reasonable physically-based explanation. Indeed, carbonate cements may precipitate preferentially at reef shelf margins when compared to their more physically and chemically protected lagoons [*Moore*, 2001]. The precipitation of cements that are more resistive than seawater (i.e., $CaCO_3$) and fill the pore spaces would increase the ρ_b of the medium, as seen when comparing a mid-lagoon ERT profile (e.g., M9) with one near the reef crest (e.g., M5) (Figure 4.6). The ubiquity of high ρ_b along the reef crest is more consistent with a lithologic rather than a porewater composition explanation. Therefore, I interpret this distal portion of the lagoon to be comprised of cemented reef materials. Hence, more conductive materials at depth within 300 m of the shore (e.g., M7-M9) would correspond to uncemented and/or less cemented carbonate sands. Interestingly, a single gap in the $\rho_b > 1.5$ Ωm values along the reef crest (northeastern end of M5 in Figure 4.6) fit the linear

extrapolation of Parengaru Creek; but, no other morphologic evidence is available to support a connection between these low ρ_b values and geomorphic processes.

While the local geology provides potential reasons for the resistive anomalies beneath the lagoon, fresher, and therefore more resistive, porewater could also contribute to high ρ_b in the ERT surveys. Applying Equation 4.1 to get $\rho_b > 3$ Ωm measured in the CRP surveys required brackish porewater with $\rho_f > 0.9$-1.5 Ωm (~6.7 PSU). However, if the effects of current channeling and resolution are considered, the porewater ρ_f must have been much fresher (> 150-255 Ωm, PSU < 0.04) to create an anomaly with $\rho_b \sim 500$ Ωm. Very fresh porewater could exist in the lagoon subsurface, especially near the Taakoka passage where these ER values were detected and the highest ^{222}Rn activities, an indicator of SGD, were measured in the lagoon water [*Tait et al.*, 2013]. Porewater samples from three boreholes (B4-B6) drilled to 2 m below the SWI showed lagoon water salinities. No core was recovered from these boreholes. Ground truth measurements reaching 5 m below the SWI in the lagoon are required to separate the geologic and hydrologic $\rho_{b,true}$ contributions and was beyond the capabilities of the equipment available. Thus, the source of ρ_b anomalies in the lagoon subsurface may arise from porewater salinity and/or lithology with spatially heterogeneous proportions of each.

4.5.3. Implications for groundwater flow

The ERT surveys imaged the electrical signature of the geologic structures and salinity distributions of the Muri Lagoon area that together constrain the hydrogeologic setting. Thus, these ERT surveys provided evidence for geologic structure that could control groundwater flowpaths towards and into the lagoon. In turn, my results resolved basic hydrogeologic variability that may be common in reef lagoons and coastal aquifers and offer insight into heterogeneous coastal environments.

Interpreting geologic structure with ERT surveys in coastal settings is obscured by changes in the porewater salinity, both onshore and offshore. Current channeling in marine waters and saltwater-saturated sediment limit the ability of ERT surveys to resolve underlying features, as shown in the simulations in this study and by others [*Loke and Lane*, 2004; *Day-Lewis et al.*, 2006; *Orlando*, 2013]. Disentangling the lithologic and porewater contributions should be performed only after this sensitivity analysis, which is itself a complex source of uncertainty that requires additional evidence (i.e., ground truth) to unravel.

At the outlet of Parengaru Creek, the terrestrial ERT surveys imaged what may be a well-developed freshwater lens overlying a saltwater wedge (L3 and L4, Figure 4.4b). This near-ideal geometry indicated the absence of significant low permeability layers within the shallowest 10 m of the subsurface that would reshape the near parabolic salinity interface [*Dose et al.*, 2013; *Lu et al.*, 2013]. Instead, the ERT results more closely matched the porewater salinity distribution that results from parabolic groundwater pathways of a homogenous coastal aquifer [*Glover*, 1959]. However, deeper flowpaths to the lagoon may exist: the stratigraphy outlined on land by L7 and L8 (Figure 4.3) detected an electrically conductive feature at depth, interpreted as saturated sediment or clays, that may allow or confine groundwater flow, respectively, in the older mafic lavas and buried colluvium. Additionally, L3 and L4 (Figure 4.4b) had narrower transitions from resistive to conductive material (i.e., mixing zone) moving seawards than the tidally-affected L5, suggesting more uniform groundwater flow away from the hydrodynamics of the tidal creek. The dimensions of the mixing zone can only be inferred with these ERT measurements, as the absolute porewater salinities remain unknown. Thus, this study demonstrates the suitability of ERT for providing information needed for qualitatively constraining coastal aquifer structure. Building off of this study, future ERT investigations of the mixing zone could

use select ground truth measurements (e.g., wells for porewater samples) to quantitatively constrain the ρ_f and ρ_b signatures of mixing zones for more robust characterization of coastal stratigraphy and hydrogeology.

Mapping the geology and subsurface variability of the lagoon with the interpreted ERT sections indicated that the Raemaru volcanic flow deposits may promote the terrestrial groundwater discharge ≥ 200 m into the lagoon (Figure 4.8). Some volcanic islands are recognized to support extensive SGD where lava tubes are common [*Dimova et al.*, 2012], but there is no independent evidence for lava tubes existing on Rarotonga. However, contemporaneous mapping of radioisotopes in the Muri Lagoon tracked high ^{222}Rn activities and low salinity lagoon water exactly where my ERT surveys imaged the extension of the Raemaru phonolite into the lagoon [*Tait et al.*, 2013]. Thus, the basaltic rock between mainland Rarotonga and the Taakoka islet appears to support active groundwater flow to the lagoon. Additionally, a southern branch of the Raemaru deposits may provide an additional conduit for terrestrial groundwater to the lagoon (Figure 4.8), where other high ^{222}Rn activities were measured but no ERT surveys were conducted [*Tait et al.*, 2013]. Indeed, these lava flows may even extend to the reef crest [*Thompson et al.*, 1998], allowing terrestrial groundwater and solutes to reach the reef face. This study mapped the role of basalts as an active hydrostratigraphic unit, serving discontinuously as a fractured medium, a conduit system, and/or a confining unit that can deliver fresh SGD and its chemical constituents to coastal waters.

As most of the Rarotongan lagoon is assumed to have no volcanic rocks near the SWI, the hydrogeologic structure of the nearshore lagoon would be controlled by carbonate sands and limestone (Figure 4.8), similar to many carbonate islands [*Vacher and Quinn*, 2004; *Rankey and Garza-Perez*, 2012]. On Rarotonga, little limestone is present at the

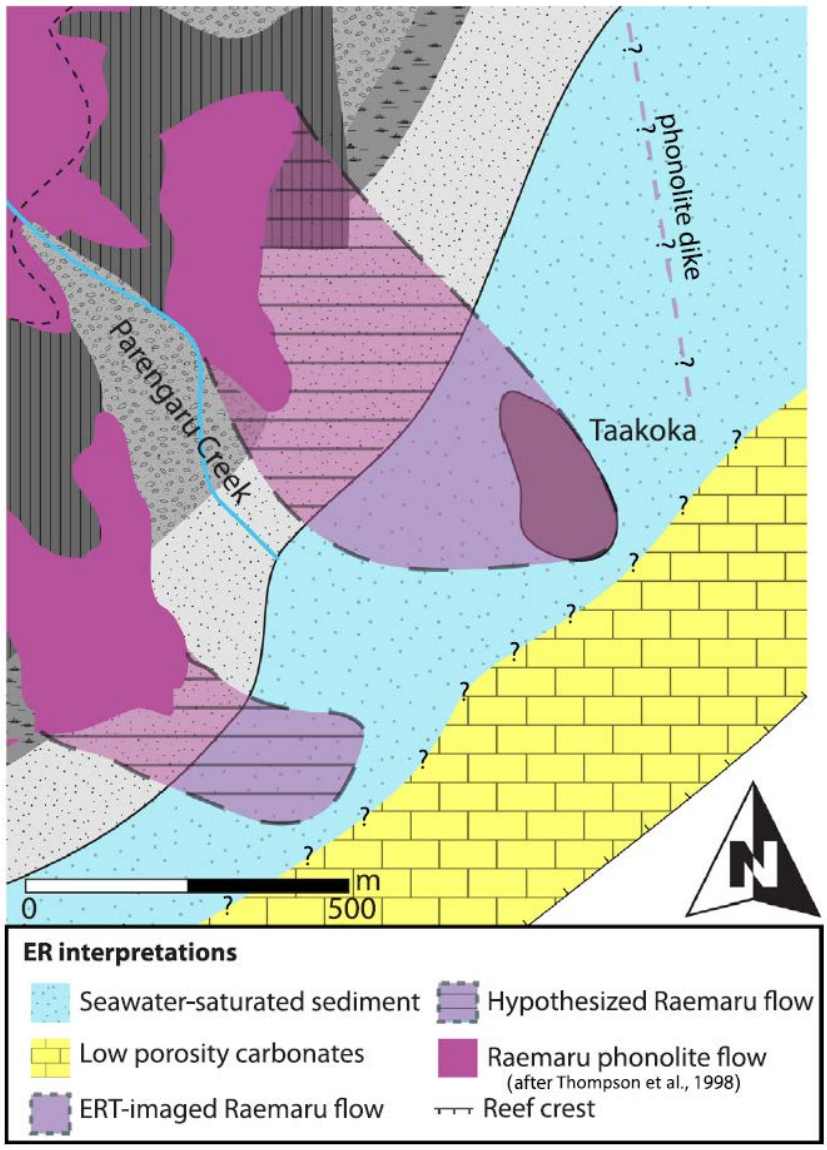

Figure 4.8. Interpreted hydrostratigraphy of the Muri Lagoon. The Raemaru phonolite flows are hypothesized to extend into the lagoon subsurface and allow SGD > 50 m beyond shore. The more resistive subsurface along the reef crest suggested reductions in porosity and more advanced diagenesis of the carbonate sediment than closer to shore. Geology identical to previous studies (see Figure 4.1) are shown in grey.

surface [*Moriwaki et al.*, 2006], but there is unknown potential for carbonate formation and consequent dissolution since the late Pleistocene eruptions that created the island. Limestones from other reefs in the southern Cook Islands of Pleistocene age have undergone significant dissolution, whereas Holocene reef deposits are much less cemented but retain most of their primary porosity [*Hein et al.*, 2004]. Focused dissolution and karstification may occur in carbonates where they overlie volcanic basement [*Ramalho et al.*, 2013], such as in northern Guam and Bermuda [*Mylroie and Vacher*, 1999; *Taboroši et al.*, 2003; *Mink and Vacher*, 2004]. In these systems, the less permeable and less reactive basement rocks preserve the aggressive acidity of groundwater along the basement-carbonate contact, forming dissolution features [*Mylroie and Vacher*, 1999]. As a composite carbonate island, Rarotonga has a yet unknown potential for karstification providing conduits for groundwater flow, but the thin apron of coastal, non-volcanic, deposits offer a limited area for conduit formation. Thus, vuggy to karstic limestones may provide additional pathways for groundwater to discharge into the Rarotongan lagoon as well as from the reef shelf face, where underwater springs have been seen by divers, but remain undocumented. Carbonate dissolution may provide hidden conduits for groundwater flow in reef and other coastal environments that ERT surveys can expose.

The ERT surveys in this study explored only the electrical structure of the shallow (<10 m) lagoon deposits and, thus, may have imaged only the Holocene limestones and more recent reef deposits and detritus, given an assumed reef accumulation rate of ~2 m/ky [*Hein et al.*, 2004]. Rather than exposing dissolution features that would be expected in older carbonate deposits on neighboring islands [*Hein et al.*, 2004], the ERT surveys may have imaged the cementation state of these deposits through the consistently high ρ_b ($\geq$ 1.5 Ωm) beginning ~400 m into the lagoon (Figure 4.6). Therefore, less circulation of seawater and a lower potential for SGD is expected through the less porous lagoon subsurface

materials within 200-300 m of the reef crest. The persistence of terrestrial groundwater flowpaths through the Holocene deposits is unlikely to extend far into the lagoon, unless the resistive layer imaged in L7 and L8 serves as a confining unit and continues below the lagoon sediment, deeper than the CRP surveys imaged (~5-10 m). Alternatively, the interpreted reduction in porosity at the reef crest may reduce the permeability of the lagoon substrate, creating a transient focusing of both recirculated seawater and potentially fresh groundwater over long timescales, either redistributing cementation zones or accelerating dissolution [*Evans*, 2003], respectively. Thus, marine ERT surveys can be used to map and track incipient diagenesis in reef deposits or any littoral sedimentary system, under the constraint that these features can be accurately detected.

Together, the link between geologic structure of the nearshore environment and groundwater flowpaths on Rarotonga create pathways for dissolved chemicals. SGD can provide abundant nutrients to littoral waters, altering the biogeochemical reactions [*Slomp and Van Cappellen*, 2004; *Kroeger and Charette*, 2008] and biological activity [*Miller and Ullman*, 2004; *Waska and Kim*, 2010]. Impermeable geologic features can deform the interface between porewater and groundwater [*Dose et al.*, 2013; *Russoniello et al.*, 2013], changing the surface area and potential groundwater residence times that can control nutrient evolution [*Spiteri et al.*, 2008; *Santoro*, 2009; *Santos et al.*, 2012a] and other chemical processes [*Charette and Sholkovitz*, 2006; *Werner et al.*, 2006; *Cyronak et al.*, 2012]. Thus, the lava flow deposits in the Muri Lagoon may provide a conduit for elevated nutrient fluxes from onshore, if the supplying groundwater system became contaminated. However, the volcanic rocks may alternatively serve as an impermeable barrier that would block nutrient transport into the hydrostratigraphic unit supplying the SGD.

Finally, the development and transformations of coastlines alter the topographic and hydrogeologic framework through which groundwater flows over many spatio-

temporal scales [*Turner and Nielsen*, 1997; *Horn*, 2002; *Russoniello et al.*, 2013]. Erosional and depositional processes affect the shallow subsurface, creating sediment aprons over heterogeneous geologic systems [*Rankey and Garza-Perez*, 2012; *Ramalho et al.*, 2013]. This dynamic, composite coastal structure controls groundwater pathways, contributing to and creating the potential for SGD into littoral and marine environments. SGD and coastal groundwater studies must consider such hydrostratigraphic complexity and incorporate the time and length scales appropriate to the local system to avoid inaccurate accounts of the targeted physical and chemical processes.

4. SUMMARY AND CONCLUSIONS

I investigated the hydrogeologic setting of Muri Lagoon, Rarotonga, using an extensive network of electrical resistivity surveys. The surveys revealed the local terrestrial and reef hydrostratigraphy and outlined the geometry of the coastal mixing zone. My results suggested the lagoon is partially underlain by volcanic rocks in addition to carbonate sediment at various stages of cementation and which may become increasingly cemented towards the reef crest. With these insights, I interpreted potential groundwater pathways towards and into the Muri reef lagoon, providing the hydrogeologic framework for more detailed SGD and subterranean estuary studies. These results illustrate the importance of studying coastal groundwater flow and SGD in the context of the geologic setting. Additionally, I demonstrated that heterogeneity in the hydrostratigraphy persisted across the land-ocean interface, and this complexity may control coastal groundwater pathways.

ERT surveys on land explored the potential for groundwater discharge into the reef lagoon. I used ground truth measurements, Archie's Law, and previous studies to guide my analysis of ERT surveys. Near the outlet of Parengaru Creek, these surveys imaged a thin vadose zone (1-3 m) above an inland thickening freshwater lens. Higher electrical

conductivities below this interpreted freshwater lens corresponded to the saltwater wedge. This classical freshwater lens geometry suggested the shallowest water-bearing layer was unconfined and may discharge into the lagoon. Directly adjacent to Parengaru Creek (L5), the interpreted mixing zone appeared broader than in the other transects, where tides may force dynamic porewater mixing. Despite this tidal mixing, ρ_b values consistent with fresh groundwater extended 20 m into the lagoon.

Waterborne ERT surveys in Muri Lagoon revealed non-uniform ρ_b structure within the lagoon subsurface. Most of the lagoon was underlain by conductive media that became slightly more resistive with depth, characteristic of seawater-saturated sediment. Southwest of the Taakoka islet, high ρ_b values were interpreted as a buried continuation of the Raemaru volcanic flow that connects to the islet. This portion of the lagoon also had high ^{222}Rn activities and lower salinity, both indicating a hotspot for groundwater discharge into the lagoon [*Tait et al.*, 2013; *Erler et al.*, 2014]. Thus, the volcanic structures within the lagoon may provide conduits for or confine groundwater flow, supporting SGD beyond 50 m from shore. Pervasive high ρ_b along the reef crest was interpreted as the reduction of porosity in the reef carbonates, forming a barrier to porewater flow. Thus, the hydrostratigraphy of the reef lagoon consists of carbonate sediment undergoing variable cementation with discrete volcanic structures.

To test the reliability of assigning conductive inversion results ($\rho_b \leq 10$ Ωm) to locally very resistive materials, I modeled ERT survey responses to a known $\rho_{b,true}$ structure. Both seafloor and marine configurations could not fully recover high $\rho_{b,true}$ magnitudes, which were shielded by overlying and adjacent conductive materials (current channeling). However, both simulations accurately located the onset and edges of the resistive body and resulted in similar anomalies to those detected in the inverted field sections. Therefore, these suggested that resistive materials could be imaged in the Muri

Lagoon and differentiated from conductive material. Given this potential for accurate detection and the similar ρ_b magnitudes imaged for a 500 Ωm resistor in the simulated and field surveys, the lava flow deposits imaged on land (L7 and L8) were also likely imaged by CRP (M3,M10-M12) and seafloor (S5-S8) ERT sections, mapping the lava deposits into the subsurface of the Muri Lagoon.

With a network of ERT surveys, I comprehensively studied the hydrostratigraphy of a coastal groundwater system from onshore to submarine discharge and porewater recirculation zones. My results indicated SGD preferentially occurred where volcanic rocks were detected in the lagoon. Thus, the buried geologic structure of the coastal subsurface contributed to the location and magnitude of SGD. Future studies of coastal groundwater discharge in areas with heterogeneous geology must consider such complexity.

Chapter 5:

Quantifying global groundwater ages[4]

Letting the days go by,
water flowing underground.
Into the blue again,
after the money's gone.
Once in a lifetime,
water flowing underground.

- from "Once in a lifetime"
by *Talking Heads* [1980]

ABSTRACT

Timescales of groundwater dynamics can control how groundwater interacts with many Earth system processes, including weathering, the transport of solutes or contaminants, and hydrologic responses to climate change. In this study, I quantified the global volume and distribution of groundwater age that has been stored in shallow aquifers. First, I develop the methodology using a timescale of 50 years, a period relevant to current policy planning and similar to human generations. Then, I quantified the volume of groundwater storage associated with timespans ranging from 1-10,000 years. I modeled groundwater ages for shallow groundwater systems worldwide with 43,659 two-dimensional flow and age-as-mass transport simulations guided by global datasets of basin geometric and hydraulic properties. The models suggested that less than 20% of the groundwater on Earth down to 2 km depth was recharged on average in the past 50 years.

---

[4] Gleeson, T. P., K. M. Befus, S. Jasechko, E. Luijendijk, and M. B. Cardenas (submitted), The global volume, distribution, and lifespan of modern groundwater.

Gleeson was the project lead, initiated the project with the ambition of using models to constrain young groundwater globally, and ran many of the spatial analyses. Jasechko amassed tritium analyses from around the world and modeled the percent modern groundwater in the samples. Luijendijk collected lithology and porosity datasets to compute the new volume of total shallow groundwater, developed the global average porosity curve, and found the best lithology-specific porosity-depth relationships. Cardenas provided overall guidance and constructive criticism throughout the project. I was responsible for the model development, implementation, quantitative post-processing of the datasets, and spatial analysis. All of us met almost weekly via video conference to discuss our progress, potential improvements, ways forward, and ways to keep me busy in perpetuity.

For most watersheds on Earth, this young groundwater was restricted to the upper 10 m of aquifers based on the models, but tritium samples show that young groundwater can be found much deeper in the real aquifers. For the full time series, the estimates of groundwater storage followed a cubic root of the groundwater age. Uncertainty in the storage estimate stemmed from the simplification of two-dimensional flow and uncertainty in permeability and porosity. This chapter represents my contributions to a collaborative project [*Gleeson et al.*, submitted], and herein, I focus on the modeling and analysis components of this study within the context of the full study in addition to supplementary analyses and extensions.

5.1. INTRODUCTION

Groundwater can be considered a renewable resource, where under natural conditions dynamic equilibrium exists that balances "new" groundwater from recharge fluxes with losses from groundwater discharges. As a result of changing climatic conditions or groundwater extraction, this balance can be upset and results in changes to the volume of groundwater stored in aquifers through time. While groundwater is an ample resource for meeting agricultural, industrial, and municipal water needs, water extractions to meet these needs can lead to stressed and depleted groundwater systems [*Wada et al.*, 2010; *Gleeson et al.*, 2012].

Within the context of sustainable development, defined concisely as "development that meets the needs of the present without compromising the ability of future generations to meet their own needs" [*Development*, 1987], the preservation of groundwater resources depends on the balance between the demand for groundwater and replenishment of groundwater storage. In the past, sustainable groundwater use has been primarily quantified using the annual recharge rates, essentially following a simplified mass balance approach where the withdrawls are negated by the inputs, often overlooking the effects on and

responses of natural discharge features to pumping [*Bredehoeft*, 1997; *Sophocleous*, 2000; *Bredehoeft*, 2002]. To both protect groundwater supplies for future generations and meet present-day needs, mass balance approaches to managing groundwater must incorporate precise balances between groundwater recharge and discharge fluxes to quantify groundwater storage.

Estimates of the inventory of groundwater age have been used to understand the sustainability of specific aquifers [*Fogg et al.*, 1999; *Zongyu et al.*, 2005], but a generic framework for understanding physical groundwater renewability has not been developed. In this chapter, I introduce a conceptual framework for quantifying aquifer-wide storage of groundwater renewed over a given timespan. These volumes of renewable groundwater provide pre-development estimates of the maximum groundwater storage in an aquifer over an established timespan, treating older groundwater supplies as not renewable over the same time period. This physical renewability of groundwater is itself a new conceptual model and is separate from viewing groundwater as an economically renewable resource. However, the physical renewability groundwater can be compared to consumptive groundwater use to potentially determine the sustainability of those groundwater practices.

But then, how old is groundwater? Groundwater age is conceptually the duration water resides in hydrogeologic systems. Given the potential for water to enter groundwater systems multiple times over millennial timescales, a datum must be chosen to mark what constitutes the resetting of groundwater age. The moment infiltrating water reaches the water table (i.e., groundwater recharge) is a common definition of the beginning of groundwater aging [*Bethke and Johnson*, 2008]. Thus, groundwater ages in aquifer recharge zones are expected to be young, at least near the water table, while in discharge zones a parcel of water has presumably spent a longer time as groundwater. Therefore, groundwater age increases along flowpaths, yielding a distribution of groundwater ages

across an aquifer that depends on both the hydraulics and hydrodynamics in the groundwater system.

Groundwater residence time distributions (RTDs) characterize groundwater age in aquifers and have primarily been used to evaluate how chemical species, mainly contaminants, travel and are delivered through groundwater systems [*Phillips and Castro*, 2005]. Both aquifer heterogeneity and hydrologic transience alter RTDs from similar homogeneous and steady-state configurations, leading to discrete areas of older and/or younger groundwater that retard or accelerate the transport of solutes used to construct RTDs, respectively [*Cardenas and Jiang*, 2010; *Jiang et al.*, 2010; *Gassiat et al.*, 2013; *Gomez and Wilson*, 2013; *McCallum et al.*, 2014].

Characterizing groundwater age in natural systems generally relies on tracking chemical tracers from known recharge zones to wells or discharge locations. As the chemical tracer traverses an aquifer, diffusion and dispersion mix the target water with surrounding water and water-rock interactions occur, resulting in variable chemical concentrations through time reaching the sampling location recorded as breakthrough curves. The time it takes for the onset of the chemical to discharge until the last trace is gone marks the maximum extent of the groundwater RTD, where the species concentration through time can be used to understand flowpath lengths, aquifer properties, and the relative importance and/or mixing potential of given flowpaths.

Groundwater RTDs have been studied using tracer experiments, naturally-occurring chemical species in groundwater, and numerical methods. Man-made tracer experiments for obtaining groundwater RTDs are primarily useful over short flowpaths or in very permeable systems (e.g., karst), as groundwater residence times can exceed thousands of years. Naturally-occurring geochemical tracers can also constrain groundwater ages by using known or estimated recharge concentrations and supplying

models for the physical processes that can transform the tracers (e.g, radioactive decay, water-rock interactions, and mixing).

Numerical analyses of groundwater age have progressed from simplified systems of only head-driven advection (i.e., plug flow) to incorporate a wide range of hydrodynamics [*Bethke and Johnson*, 2008]. Solute transport simulations following the tracer experiments provide breakthrough curves and thus groundwater RTDs sampled at wells or discharge features. Particle tracking is another method for numerically modeling RTDs and uses a pre-calculated groundwater flow field to track and time the movement of artificial particles through an aquifer [*Suckow*, 2014]. Another method for simulating RTDs treats groundwater age as mass in an advection-diffusion-dispersion framework that allows for the direct simulation of continuous groundwater ages throughout hydrologic systems [*Goode*, 1996; *Ginn*, 1999], rather than measuring groundwater ages at discharge locations as required by other methods.

Instead of using RTDs in the traditional application for assessing the fate and transport of chemical species in groundwater, I modeled groundwater age to investigate the potential global storage of groundwater younger than 50 years old. Surface hydrology constrained the model domains and was used to assign the best currently available hydrologic and hydrogeologic global datasets to the models. These groundwater volumes provided estimates of the total volume and spatial distribution of groundwater renewed every 50 years under steady state conditions (i.e., without pumping or transient boundary conditions). This study aimed to quantify the volume of groundwater naturally renewed and stored over a timescale (50 years) on the order of a single human generation. This estimate provided a baseline for understanding how much of the groundwater on Earth is renewed over time periods relevant to human generations and considered in policy

planning. Then, the framework for quantifying groundwater storage was used to estimate the volume of groundwater renewed over timescales of one to ten thousand years.

5.2. Quantitative Analysis of Groundwater Age

5.2.1. Hydrologic datasets

Global datasets of hydrologic parameters guide the groundwater age models. The data were extracted from a wide range of published lithologic and modeling analyses. First, the HydroSHEDS watershed delineation [*Lehner et al.*, 2008] was used to set the geometry for the models and extract values from other datasets, where each watershed on Earth was assigned an underlying hydraulic gradient, near-surface permeability [*Gleeson et al.*, 2014], near-surface porosity [*Gleeson et al.*, 2014], a characteristic value for the decay of porosity with depth [*Ehrenberg and Nadeau,* 2005], and half the mean distance between first-order perennial streams [after *Lehner et al.*, 2008]. Each of these input parameters were assigned to individual watersheds (n=931,883 watersheds). My analysis with the HydroSHEDS watersheds only includes ice-free and permafrost-free land areas, excluding Antarctica and large portions of arctic and subarctic Asia, Europe, and North America. Thus, the watersheds included in the estimation of groundwater age are also restricted to ice- and permafrost-free regions. The hydraulic gradient was calculated using a 500 m by 500 m interpolation of modeled steady-state water table depths [*Fan et al.*, 2013] and a global elevation dataset [*Danielson and Gesch,* 2011]. The average hydraulic gradient of cells within each watershed was assigned as the model input. Near-surface permeability and porosity values were assigned using published values where available and lithologic averages elsewhere [*Gleeson et al.*, 2014]. Porosity decay was assigned by the compressibility of each lithology with permeability decay proportional to porosity decay [*Bernabé et al.*, 2003; *Ehrenberg and Nadeau*, 2005]. Once assigned to the watersheds, the

median values for the model parameters were 0.013 for the hydraulic gradient, 1.5 x 10^{-14} m^2 for the near-surface permeability, 0.19 for the near-surface porosity, and 5.2 km for the watershed-halfwidth.

In addition to hydrologic datasets used for the groundwater age simulations, a global synthesis of tritium (^{3}H) samples and mixing models by *Gleeson et al.* [submitted] provided a separate estimate of the global groundwater volume younger than 50 years old. ^{3}H concentrations in meteoric water peaked in the early 1960's with the continued practice of above-ground thermonuclear testing, followed by a steady decay in ^{3}H concentrations initiated by an international ban on these tests [*Phillips and Castro,* 2005]. ^{3}H concentrations allow the estimation of groundwater ages by accounting for the radioactive decay of ^{3}H in combination with models for how waters from different sources mix, which also requires the estimation of the spatiotemporal distribution of ^{3}H [*Phillips and Castro*, 2005]. In this way, approximate ratios can be calculated of the amount of modern groundwater in a sample. By also analyzing for ^{4}He with ^{3}H, an estimate can be made for the amount of time elapsed since the water molecules entered the groundwater system. However, in the ^{3}H analysis from *Gleeson et al.* [submitted], only the ratio of modern groundwater was considered because the ^{4}He data were less available internationally. More information on the calculation of the ratio of modern groundwater for the estimation of renewable groundwater storage is available in *Gleeson et al.* [submitted].

5.2.2. Binning hydrologic datasets for modeling

To avoid simulating the groundwater flow and age transport problem for all 931,883 watersheds, similar hydrologic attributes were binned to reduce the number of parameter combinations. Near-surface permeability, porosity, and the decay of each of these parameters are primarily controlled by surface lithology, so the published values for these

parameters were used directly from the assignment to the watersheds [*Gleeson et al.*, 2014]. When a watershed extended over lithologic contacts, the most areally-extensive value was used, resulting in no more than a quarter order of magnitude difference in permeability in the data and was much less than the uncertainty in the permeability data (0.9-2 orders of magnitude) [*Gleeson et al.*, 2014]. For the continuous distributions of water table gradients and watershed half-widths, binned model values were used to characterize the data based on the percentiles of each distribution (Figure 5.1). The water table gradients are roughly log-normally distributed, and 33 bins were used based on the logarithms of water table gradients, with increasing bin sizes away from the median value. Watershed half-widths had a long-tailed normal distribution, and so again 33 bins were used to discretize the half-widths. To represent the larger watersheds ($> 10^4$ m), sixteen evenly spaced bins for every 5 km were added to the original 33 watershed half-width bins startingwith 10 km up to 100 km, the maximum allowed in the HydroSHEDS analysis. By simulating only combinations of these discretized parameters from the global datasets, only 43,659 model runs could be used to describe all 931,883 watersheds considered in this analysis.

5.2.3. Numerical simulation of groundwater flow and age transport

Groundwater age fields were modeled with two-dimensional (2D), steady-state groundwater flow and age transport simulations for water table-driven flow in fully water-saturated conditions. The models were solved numerically with finite element models in COMSOL Multiphysics for the HydroSHEDS-based spatial assignment of input parameters. The domain geometry was designed after Tóth [1963] to describe groundwater flow from a watershed boundary (e.g., groundwater divide) to a corresponding drainage feature (e.g., river) (Figure 5.2). I assigned the model domains with lengths based on the average distance from the watershed boundary to the corresponding river, termed the

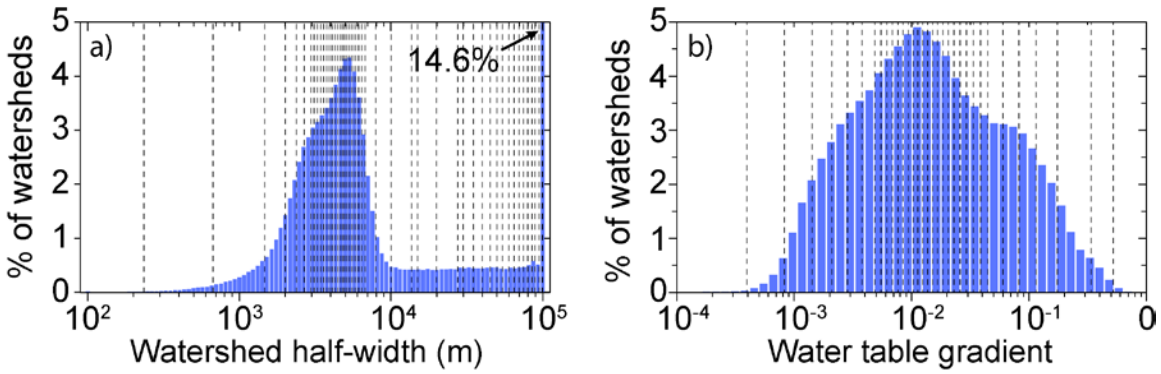

Figure 5.1. Distribution and binning of a) watershed half-widths and b) water table gradients from the assignment of hydrologic parameters to the global watersheds. Vertical dashed lines mark the locations of bin centers.

watershed half-width. The depth of the aquifer was assigned to be one fifth of the domain length. Thus, each model consisted of an effective ridge-to-valley groundwater flow system to simulate groundwater flow in each watershed. The effects of along-valley flowpaths and flowpaths not orthogonal to rivers on groundwater age distributions were not considered in this analysis, but subwatershed-scale hydrodynamics and heterogeneity can significantly alter groundwater flowpaths and residence times [*Cardenas and Jiang*, 2010; *Jiang et al.*, 2010; *Gassiat et al.*, 2013; *Gomez and Wilson*, 2013]. The use of a watershed-based two-dimensional model also does not incorporate regional flowpaths that could flow below and across the watershed boundaries used for the current analysis. However, the focus of these models are to elucidate the young groundwater component in groundwater systems. Considering multi-scale groundwater flow (i.e., regional and watershed-based systems) would more accurately determine the total distribution of groundwater ages in the subsurface. But, as long as the watershed-based domains encompass the range of ages used in the analysis of renewable groundwater, introducing larger scales of groundwater flow would only add insight to deeper and older portions of the flow fields.

Instead of estimating water residence times through the whole surface and subsurface hydrologic system including precipitation, evapotranspiration, vadose zone processes, and groundwater, I focused on water residence times in the water-saturated subsurface. A global estimate of the water table at 30-arcsecond (~1 km) resolution [*Fan et al.*, 2013] defined the uppermost boundary condition, using the mean watershed-wide gradient. Previous models of groundwater age and regional groundwater flow systems have often assumed the water table is at or near the surface as a subdued replica of topography [*Tóth*, 1963; *Jiang et al.*, 2009; *Cardenas and Jiang*, 2010; *Jiang et al.*, 2010], which can lead to artificially deeper groundwater circulation and/or greater than measured recharge

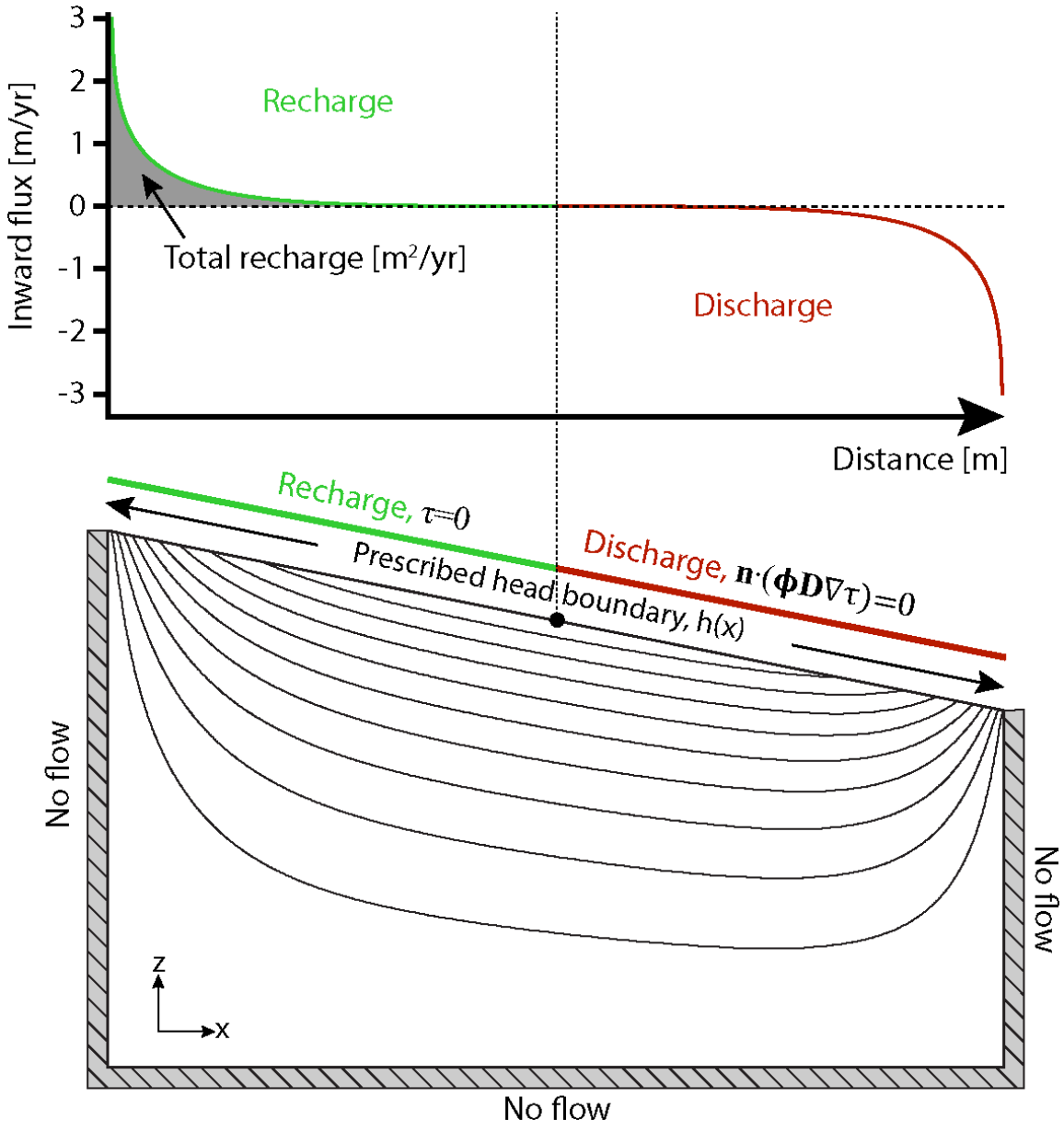

Figure 5.2. Model domain and boundary conditions for the flow and age-as-mass transport simulations. Thin black lines represent groundwater flowpaths to give an example but change depending on the hydraulic parameters. The black circle in the center of the upper boundary marks the hinge line between recharge and discharge zones. See discussion in text for a description of the variables.

rates. By using the distributed water table information, this analysis eliminated the need for relying on the similarity of the water table and topography.

The permeability used at the surface of the flow models followed the spatial analysis of *Gleeson et al.* [2014]. These permeability values (***k***) decayed as a function of depth:

$$\boldsymbol{k}(x,z) = k_0 \mathrm{e}^{-\beta a[z_s(x)-z]} \tag{5.1}$$

with k_0 the permeability of near surface materials, β the sediment compressibility, a a conversion factor from porosity to permeability decay held at a constant value of 2 for this study [*Bernabé et al.*, 2003], and z_s the elevation of the water table. No anisotropy was assigned to **k**. Porosity, $\boldsymbol{\phi}$, was similarly assigned to the models with:

$$\boldsymbol{\phi}(x,z) = \phi_0 \mathrm{e}^{-\beta[z_s(x)-z]} \tag{5.2}$$

The steady-state groundwater flow equation was solved for the hydraulic head distribution (h) and used to set the advection and dispersion terms in the age-as-mass equation:

$$\nabla \cdot (\mathbf{k} \nabla \mathrm{h}(\mathrm{x},\mathrm{z})) = 0 \tag{5.3}$$

with **k** the two-dimensional, spatially heterogeneous permeability tensor calculated from the permeability distribution in Equation 5.1.

The groundwater age transport equation treats groundwater age (τ) as mass in a steady-state advection-dispersion-diffusion equation (after Equation 10 of *Goode* [1996]):

$$\nabla \cdot (\boldsymbol{\phi} \boldsymbol{D} \nabla \tau(x,z)) - \nabla(\mathbf{u}\boldsymbol{\phi}\tau(x,z)) + \boldsymbol{\phi} = 0 \tag{5.4}$$

with porosity, $\boldsymbol{\phi}$, as an age-as-mass source term, $\mathbf{u} = [u_x, u_z]$ the average linear groundwater velocity, and $\boldsymbol{D}$ the diffusion-dispersion coefficient tensor [*Bear*, 1979]:

$$\boldsymbol{D} = \alpha_T|\mathbf{u}|\delta_{ij} + \frac{(\alpha_L - \alpha_T)u_i u_j}{|\mathbf{u}|} + D_m \tag{5.5}$$

In $\boldsymbol{D}$, the molecular diffusion coefficient, D_m, was assigned a constant value of 10^{-8} m^2/s, the longitudinal dispersivity (α_L) was scaled as a tenth of the square root of the domain dimensions with the transverse dispersivity (α_T) an order of magnitude lower, and δ_{ij} is the Kronecker delta function. The domain and boundary conditions used to solve Equations 5.3 and 5.4 are shown in Figure 5.2. No-flow conditions were prescribed on all but the top, sloping boundary that was a Dirichlet head boundary for the flow problem and split into τ=0 years across the recharge zone and only advection of τ (i.e., no diffusion or dispersion) across the discharge zone. Using the parameter discretization scheme described above, 43,659 of these coupled groundwater flow and age transport models were run for each parameter combinations. The hydraulic head and age fields were saved for every model for post-processing and archiving.

I used an unstructured finite-element mesh with triangular elements to solve Equation 5.3 and Equation 5.4. An adaptive meshing algorithm allowed automated mesh refinement to more accurately solve and stabilize the age transport problem. When refinement was necessary, the mesh was refined for 60% of the elements with the highest solution errors using an a posteriori approximation of the L_2 norm [*Verfürth*, 1996]. If the coupled models did not converge on a solution after two such refinements, a universal mesh refinement was applied before restarting the model run. This process was repeated up to three times until all of the model runs successfully converged. The number of triangular

mesh elements ranged from 3,000-656,000 with an average of 90,000 elements. Due to the automated nature of running thousands of models, a detailed analysis of mesh convergence was not possible, but the combined effects of the adaptive mesh and universal mesh refinement led to consistent results when compared to finer meshes during the early model development and vetting. The model runs took a total of 90 computer days with an average model solution time of 3 minutes and some taking several hours to solve.

5.2.4. Calculating the effective depth to renewable groundwater and the renewable groundwater equivalent

The objective of the groundwater flow and age-as-mass transport modeling here was to quantify the groundwater storage renewed over a certain timespan. By using 2D models, I could calculate the area between the 50-year isochrone and the water table, but this only provides storage information for a 2D groundwater system and was not immediately useful for characterizing the 3D storage of this young groundwater. Instead, my approach was to develop two length-scales that represent the watershed-wide storage of renewable groundwater that can be multiplied by the watershed area to give an estimate of the volume of renewable groundwater stored below that watershed. Thus, these length-scales must integrate the potential for renewable groundwater in both the recharge and discharge zones for real and simulated groundwater systems.

The first of the length-scales describing the renewable groundwater storage throughout a watershed is the effective depth of renewable groundwater ($d_{effective}$). The $d_{effective}$ is defined as the average depth below the water table that renewable groundwater is found for an entire watershed (Figure 5.3a). Thus, $d_{effective}$ represents the watershed-wide storage thickness of renewable groundwater, but the total storage is still tied to the spatial properties of the porosity.

The second renewable storage length-scale accounts for the porosity and is, therefore, termed the renewable groundwater equivalent ($d_{equivalent}$). Similar to $d_{effective,}$ $d_{equivalent}$ is conceptually a watershed-wide average value, but $d_{equivalent}$ is the uniform depth to which renewable groundwater would pond over a watershed if extracted from the ground (Figure 5.3b). Since $d_{equivalent}$ is only a measure of the renewable groundwater storage, $d_{equivalent}$ can be multiplied by the area of the corresponding watershed to give the total volume of renewable groundwater residing below that watershed.

The $d_{effective}$ and $d_{equivalent}$ can now be used to elucidate the renewable groundwater storage for the watersheds of Earth using the 2D models of groundwater flow and age-as-mass transport. To accomplish this, I first defined physically renewable groundwater to be 50 years old and younger. Then, I developed a probability-based approach for determining the likelihood of encountering renewable groundwater as a function of depth, where integrating this probability in depth yields the length groundwater age fields from the numerical simulations were used to calculate both the $d_{effective}$ and the $d_{equivalent}$ for every watershed globally.

First, each modeled age field was transformed from elevation to depth (z'), referenced from the surface of the model domain (Figure 5.4d-f) (i.e., water table and/or ground surface). Next, the relative frequency of given groundwater ages, f ($\tau(z')$), was calculated for 500 horizontal cross sections (i.e., at 500 depth intervals) to a depth of 2000 m or the maximum domain depth, using 500 logarithmically-spaced bins in time from 10^{-1}-10^{4} yrs (Figure 5.4g-i). With the large number of samples in this analysis, the relative frequency distribution approximated a probability distribution. The depth-specific age probability distribution was integrated over 0-50 yr for each of the 500 depths, giving a -scale of interest. In this way, the depth profile for the cumulative probability of finding groundwater 50 yr old or younger (Figure 5.3j-l). This basin-wide, truncated cumulative

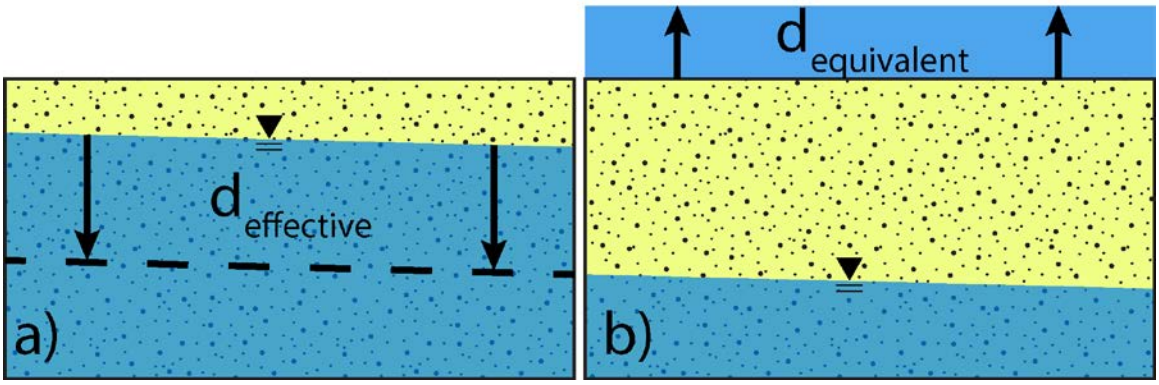

Figure 5.3. Cartoon representations of the a) effective depth of renewable groundwater ($d_{effective}$) and b) the renewable groundwater equivalent depth ($d_{equivalent}$).

probability is the ratio of renewable groundwater, $R_{renewable}(z')$:

$$R_{renewable}(z') = \int_0^{50\,yr} f(\tau(z'))d\tau \tag{5.6}$$

where $f(\tau(z'))$ is the number of samples per age bin divided by the total number of bins with units of yr^{-1}, and $R_{renewable}$ is unitless. $R_{renewable,3H}$ was also calculated using the ^3H analysis by *Gleeson et al.*[submitted], providing a comparison between the model results and geochemical samples of the proportion of groundwater younger than a given age, 50 years in this example, as a function of depth.

Despite this similarity in what they measure, the model-based $R_{renewable}$ and $R_{renewable,3H}$ represent the groundwater ages differently. For $R_{renewable}$, the groundwater ages for an entire depth slice through a groundwater system is integrated, whereas $R_{renewable,3H}$, integrates only the proportion of groundwater ages in the groundwater samples from an aquifer. Thus, $R_{renewable}$ and $R_{renewable,3H}$ will only be equal if $R_{renewable,3H}$ is comprised of an even mixture of all groundwater at a given depth below the water table across the entire aquifer. Therefore, the model and ^3H estimates of renewable groundwater are not expected to be identical, but instead provide two separate approaches for quantifying the storage of groundwater renewed on a 50 year timescale.

Next, integrating $R_{renewable}(z')$ in depth gives either the $d_{effective}$:

$$d_{effective} = \int_0^{z'max} R_{renewable}(z')\,dz' \tag{5.7}$$

or the $d_{equivalent}$ if porosity is included in the integrand:

$$d_{equivalent} = \int_0^{z'max} \boldsymbol{\phi}(z')\,R_{renewable}(z')\,dz' \tag{5.8}$$

with z'_{max} the maximum depth of the models from the top boundary. $d_{effective}$ represents the depth to which $R_{renewable}(z') = 1$ if all $R_{renewable}(z') > 0$ contributions were summed starting from the surface. Thus, $d_{effective}$ represents a characteristic depth scale for encountering a specific age of groundwater in a hydrogeologic system, chosen as 50 year for this example. Similarly, $d_{equivalent}$ provides a porosity-corrected characteristic depth scale that more readily accounts for the total volume of groundwater $\leq$ 50 yr. Equations 5.6-5.8 were integrated numerically: a three-point Newton-Cotes quadrature was for Equation 5.7 and Equation 5.8 for both the model-derived and ^{3}H-derived ratio of renewable groundwater and a summation was used for Equation 5.6. Both $d_{effective}$ and $d_{equivalent}$ are scalars that were then assigned to the global watersheds based on the extracted values of the hydrologic spatial datasets.

5.2.5. Assignment of modeled renewable metrics to watersheds globally

Model results as well as $d_{effective}$ and $d_{equivalent}$ were assigned to the HydroSHEDS watersheds by matching the simulation parameters with the spatial parameters extracted from the global datasets to the watersheds. Model results with one order of magnitude change in the k_0 above and below the published data were also assigned to each watershed as an estimate of the uncertainty introduced by the input parameters on the metrics of renewable groundwater. The volume of renewable groundwater was then calculated by multiplying the area of each watershed by $d_{equivalent}$.

5.2.6. Renewable groundwater comparison for thirty aquifers

Tritium concentrations are only available for a minority of aquifers globally. Therefore, I developed two approaches for testing the agreement between the simulation and ^{3}H-derived estimates of modern groundwater storage. The first method compared the volume of renewable groundwater storage for all of the watersheds within the footprint of the well

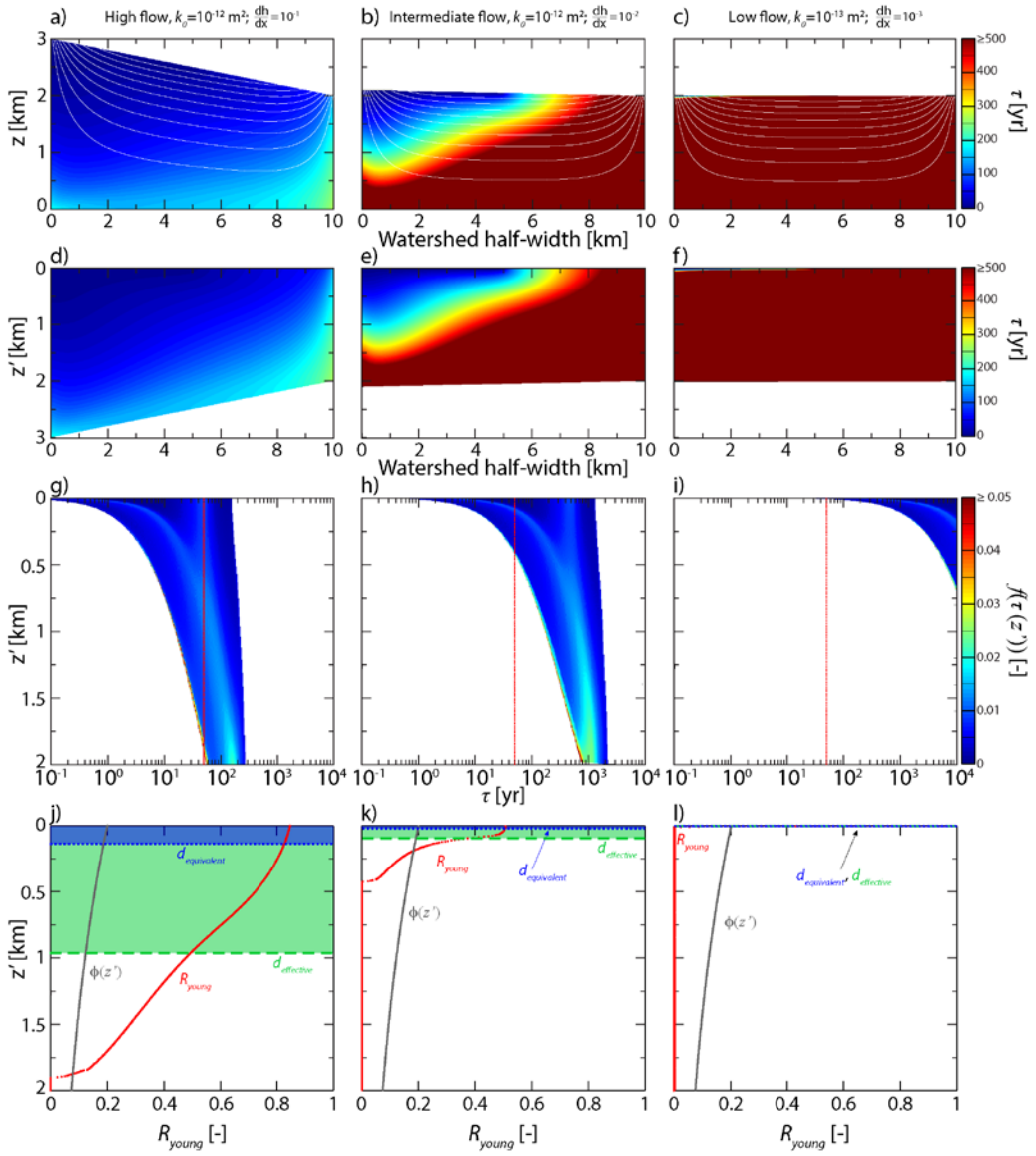

Figure 5.4. Examples of groundwater age distributions within the original flow domain (a-c), the same age distributions referenced from the surface (d-f), the resulting depth-specific age probability distribution for each model (g-i), and the calculated $R_{renewable}$ for each flow system (j-l). These example age distributions are for 10 km long groundwater flow domains with an ϕ_0=0.2, $\beta \cdot a$=0.01 m^{-1}, and no anisotropy. Continuous zero values in g)-i) are removed for plotting purposes. Each row of data in g)-i) sums to unity and the red vertical line marks τ = 50 yr.

samples (i.e., approximating the aquifer extent) from the ^{3}H approach with the total storage volume calculated from integrating $R_{renewable,3H}$ with estimated aquifer properties. In the second method, the $d_{effective,3H}$ calculated from integrating $R_{renewable,3H}$ was compared with the $d_{effective}$ based on the watershed-scale modeling result for 30 aquifers containing the largest amount of tritium samples.

The first step for these comparisons was to determine the hydrologic properties of the aquifers. To do this, each well used for ^{3}H samples was assigned hydrologic data from the global spatial data synthesis using its location. Then, these hydrologic data were used to assign outputs from the numerical simulation. The same binning procedure was used to assign the hydrologic inputs to the simulation parameter space. Additional models were run with the permeability at the surface for the ^{3}H data changed by one order of magnitude from the base value [*Gleeson et al.*, 2014].

Once the model results were assigned to the aquifer-related watersheds, the two comparison methodologies diverged. For the volume-based comparison, the results from all watersheds within 10 km of the well locations for a given aquifer were collected. Renewable groundwater volumes for each watershed were summed to give the aquifer-wide estimate of renewable storage ($V_{storage}$), and the areas of these watersheds were also summed. The most common lithology (i.e., for porosity and permeability decay values) in these watersheds was then used with $R_{renewable,3H}$ for Equation 5.8 to calculate the $d_{equivalent,3H}$ over each aquifer. Next, $d_{equivalent,3H}$ was multiplied by the total area of the enveloped watersheds to give an aquifer-wide ^{3}H estimate of the volume of renewable groundwater storage ($V_{storage,3H}$). This comparison of aquifer renewable groundwater volumes provided a consistent spatial framework for comparing the simulation and ^{3}H results. However, the comparison relied upon an unbiased sampling of the aquifer (i.e.,

well locations are evenly or randomly distributed throughout the aquifer) and the accuracy of enforcing lithologic homogeneity in the calculation of $d_{equivalent,3H}$.

In the comparison of $d_{effective}$ values, the $R_{renewable,3H}$ was integrated in depth following Equation 5.7 with the well data for each aquifer, yielding a single value for each aquifer. However, the simulation-based analysis operated at the watershed-scale, whereby each well sample had a corresponding watershed in which it was located. Thus, for this analysis, the $d_{effective}$ was used as the terminal indicator of renewable groundwater storage so as not to require additional assumptions of hydrogeologic properties and distributions across the aquifer. Since different scales were considered (i.e. aquifer vs. watershed), the simulation-based estimates should be lower to much lower than the ^3H estimates.

The modeling and tritium analyses provided separate methods for estimating young groundwater storage, but both approaches incorporated different simplifying assumptions that make calibration of one with the other not possible. Firstly, the modeled $d_{effective}$ and $d_{equivalent}$ values were based on a depth-integrated probability of the occurrence of renewable groundwater across an entire flow system, but the $d_{effective,3H}$ and $d_{equivalent,3H}$ were based on the proportion of renewable groundwater in well samples that integrate multiple scales of flow and potentially the effects of heterogeneity. However, the models restricted these storage metrics to include only the shallowest topographically-driven flow system bounded by perennial streams. In regions with small surface watersheds, the models would incorrectly limit the extent of renewable groundwater to shallower flow systems that in reality could mix with larger scale, more regional flowpaths. The models also only considered a single lithology per domain, whereas the ^3H samples integrate the complexity of their hydrologic and hydrogeologic histories. Secondly, the simulations modeled the age of the groundwater, not the transport of ^3H, whereby specifying a ^3H molecular diffusivity value would be required. Additionally, the processes that led to the measured ^3H

concentrations occurred in three-dimensional space and through time, whereas the models were steady-state and two-dimensional. Within the ^{3}H analysis, uncertainty arose predominantly from the estimated ^{3}H concentration in groundwater recharge and the stochastic groundwater mixing model, which did not include groundwater dynamics. Thus, the purpose of comparing the model and ^{3}H results was to understand how the uncertainty in each analysis biased the renewability estimates and check if, despite these differences, the two analyses resulted in similar renewable groundwater storage for each aquifer.

Additional uncertainty in the comparisons arose from the uncertainty in the model input parameters. A number of assumptions are inherent in the calculation and use of the watershed half-widths (e.g., what is the characteristic length scale for a watershed and how that translates to groundwater flow) and hydraulic gradients (e.g., soil permeability and only horizontal groundwater flow were used in the global water table depth dataset, while vertical flow and near-surface bedrock permeability were used in my analysis) in the numerical models. However, quantifying the uncertainty in these parameters is not straightforward and could require the monumental task of reproducing multiple previous studies. Instead, the uncertainty in the models is addressed using the near-surface permeability, which has published uncertainty ranges [*Gleeson et al.*, 2014].

5.3. RESULTS

5.3.1. Comparison of aquifer geochemical and modeling results

Comparing the volumes of renewable groundwater storage from the numerical simulations with the ^{3}H-based volumes, calculated using data from thirty aquifers (Figure 5.5), showed twenty aquifers had storage volumes within the uncertainties considered in the two approaches (Figure 5.7a). Only one third of the aquifers had storage estimates that

were within one order of magnitude if only the average permeability modeling and median tritium scenarios were used (Table 5.1).

The results of the comparison of the aquifer-wide tritium $d_{effective,3H}$ values (Figure 5.5) with the well-specific watershed-based groundwater simulations showed nearly twenty of the aquifers matched model-derived $d_{effective}$ estimates to within the uncertainty ranges of the two methods (Figure 5.6 and 5.7b, Table 5.1). The ratio of $d_{effective}/d_{effective,3H}$ was used as a metric of the misfit between the geochemical and simulated renewable groundwater estimates. Considering only the median $d_{effective}$ from the models with the median $d_{effective,3H}$ resulted in mainly one order of magnitude difference between the methods (Table 5.1, black dots in Figure 5.7b), but the disparity reached four orders of magnitude for the Najd Aquifer. Median simulation-derived $d_{effective}$ results primarily under-predicted the $d_{effective,3H}$. Uncertainty in the $d_{effective,3H}$ arose from the uncertainty in $R_{renewable,3H}$, whereas the uncertainty in the $d_{effective}$ from the simulations arises from both the heterogeneity in the hydrologic datasets sampled by the distribution of wells in each aquifer and the uncertainty within the hydrologic datasets. The colored uncertainty range in the $d_{effective}$ ratio in Figure 5.7b considered only the 25^{th}-75^{th} percentiles of $d_{effective,3H}$ with published permeability values [*Gleeson et al.*, 2014] to guide the models and taking the median of the simulated $d_{effective}$. Combining the uncertainty of $d_{effective,3H}$ and model $d_{effective}$ together defined the range of the grey boxes in Figure 5.7b. Combining all of the geochemical and modeling uncertainties led to favorable (i.e., overlapping) comparisons of $d_{effective}$ and $d_{effective,3H}$ for a majority of the aquifers tested (Figure 5.7b). Aquifers that did not show consistent results between the geochemical and model analyses did not follow any consistent geographic, spatial, or hydrologic trends.

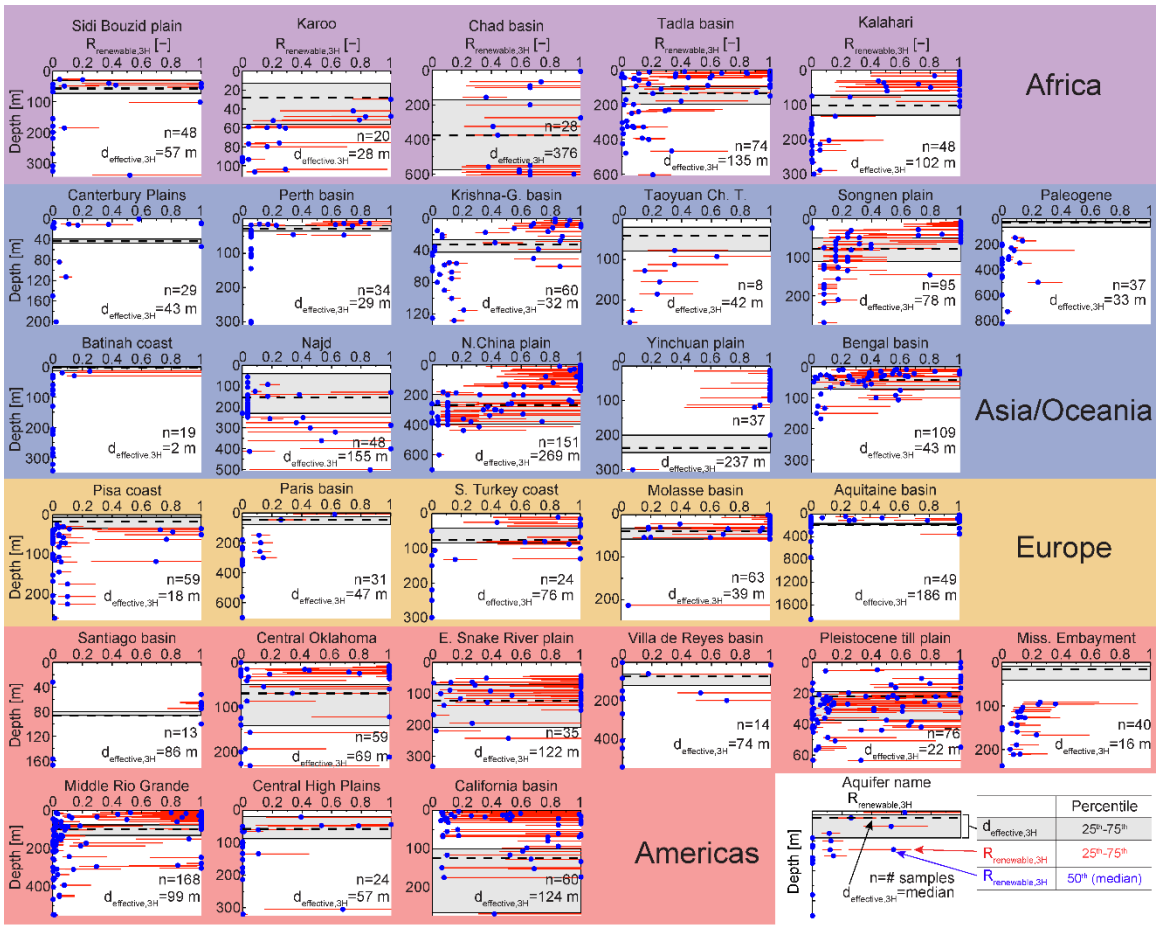

Figure 5.5. Aquifer profiles of $R_{renewable,3H}$ and resulting estimates in the effective depth to renewable groundwater calculated from the tritium profiles ($d_{effective,3H}$, horizontal dashed line and grey area). Table 5.1 reports the median values (dashed line) of $d_{effective,3H}$ for each aquifer.

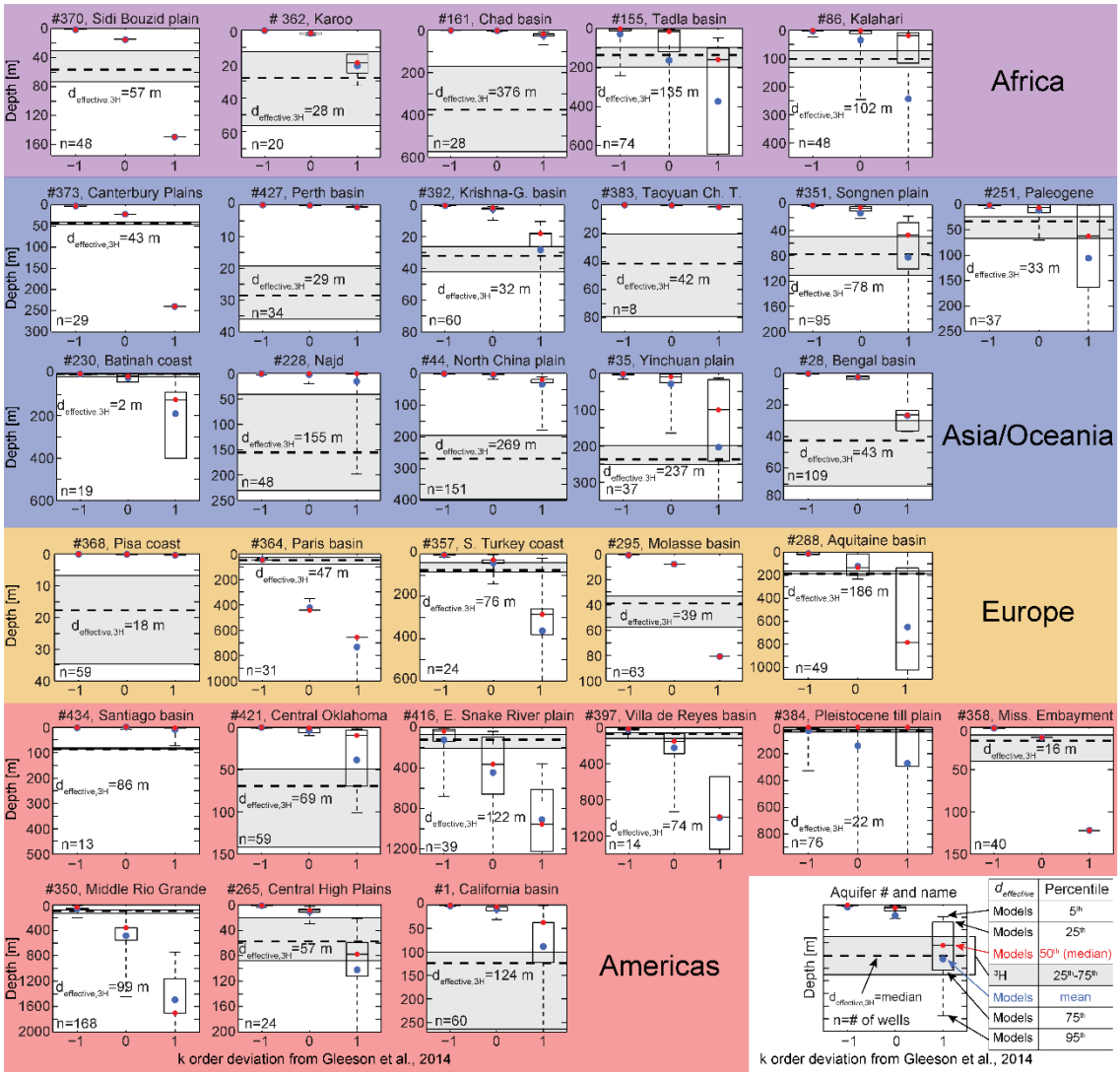

Figure 5.6. Comparison of the effective depth to renewable groundwater calculated from the tritium profiles and numerical simulations with all sources of uncertainty for each data-rich aquifer.

Table 5.1. Aquifers used for the comparison of $d_{effective}$ derived from ^3H samples and $d_{effective}$ calculated from numerical models using hydrologic parameters extracted to the well locations from the spatial datasets. The model results presented here do not include the uncertainty introduced by permeability nor in the ^3H data.

Continent	Aquifer	Wells	$V_{storage,3H}$	$V_{storage}$	$V_{storage}$ ratio	$d_{effective\ ,3H}$	$d_{effective}$	$d_{effective}$ ratio
		#	[km^3]	[km^3]	Log_{10} (Models/^3H)	[m]	[m]	Log_{10} (Models/^3H)
Africa	Sidi Bouzid plain	48	2.5	0.12	-1.32	56.7	14.7	-0.59
	Karoo	20	18.4	0.10	-2.25	28.1	1.5	-1.27
	Chad basin	28	1212.9	3.96	-2.49	376.2	1.7	-2.35
	Tadla basin	74	115.7	121.46	0.02	135.2	15.6	-0.94
	Kalahari	48	4242.4	20.74	-2.31	101.9	1.5	-1.83
Asia	Canterbury Plains	29	3.5	0.09	-1.60	43.4	23.7	-0.26
	Perth basin	34	3.6	0.01	-2.69	28.5	0.2	-2.10
	Krishna-Godavari basin	60	31.5	0.59	-1.72	32.2	1.8	-1.26
	Taoyuan Chungli Tableland	8	4.7	0.02	-2.47	41.7	0.3	-2.08
	Songnen Plain	95	2089.2	52.72	-1.60	77.7	4.7	-1.22
	Paleogene limestone	37	23.2	0.84	-1.44	32.8	6.1	-0.73
	Batinah coast	19	0.1	0.51	0.61	1.7	12.2	0.86
	Najd	48	457.6	0.97	-2.67	155.3	0.0	-4.41
	North China plain	151	2018.0	10.56	-2.28	268.6	1.8	-2.17
	Yinchuan plain	37	486.7	12.34	-1.60	236.5	10.0	-1.37
	Bengal basin	109	466.5	5.83	-1.90	42.6	2.6	-1.21
Europe	Pisa coast	59	0.6	1.19	0.30	17.6	0.1	-2.11
	Paris basin	31	1.0	5.67	0.73	47.4	442.6	0.97
	S. Turkey coast	24	209.5	84.40	-0.39	76.1	27.7	-0.44
	Molasse basin	63	5.0	0.18	-1.43	39.0	7.9	-0.69
	Aquitaine basin	49	183.9	47.81	-0.58	185.5	132.4	-0.15
Americas	Santiago basin	13	0.9	0.08	-1.02	86.3	0.2	-2.59
	Central Oklahoma	59	43.8	0.43	-2.01	69.3	0.9	-1.86
	E. Snake River plain	39	146.7	379.37	0.41	122.0	361.8	0.47
	Villa de Reyes basin	14	15.8	7.50	-0.32	73.7	151.9	0.31
	Pleistocene till plain	76	3.6	24.72	0.84	22.0	0.1	-2.35
	Miss. Embayment: Memphis	40	0.6	0.12	-0.71	15.9	12.0	-0.12
	Middle Rio Grande	168	185.8	91.99	-0.31	99.3	356.6	0.56
	Central High Plains	24	353.1	15.91	-1.35	57.3	7.6	-0.88
	California basin	60	239.2	2.67	-1.95	123.6	3.6	-1.53

Wells with ^3H samples for comparison = 1564

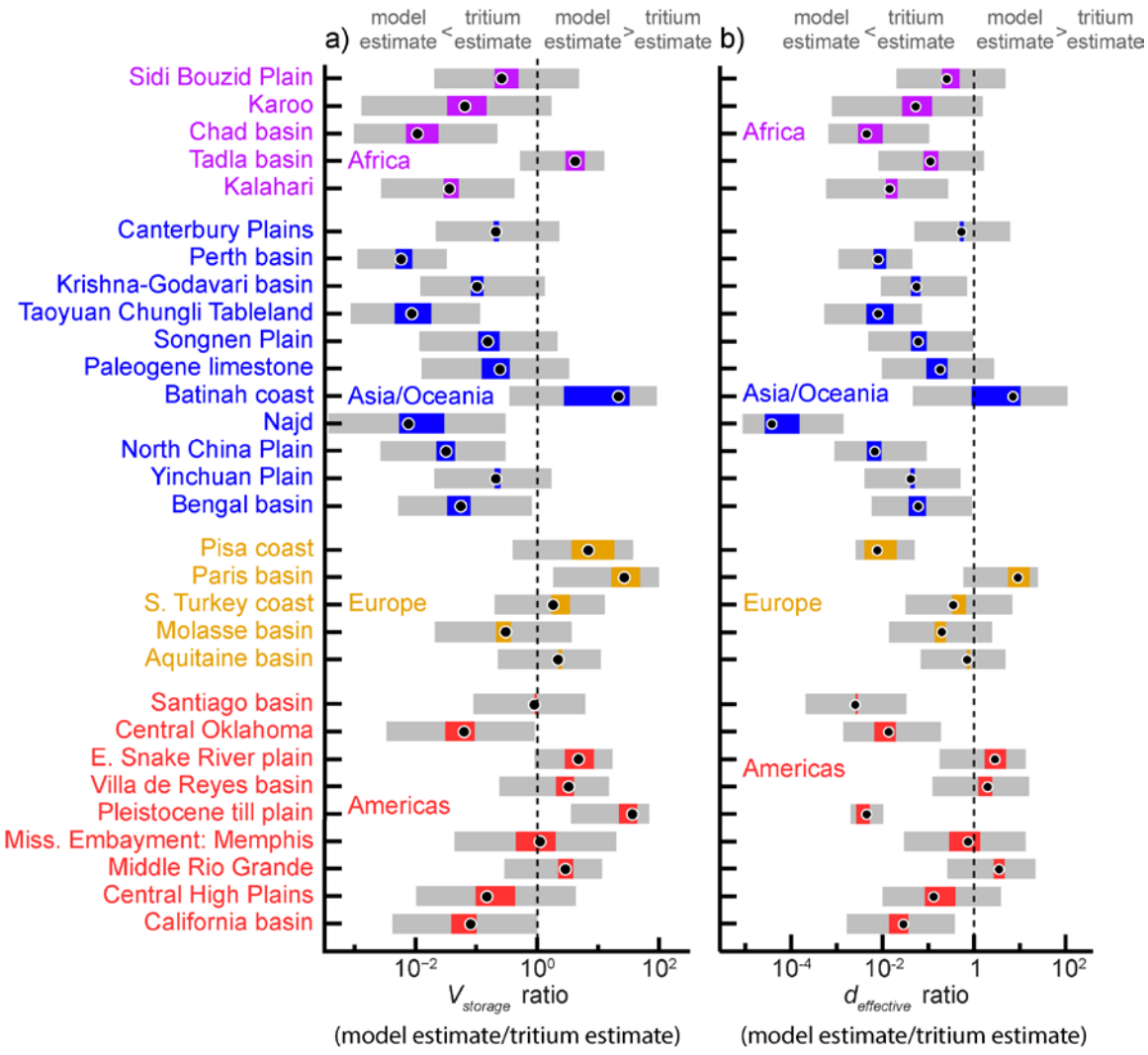

Figure 5.7. Comparison of modeled and ^{3}H-based estimates of a) the volume of renewable storage ($V_{storage}$), and b) effective depth of renewable groundwater ($d_{effective}$) for 30 aquifers with the most ^{3}H samples. The colored bar shows the uncertainty range only considering the ^{3}H analysis, and the grey bars show the combined uncertainty from the ^{3}H calculation and permeability in the numerical simulations. Black dots in a) show the ratio of storage volumes calculated from the average permeability models and the median $d_{equivalent,3H}$ and in b) show the ratio of the median $d_{effective}$ from the models and the median $d_{effective,3H}$ for each aquifer.

5.3.2. Global distribution of renewable groundwater

By transforming renewable groundwater storage into a length scale to describe average conditions for a surface watershed, I calculated the $d_{effective}$ and $d_{equivalent}$ for every watershed on Earth using the numerical models of groundwater flow and age-as-mass transport (Figure 5.8 and 5.9). The global median $d_{effective}$ was 8.1 m (1.0-58.5 m for the 25^{th}-75^{th} percentiles), and the global median $d_{equivalent}$ was 0.6 m (0.1-3.8 m for the 25^{th}-75^{th} percentiles). Neither $d_{effective}$ nor $d_{equivalent}$ strictly matched a statistical distribution (Figure 5.10), but both resembled a log-normal distribution with some multi-modality.

The spatial patterns of $d_{effective}$ and $d_{equivalent}$ both predominantly followed two of the input parameters: the permeability at the surface and the hydraulic gradient. The connection between these input parameters is complex and is demonstrated with some examples. However, more detailed analysis of the effect of input parameters is planned using the model results in future work. Despite having relatively high permeability across much of Australia (~10^{-13} m^2), low hydraulic gradients resulted in most of the continent showing a $d_{equivalent}$ of less than 1 m, likely related to low topographic gradients implicit through the analysis of *Fan et al.*, [2013]. A similar combination of high permeability and low hydraulic gradients resulted in minimal renewable groundwater storage in Somalia. On the opposite side of this spectrum, the U.S. Rocky Mountains have low permeabilities (~$10^{-16.5}$ m^2) but have sufficient topographic gradients to support steep hydraulic gradients, resulting in $d_{equivalent}$ values >10-100 m. In most of the watersheds on Earth, both permeability and the hydraulic gradient control the storage of young groundwater, making the deconvolution of their individual combinations to the renewable groundwater storage more complex.

The uncertainty arising from two orders of magnitude change in the permeability

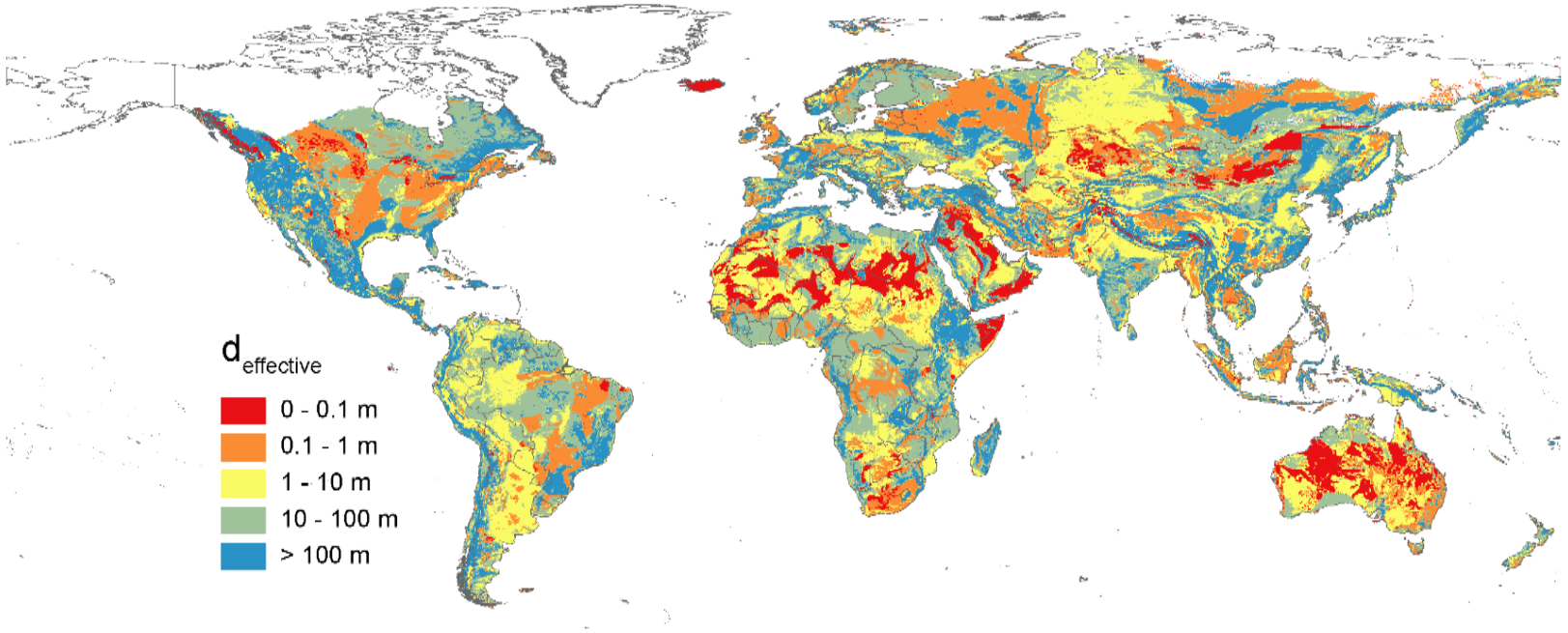

Figure 5.8. Global map of the effective depth of renewable groundwater ($d_{effective}$) calculated from the numerical simulations.

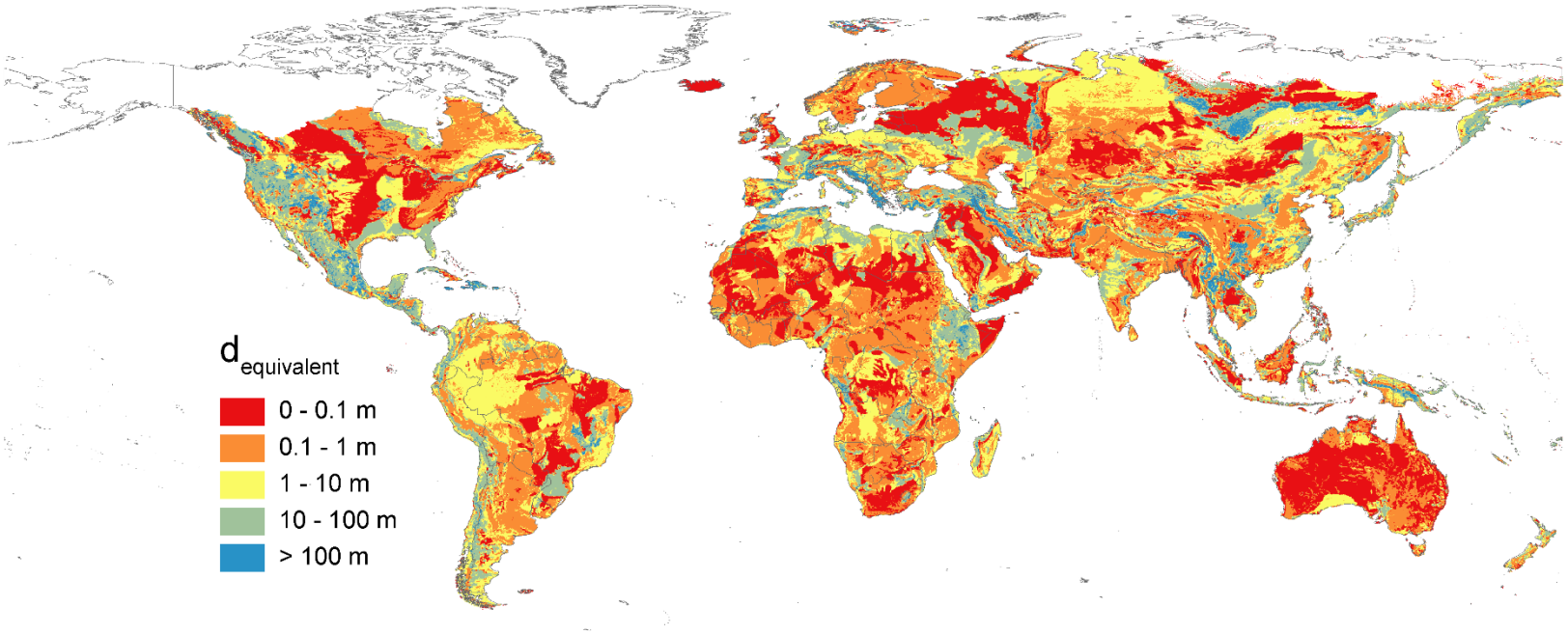

Figure 5.9. Global map of the renewable groundwater equivalent ($d_{equivalent}$) calculated from the numerical simulations.

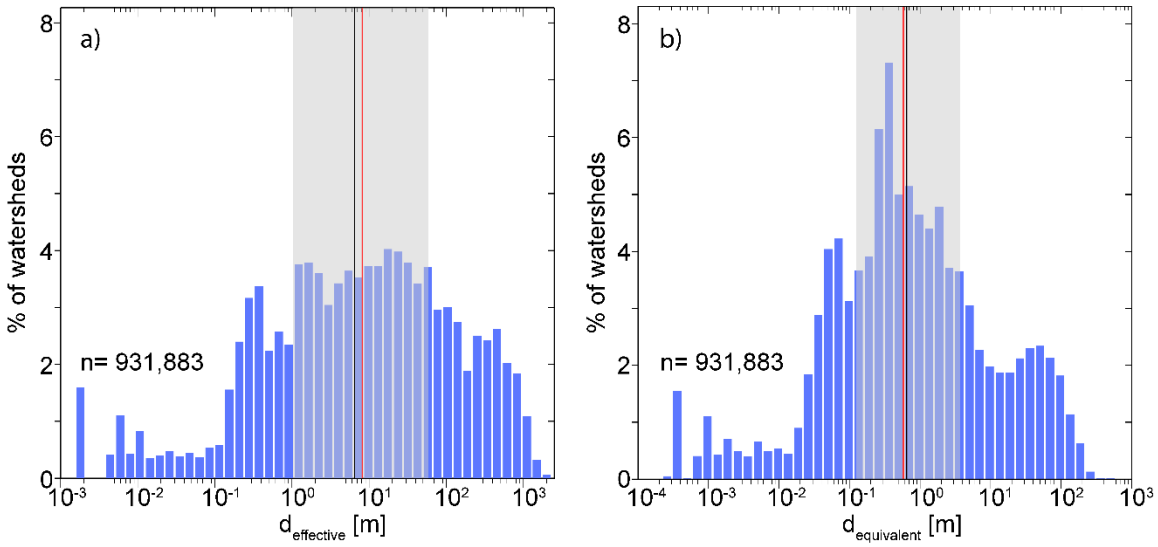

Figure 5.10. Histograms of global a) $d_{effective}$ and b) $d_{equivalent}$ values. The grey area marks the 25th-75th percentiles in the data, the vertical red line marks the median value, and the black vertical line marks the arithmetic mean.

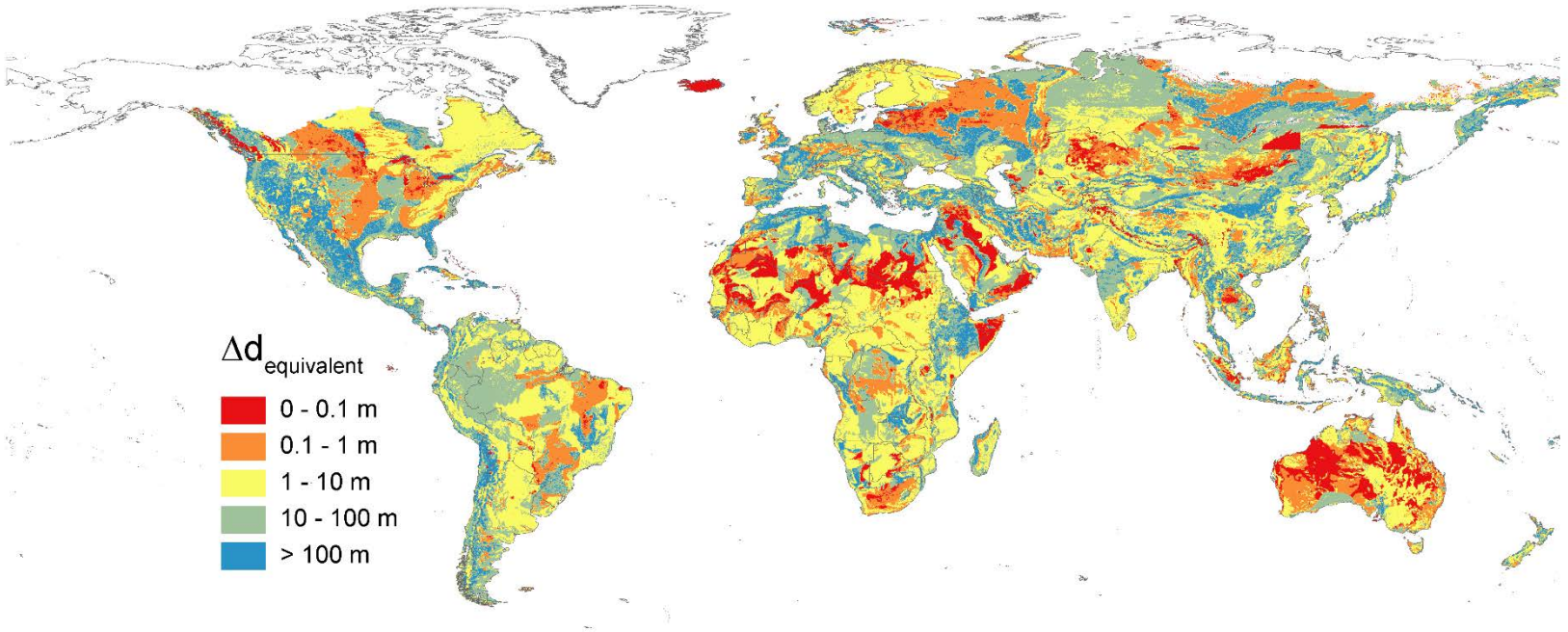

Figure 5.11. Global map of the total range in the $d_{equivalent}$ for simulations with one order of magnitude above and below the permeability assigned to each watershed (i.e., two orders of magnitude range in permeability centered around the assigned lithology-average values).

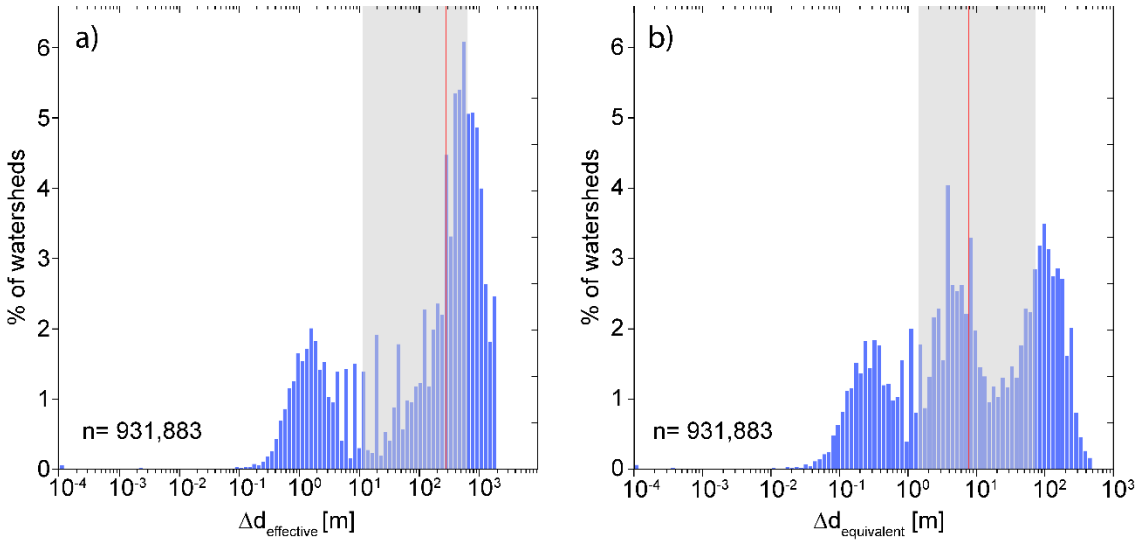

Figure 5.12. Statistical distributions of the range of a) $d_{effective}$ and b) $d_{equivalent}$ values resulting from prescribing the global collection of models with a permeability range of two orders of magnitude around the lithologic mean. The shade grey area extends from the 25th-75th percentiles in the data, and the vertical red bar marks the location of the median value.

on $d_{equivalent}$ for the watersheds on Earth shows the sensitivity of the renewable groundwater storage to permeability and likely represents the largest source of uncertainty in these calculations (Figure 5.11).The median uncertainty range for a two orders of magnitude change in permeability on $d_{equivalent}$ is 7.8 m (Figure 5.12). In general, watersheds with low $d_{equivalent}$ values have less variability introduced by changing the permeability at the surface. Implicit in this analysis is the assumption that changing the permeability at the surface does not change the depth decay of permeability (i.e., β in Equation 5.1). Additional analysis of the effect of permeability and porosity decay on groundwater age fields and the renewability metrics will be the subject of future work, but will certainly change the groundwater age field [*Cardenas and Jiang*, 2010; *Jiang et al.*, 2010].

5.3.3. Volume of renewable groundwater

Multiplying $d_{equivalent}$ by the area of each watershed yields the estimated volume of renewable groundwater stored in each watershed (Figure 5.13). The map of renewable groundwater storage provides quantitative estimates at the watershed scale, but without the watershed boundaries, visual inspection of the global map does not indicate regional storage trends, since the volume is also controlled by the size of the watershed. For example, west Texas appears to have a large region of very little renewable groundwater storage (Figure 5.14), but this area is composed of smaller watersheds that each store small volumes of renewable groundwater that sum to a significant volume (9687 km^3 with all 5504 watersheds, reducing to 4113 km^3 when removing 759 watersheds with over-predicted recharge). However, as discussed in Section 5.4., the more arid portions of Texas may have over-predicted volumes of renewable groundwater arising from both the simplifications in the model setup and underlying datasets. An example of this over-prediction is apparent in west Texas near El Paso, where mountainous areas create the potential for steep hydraulic gradients that are in reality recharge-limited, but in the modeling of groundwater age, too much applied recharge creates too much renewable groundwater storage.

By summing the renewable groundwater storage volumes for every ice- and permafrost-free watershed on Earth, the total volume of groundwater renewed on a 50 year timescale is 1,410,000 km^3 (257,000-4,18,000 with +/- one order of magnitude in the near surface permeability). Therefore, with the numerical modeling approach, I calculated that 6.2% (1.1-19%) of the world's groundwater supply to a depth of 2000 m (22,600,000 km^3) is renewable [*Gleeson et al.*, submitted]. In comparison, the percent of groundwater renewed in 50 years was calculated using only geochemical data was estimated to be 5.6%

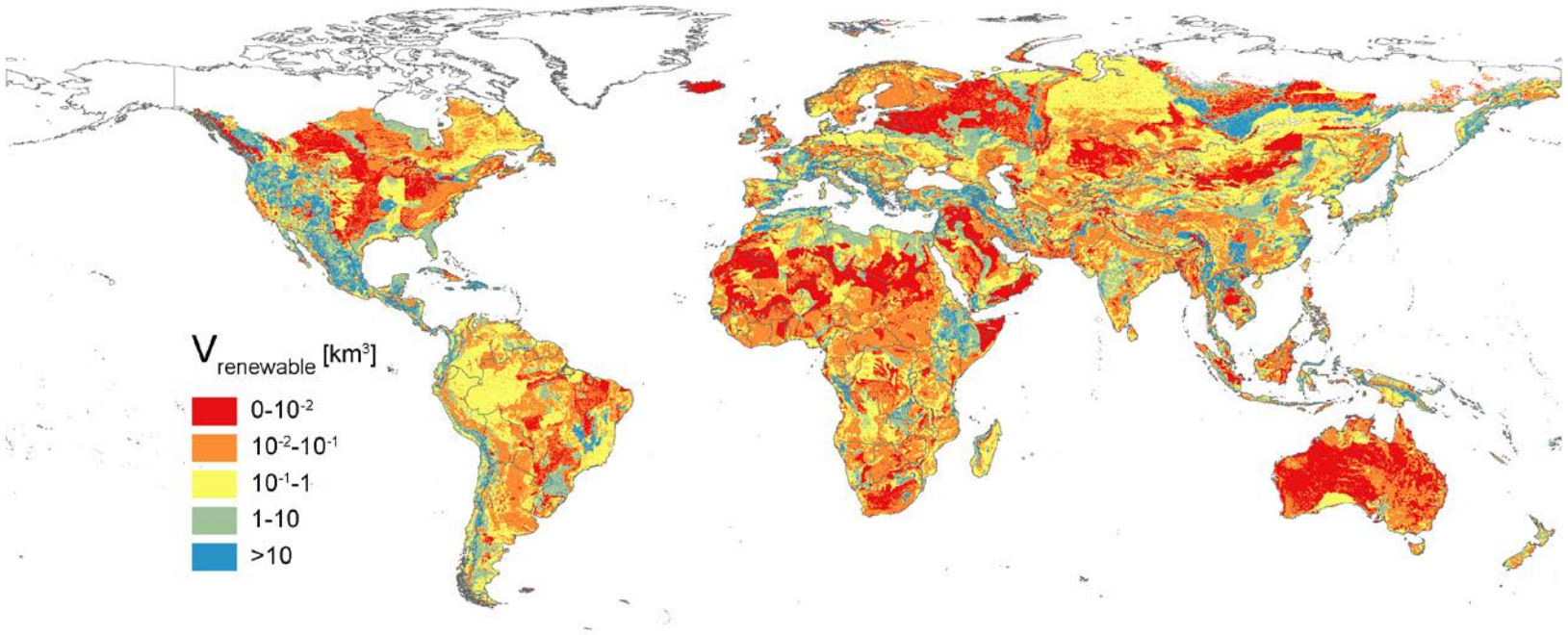

Figure 5.13. Global map of the volume of renewable groundwater ($V_{renewable}$). Watershed boundaries are omitted.

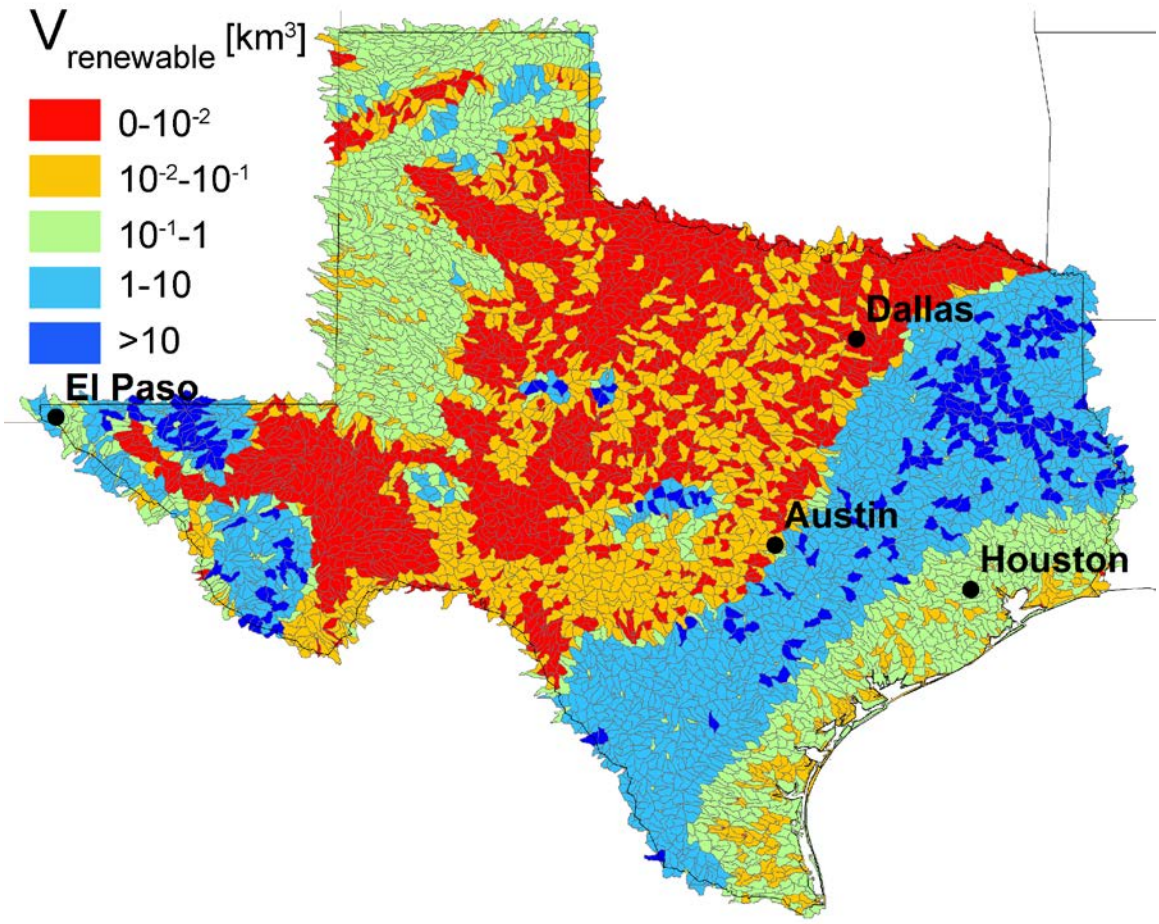

Figure 5.14. Renewable groundwater volume ($V_{renewable}$) map of Texas showing watershed boundaries from HydroSHEDS.

(1-16% including the uncertainty in the mixing models and the global porosity function) of the total groundwater in the upper 2 km of the crust [*Gleeson et al.*, submitted]. Therefore, through two very different approaches, ~6% of the more accessible and more likely to be fresh groundwater [*Frape et al.*, 2003; *Kharaka and Hanor*, 2003] on Earth is replenished on a fifty year timescale.

5.3.4. Volumes of Holocene-aged groundwater storage

The selection of groundwater younger than 50 years old in the calculation of $R_{renewable}$ was arbitrary and can be exchanged for other timescales. The cumulative proportions of groundwater age can be computed for any relevant timescale. Thus, I extended the probability-analysis developed in *Section 5.2.4.* to calculate the volumetric distribution of groundwater ages on Earth. Hydrologic transience certainly affects the groundwater age fields [*Gomez and Wilson*, 2013], so the steady-state simulations in the current study can be used to estimate storage for groundwater under current climate conditions. Therefore, I calculated the groundwater storage for timespans of up to 9,500 years, potentially spanning much of the Holocene, but the simulated groundwater ages do not integrate the time spent in the vadose zone and, thus, should not be associated with specific historic time periods. The time lag introduced by water traversing the vadose zone is not included in the calculation of groundwater age by definition. Quantifying storage for longer timescales would need to account for different recharge conditions arising from the last glacial period and the transition to interglacial climate, which is not possible with the current steady state simulations. However, even intra-annual transience can affect groundwater ages [*Gomez and Wilson*, 2013], and the resulting changes to the calculated storage of groundwater for short timescales (< 1 yr) are below the temporal resolution of the current analysis. Similarly, as longer timescales are considered for calculating the

storage volume, boundary effects on the age fields become more significant, especially for small watersheds: either the watershed-based groundwater system may be too shallow to fully constrain the location of old groundwater, or erroneously old groundwater ages could occur near the no-flow boundary conditions.

With the underlying acknowledgement of these limitations, I calculated the first temporally-constrained global distribution of groundwater storage volumes (Figure 5.15). Groundwater storage increased as roughly the cube root of groundwater age. Uncertainty in the storage volume resulting from an order of magnitude change in permeability increases when considering larger timescales. While non-linearity between groundwater storage and groundwater age may be expected due to the complexity of hydrogeologic systems, this is the first attempt at quantifying the relationship at the global scale. According to this analysis, 47.3% (23.5-75.2% with permeability changed one order of magnitude) of all groundwater in the upper 2 km of the crust is renewed over less than 9,500 years. From a different perspective, 10% of groundwater storage is renewed on a timescale of 120 yrs (12-1200 yrs for an order increase and decrease in permeability, respectively).

5.4. DISCUSSION

5.4.1. Model simplifications

Simplifications of groundwater systems were required in using 2D models to investigate real 3D watersheds globally. The upper boundary condition of the models was based on previously-modeled water table depths that only incorporated horizontal groundwater fluxes under topography-driven flow and unconfined conditions using the Dupuit-Forchheimer approximation [*Fan et al.*, 2013]. Using these data, the spatial head

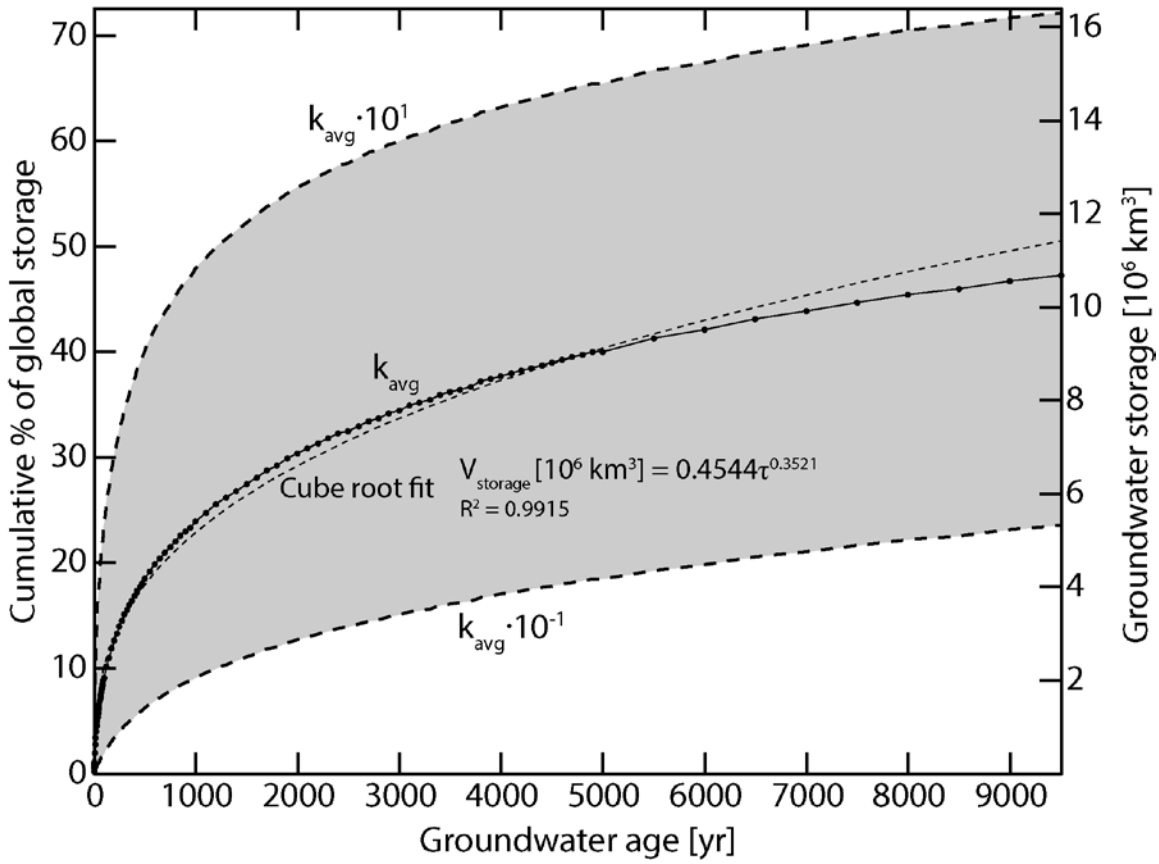

Figure 5.15. The distribution of groundwater storage renewed over timescales of up to 9,500 years. The average permeability (k_{avg}) case shows points for the timescales calculated, and the best fit to this curve is shown as the thin dashed line. The area in grey is the range of uncertainty in the storage introduced by changing the model permeability at the surface one order of magnitude. The percent of global storage uses a groundwater volume of 22.6 million km^3.

gradients used in my models were calculated by subtracting the water table depth from topography and then differentiating. Finally, the mean hydraulic gradient was calculated for each watershed to transform the 3D water table into my 2D model domain.

Simplifying the hydrogeologic expression of both the topography and morphology of watersheds into a planar, uni-directionally sloping water table undoubtedly led to inaccuracies in the modeled groundwater age distributions when attributing them to real groundwater systems. For the model results to simulate real groundwater age fields adequately, either a very simple watershed geometry is required or the model needs to be expanded to include multiple scales of flow systems and ideally include 3D topography and transience. Only a watershed that is symmetric across the drainage feature (e.g., stream) and has an equidistant ridge orthogonal from that drainage feature would be accurately characterized by the 2D model domain used in this analysis.

Separate from the transformation of the flow system from 3D to 2D, the assignment of the hydraulic gradient using a water table configuration based on the Dupuit-Forchheimer assumptions was somewhat paradoxical [*Kirkham*, 1967]. In the analysis of *Fan et al.*, [2013], only horizontal head gradients exist. Whereas in my simulations, the calculated groundwater age field was primarily controlled by vertical head gradients imposed by the top boundary condition. A more complete analysis of groundwater flow and age would solve directly for the water table as a free surface and not rely on predetermined, assumption-laden head gradients [*Haitjema and Mitchell-Bruker*, 2005]. However, such an analysis would require a more sophisticated global analysis of groundwater flow than has been attempted to date.

No pumping nor artificial recharge conditions were considered in the numerical models, which were instead designed to understand so-called “natural” hydrogeologic conditions prior to the introduction of pumping wells. By pumping wells and changing the

recharge regime through irrigation, the groundwater residence time for an aquifer would change as the groundwater system adjusted to the new hydrodynamic setting. In the two-dimensional models discussed above, introducing additional groundwater recharge or discharge features to the models would in turn create different simulated groundwater age distributions. Adding a pumping well anywhere in the model domain would lead to larger head gradients and overall younger groundwater residence ages, though models with rapid permeability decays with depth could restrict the younger groundwater near the surface and lead to overall older groundwater throughout the domain. Additional recharge features in the recharge zone would similarly increase head gradients and lead to younger groundwater. However, recharge features in the original discharge zone would lead to localized groundwater flow systems that can lead to both older and younger groundwater depending on the permeability distribution [*Jiang et al.*, 2010]. Thus, the 2D steady-state models in this analysis provide a first estimate of global groundwater age distributions based on much simpler flow systems than in reality, and this simplification can have different effects on the groundwater age distributions depending on the locations of groundwater extraction and recharge features.

Another simplification in the numerical analysis was that the most areally-extensive near-surface lithology was used to prescribe both a watershed-wide porosity and permeability. This areal homogeneity of the subsurface properties does not account for geologic structure nor variability that would alter groundwater flowpaths and age fields. Additionally, any hydrogeologically relevant stratigraphy is not considered. These additional hydrogeologic complexities would provide more accurate groundwater age fields but would require a full understanding of the 3D structure and stratigraphy of the upper 2 km of the lithosphere.

Finally, the contribution of renewable groundwater from karst was not explicitly considered, though carbonates were one of the lithologies used to parameterize the simulations. Karst occurs in ~16% of the land on Earth and plays a significant role in groundwater flow [*Ford and Williams*, 2007]. Thus, the contribution of karstic groundwater systems to the storage of renewable groundwater is also substantial. However, groundwater residence times in karst integrate contributions from a complex network of fractures, conduits, and primary porosity in the carbonate matrix [*Worthington*, 2007]. Therefore, to simulate the groundwater age for the system, the relative proportions of each hydrogeologic component of karst systems must also be known. Even so, nearly all (~90%) of the flow through karst aquifers is through conduits, whereas nearly all of the groundwater storage volume (> 90%) is in the matrix [*Worthington*, 2007]. Using this delineation of storage and flow, then nearly all karst conduit flow is likely to be renewable on a 50 year timescale if the flowpaths are short enough and gradients steep enough, and most of the groundwater stored in karst systems could be much older than 50 years. In this way, if the total volume of groundwater in karst conduits and in the surrounding matrix where known, then karst groundwater storage could be compartmentalized as renewable and nonrenewable, respectively, but currently not enough data are available to execute this analysis at the continental scale.

5.4.2. Analysis of groundwater recharge in the numerical simulations

Groundwater recharge is the mechanism for the replenishment of groundwater resources and is critical for understanding the hydrodynamics in hydrogeologic systems. In the numerical simulations, groundwater recharge was assigned to the domain by prescribing a Dirichlet head condition at the upper boundary that distributed the recharge and discharge fluxes as a function of the hydrologic properties in the modeling domain.

Thus, recharge fluxes can be calculated from my models but was not an input parameter. However, the assigned head gradients were calculated from water table depths [*Fan et al.*, 2013] that were modeled using globally-distributed, average modern recharge estimates from *Döll et al.*, [2008]. Other global groundwater recharge estimates are calculated by *Wada et al.*, [2010] and using land surface climate models through the Global Land Data Assimilation System (GLDAS) [*Rodell et al.*, 2004].

Few quantitative estimates of groundwater recharge exist at the continental scale that can be compared to the simulation results (Table 5.2). Indeed, no consensus exists for what the average global groundwater recharge is, given the lack of and uncertainty in hydrologic and subsurface data. Complicating the quantification of groundwater recharge to shallow aquifers, the comparison between different recharge estimates on the shallow, unconfined water table position are relatively insensitive to significantly different recharge conditions [*Fan et al.*, 2013]. Thus, previous estimates are the state of the science but may not consider all of the hydrological processes nor fully incorporate hydrological heterogeneity commented on below.

Global estimates of groundwater recharge are calculated with mass balance models that try to close the water budget, whereby precipitation and evapotranspirative fluxes control surface and subsurface flows [*Nace*, 1969; *Garmonov et al.*, 1974; *L'Vovich*, 1974; *Trenberth et al.*, 2007; *Döll and Fiedler*, 2008]. Agreement between modeled and measured stream hydrographs provides the main test of model performance in these studies, where the assumption is that all of runoff and groundwater discharges enter terminally into river networks. While the majority of recharge likely enters the river network at some point before leaving the terrestrial system, direct groundwater discharges into the ocean are widespread [*Burnett et al.*, 2003; *Post et al.*, 2013; *Kwon et al.*, 2014] and may serve as an outlet for recharged groundwater that is not accounted for in some

Table 5.2. Summary of previous groundwater storage, groundwater recharge, and surface water runoff estimates. For the Global Land Data Assimilation System (GLDAS) estimates [*Rodell et al.*, 2004], the calculation of groundwater recharge is assumed to equal the remainder of precipitation after both surface runoff and evapotranspiration have been removed.

	Fresh storage	**Recharge**	**Surface runoff**	**Recharge/Runoff**
	10^6 km^3	10^3 km^3/yr	10^3 km^3/yr	%
Nace [1969]	1 to 7	1.5	29.5	5.1
Nace [1971]	4 to 60	6.0	-	-
Garmonov [1974]	23.4 (3.6 active)	13.3	43.8	30.4
L'Vovich [1974]	60 (4 active)	12.0	38.8	30.9
Döll et al. [2002]	-	13.8	38.3	36.0
NRC [1986]	15.3	-	40.0	-
Döll and Fiedler [2008]	-	12.7	39.4	32.2
Wada et al. [2010]	-	15.2	36.2	42.0
GLDAS CLM annual mean	-	17.7	21.6	81.9
GLDAS MOS annual mean	-	15.3	5.59	273
GLDAS NOAH annual mean	-	24.8	5.80	427
Gleeson et al. [submitted] *	22.6 (1.3 young)	48.0	-	-

*current analysis, average permeability case only

global estimates of recharge. Another assumption in groundwater recharge estimates is that once water enters a surface water feature it is unable to recharge groundwater systems, forcing all surface waters to be groundwater discharge features and without considering losing conditions. This simplification would lead to overestimating groundwater discharge using the balance of precipitation, evapotranspiration, and runoff alone. Thus, the global estimates of groundwater recharge may underestimate the magnitude of groundwater recharge with respect to not accounting for submarine groundwater discharge but in places may overestimate recharge where losing conditions (i.e., groundwater recharge from surface waters) exist, as in arid regions where the models underperform [*Döll and Fiedler*, 2008].

Despite the potential shortcomings of these global estimates of groundwater recharge, they provide benchmarks for understanding how well my numerical simulations characterized the real hydrogeologic systems. My models transformed the lateral two-dimensional water table depth analysis into a simplified vertical cross-section domain that was meant to integrate both the hydrologic and hydrogeologic systems at the watershed scale. Furthermore, all previous recharge analyses are discretized based on a regular grid, my recharge analysis explained below used the HydroSHEDs watersheds as the spatial unit, which complicated how previous estimates were compared with the current work given different organizational units. To test the validity of the simulations to quantify the young groundwater storage, the recharge calculated from the groundwater models should be consistent with the underlying recharge data, of which *Döll et al.*, [2008] was used as the input for the water table study [*Fan et al.*, 2013] that parameterized my models.

To calculate the watershed-integrated groundwater recharge that my models indirectly impose, a similar methodology to that used for the storage length-scales was adopted. Given that the simulations were in steady state, the groundwater recharge imposed

by the prescribed head condition equals the groundwater discharge from the domain, which is required to conserve mass (Equation 5.3; Figure 5.2). Thus, the up-gradient half of the domain was the recharge zone with a flux magnitude equal to the discharge flux but with the opposite sign. Total recharge and discharge fluxes [m^2/yr] are calculated for each of the simulations by integrating the fluxes into and from the upper domain boundary. The recharge equivalent, $r_{equivalent}$ [m/yr], for a watershed was then calculated by dividing the total recharge flux by the watershed half-width ($L_{half\text{-}width}$):

$$r_{equivalent,\tau} = \frac{\tau}{L_{half-width}} \int_{L_{recharge}} r(x)dx \tag{5.12}$$

with $r(x)$ the recharge rate into the domain over the recharge zone, $L_{recharge}$. Then, $r_{equivalent}$ can be multiplied by a time-scale to give a length-scale of recharge that occurs over a given time period, τ. Using τ = 1 year, $r_{equivalent,1}$ gives a watershed-wide integrated length-scale of recharge that can be multiplied by the watershed areas to give the volumetric rate of groundwater recharge in those watersheds. These recharge rates can then be summed globally to compare with previous recharge estimates. Similarly, a time-scale of 50 years can be chosen to compare the volume of groundwater storage younger than 50 years with the expected volume of recharge that would occur over 50 years. Since the storage calculation accounts for groundwater of various ages mixing, the storage volume is expected to be less than the recharged volume because older groundwater mixes with incoming younger groundwater, especially where heterogeneity is significant [*Cardenas and Jiang*, 2010; *Gassiat et al.*, 2013]. Equivalent recharge volumes less than young groundwater storage volumes could be expected in groundwater systems where very active

young groundwater dispersively mixes with older groundwater, yielding a mean age younger than the cutoff for the definition of groundwater youth (e.g., 50 years).

My initial estimate of the global recharge rate for all ice-free watersheds using the average permeability values was $50.6 \cdot 10^3$ km^3/yr ($5.21\text{-}523 \cdot 10^3$ km^3/yr for permeability one order of magnitude below and above the average permeability values, respectively). Previous global groundwater recharge estimates are listed in Table 5.2. Indeed, global estimates of precipitation available after evapotranspiration for runoff and potential groundwater recharge based on measurements range from $36\text{-}40 \cdot 10^3$ km^3/yr [*Schneider et al.*, 2014] and others listed in Table 5.2, which set the upper limit of realistic potential groundwater recharge (i.e., groundwater recharge is generally less than precipitation, regionally). Thus, I investigated the effect of culling watersheds with extreme modeled recharge rates on the global groundwater recharge and the modeled young groundwater storage. However, the uncertainty introduced by the permeability, which sets the recharge rate, contained the entire range of previous recharge estimates.

The results of the culling are summarized in Table 5.3. First, I culled watersheds (n=48,364; area = $7.3 \cdot 10^6$ km^2, 6.0% of land surface) where the water table from *Fan et al.*, [2013] was beyond the scope of their analysis (i.e., > 100 m), reducing my global recharge estimate by $2.6 \cdot 10^3$ km^3/yr (5.1%). In my analysis, these areas would have hydraulic gradients set only by the topography since they were prescribed a constant water table depth of 100 m. Additionally, these areas with deep water tables are primarily in arid and semi-arid regions with significant topography that would likely have groundwater systems controlled by recharge rates rather than topography [*Haitjema and Mitchell-Bruker*, 2005; *Gleeson et al.*, 2011], where the latter is the assumption in my numerical simulations. In addition, I culled all watersheds with annual groundwater recharge values that were greater than mean annual precipitation using Climate Prediction Center Merged

Analysis of Precipitation (CMAP) data[5] [*Xie and Arkin*, 1997], where 92,540 watersheds (10.0% of land surface) accounted for $42.1 \cdot 10^3$ km^3/yr (83.2%) of my recharge estimate for the original permeability models. Thus, the culled estimate of the global recharge rate as specified by the flow models was $5.9 \cdot 10^3$ km^3/yr without areas where model inputs were inconsistent with observational data or poorly constrained. This estimate may be within the range of uncertainty in the previous recharge estimates, given the misfit between the recent models is $2.5 \cdot 10^3$ km^3/yr [*Wada et al.*, 2010]. However, the true uncertainty in the model results is unknown, and large groundwater fluxes ($0.1\text{-}6.5 \cdot 10^3$ km^3/yr from submarine groundwater discharge [*Burnett et al.*, 2003]) and hydrological processes (e.g., groundwater recharge from surface waters) were not considered in these analyses that would require additional recharge to balance the groundwater budget.

Watersheds with groundwater recharge equivalents greater than the CMAP precipitation rate were primarily located in arid and mountainous regions (Figure 2.16). These areas of high modeled recharge values highlight the current disconnect between surface and subsurface hydrologic models, since groundwater flow in my models attempted to consolidate results from both: my hydraulic gradient is derived from ground-truthed water table depths modeled using shallow soil permeability [*Fan et al.*, 2013] and groundwater recharge estimates from a surface hydrologic model [*Döll and Fiedler*, 2008]. Large-scale surface hydrologic models do not include subsurface processes and data important to my study, including lateral and vertical flows, hydrodynamic dispersion, and lithology-based permeability and porosity values. Similarly, the water table data are derived from a global model that uses soil permeability rather bedrock permeability, even though soil permeability does not likely control regional water tables.

[5]provided by the NOAA/OAR/ESRL PSD, Boulder, Colorado, USA, from their website at http://www.esrl.noaa.gov/psd/

Table 5.3. Summary of the final estimates for the modeled groundwater recharge and storage renewal rates using all ice-free watersheds, watersheds with a water table depth less than 100 m and watersheds with recharge equivalents less than the precipitation rate. Since recharge rates are calculated using the assigned permeability, different recharge rates were calculated for the same watersheds for the different permeability scenarios. The relative contributions and extent of the culls are shown in the subtractions section.

	Watersheds		Area		Model recharge						Storage renewal					
					Base k		$k \cdot 10^{-1}$		$k \cdot 10^{1}$		*Base k*		$k \cdot 10^{-1}$		$k \cdot 10^{1}$	
Watersheds	#	%	10^6 km^3	%	10^3 km^3/yr	%	10^3 km^3/yr	%	10^3 km^3/yr	%	10^3 km^3/yr	%	10^3 km^3/yr	%	10^3 km^3/yr	%
All ice-free	933639	100	121.7	100	50.6	100	5.2	100	522.9	100	28.2	100	5.1	100	83.6	100
Water table < 100 m	885275	94.8	114.4	94.0	48.0	94.9	5.0	95.0	496.8	95.0	25.8	91.6	4.8	93.8	74.7	89.4
$r_{equivalent}$ < precipitation (CMAP)																
Base k	790982	84.7	102.3	84.0	5.9	11.7	-	-	-	-	6.9	24.6	-	-	-	-
$k \cdot 10^{-1}$	866577	92.8	112.3	92.2	-	-	2.7	50.8	-	-	-	-	2.8	55.3	-	-
$k \cdot 10^{1}$	633825	67.9	81.6	67.1	-	-	-	-	11.0	2.1	-	-	-	-	11.2	13.4
Subtractions																
Water table > 100 m	48364	5.2	7.3	6.0	2.6	5.1	0.3	5.0	26.1	5.0	2.4	8.4	0.3	6.2	8.9	10.6
$r_{equivalent}$ > precipitation (CMAP)																
k permeability	92540	9.9	12.2	10.0	42.1	83.2	-	-	-	-	18.9	67.0	-	-	-	-
$k \cdot 10^{-1}$	16877	1.8	2.2	1.8	-	-	2.3	44.2	-	-	-	-	2.0	38.4	-	-
$k \cdot 10^{1}$	250776	26.9	32.8	26.9	-	-	-	-	485.7	92.9	-	-	-	-	63.5	76.0

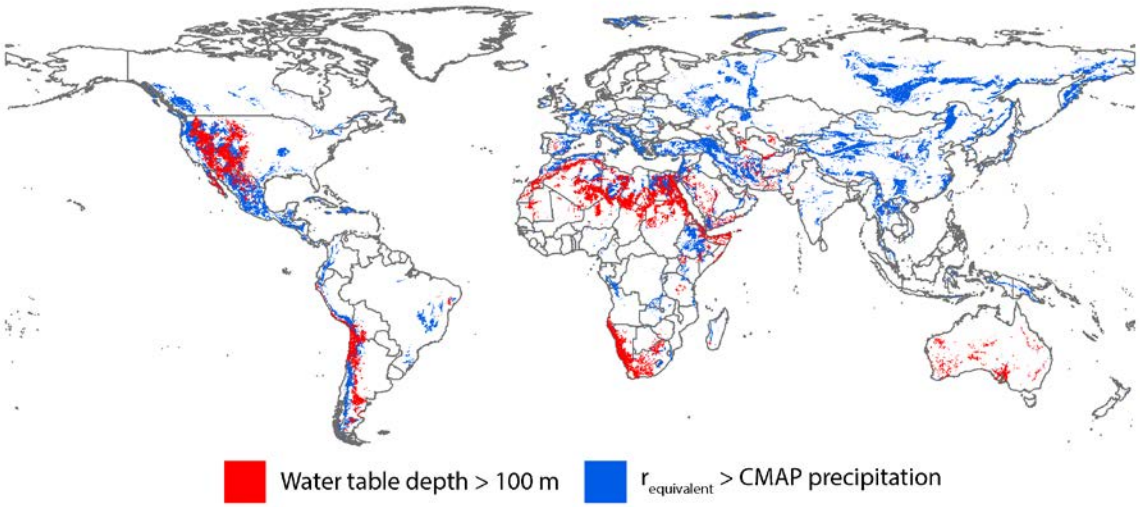

Figure 5.16. Watershed locations with a water table depth greater than 100 m (red) [*Fan et al.*, 2013] and a recharge equivalent greater than expected precipitation values for the average permeability case (blue). Increasing the permeability one order of magnitude increased the number of erroneous watersheds, whereas decreasing the permeability resulted fewer watersheds with groundwater recharge greater than precipitation.

This recharge analysis also demonstrated the plausibility of magnitude changes of permeability on the global scale. Part of the misfit of the global recharge rate for this study resulted from the assumptions built into the numerical models, restricting the analysis with lithology-average permeability primarily to less arid regions of the world (i.e., primarily topography-limited flow), but an order of magnitude change in permeability also resulted in an expected order of magnitude change in the calculated global recharge rate. Thus, for the base permeability case, overestimating the recharge was a result of introducing too much recharge into arid and semi-arid regions and potentially from uncertainties in the cross-dimensional transformation of head gradients and in assigning hydrologic properties to watersheds. Thus, the estimate of young groundwater storage prior to considering recharge could represent an upper limit of this storage, given that my average permeability case may overestimate global groundwater recharge by a factor of two or more. However, also integrated into the recharge analysis is the unknown effect of the transformation of the laterally two-dimensional water table data into a watershed-based characteristic two-dimensional groundwater flow domain with one lateral and one vertical dimension.

5.4.3. Lifespan and vulnerability of renewable groundwater

The calculated volume and spatial distribution of young groundwater on Earth can now elucidate how worldwide groundwater demand and use compare to the distributed renewal of groundwater storage. It is important to note that my simulations did not try to quantify how changing recharge, discharge, or extraction alter groundwater dynamics and the resulting age fields. Therefore, this analysis was solely to explore the consumption of the steady state storage of renewable groundwater calculated from my models.

Following the analysis in *Gleeson et al.*, [submitted], I calculated the lifespan of renewable groundwater under modern pumping rates (Figure 5.17). Dividing the spatial datasets of

the volume of renewable groundwater by the volumetric rates of modern extraction for irrigation [*Wada et al.*, 2012] gave the lifespan of the renewable groundwater if only renewable groundwater is extracted. Thus, this lifespan was a minimum estimate, since groundwater extractions are not necessarily concentrated in recharge zones where younger, and therefore renewable using my conceptual model, groundwater is located: extracted groundwater will actually be a mixture of renewable and older groundwater as a function of the hydrologic setting as well as the well location, well depth, and screen length.

This lifespan of renewable groundwater provides a new measure of the sustainability of modern groundwater use, estimating how long it takes for groundwater extractions to completely remove the storage of renewable groundwater from an aquifer. A lifespan greater than 50 years implies that the current rate of groundwater extractions will not deplete the storage of groundwater renewed over 50 years. However, more complex groundwater dynamics than those considered in my analysis from pumping will alter the groundwater age distributions, so a lifespan of renewable groundwater that is longer than 50 years does not define the consumption as sustainable. Using the 50 km by 50 km resolution of the groundwater extraction data, 82.8% of areas irrigated with groundwater have lifespans of renewable groundwater over 50 years.

Importantly, the lifespan of renewable groundwater also revealed regions where groundwater consumption was likely to surpass the rate of groundwater renewal. Anywhere with a lifespan that was less than 50 years indicated the potential for current unsustainable groundwater use, with increasing severity as the lifespan shrinks. 17.2% of the world's irrigated areas had a lifespan of renewable groundwater under 50 years. 12.7%, 8.4%, and 1.4% of renewable groundwater had a lifespan less than 25, 10, and 1 years, respectively.

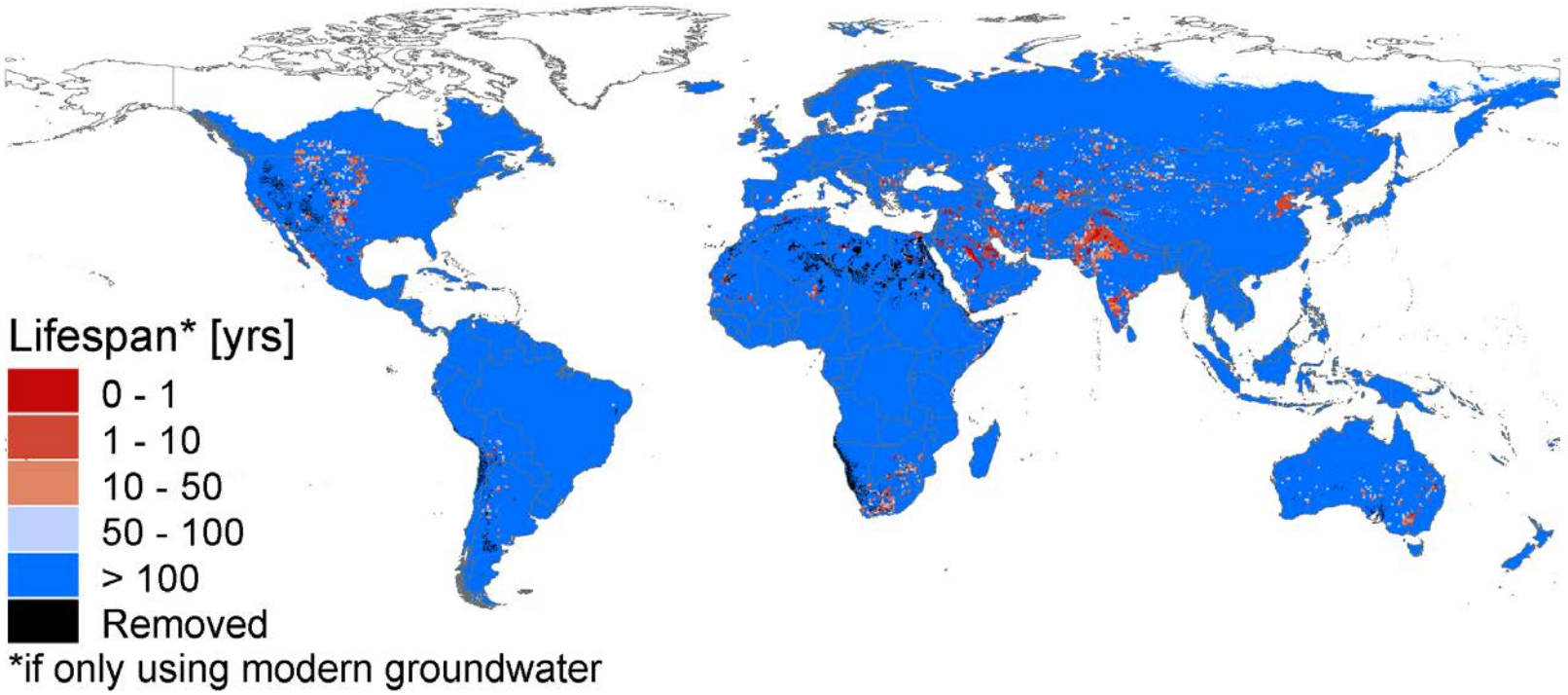

Figure 5.17. Global map of the lifespan of renewable groundwater if all groundwater extracted only removes modern groundwater. Removed portions of the map show areas where the water table depth was modeled to be greater than 100 m in the previous study [*Fan et al.*, 2013].

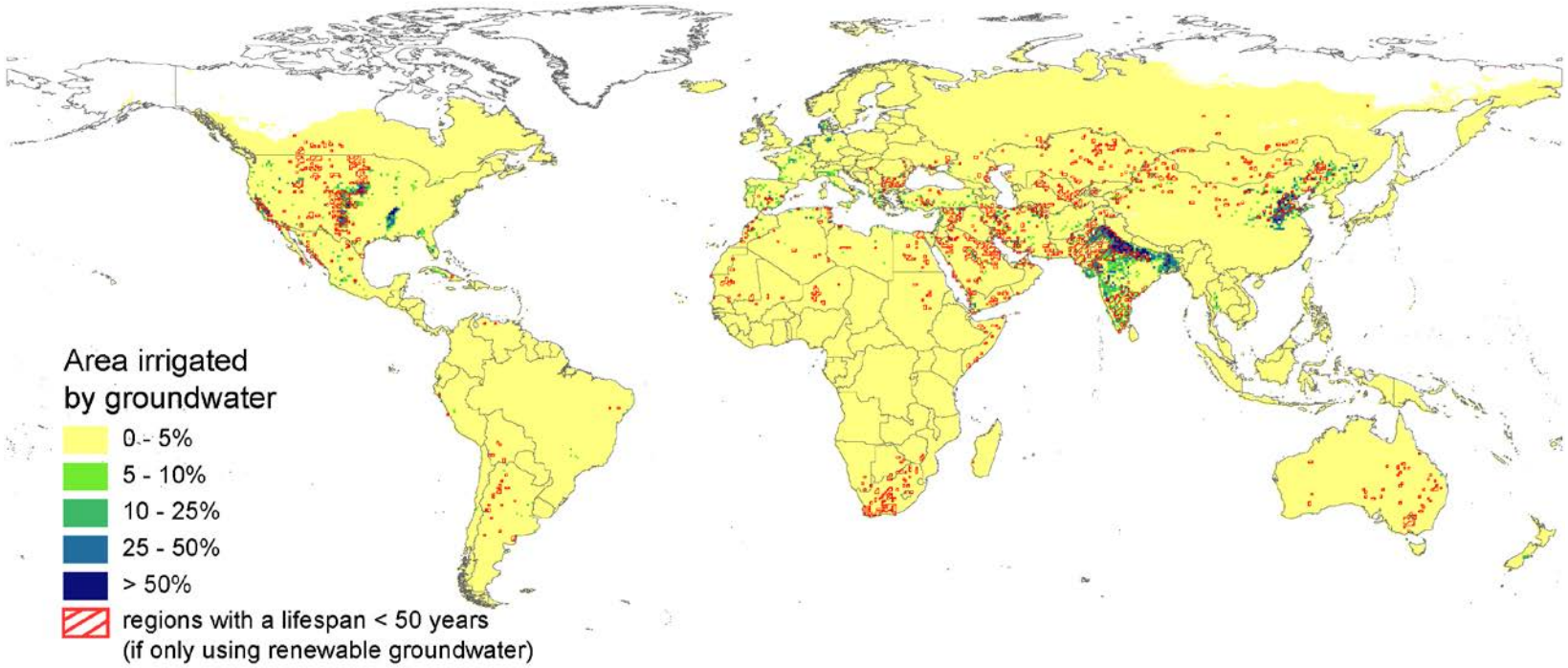

Figure 5.18. Global map of the percent of irrigation using groundwater after *Siebert et al.*, [2010] overlaid by areas with a lifespan of renewable groundwater less than 50 years (red).

Despite this small overall proportion of the world having unsustainable lifespans of renewable groundwater, the relative importance of groundwater in meeting the demand for water, primarily for agriculture [*Siebert et al.*, 2010], in these areas was also significant [*Gleeson et al.*, submitted]. Thus, comparing the extent to which groundwater was used for irrigation with the unsustainable groundwater use following the lifespan analysis offered more insight into how important this overconsumption was for the sustainability of current agricultural practices (Figure 5.18). Where at least 25% and 50% groundwater was used for irrigation, 46.5% and 57.9% of these areas have lifespans of renewable groundwater that were less than 50 years [*Gleeson et al.*, submitted]. Thus, in agricultural areas that depend upon groundwater for irrigation, approximately half of those areas had the potential to be using groundwater unsustainably.

Overestimating groundwater recharge for watersheds with the numerical simulations also affects the reliability of the lifespan of modern groundwater in those areas. More recharge, leading to larger young groundwater storage, would erroneously suggest that these regions have a sustainable balance between young groundwater renewal and modern groundwater consumption. However, real groundwater recharge in these areas are likely much lower, potentially by a factor of 10 using global averages of other estimates of groundwater recharge versus precipitation [*L'Vovich*, 1974; *Rodell et al.*, 2004; *Trenberth et al.*, 2007; *Schneider et al.*, 2014]. Thus, for areas where my simulations over-predict groundwater recharge, I expect the lifespan of modern groundwater to be much shorter and quite possiblely < 50 years. I cannot constrain these areas better with the current numerical simulations and data available at the global scale of this analysis.

This study calculated the renewable groundwater resources by focusing on the problem of groundwater quantity, but the quality of this water also determines its usefulness. By using groundwater age to constrain groundwater renewability, the volume

of renewable groundwater is inherently the more vulnerable groundwater in the subsurface to contamination. To calculate the global volume of groundwater renewable on a 50 year timescale, I transformed near-surface groundwater systems into 2D for computational simplicity, but the length-scales I calculated for each watershed represent a watershed-wide average storage of this young groundwater. However, using the onset of groundwater aging as the moment of recharge, young groundwater is the most recently recharged, regardless of the complexity or heterogeneity of a flow system. Therefore, young groundwater occurs predominantly in recharging areas, and recharge, whether natural or induced, can introduce chemical species and contaminants into the flow system. Thus, when quantifying groundwater renewability within the context of groundwater age, it is important to also consider the quality of this groundwater, and not just the quantity. However, quantifying the proportion of clean versus contaminated renewable groundwater would be challenging and location specific, given the diversity of potential contaminants, differences in the sources, unique transport dynamics, and solute-dependent attenuation processes.

5.5. CONCLUSIONS

How much groundwater is renewable? The renewal of groundwater is dependent on the dynamics of a groundwater system that control the characteristic timescales of groundwater flow. In this chapter, I instead use a timescale of 50 years to define a benchmark of groundwater renewability from an outward-looking-in perspective that incorporates the importance of groundwater as a resource, ideally to be sustained and managed for perpetual human consumption.

The global volume of modern groundwater was estimated to be 1,290,000 km^3 using 2D groundwater flow and age-as-mass transport models parameterized with global hydrologic and hydrogeologic datasets. The resulting groundwater age fields from these

simulations were analyzed using the probability of modern groundwater occurring at a given depth below the water table to yield length-scales of renewable groundwater storage that described the entire flow system. The $d_{effective}$ indicated the thickness of renewable groundwater storage in-situ underground, whereas the $d_{equilvalent}$ was defined as the length scale of the renewable groundwater storage, considering only the fluid phase underground. Since these length-scales account for the watershed-wide probability of the presence of renewable groundwater, they apply to both the 2D simulations and the real 3D watersheds to the degree that the 2D model parameters can accurately describe the 3D system. Thus, multiplying the $d_{equivalent}$ by the watershed area gives the volume of renewable groundwater under the assumption of topographically-driven groundwater systems.

Modeled estimates of $d_{effective}$ compared favorably with ^{3}H-based estimates of $d_{effective}$ for 30 major aquifers on Earth. Accounting for the sources of uncertainty in both analyses resulted in most aquifers having both a $V_{storage}$ and $d_{effective}$ that were within the uncertainty of the two methods, suggesting that the models were sufficiently characterizing the groundwater age fields with respect to the overall proportion of renewable groundwater in the systems. Additional similarity in the final proportion of renewable groundwater from the model analysis (6.2%) and the ^{3}H analysis (5.6%) also supported the relevance of the simulations. Together, the ^{3}H and numerical modeling approaches both agree remarkably well that roughly 6% of the groundwater in the upper 2 km of the crust is renewed over 50 years, with as little as 1% or as much as 20% when accounting for the uncertainty in the two analyses.

By estimating the distribution of renewable groundwater on the watershed scale, groundwater sustainability is addressed by subjecting this renewable groundwater storage to present-day pumping rates, yielding the lifespan of renewable groundwater. Using irrigation-related groundwater extractions, a majority (82.8%) of the world's irrigation

currently extracts groundwater at rates slower than groundwater is renewed. The remaining agricultural areas not only use groundwater unsustainably using the lifespan of renewable groundwater as the metric of sustainability, but half of these unsustainable practices rely significantly on groundwater for irrigation (> 25%). Thus, this analysis reveals that while modern groundwater provides a significant, sustainable water resource, groundwater extraction can rapidly and irreplaceably exhaust this storage. Indeed, the natural storage of 50 year old groundwater may have already been abstracted in areas with high groundwater consumption.

The renewability of groundwater depends upon the timescale of interest in addition to groundwater use practices. In this chapter, I introduce a new approach for quantifying physical groundwater renewability by determining the storage volume renewed over multiple timespans. By linking groundwater storage to a timescale of renewal, groundwater users can make more informed decisions on how to manage and regulate groundwater consumption. These users and managers can refer to the global distribution of renewable groundwater storage using a 50 year timescale and storage over longer timescales to get an estimate of their local groundwater resources.

Chapter 6:

Conclusion

Water of love, deep in the ground:
no water here to be found.
Someday, baby, when the river runs free,
it'll carry that water of love to me.

-from “Water of Love” by Dire Straits [1978]

6.1. Dissertation Summary

The purpose of my dissertation was to explore the storage and fluxes of groundwater within the framework of groundwater renewal. Inherent within this renewal are the inward and outward fluxes of water at the interface between groundwater systems and other components of the water cycle, primarily surface water bodies. Thus, my dissertation progressed from field measurements of groundwater flow in lacustrine and marine settings to a global, large-scale analysis of the storage of groundwater with a mean age of 50 years.

In Chapter 2, electrical geophysical measurements in three lakes in the Nebraska Sand Hills were used to delineate groundwater-lake water mixing in the lacustrine subsurface. The spatial patterns of electrical resistivity (ER) arose from differences in water salinity created by originally fresh groundwater mixing with evaporatively solute-laden lake water. The ER surveys imaged lateral transitions in subsurface ER across both Wilson and Gimlet Lakes, which were interpreted as groundwater flow-through lakes. A larger magnitude change in ER under Wilson Lake indicated longer lake water residence times than in Gimlet Lake due to more evaporation leading to higher salinities in the surface water. The lakebed ER pattern of Alkali Lake showed a systematic increase in ER with depth that suggested fresh groundwater discharges to the lake, but little to no groundwater

recharge occurs from Alkali Lake, as evaporation removes water mass and leads to solute accumulation in both the lake water and lakebed. Importantly, the spatial patterns of groundwater flow revealed by the ER surveys showed that these shallow lakes created hydraulic gradients that overprinted the regional groundwater system. Within the context of groundwater renewability, these shallow groundwater flow systems are below the resolution of the global analysis of renewable groundwater storage from Chapter 5, especially in the Nebraska Sand Hills where very few perennial streams exist. However, the lake-driven groundwater systems contain unaccounted for young groundwater, albeit of highly variable quality.

In Chapter 3, I investigated the influence of groundwater flow on heat transport in a sandy intertidal zone. The relatively stable temperatures of groundwater had been previously shown to be important for supporting coastal ecosystems, but I revealed how the hydrodynamics of the intertidal zone interact to create a thermal regime that can be buffered by groundwater. Using a beach on Rarotonga, I used ER surveys combined with temperature and water level measurements from the intertidal surface and subsurface to develop a conceptual model for how the subterranean thermal regimes were influenced by the hydrodynamics. In the upper foreshore, large variations in temperature were forced by swash infiltration and diel heating patterns. The remainder of the intertidal subsurface temperatures were controlled by conduction in the upper 10 cm of the sediment with groundwater setting temperatures below. Near a break in slope of the intertidal zone with ER surveys imaged fresher groundwater, cool and stable temperatures persisted. Beyond this change in slope, warm and stable temperatures were likely controlled by recirculated lagoon water. This study revealed the importance of groundwater flow on intertidal heat transport resulting from both terrestrial and marine forcings, and this study was the first to quantify both vertical and horizontal distributions of temperature in the subsurface of an

intertidal zone while quantifying the groundwater flow and sources. Moderating temperature dynamics in an intertidal zone represents a key ecosystem service of groundwater discharge that is dependent upon that groundwater being renewable. The perpetual replenishment of the supporting groundwater systems is required in order to sustain groundwater discharges at the coast. Thus, my contributions to the understanding the thermal regimes and hydrodynamics of the intertidal zone can be used to better constrain the importance of groundwater renewal to sustaining coastal habitats.

In Chapter 4, I expanded my analysis of groundwater features on Rarotonga to extend from the island interior and into the reef lagoon. ER surveys constrained differences in bulk electrical conductivity that arose from the subsurface geologic materials and changes in fluid conductivity. Building off of the intertidal work in Chapter 4, the ER surveys imaged the potential for low salinity porewater discharges into the reef lagoon up to 100 m offshore. On land, a classical freshwater lens with underlying saltwater were imaged near the coast, which paradoxically suggested low potential for groundwater discharges to occur far beyond shore. The potential for conduit flow into the lagoon may occur through or beneath basaltic rocks, based on applying terrestrial ER results over lava flows in addition to numerical simulations to estimate the expected ER signal of submarine, seawater-saturated basalts. Areas where the ER surveys imaged potential lava flows in the subsurface also correlated to parts of the lagoon where high groundwater discharge had been previously measured. Another result of the ER surveys in the lagoon showed a transition from more porous sub-lagoon materials to less porous materials, presumably all carbonates, approaching the reef crest and may represent the first application of geophysics to show differential diagenesis across a fringing reef system. Together, these ER surveys imaged patterns of fresh and saline groundwater within the complicating setting of geologic heterogeneity, which in turn controls the hydrogeologic properties for the interacting

marine and terrestrially-driven groundwater flow systems. Thus, with this ER investigation of the hydrogeology of coastal Rarotonga, I showed an example of the importance of studying coastal hydrological processes with a spatially well-constrained understanding of the local geology and geologic heterogeneity.

In Chapter 5, I developed a new framework for understanding the renewability of groundwater as a global resource by calculating a timescale associated with groundwater storage than can be chosen to address a problem of interest. For this analysis, I chose 50 years to cover a timespan that marks the turnover of human generations and the time-scale of many management planning and policy decisions. A colossal amount of data was assimilated to guide the development of numerical simulations of groundwater flow and age-as-mass applied at the resolution of small watersheds. The $d_{effective}$ and the $d_{equivalent}$ were introduced as two length-scales that describe the integrated groundwater storage over a given area, in this case a surface watershed. Multiplying $d_{equivalent}$ by the watershed area yielded the storage of young groundwater held beneath that watershed. By summing all of the ice-free watersheds on Earth, I estimated the global volume of groundwater younger than 50 years on average to be 1.41 million km^3 or 6.2% of the total groundwater storage to a depth of 2 km. Uncertainty in the permeability used in the models would change this estimate to 20.1% and 1.1% for an order of magnitude increase and decrease in permeability, respectively. A separate global analysis of tritium in groundwater samples included in the publication estimated 5.6% of groundwater to be young, again with large uncertainty (1-20%) arising from the uncertainty in the mixing and recharge models as well as the total volume of groundwater in the upper 2 km of the crust. Given the availability of two separate metrics of young groundwater storage, I compared the young groundwater storage in 30 aquifers using both a metric of renewable groundwater storage and estimates of renewable groundwater volumes, which showed general agreement between the

methods, given the uncertainties in both methods. The numerical simulations generally predicted less renewable groundwater than the tritium estimate. My simulations led to over-predicted global groundwater recharge rates using the average permeability scenarios, while decreasing the permeability an order of magnitude led to a global recharge rate that was lower than other previous estimates. Thus, the estimates of renewable groundwater storage for the average permeability scenario likely represents an upper limit on renewable groundwater both globally and for mainly the arid and mountainous regions of the world.

While the purpose of the fifth chapter was to quantify groundwater storage, the earlier chapters focused on characterizing and quantifying groundwater fluxes near surface water bodies. Groundwater fluxes to and from surface waters remain poorly constrained globally but are important for understanding issues of groundwater sustainability and groundwater responses to changing climate that were beyond the scope of the analysis of renewable groundwater.

6.2. FUTURE RESEARCH

Each of the chapters of this dissertation contribute to quantifying and characterizing groundwater flow and its effects on water quality and quantity at either the local or continental scale. In this section, I will share possible future research questions building off of this dissertation that are based both on the challenges that arose during the analyses and on the findings from these studies.

6.2.1. Groundwater age and groundwater renewal

Using the model outputs from the analysis in Chapter 5, I hope to explore, in more detail, the feedbacks between the different model parameters. The hydraulic gradient and the permeability distribution both control the potential for groundwater flow (i.e., Darcy's

Law) and therefore are the dominant drivers of the advection of groundwater age-as-mass. However, the large number of parameter combinations and spatial scales considered in this analysis, along with the depth-decaying permeability and porosity, provide a unique dataset of groundwater age fields that can be used to improve my understanding of groundwater age and groundwater renewability.

Building off of the estimation of groundwater storage over the past 10,000 years, I plan on constraining the potential for geochemical reactions to occur based on different reaction timescales. One of the end products of this study would allow me to estimate the mass of various solutes based on both the reaction rate and solubility. I would focus primarily on one-way dissolution reactions reaching chemical equilibrium and not allow precipitation to occur for at least this initial study.

I would also like to address and improve upon some of the simplifications in this analysis in future work. I hope to explore the effect of modeling real groundwater systems with 2D instead of 3D domains to better quantify the information lost and potential accuracy remaining when transforming from one dimensional system to the other. Also, introducing transience into the groundwater age models would begin to allow more accurate quantification of groundwater ages under the influence of changing climate. As an ultimate goal, I would like to model full 3D landscapes and mutli-scale groundwater flow with realistic groundwater-surface water interactions and boundary fluxes to solve for a more accurate global water table/potentiometric surface dataset and a spatially-cohesive groundwater age field.

6.2.2. Groundwater-surface water interactions

My work on coastal groundwater systems has shown that hydrogeologic spatial heterogeneity is likely the norm for most groundwater-surface water interactions,

especially in coastal settings. Despite this increasingly well-acknowledged importance of heterogeneity in the hydrologic sciences, much of my work is restricted to well-manicured transects of sensors and sampling that inherently rely on the assumption of lateral homogeneity. I intend to develop both geophysical and sampling studies that continue to advance my understanding of groundwater-surface water interactions in heterogeneous environments and at specific locations. I will then use these insights to develop numerical simulations that will constrain the hydrologic responses of both groundwater and surface water under different heterogeneity scenarios. I believe it is crucial for hydrologists to quantify 3D groundwater-surface water interactions through time.

6.3. BROADER DISSERTATION SIGNIFICANCE

My hope is that this dissertation and the time I spent at The University of Texas will serve to advance more than just the academic discipline of hydrogeology. Here I outline some of the ways I see my research informing research in other scientific disciplines, on specific societal concerns, and general perceptions on groundwater and water resources.

The focal topic of my dissertation is the renewability of groundwater, integrating the timescales of groundwater flow with smaller scale dynamics and patterns that its flow control. I hope my discussion of groundwater renewal, and the spatial variability of the storage of groundwaters recharged over different timespans, eventually leads to better groundwater literacy for the scientific community and the general public. I believe that associating a timescale with groundwater storage reiterates the fact that groundwater indeed flows. My quantification of groundwater storage volumes that are replenished over short to long timescales is a significant improvement to the common depiction of groundwater residence times spanning orders of magnitude without any sense of how much

groundwater is associated with a particular residence time. Therefore, my analysis of groundwater renewal initiates a new hydrogeologic endeavor to quantify groundwater as a temporally-relevant resource rather, than as one devoid of any connections to current groundwater or land use practices. My hope is that groundwater will be viewed as a resource with differing degrees of renewability based on hydrologic, geologic, and anthropogenic settings, even though I would argue that all groundwater systems are renewable to a certain degree over a long enough timespan.

My geophysical delineations of groundwater-surface water mixing patterns, and the potential for them, show the heterogeneity of this mixing and their dependence on the local geology. I hope that future studies of coastal hydrology, geochemistry, and ecology incorporate the insights from my work and strive to understand the various processes within the framework of complexity that arises from stratigraphy and geologic structures.

I hope that my research on Rarotonga can be used to understand the influence of groundwater discharges on the health of their coastal and reef ecosystems. I showed both the importance of groundwater discharges to the nearshore and foreshore sediment with connections to the temperature patterns in Chapter 3 and the larger scale potential for groundwater discharges in Chapter 4. While I think my ER surveys in the reef lagoon primarily depict the geologic framework for groundwater flow, and not fresh groundwater directly, the location and distribution of the carbonate and basaltic rocks in the reef may be crucial variables in both how and where groundwater enters the lagoon, affecting flowpaths and timescales that can carry unwanted contaminants to the lagoon.

6.4. CONCLUDING REMARKS

Is groundwater renewable? Is groundwater a renewable resource? If so, how much groundwater is renewable? These questions motivated my dissertation, and they will

continue to motivate my research in the future. I have learned that renewable is a controversial and ambiguous term, especially in relation to groundwater. Part of the problem with the term renewable or renewability is the potential for connecting the topic of the renewal (i.e., groundwater) with other processes that depend on its current manifestation (e.g., wetlands or rivers). Adding these connections into renewability can result in the conclusion that any consumption of groundwater is unsustainable, and all groundwater use damages its renewability. The counter argument can be made that all groundwater is renewable regardless of consumption as long as recharge continues to occur, even if that recharge is captured from other water sources. While any definition of groundwater renewability is acceptable and may be appropriate for a certain application, what it means for groundwater to be renewable must be clearly communicated within cross-discipline conversations and when reaching beyond the scientific community.

My use of groundwater renewability in this dissertation has been focused on an uncommon usage of renewability, one that arises from the physical renewal of groundwater and is free from assigning groundwater an economic or environmental value. However, water consumption or conservation is ultimately tied to both economics and environmental needs and has immense value. Thus, physical groundwater renewability, as I use the term, is the metric of how quickly groundwater can be replenished based on groundwater recharge and the physical properties of the subsurface. Also, by using steady state simulations of groundwater age, my analysis of groundwater renewal was restricted to pre-development conditions, where groundwater extractions could not alter flowpaths and groundwater residence times. The question now becomes: can physical groundwater renewability conceptually exist separate from the demand for or consumption of groundwater?

I now offer a perspective on what it means for groundwater to be renewable that was developed in collaboration with T.P. Gleeson (personal communication). To do this, I use an analogy: groundwater is physically renewable similar to how lumber is renewable. Just as trees grow at different rates due to species differences (e.g., bamboo vs. sequoia) or a multitude of environmental factors (e.g., soil thickness, water availability, solar intensity), groundwater flow rates are controlled by the integrated effects of the lithologic setting and adjoining hydrologic conditions. As numerous trees comprise a forest, a variety of hydrogeologic conditions can simultaneously control the flowpaths in a groundwater system, incorporating both heterogeneities and transience.

With these general similarities between groundwater and lumber, the extension to renewability can be made. Both lumber and groundwater can be extracted using different management strategies that control the degree of renewability, often weighing resource yields for environmental concerns. In this way, clear-cutting a forest is analogous to rampantly drawing down and depleting an aquifer. More minimalist approaches can be taken to reduce the environmental impacts of the resource consumption, but, given enough time left alone, both systems could return to a near original natural state. However, permanent damage can also be done to groundwater (e.g., compaction) just like forests (e.g., ecosystem shifts). What is currently lacking for many depleting groundwater systems is the timescale dependence of renewability that is built into forestry management practices, and this is what I hope to offer with my dissertation. Part of the added difficulty in managing groundwater is that it is "hidden" underground and operates over a wide range of timescales for a given system, whereas a forest of one tree species grows at more or less the same rate.

Another important lesson about groundwater renewability that can be learned from this analogy is that lumber is a renewable resource despite widespread human impacts and

management. I suggest groundwater is also physically renewable even though it may be stressed or contaminated. Thus, while groundwater can be degraded by human activities or as a result of climate change, all groundwater is physically renewable, though the degree to which it is renewable may change. Stated in a different way, aquifers are a renewable source of groundwater, but the renewability of groundwater as a resource is determined by the rates of withdrawals versus the rate of replenishment that depends on the aquifer properties and hydrologic conditions. The infinite physical renewability of groundwater that I refer to does not imply groundwater is infinitely available for consumption, as this is limited by both the economics of drilling deeper wells and potential changes in groundwater quality with depth.

While this tree analogy may elucidate some components of what makes groundwater renewable or nonrenewable as a resource, I think that groundwater renewability remains and should remain an open forum for debate and conversation between scientists, economists, governments, and the public. From the scientific perspective, groundwater storage and processes must continue to be quantified within the holistic network of hydrological, biological, geological, and chemical connections in which groundwater is an active participant. A better understanding of these connections can be used to address the full range of the implications of groundwater use and enlighten the value judgments required for sustainable management of groundwater resources.

As Chapters 2-4 show, understanding how groundwater connects to the surface of the Earth continues to hold many unknowns that are intimately tied to the ability to quantify hydrogeologic heterogeneity in space and through time. These fluxes and interactions at the surface control how groundwater systems respond to changing climate as well as retain remnants of previous climatic conditions. Moving forward, questions connecting groundwater flow to groundwater quantity and quality will lead to a better understanding

of the relevant spatiotemporal scales and hydrogeologic processes that dictate the feedbacks between groundwater and other earth surface and subsurface processes. Onward.

References

Al-Raei, A., K. Bosselmann, M. Böttcher, B. Hespenheide, and F. Tauber (2009), Seasonal dynamics of microbial sulfate reduction in temperate intertidal surface sediments: controls by temperature and organic matter, Ocean Dyn., 59(2), 351-370, doi: 10.1007/s10236-009-0186-5.

Alexander, M. D., and K. T. B. MacQuarrie (2005), The measurement of groundwater temperature in shallow piezometers and standpipes, Can. Geotech. J., 42(5), 1377-1390, doi: 10.1139/t05-061.

Alumbaugh, D., and G. Newman (2000), Image appraisal for 2-D and 3-D electromagnetic inversion, Geophysics, 65(5), 1455-1467, doi: 10.1190/1.1444834.

Amidu, S. A., and J. A. Dunbar (2008), An evaluation of the electrical-resistivity method for water-reservoir salinity studies, Geophysics, 73(4), G39-G49, doi: 10.1190/1.2938994.

Anschutz, P., T. Smith, A. Mouret, J. Deborde, S. Bujan, D. Poirier, and P. Lecroart (2009), Tidal sands as biogeochemical reactors, Estuar. Coast. Shelf Sci., 84(1), 84-90, doi: 10.1016/j.ecss.2009.06.015.

Archie, G. E. (1942), The electrical resistivity log as an aid in determining some reservoir characteristics, Trans. Am. Inst. Min. Metall. Eng., 146, 54-62.

Ataie-Ashtiani, B., R. E. Volker, and D. A. Lockington (1999), Tidal effects on sea water intrusion in unconfined aquifers, J. Hydrol., 216(1–2), 17-31, doi: 10.1016/s0022-1694(98)00275-3.

Badon-Ghyben, W. B. (1888), Nota in verband met de voorgenomen putboring nabil AmsterdamRep., 27 pp, Tijdschr. K. Inst. Ing., The Hague, The Netherlands.

Bailey, R. T., and J. W. Jenson (2013), Effects of Marine Overwash for Atoll Aquifers: Environmental and Human Factors, Ground Water, doi: 10.1111/gwat.12117.

Bauer, P., R. Supper, S. Zimmermann, and W. Kinzelbach (2006), Geoelectrical imaging of groundwater salinization in the Okavango Delta, Botswana, J. Appl. Geophys., 60(2), 126-141, doi: 10.1016/j.jappgeo.2006.01.003.

Bear, J. (1979), Hydraulics of groundwater, 544 pp., McGraw-Hill, New York.

Bear, J. (1979), Hydraulics of Groundwater, 569 pp., McGraw-Hill.

Befus, K. M., M. B. Cardenas, J. B. Ong, and V. A. Zlotnik (2012), Classification and delineation of groundwater–lake interactions in the Nebraska Sand Hills (USA) using electrical resistivity patterns, Hydrogeol. J., doi: 10.1007/s10040-012-0891-x.

Befus, K. M., M. B. Cardenas, D. V. Erler, I. R. Santos, and B. D. Eyre (2013), Heat transport dynamics at a sandy intertidal zone, Water Resour. Res., 49, 1-17, doi: 10.1002/wrcr.20325.

Bennett, D. M., S. C. Fritz, J. C. Holz, A. A. Holz, and V. A. Zlotnik (2007), Evaluating climatic and non-climatic influences on ion chemistry in natural and man-made lakes of Nebraska, USA, Hydrobiologia, 591, 103-115, doi: 10.1007/s10750-007-0798-z.

Bernabé, Y., U. Mok, and B. Evans (2003), Permeability-porosity Relationships in Rocks Subjected to Various Evolution Processes, Pure Appl. Geophys., 160(5-6), 937-960, doi: 10.1007/PL00012574.

Bethke, C. M., and T. M. Johnson (2008), Groundwater Age and Groundwater Age Dating, Annual Review of Earth and Planetary Sciences, 36(1), 121-152, doi: 10.1146/annurev.earth.36.031207.124210.

Birt, M. J., and I. R. Tibbetts (2007), Temperature changes in the tidal excursion front and surface sediment of a subtropical mudflat in autumn, J. Sea Res., 58(2), 113-119, doi: 10.1016/j.seares.2007.03.003.

Blanchard, G. F., J. M. Guarini, P. Richard, P. Gros, and F. Mornet (1996), Quantifying the short-term temperature effect on light-saturated photosynthesis of intertidal microphytobenthos, Marine Ecology Progress Series, 134, 309-313, doi: 10.3354/meps134309.

Born, S. M., S. A. Smith, and D. A. Stephenson (1979), Hydrogeology of glacial-terrain lakes, with management and planning applications, J. Hydrol., 43(1-4), 7-43, doi: 10.1016/0022-1694(79)90163-x.

Bratton, J. F. (2010), The Three Scales of Submarine Groundwater Flow and Discharge across Passive Continental Margins, The Journal of Geology, 118(5), 565-575, doi: 10.1086/655114.

Bredehoeft, J. (1997), Safe Yield and the Water Budget Myth, Ground Water, 35(6), 929-929, doi: 10.1111/j.1745-6584.1997.tb00162.x.

Bredehoeft, J. D. (2002), The Water Budget Myth Revisited: Why Hydrogeologists Model, Ground Water, 40(4), 340-345, doi: 10.1111/j.1745-6584.2002.tb02511.x.

Breier, J. A., C. F. Breier, and H. N. Edmonds (2005), Detecting submarine groundwater discharge with synoptic surveys of sediment resistivity, radium, and salinity, Geophys. Res. Lett., 32(23), L23612, doi: 10.1029/2005gl024639.

Burnett, W. C., H. Bokuniewicz, M. Huettel, W. S. Moore, and M. Taniguchi (2003), Groundwater and pore water inputs to the coastal zone, Biogeochemistry, 66(1-2), 3-33, doi: 10.1023/B:BIOG.0000006066.21240.53.

Butler, S. L., and G. Sinha (2012), Forward modeling of applied geophysics methods using Comsol and comparison with analytical and laboratory analog models, Comput. Geosci., 42, 168-176, doi: 10.1016/j.cageo.2011.08.022.

Cardenas, M. B. (2008), Surface water-groundwater interface geomorphology leads to scaling of residence times, Geophys. Res. Lett., 35(8), -, doi: 10.1029/2008gl033753.

Cardenas, M. B. (2010), Thermal skin effect of pipes in streambeds and its implications on groundwater flux estimation using diurnal temperature signals, Water Resour. Res., 46, doi: 10.1029/2009wr008528.

Cardenas, M. B., and X. W. Jiang (2010), Groundwater flow, transport, and residence times through topography-driven basins with exponentially decreasing permeability and porosity, Water Resour. Res., 46, doi: 10.1029/2010wr009370.

Cardenas, M. B., and H. Jiang (2011), Wave-driven porewater and solute circulation through rippled elastic sediment under highly transient forcing, Limnology & Oceanography: Fluids & Environment, doi: 10.1215/21573698-1151658.

Cardenas, M. B., and M. S. Markowski (2011), Geoelectrical Imaging of Hyporheic Exchange and Mixing of River Water and Groundwater in a Large Regulated River, Environmental Science & Technology, 45(4), 1407-1411, doi: 10.1021/es103438a.

Cardenas, M. B., J. L. Wilson, and R. Haggerty (2008), Residence time of bedform-driven hyporheic exchange, Adv. Water Resour., 31(10), 1382-1386, doi: 10.1016/j.advwatres.2008.07.006.

Cardenas, M. B., P. B. Zamora, F. P. Siringan, M. R. Lapus, R. S. Rodolfo, G. S. Jacinto, M. L. San Diego-McGlone, C. L. Villanoy, O. Cabrera, and M. I. Senal (2010), Linking regional sources and pathways for submarine groundwater discharge at a reef by electrical resistivity tomography, Rn-222, and salinity measurements, Geophys. Res. Lett., 37, L16401, doi: 10.1029/2010gl044066.

Carson, R. (1955), The Marginal World, in The edge of the sea, edited, p. 276, Houghton Mifflin, New York.

Charette, M. A., and E. R. Sholkovitz (2006), Trace element cycling in a subterranean estuary: Part 2. Geochemistry of the pore water, Geochim. Cosmochim. Acta, 70(4), 811-826, doi: 10.1016/j.gca.2005.10.019.

Chebotarev, I. I. (1955), Metamorphism of natural waters in the crust of weathering—1, Geochim. Cosmochim. Acta, 8(1–2), 22-48, doi: 10.1016/0016-7037(55)90015-6.

Cho, Y.-K., T.-W. Kim, K.-W. You, L.-H. Park, H.-T. Moon, S.-H. Lee, and Y.-H. Youn (2005), Temporal and spatial variabilities in the sediment temperature on the Baeksu tidal flat, Korea, Estuar. Coast. Shelf Sci., 65(1-2), 302-308, doi: 10.1016/j.ecss.2005.06.010.

Clément, R., M. Descloitres, T. Günther, O. Ribolzi, and A. Legchenko (2009), Influence of shallow infiltration on time-lapse ERT: Experience of advanced interpretation, C.R. Geosci., 341(10-11), 886-898, doi: 10.1016/j.crte.2009.07.005.

Coleridge, S. T. (1798), The rime of the ancyent marinere, in Lyrical ballads: with a few other poems, edited, pp. 1-52, J. and A. Arch, London.

Council, N. R. (1986), Global hydrologic cycle, in Global change in the geosphere-biosphere: initial priorities for an IGBP, edited, pp. 72-82, National Academy Press, Washington, D.C.

Cyronak, T., I. R. Santos, D. V. Erler, and B. D. Eyre (2012), Groundwater and porewater as a major source of alkalinity to a fringing coral reef lagoon (Muri Lagoon, Cook Islands), Biogeosciences Discuss., 9(11), 15501-15540, doi: 10.5194/bgd-9-15501-2012.

Cyronak, T., I. R. Santos, A. McMahon, and B. D. Eyre (2013), Carbon cycling hysteresis in permeable carbonate sands over a diel cycle: Implications for ocean acidification, Limnol. Oceanogr., 58(1), 131-143, doi: 10.4319/lo.2013.58.1.0131.

Dale, R. K. (2006), Salinity, temperature, and macroinfaunal communities in groundwater seeps, M.S. dissertation thesis, 198 pp, University of Delaware.

Dale, R. K., and D. C. Miller (2007), Spatial and temporal patterns of salinity and temperature at an intertidal groundwater seep, Estuar. Coast. Shelf Sci., 72(1-2), 283-298, doi: 10.1016/j.ecss.2006.10.024.

Dale, R. K., and D. C. Miller (2008), Hydrologic interactions of infaunal polychaetes and intertidal groundwater discharge, Marine Ecology Progress Series, 363, 205-215, doi: 10.3354/meps07455.

Danielson, J., and D. Gesch (2011), Global multi-resolution terrain elevation data 2010 (GMTED2010)Rep., 26 pp.

Day-Lewis, F. D., and J. W. Lane (2004), Assessing the resolution-dependent utility of tomograms for geostatistics, Geophys. Res. Lett., 31(7), doi: 10.1029/2004gl019617.

Day-Lewis, F. D., K. Singha, and A. M. Binley (2005), Applying petrophysical models to radar travel time and electrical resistivity tomograms: Resolution-dependent limitations, Journal of Geophysical Research-Solid Earth, 110(B8), doi: 10.1029/2004jb003569.

Day-Lewis, F. D., E. A. White, C. D. Johnson, J. W. J. Lane, and M. Belaval (2006), Continuous resistivity profiling to delineate submarine groundwater discharge - examples and limitations, The Leading Edge, 25(6), 724-728, doi: 10.1190/1.2210056.

Decho, A. W. (2000), Microbial biofilms in intertidal systems: an overview, Cont. Shelf Res., 20(10-11), 1257-1273, doi: 10.1016/s0278-4343(00)00022-4.

Development, W. C. o. E. a. (1987), Our common future, Oxford University Press, New York, NY.

Dimova, N. T., P. W. Swarzenski, H. Dulaiova, and C. R. Glenn (2012), Utilizing multichannel electrical resistivity methods to examine the dynamics of the fresh water-seawater interface in two Hawaiian groundwater systems, J. Geophys. Res., 117(C2), C02012, doi: 10.1029/2011jc007509.

Döll, P., and K. Fiedler (2008), Global-scale modeling of groundwater recharge, Hydrol. Earth Syst. Sci., 12(3), 863-885, doi: 10.5194/hess-12-863-2008.

Döll, P., B. Lehner, and F. Kaspar (2002), Global modeling of groundwater recharge, paper presented at Third International Conference on Water Resources and the Environment Research, Technical University of Dresden, Germany.

Dose, E. J., L. Stoeckl, G. J. Houben, H. L. Vacher, S. Vassolo, J. Dietrich, and T. Himmelsbach (2013), Experiments and modeling of freshwater lenses in layered aquifers: steady state interface geometry, J. Hydrol., doi: 10.1016/j.jhydrol.2013.10.010.

Ehrenberg, S. N., and P. H. Nadeau (2005), Sandstone vs. carbonate petroleum reservoirs: A global perspective on porosity-depth and porosity-permeability relationships, AAPG Bull., 89(4), 435-445, doi: 10.1306/11230404071.

Emery, D., and K. Myers (2009), Sequence Stratigraphy, 297 pp., Blackwell Publishing, Oxford, UK.

Erler, D. V., I. R. Santos, Y. Zhang, D. R. Tait, K. M. Befus, A. Hidden, L. Li, and B. D. Eyre (2014), Nitrogen transformations within a tropical subterranean estuary, Mar. Chem., 164(0), 38-47, doi: 10.1016/j.marchem.2014.05.008.

Evans, R. L. (2003), Geophysical evidence for karst formation associated with offshore groundwater transport: An example from North Carolina, Geochem. Geophys. Geosyst., 4(8), doi: 10.1029/2003gc000510.

Evans, R. L., and D. Lizarralde (2011), The competing impacts of geology and groundwater on electrical resistivity around Wrightsville Beach, NC, Cont. Shelf Res., 31(7-8), 841-848, doi: 10.1016/j.csr.2011.02.008.

Ewing, R. P., and A. G. Hunt (2006), Dependence of the Electrical Conductivity on Saturation in Real Porous Media, Vadose Zone J., 5(2), 731-741, doi: 10.2136/vzj2005.0107.

Fan, Y., H. Li, and G. Miguez-Macho (2013), Global Patterns of Groundwater Table Depth, Science, 339(6122), 940-943, doi: 10.1126/science.1229881.

Fenchel, T. M., and R. J. Riedl (1970), The sulfide system: a new biotic community underneath the oxidized layer of marine sand bottoms, Mar. Biol., 7(3), 255-268, doi: 10.1007/bf00367496.

Ferguson, G., and T. Gleeson (2012), Vulnerability of coastal aquifers to groundwater use and climate change, Nature Clim. Change, 2(5), 342-345, doi: 10.1038/nclimate1413.

Fogg, G. E., E. M. Labolle, and G. S. Weissmann (1999), Groundwater Vulnerability Assessment: Hydrogeologic Perspective and Example from Salinas Valley, California, in Assessment of Non-Point Source Pollution in the Vadose Zone, edited, pp. 45-61, American Geophysical Union.

Ford, D., and P. D. Williams (2007), Karst hydrogeology and geomorphology, John Wiley & Sons, West Sussex, England.

Frape, S. K., A. Blyth, R. Blomqvist, R. H. McNutt, and M. Gascoyne (2003), Deep Fluids in the Continents: II. Crystalline Rocks, in Treatise on Geochemistry, edited by H. D. Turekian and K. K. Holland, pp. 541-580, Pergamon, Oxford.

Garmonov, I. V., A. A. Konoplyantsev, and N. P. Lushnikova (1974), Water storage in the upper part of the earth's crust, in The World Water Balance and Water Resources of the Earth, edited by K. I. Korzun, pp. 48-50, Hydrometeoizdat, Leningrad.

Gassiat, C., T. Gleeson, and E. Luijendijk (2013), The location of old groundwater in hydrogeologic basins and layered aquifer systems, Geophys. Res. Lett., 40(12), 3042-3047, doi: 10.1002/grl.50599.

Gibbes, B., C. Robinson, H. Carey, L. Li, and D. Lockington (2008a), Tidally driven pore water exchange in offshore intertidal sandbanks: Part I. Field measurements, Estuar. Coast. Shelf Sci., 79(1), 121-132, doi: 10.1016/j.ecss.2008.03.021.

Gibbes, B., C. Robinson, L. Li, D. Lockington, and H. Li (2008b), Tidally driven pore water exchange within offshore intertidal sandbanks: Part II numerical simulations, Estuar. Coast. Shelf Sci., 80(4), 472-482, doi: 10.1016/j.ecss.2008.08.021.

Ginn, T. R. (1999), On the distribution of multicomponent mixtures over generalized exposure time in subsurface flow and reactive transport: Foundations, and formulations for groundwater age, chemical heterogeneity, and biodegradation, Water Resour. Res., 35(5), 1395-1407, doi: 10.1029/1999WR900013.

Gleeson, T., L. Marklund, L. Smith, and A. H. Manning (2011), Classifying the water table at regional to continental scales, Geophys. Res. Lett., 38(5), doi: 10.1029/2010gl046427.

Gleeson, T., N. Moosdorf, J. Hartmann, and L. P. H. van Beek (2014), A glimpse beneath earth's surface: GLobal HYdrogeology MaPS (GLHYMPS) of permeability and porosity, Geophys. Res. Lett., 2014GL059856, doi: 10.1002/2014GL059856.

Gleeson, T. P., Y. Wada, M. F. Bierkens, and L. P. van Beek (2012), Water balance of global aquifers revealed by groundwater footprint, Nature, 488(7410), 197-200, doi: 10.1038/nature11295.

Gleeson, T. P., K. M. Befus, S. Jasechko, E. Luijendijk, and M. B. Cardenas (submitted), The global volume, distribution, and lifespan of modern groundwater.

Glover, R. (1959), The pattern of fresh-water flow in a coastal aquifer, J. Geophys. Res., 64(4), 457-459, doi: 10.1029/JZ064i004p00457.

Gomez, J. D., and J. L. Wilson (2013), Age distributions and dynamically changing hydrologic systems: Exploring topography-driven flow, Water Resour. Res., 49(3), 1503-1522, doi: 10.1002/wrcr.20127.

Gomez, J. D., J. L. Wilson, and M. B. Cardenas (2012), Residence time distributions in sinuosity-driven hyporheic zones and their biogeochemical effects, Water Resour. Res., 48(9), W09533, doi: 10.1029/2012WR012180.

Gonneea, M. E., A. E. Mulligan, and M. A. Charette (2013), Climate-driven sea level anomalies modulate coastal groundwater dynamics and discharge, Geophys. Res. Lett., 40(11), 2701-2706, doi: 10.1002/grl.50192.

Goode, D. J. (1996), Direct Simulation of Groundwater Age, Water Resour. Res., 32(2), 289-296, doi: 10.1029/95wr03401.

Gosselin, D. C., S. Sibray, and J. Ayers (1994), Geochemistry of K-rich alkaline lakes, Western Sandhills, Nebraska, USA, Geochim Cosmochim Ac, 58(5), 1403-1418, doi: 10.1016/0016-7037(94)90545-2.

Grant, J. (1986), Sensitivity of benthic community respiration and primary production to changes in temperature and light, Mar. Biol., 90(2), 299-306, doi: 10.1007/bf00569142.

Haitjema, H. M., and S. Mitchell-Bruker (2005), Are Water Tables a Subdued Replica of the Topography?, Ground Water, 43(6), 781-786, doi: 10.1111/j.1745-6584.2005.00090.x.

Harley, C. D. G., and B. S. T. Helmuth (2003), Local- and Regional-Scale Effects of Wave Exposure, Thermal Stress, and Absolute versus Effective Shore Level on Patterns of Intertidal Zonation, Limnol. Oceanogr., 48(4), 1498-1508, doi: 10.4319/lo.2003.48.4.1498.

Harrison, S. J., and A. P. Phizacklea (1987), Temperature fluctuation in muddy intertidal sediments, Forth Estuary, Scotland, Estuar. Coast. Shelf Sci., 24(2), 279-288, doi: 10.1016/0272-7714(87)90070-9.

Harrison, S. J., and P. Morrison (1993), Temperatures in a Sandy Beach Under Strong Solar Heating: Patara Beach, Turkey, Estuar. Coast. Shelf Sci., 37(1), 89-97, doi: 10.1006/ecss.1993.1043.

Hatch, C. E., A. T. Fisher, J. S. Revenaugh, J. Constantz, and C. Ruehl (2006), Quantifying surface water–groundwater interactions using time series analysis of streambed thermal records: Method development, Water Resour. Res., 42(10), doi: 10.1029/2005wr004787.

Hayashi, M. (2004), Temperature-Electrical Conductivity Relation of Water for Environmental Monitoring and Geophysical Data Inversion, Environ. Monit. Assess., 96(1), 119-128, doi: 10.1023/b:emas.0000031719.83065.68.

Hayley, K., L. R. Bentley, M. Gharibi, and M. Nightingale (2007), Low temperature dependence of electrical resistivity: Implications for near surface geophysical monitoring, Geophys. Res. Lett., 34(18), doi: 10.1029/2007gl031124.

Heads, T. (1980), Once in a lifetime, in Remain in light, edited, Sire Records, New York.

Hein, J. R., S. C. Gray, and B. M. Richmond (2004), Geology and hydrogeology of the Cook Islands, in Geology and hydrogeology of carbonate islands, edited by H. L. Vacher and T. M. Quinn, pp. 503-535, Elsevier Science, Amsterdam, The Netherlands.

Heiss, J. (2011), Intertidal mixing zone dynamics and swash induced infiltration in a sandy beach aquifer, Cape Henlopen, Delaware, 99 pp, University of Delaware.

Helmuth, B. S. T., and G. E. Hofmann (2001), Microhabitats, Thermal Heterogeneity, and Patterns of Physiological Stress in the Rocky Intertidal Zone, Biological Bulletin, 201(3), 374-384.

Hemond, H. F., W. K. Nuttle, R. W. Burke, and K. D. Stolzenbach (1984), Surface Infiltration in Salt Marshes: Theory, Measurement, and Biogeochemical Implications, Water Resour. Res., 20(5), 591-600, doi: 10.1029/WR020i005p00591.

Henderson, R. D., F. D. Day-Lewis, E. Abarca, C. F. Harvey, H. N. Karam, L. B. Liu, and J. W. Lane (2010), Marine electrical resistivity imaging of submarine groundwater discharge: sensitivity analysis and application in Waquoit Bay, Massachusetts, USA, Hydrogeol. J., 18(1), 173-185, doi: 10.1007/s10040-009-0498-z.

Herzberg, A. (1901), Die wasserversorgung einiger Nordseebader, J. Gasbeleucht Wasserversorg., 44, 815–819.

Horn, D. P. (2002), Beach groundwater dynamics, Geomorphology, 48(1-3), 121-146, doi: 10.1016/s0169-555x(02)00178-2.

Jackson, P. D., K. B. Briggs, R. C. Flint, R. J. Holyer, and J. C. Sandidge (2002), Two- and three-dimensional heterogeneity in carbonate sediments using resistivity imaging, Mar. Geol., 182(1-2), 55-76, doi: 10.1016/S0025-3227(01)00228-6.

Jeng, D. S., D. A. Barry, B. R. Seymour, P. Dong, and L. Li (2005), Two-dimensional approximation for tide-induced watertable fluctuations in a sloping sandy beach, Adv. Water Resour., 28(10), 1040-1047, doi: 10.1016/j.advwatres.2004.06.002.

Jiang, X.-W., L. Wan, X.-S. Wang, S. Ge, and J. Liu (2009), Effect of exponential decay in hydraulic conductivity with depth on regional groundwater flow, Geophys. Res. Lett., 36(24), L24402, doi: 10.1029/2009GL041251.

Jiang, X.-W., L. Wan, M. B. Cardenas, S. Ge, and X.-S. Wang (2010), Simultaneous rejuvenation and aging of groundwater in basins due to depth-decaying hydraulic conductivity and porosity, Geophys. Res. Lett., 37(5), doi: 10.1029/2010gl042387.

Jickells, T. D. (1998), Nutrient Biogeochemistry of the Coastal Zone, Science, 281(5374), 217-222, doi: 10.1126/science.281.5374.217.

Keery, J., A. Binley, N. Crook, and J. W. N. Smith (2007), Temporal and spatial variability of groundwater–surface water fluxes: Development and application of an analytical method using temperature time series, J. Hydrol., 336(1-2), 1-16, doi: 10.1016/j.jhydrol.2006.12.003.

Keller, G. V., and F. C. Frischknect (1966), Electrical methods in geophysical prospecting, 517 pp., Pergamon Press, Inc, Oxford.

Kharaka, Y. K., and J. S. Hanor (2003), Deep Fluids in the Continents: I. Sedimentary Basins, in Treatise on Geochemistry, edited by H. D. Turekian and K. K. Holland, pp. 1-48, Pergamon, Oxford.

King, J., A. Mehta, and R. Dean (2010), Analytical models for the groundwater tidal prism and associated benthic water flux, Hydrogeol. J., 18(1), 203-215, doi: 10.1007/s10040-009-0519-y.

Kipling, R. (1903), Sussex, in The Five Nations, edited, pp. 69-73, Methuen and Co., London.

Kirkham, D. (1967), Explanation of paradoxes in Dupuit-Forchheimer Seepage Theory, Water Resour. Res., 3(2), 609-622, doi: 10.1029/WR003i002p00609.

Konikow, L. F., M. Akhavan, C. D. Langevin, H. A. Michael, and A. H. Sawyer (2013), Seawater circulation in sediments driven by interactions between seabed topography and fluid density, Water Resour. Res., 49(3), 1386-1399, doi: 10.1002/wrcr.20121.

Kroeger, K. D., and M. A. Charette (2008), Nitrogen biogeochemistry of submarine groundwater discharge, Limnol. Oceanogr., 53(3), 1025-1039, doi: 10.4319/lo.2008.53.3.1025.

Kuan, W. K., G. Jin, P. Xin, C. Robinson, B. Gibbes, and L. Li (2012), Tidal influence on seawater intrusion in unconfined coastal aquifers, Water Resour. Res., 48(2), W02502, doi: 10.1029/2011wr010678.

Kwon, E. Y., G. Kim, F. Primeau, W. S. Moore, H.-M. Cho, T. DeVries, J. L. Sarmiento, M. A. Charette, and Y.-K. Cho (2014), Global estimate of submarine groundwater discharge based on an observationally constrained radium isotope model, Geophys. Res. Lett., 2014GL061574, doi: 10.1002/2014GL061574.

L'Vovich, M. I. (1974), World Water Resources and their Future, edited by R. L. Nace, pp. 13-23, American Geophysical Union.

Labaugh, J. W. (1986), Limnological characteristics of selected lakes in the Nebraska Sandhills, USA, and their relation to chemical characteristics of adjacent groundwater, J. Hydrol., 86(3-4), 279-298, doi: 10.1016/0022-1694(86)90168-x.

Lanyon, J. A., I. G. Eliot, and D. J. Clarke (1982), Groundwater-level variation during semidiurnal spring tidal cycles on a sandy beach, Marine and Freshwater Research, 33(3), 377-400, doi: 10.1071/MF9820377.

Lehner, B., K. Verdin, and A. Jarvis (2008), New Global Hydrography Derived From Spaceborne Elevation Data, Eos Trans. AGU, 89(10), 93-94, doi: 10.1029/2008EO100001.

Leland, W. P., and W. D. Hummon (1971), Cyclic Changes in Interstitial Water Content, Atmospheric Exposure, and Temperature in a Marine Beach, Limnol. Oceanogr., 16(3), 522-535, doi: 10.4319/lo.1971.16.3.0522.

Lenkopane, M., A. D. Werner, D. A. Lockington, and L. Li (2009), Influence of variable salinity conditions in a tidal creek on riparian groundwater flow and salinity dynamics, J. Hydrol., 375(3-4), 536-545, doi: 10.1016/j.jhydrol.2009.07.004.

Leslie, D. (1980), Soils of Rarotonga, Cook Islands, 70 pp., New Zealand Soil Bureau, Wellington, NZ.

Li, L., and D. A. Barry (2000), Wave-induced beach groundwater flow, Adv. Water Resour., 23(4), 325-337, doi: 10.1016/s0309-1708(99)00032-9.

Li, L., D. A. Barry, and C. B. Pattiaratchi (1997), Numerical modelling of tide-induced beach water table fluctuations, Coastal Eng., 30(1-2), 105-123, doi: 10.1016/s0378-3839(96)00038-5.

Li, L., D. A. Barry, F. Stagnitti, J. Y. Parlange, and D. S. Jeng (2000), Beach water table fluctuations due to spring-neap tides: moving boundary effects, Adv. Water Resour., 23(8), 817-824, doi: 10.1016/s0309-1708(00)00017-8.

Li, X., B. X. Hu, W. C. Burnett, I. R. Santos, and J. P. Chanton (2009), Submarine ground water discharge driven by tidal pumping in a heterogeneous aquifer, Ground Water, 47(4), 558-568, doi: 10.1111/j.1745-6584.2009.00563.x.

Loke, M. H., and R. D. Barker (1996), Rapid least-squares inversion of apparent resistivity pseudosections by a quasi-Newton method, Geophys. Prospect., 44(1), 131-152, doi: 10.1111/j.1365-2478.1996.tb00142.x.

Loke, M. H., and J. W. Lane (2004), Inversion of data from electrical resistivity imaging surveys in water-covered areas, Explor. Geophys., 35(4), 266-271, doi: 10.1071/EG04266.

Loke, M. H., J. E. Chambers, D. F. Rucker, O. Kuras, and P. B. Wilkinson (2013), Recent developments in the direct-current geoelectrical imaging method, J. Appl. Geophys., 95, 135-156, doi: 10.1016/j.jappgeo.2013.02.017.

Loope, D. B., J. B. Swinehart, and J. P. Mason (1995), Dune-dammed paleovalleys of the Nebraska Sand Hills: Intrinsic versus climatic controls on the accumulation of lake and marsh sediments, Geol. Soc. Am. Bull., 107(4), 396-406, doi: 10.1130/0016-7606(1995)107<0396:DDPOTN>2.3.CO;2

Lu, C., Y. Chen, C. Zhang, and J. Luo (2013), Steady-state freshwater–seawater mixing zone in stratified coastal aquifers, J. Hydrol., 505, 24-34, doi: 10.1016/j.jhydrol.2013.09.017.

Maji, R., and L. Smith (2009), Quantitative analysis of seabed mixing and intertidal zone discharge in coastal aquifers, Water Resour. Res., 45(11), W11401, doi: 10.1029/2008wr007532.

Manheim, F. T., D. E. Krantz, and J. F. Bratton (2004), Studying Ground Water Under Delmarva Coastal Bays Using Electrical Resistivity, Ground Water, 42(7), 1052-1068, doi: 10.1111/j.1745-6584.2004.tb02643.x.

Mansoor, N., and L. Slater (2007), Aquatic electrical resistivity imaging of shallow-water wetlands, Geophysics, 72(5), F211-F221, doi: 10.1190/1.2750667.

McCallum, J. L., P. G. Cook, C. T. Simmons, and A. D. Werner (2014), Bias of Apparent Tracer Ages in Heterogeneous Environments, Groundwater, 52(2), 239-250, doi: 10.1111/gwat.12052.

McLachlan, A. (1983), Sandy beach ecology - a review, in Developments in Hydrobiology: Sandy Beaches as Ecosystems, edited by A. McLachlan and T. Erasmus, pp. 321-380, DR W. Junk, The Hague, The Netherlands.

McLachlan, A., and I. Turner (1994), The Interstitial Environment of Sandy Beaches, Marine Ecology, 15(3-4), 177-212, doi: 10.1111/j.1439-0485.1994.tb00053.x.

Michael, H. A., A. E. Mulligan, and C. F. Harvey (2005), Seasonal oscillations in water exchange between aquifers and the coastal ocean, Nature, 436(7054), 1145-1148, doi: 10.1038/nature03935.

Miller, D. C., and W. J. Ullman (2004), Ecological Consequences of Ground Water Discharge to Delaware Bay, United States, Ground Water, 42(7), 959-970, doi: 10.1111/j.1745-6584.2004.tb02635.x.

Mink, J. F., and H. L. Vacher (2004), Hydrogeology of Northern Guam, in Geology and hydrogeology of carbonate islands, edited by H. L. Vacher and T. M. Quinn, pp. 743-761, Elsevier Science, Burlington.

Misonou, T., H. Asaue, T. Yoshinaga, Y. Matsukuma, K. Koike, and J. Shimada (2013), Hydrogeologic-structure and groundwater-movement imaging in tideland using electrical sounding resistivity: a case study on the Ariake Sea coast, southwest Japan, Hydrogeol. J., 21(7), 1593-1603, doi: 10.1007/s10040-013-1022-z.

Mitbavkar, S., and A. C. Anil (2005), Diatoms of the microphytobenthic community in a tropical intertidal sand flat influenced by monsoons: spatial and temporal variations, Mar. Biol., 148(4), 693-709, doi: 10.1007/s00227-005-0112-4.

Montaggioni, L. F., and C. J. R. Braithwaite (2009), Reef Hydrogeology, in Dev. Mar. Geol., edited by L. F. Montaggioni and C. J. R. Braithwaite, pp. 271-321, Elsevier, Amsterdam, The Netherlands.

Moore, C. H. (2001), Carbonate reservoirs: porosity evolution and diagenesis in a sequence stratigraphic framework, 461 pp., Elsevier, Amsterdam, The Netherlands.

Moore, W. S. (1999), The subterranean estuary: a reaction zone of ground water and sea water, Mar. Chem., 65(1-2), 111-125, doi: 10.1016/S0304-4203(99)00014-6.

Moore, W. S., and A. M. Wilson (2005), Advective flow through the upper continental shelf driven by storms, buoyancy, and submarine groundwater discharge, Earth Planet. Sci. Lett., 235(3-4), 564-576, doi: 10.1016/j.epsl.2005.04.043.

Morelissen, B., and C. D. G. Harley (2007), The effects of temperature on producers, consumers, and plant–herbivore interactions in an intertidal community, Journal of Experimental Marine Biology and Ecology, 348(1-2), 162-173, doi: 10.1016/j.jembe.2007.04.006.

Moriwaki, H., M. Chikamori, M. Okuno, and T. Nakamura (2006), Holocene changes in sea level and coastal environments on Rarotonga, Cook Islands, South Pacific Ocean, Holocene, 16(6), 839-848, doi: 10.1191/0959683606hol976rp.

Mylroie, J., and H. Vacher (1999), A conceptual view of carbonate island karst, in Karst Modeling, edited by A. N. Palmer, M. V. Palmer and I. D. Sasowsky, pp. 48-57, Karst Waters Institute, Inc, Charles Town, WV.

Nace, R. L. (1969), World water inventory and control, in Water, earth, and man: a synthesis of hydrology, geomorphology, and socio-economic geography, edited by R. J. Chorley, pp. 31-42, Methuen and Co. Ltd., London.

Nace, R. L. (Ed.) (1971), Scientific framework of world water balance, 27 pp., UNESCO Tech. Papers Hydrol.

Nakada, S., J. Yasumoto, M. Taniguchi, and T. Ishitobi (2011), Submarine groundwater discharge and seawater circulation in a subterranean estuary beneath a tidal flat, Hydrol. Process., 25(17), 2755-2763, doi: 10.1002/hyp.8016.

Nielsen, P. (1990), Tidal dynamics of the water table in beaches, Water Resour. Res., 26(9), 2127-2134, doi: 10.1029/WR026i009p02127.

Nyquist, J. E., M. J. Heaney, and L. Toran (2009), Characterizing lakebed seepage and geologic heterogeneity using resistivity imaging and temperature measurements, Near Surf. Geophys., 7(5-6), 487-498, doi: 10.3997/1873-0604.2009022.

Ochsner, T. E., R. Horton, and T. Ren (2001), A New Perspective on Soil Thermal Properties, Soil Sci. Soc. Am. J., 65(6), 1641-1647.

Ogilvy, R., P. Meldrum, O. Kuras, P. Wilkinson, J. Chambers, M. Sen, A. Pulido-Bosch, J. Gisbert, S. Jorreto, and I. Frances (2009), Automated monitoring of coastal aquifers with electrical resistivity tomography, Near Surf. Geophys., 7(5-6), 367-375, doi: 10.3997/1873-0604.2009027.

Oki, T., and S. Kanae (2006), Global Hydrological Cycles and World Water Resources, Science, 313(5790), 1068-1072, doi: 10.1126/science.1128845.

Ong, J. B. (2010), Investigation of spatial and temporal processes of lake-aquifer interactions in the Nebraska Sand Hills, Univ. of Nebraska-Lincoln, USA.

Ong, J. B., and V. A. Zlotnik (2011), Assessing Lakebed Hydraulic Conductivity and Seepage Flux by Potentiomanometer, Ground Water, 49(2), 270-274, doi: 10.1111/j.1745-6584.2010.00717.x.

Ong, J. B., J. W. Lane, V. A. Zlotnik, T. Halihan, and E. A. White (2010), Combined use of frequency-domain electromagnetic and electrical resistivity surveys to delineate near-lake groundwater flow in the semi-arid Nebraska Sand Hills, USA, Hydrogeol. J., 18(6), 1539-1545, doi: 10.1007/s10040-010-0617-x.

Orlando, L. (2013), Some considerations on electrical resistivity imaging for characterization of waterbed sediments, J. Appl. Geophys., doi: 10.1016/j.jappgeo.2013.05.005.

Perkin, R. G., and E. Lewis (1980), The Practical Salinity Scale 1978: Fitting the data, Oceanic Engineering, IEEE Journal of, 5(1), 9-16, doi: 10.1109/JOE.1980.1145441.

Phillips, F. M., and M. C. Castro (2005), Groundwater dating and residence-time measurements, in Surface and Ground Water, Weathering, and Soils, edited by J. I. Drever, pp. 451-497, Elsevier, Oxford, UK.

Phillips, F. M., H. W. Bentley, S. N. Davis, D. Elmore, and G. B. Swanick (1986), Chlorine 36 dating of very old groundwater: 2. Milk River Aquifer, Alberta, Canada, Water Resour. Res., 22(13), 2003-2016, doi: 10.1029/WR022i013p02003.

Piccolo, M. C., G. M. E. Perillo, and G. R. Daborn (1993), Soil Temperature Variations on a Tidal Flat in Minas Basin, Bay of Fundy, Canada, Estuar. Coast. Shelf Sci., 36(4), 345-357, doi: 10.1006/ecss.1993.1021.

Post, V. E. A., J. Groen, H. Kooi, M. Person, S. Ge, and W. M. Edmunds (2013), Offshore fresh groundwater reserves as a global phenomenon, Nature, 504(7478), 71-78, doi: 10.1038/nature12858.

Ramalho, R. S., R. Quartau, A. S. Trenhaile, N. C. Mitchell, C. D. Woodroffe, and S. P. Ávila (2013), Coastal evolution on volcanic oceanic islands: A complex interplay

between volcanism, erosion, sedimentation, sea-level change and biogenic production, Earth-Sci. Rev., 127, doi: 10.1016/j.earscirev.2013.10.007.

Rankey, E. C., and J. R. Garza-Perez (2012), Seascape Metrics of Shelf-Margin Reefs and Reef Sand Aprons of Holocene Carbonate Platforms, J. Sediment. Res., 82(1), 53-71, doi: 10.2110/jsr.2012.7.

Reeves, H. W., P. M. Thibodeau, R. G. Underwood, and L. R. Gardner (2000), Incorporation of Total Stress Changes into the Ground Water Model SUTRA, Ground Water, 38(1), 89-98, doi: 10.1111/j.1745-6584.2000.tb00205.x.

Revil, A., L. M. Cathles, III, S. Losh, and J. A. Nunn (1998), Electrical conductivity in shaly sands with geophysical applications, J. Geophys. Res., 103(B10), 23925-23936, doi: 10.1029/98jb02125.

Ricci, G., and D. Scott (1998), Groundwater potential assessment of Rarotonga coastal plain, SOPAC Technical Report(259), 81 pp.

Ricklefs, K., and K. H. Vanselow (2012), Analysis of temperature variability and determination of apparent thermal diffusivity in sandy intertidal sediments at the German North Sea coast, Estuar. Coast. Shelf Sci., 108, 7-15, doi: 10.1016/j.ecss.2011.09.015.

Robinson, C., B. Gibbes, and L. Li (2006), Driving mechanisms for groundwater flow and salt transport in a subterranean estuary, Geophys. Res. Lett., 33(3), L03402, doi: 10.1029/2005gl025247.

Robinson, C., L. Li, and D. A. Barry (2007a), Effect of tidal forcing on a subterranean estuary, Adv. Water Resour., 30(4), 851-865, doi: 10.1016/j.advwatres.2006.07.006.

Robinson, C., L. Li, and H. Prommer (2007b), Tide-induced recirculation across the aquifer-ocean interface, Water Resour. Res., 43(7), doi: 10.1029/2006wr005679.

Rocha, C. (2000), Density-driven convection during flooding of warm, permeable intertidal sediments: the ecological importance of the convective turnover pump, J. Sea Res., 43(1), 1-14, doi: 10.1016/s1385-1101(00)00002-2.

Rodell, M., et al. (2004), The Global Land Data Assimilation System, Bull. Am. Meteorol. Soc., 85(3), 381-394, doi: 10.1175/BAMS-85-3-381.

Rosenberry, D. O., J. W. LaBaugh, and R. J. Hunt (2010), Use of Monitoring Wells, Portable Piezometers, and Seepage Meters to Quantify Flow Between Surface Water and Ground Water, in Field techniques for estimating water fluxes between surface water and ground water, edited by D. O. Rosenberry and J. W. LaBaugh, pp. 43-70, U. S. Geological Survey.

Rucker, D. F., G. E. Noonan, and W. J. Greenwood (2011), Electrical resistivity in support of geological mapping along the Panama Canal, Eng. Geol., 117(1-2), 121-133, doi: 10.1016/j.enggeo.2010.10.012.

Russoniello, C. J., C. Fernandez, J. F. Bratton, J. F. Banaszak, D. E. Krantz, A. S. Andres, L. F. Konikow, and H. A. Michael (2013), Geologic effects on groundwater salinity and discharge into an estuary, J. Hydrol., 498, 1-12, doi: 10.1016/j.jhydrol.2013.05.049.

Sanford, E. (1999), Regulation of Keystone Predation by Small Changes in Ocean Temperature, Science, 283(5410), 2095-2097, doi: 10.1126/science.283.5410.2095.

Santoro, A. E. (2009), Microbial nitrogen cycling at the saltwater–freshwater interface, Hydrogeol. J., 18(1), 187-202, doi: 10.1007/s10040-009-0526-z.

Santos, I. R., B. D. Eyre, and R. N. Glud (2012a), Influence of porewater advection on denitrification in carbonate sands: Evidence from repacked sediment column experiments, Geochim. Cosmochim. Acta, 96, 247-258, doi: 10.1016/j.gca.2012.08.018.

Santos, I. R., B. D. Eyre, and M. Huettel (2012b), The driving forces of porewater and groundwater flow in permeable coastal sediments: A review, Estuar. Coast. Shelf Sci., 98(0), 1-15, doi: 10.1016/j.ecss.2011.10.024.

Santos, I. R., P. L. M. Cook, L. Rogers, J. de Weys, and B. D. Eyre (2012c), The “salt wedge pump”: Convection-driven pore-water exchange as a source of dissolved organic and inorganic carbon and nitrogen to an estuary, Limnol. Oceanogr., 57(5), 1415-1426, doi: 10.4319/lo.2012.57.5.1415.

Sanz-Lázaro, C., T. Valdemarsen, A. Marín, and M. Holmer (2011), Effect of temperature on biogeochemistry of marine organic-enriched systems: implications in a global warming scenario, Ecological Applications, 21(7), 2664-2677, doi: 10.1890/10-2219.1.

Sawyer, A. H., F. Shi, J. T. Kirby, and H. A. Michael (2013), Dynamic response of surface water-groundwater exchange to currents, tides, and waves in a shallow estuary, J. Geophys. Res.:Oceans, 118(4), 1749-1758.

Schneider, R. L., T. L. Negley, and C. Wafer (2005), Factors influencing groundwater seepage in a large, mesotrophic lake in New York, J. Hydrol., 310(1-4), 1-16, doi: 10.1016/j.jhydrol.2004.09.020.

Schneider, U., A. Becker, P. Finger, A. Meyer-Christoffer, M. Ziese, and B. Rudolf (2014), GPCC's new land surface precipitation climatology based on quality-controlled in situ data and its role in quantifying the global water cycle, Theor. Appl. Climatol., 115(1-2), 15-40, doi: 10.1007/s00704-013-0860-x.

Siebert, S., J. Burke, J.-M. Faures, K. Frenken, J. Hoogeveen, P. Döll, and F. T. Portmann (2010), Groundwater use for irrigation–a global inventory, Hydrology and Earth System Sciences Discussions, 7(3), 3977-4021, doi: 10.5194/hessd-7-3977-2010.

Slomp, C. P., and P. Van Cappellen (2004), Nutrient inputs to the coastal ocean through submarine groundwater discharge: controls and potential impact, J. Hydrol., 295(1-4), 64-86, doi: 10.1016/j.jhydrol.2004.02.018.

Smith, B. D., J. D. Abraham, J. C. Cannia, B. J. Minsley, M. Deszcz-Pan, and L. B. Ball (2010), Helicopter electromagnetic and magnetic geophysical survey data, portions of the North Platte and South Platte Natural Resources Districts, western Nebraska, May 2009, in U.S. Geological Survey Open-File Report 2010–1259, edited, p. 33.

Smith, N. (2002), Observations and simulations of water-sediment heat exchange in a shallow coastal lagoon, Estuar. Coasts, 25(3), 483-487-487, doi: 10.1007/bf02695989.

Sophocleous, M. (2000), From safe yield to sustainable development of water resources—the Kansas experience, J. Hydrol., 235(1–2), 27-43, doi: 10.1016/S0022-1694(00)00263-8.

Sophocleous, M. (2002), Interactions between groundwater and surface water: the state of the science, Hydrogeol. J., 10(1), 52-67, doi: 10.1007/s10040-001-0170-8.

Spiteri, C., C. P. Slomp, M. A. Charette, K. Tuncay, and C. Meile (2008), Flow and nutrient dynamics in a subterranean estuary (Waquoit Bay, MA, USA): Field data and reactive transport modeling, Geochim. Cosmochim. Acta, 72(14), 3398-3412, doi: 10.1016/j.gca.2008.04.027.

Staver, K., and R. Brinsfield (1996), Seepage of groundwater nitrate from a riparian agroecosystem into the Wye River estuary, Estuar. Coasts, 19(2), 359-370, doi: 10.2307/1352456.

Straits, D. (1978), Water of love, in Dire Straits, edited, Basing Street Studios, London.

Sturchio, N. C., et al. (2004), One million year old groundwater in the Sahara revealed by krypton-81 and chlorine-36, Geophys. Res. Lett., 31(5), L05503, doi: 10.1029/2003GL019234.

Suckow, A. (2014), The Age of Groundwater – definitions, models and why we do not need this term, Appl. Geochem., (0), doi: 10.1016/j.apgeochem.2014.04.016.

Swarzenski, P. W., and J. A. Izbicki (2009), Coastal groundwater dynamics off Santa Barbara, California: Combining geochemical tracers, electromagnetic seepmeters, and electrical resistivity, Estuar. Coast. Shelf Sci., 83(1), 77-89, doi: 10.1016/j.ecss.2009.03.027.

Swarzenski, P. W., H. Dulaiova, M. L. Dailer, C. R. Glenn, C. G. Smith, and C. D. Storlazzi (2013), A Geochemical and Geophysical Assessment of Coastal Groundwater Discharge at Select Sites in Maui and O'ahu, Hawai'i, in Groundwater in the Coastal Zones of Asia-Pacific, edited by C. Wetzelhuetter, pp. 27-46, Springer Netherlands.

Swarzenski, P. W., W. C. Burnett, W. J. Greenwood, B. Herut, R. Peterson, N. Dimova, Y. Shalem, Y. Yechieli, and Y. Weinstein (2006), Combined time-series resistivity and geochemical tracer techniques to examine submarine groundwater discharge at Dor Beach, Israel, Geophys. Res. Lett., 33(24), doi: 10.1029/2006gl028282.

Szilagyi, J., V. A. Zlotnik, J. B. Gates, and J. Jozsa (2011), Mapping mean annual groundwater recharge in the Nebraska Sand Hills, USA, Hydrogeol. J., 19(8), 1503-1513, doi: 10.1007/s10040-011-0769-3.

Taboroši, D., J. W. Jenson, and J. E. Mylroie (2003), Zones of enhanced dissolution and associated cave morphology in an uplifted carbonate island karst aquifer, northern Guam, Mariana Islands, Speleogenesis and Evolution of Karst Aquifers, 1(4), 16.

Tait, D. R., I. R. Santos, D. V. Erler, K. M. Befus, M. B. Cardenas, and B. D. Eyre (2013), Estimating submarine groundwater discharge in a South Pacific coral reef lagoon using different radioisotope and geophysical approaches, Mar. Chem., doi: 10.1016/j.marchem.2013.03.004.

Taniguchi, M., J. Shimada, T. Tanaka, I. Kayane, Y. Sakura, Y. Shimano, S. Dapaah-Siakwan, and S. Kawashima (1999), Disturbances of temperature-depth profiles due to surface climate change and subsurface water flow: 1. An effect of linear increase in surface temperature caused by global warming and urbanization in the Tokyo Metropolitan Area, Japan, Water Resour. Res., 35(5), 1507, doi: 10.1029/1999wr900009.

Tcherepanov, E. N., V. A. Zlotnik, and G. M. Henebry (2005), Using Landsat thermal imagery and GIS for identification of groundwater discharge into shallow groundwater-dominated lakes, Int. J. Remote Sens., 26(17), 3649-3661, doi: 10.1080/01431160500177315.

Telford, W. M., L. P. Geldart, and R. E. Sheriff (1990), Applied Geophysics, 2nd ed., 770 pp., Cambridge University Press, Cambridge, England.

Teo, H. T., D. S. Jeng, B. R. Seymour, D. A. Barry, and L. Li (2003), A new analytical solution for water table fluctuations in coastal aquifers with sloping beaches, Adv. Water Resour., 26(12), 1239-1247, doi: 10.1016/j.advwatres.2003.08.004.

Thompson, G. M., J. Malpas, and I. E. M. Smith (1998), Volcanic geology of Rarotonga, southern Pacific Ocean, New Zeal. J. Geol. Geophys., 41(1), 95-104, doi: 10.1080/00288306.1998.9514793.

Toran, L., M. Johnson, J. Nyquist, and D. Rosenberry (2010), Delineating a road-salt plume in lakebed sediments using electrical resistivity, piezometers, and seepage meters at Mirror Lake, New Hampshire, U.S.A, Geophysics, 75(4), WA75-WA83, doi: 10.1190/1.3467505.

Tóth, J. (1963), A theoretical analysis of groundwater flow in small drainage basins, J. Geophys. Res., 68(16), 4795-4812, doi: 10.1029/JZ068i016p04795.

Townley, L. R., and M. G. Trefry (2000), Surface water-groundwater interaction near shallow circular lakes: Flow geometry in three dimensions, Water Resour. Res., 36(4), 935-948, doi: 10.1029/1999wr900304.

Trenberth, K. E., L. Smith, T. Qian, A. Dai, and J. Fasullo (2007), Estimates of the Global Water Budget and Its Annual Cycle Using Observational and Model Data, J. Hydrometeorol., 8(4), 758-769, doi: 10.1175/JHM600.1.

Turner, I. L., and P. Nielsen (1997), Rapid water table fluctuations within the beach face: Implications for swash zone sediment mobility?, Coastal Eng., 32(1), 45-59, doi: 10.1016/s0378-3839(97)00015-x.

Turner, I. L., and R. I. Acworth (2004), Field Measurements of Beachface Salinity Structure Using Cross-Borehole Resistivity Imaging, J. Coast. Res., 20(3), 753-760, doi: 10.2112/1551-5036(2004)20[753:FMOBSS]2.0.CO;2.

Turner, J. V., and L. R. Townley (2006), Determination of groundwater flow-through regimes of shallow lakes and wetlands from numerical analysis of stable isotope and chloride tracer distribution patterns, J. Hydrol., 320(3-4), 451-483, doi: 10.1016/j.jhydrol.2005.07.050.

Ullman, W. J., B. Chang, D. C. Miller, and J. A. Madsen (2003), Groundwater mixing, nutrient diagenesis, and discharges across a sandy beachface, Cape Henlopen, Delaware (USA), Estuar. Coast. Shelf Sci., 57(3), 539-552, doi: 10.1016/s0272-7714(02)00398-0.

Vacher, L. H., and T. M. Quinn (2004), Geology and hydrogeology of carbonate islands, 948 pp., Elsevier, Amsterdam, The Netherlands.

Vandenbohede, A., and L. Lebbe (2006), Occurrence of salt water above fresh water in dynamic equilibrium in a coastal groundwater flow system near De Panne, Belgium, Hydrogeol. J., 14(4), 462-472, doi: 10.1007/s10040-005-0446-5.

Vandenbohede, A., and L. Lebbe (2007), Effects of tides on a sloping shore: groundwater dynamics and propagation of the tidal wave, Hydrogeol. J., 15(4), 645-658, doi: 10.1007/s10040-006-0128-y.

Vandenbohede, A., and L. Lebbe (2011), Heat transport in a coastal groundwater flow system near De Panne, Belgium, Hydrogeol. J., 19(6), 1225-1238, doi: 10.1007/s10040-011-0756-8.

Veraart, A. J., J. J. M. de Klein, and M. Scheffer (2011), Warming Can Boost Denitrification Disproportionately Due to Altered Oxygen Dynamics, PLoS ONE, 6(3), e18508, doi: 10.1371/journal.pone.0018508.

Verfürth, R. d. (1996), A review of a posteriori error estimation and adaptive mesh-refinement techniques, 127 pp., Wiley-Teubner, Chichester, UK.

Wada, Y., L. P. H. van Beek, and M. F. P. Bierkens (2012), Nonsustainable groundwater sustaining irrigation: A global assessment, Water Resour. Res., 48, doi: 10.1029/2011wr010562.

Wada, Y., L. P. H. van Beek, C. M. van Kempen, J. W. T. M. Reckman, S. Vasak, and M. F. P. Bierkens (2010), Global depletion of groundwater resources, Geophys. Res. Lett., 37(20), doi: 10.1029/2010gl044571.

Wang, T., D. Wedin, and V. A. Zlotnik (2009), Field evidence of a negative correlation between saturated hydraulic conductivity and soil carbon in a sandy soil, Water Resour. Res., 45, doi: 10.1029/2008wr006865.

Ward, A. S., M. N. Gooseff, and K. Singha (2010), Imaging hyporheic zone solute transport using electrical resistivity, Hydrol. Process., 24(7), 948-953, doi: 10.1002/hyp.7672.

Waska, H., and G. Kim (2010), Differences in microphytobenthos and macrofaunal abundances associated with groundwater discharge in the intertidal zone, Marine Ecology Progress Series, 407, 159-172, doi: 10.3354/meps08568.

Waterhouse, B., and D. R. Petty (1986), Hydrogeology of the Southern Cook Islands, South Pacific, 93 pp., Science Information Pub. Centre, Wellington, New Zealand.

Werner, A. D., and D. A. Lockington (2006), Tidal impacts on riparian salinities near estuaries, J. Hydrol., 328(3-4), 511-522, doi: 10.1016/j.jhydrol.2005.12.011.

Werner, A. D., M. Bakker, V. E. A. Post, A. Vandenbohede, C. Lu, B. Ataie-Ashtiani, C. T. Simmons, and D. A. Barry (2013), Seawater intrusion processes, investigation and management: Recent advances and future challenges, Adv. Water Resour., 51, 3-26, doi: 10.1016/j.advwatres.2012.03.004.

Werner, U., P. Bird, C. Wild, T. Ferdelman, L. Polerecky, G. Eickert, R. Jonstone, O. Hoegh-Guldberg, and D. de Beer (2006), Spatial patterns of aerobic and anaerobic mineralization rates and oxygen penetration dynamics in coral reef sediments, Marine Ecology Progress Series, 309, 93-105, doi: 10.3354/meps309093.

Westbrook, S. J., J. L. Rayner, G. B. Davis, T. P. Clement, P. L. Bjerg, and S. J. Fisher (2005), Interaction between shallow groundwater, saline surface water and contaminant discharge at a seasonally and tidally forced estuarine boundary, J. Hydrol., 302(1-4), 255-269, doi: 10.1016/j.jhydrol.2004.07.007.

White, I., and T. Falkland (2010), Management of freshwater lenses on small Pacific islands, Hydrogeol. J., 18(1), 227-246, doi: 10.1007/s10040-009-0525-0.

Wilson, K. (1983), Beach sediment temperature variations through depth and time, Estuar. Coast. Shelf Sci., 17(5), 581-586, doi: 10.1016/0272-7714(83)90010-0.

Windom, H., and F. Niencheski (2003), Biogeochemical processes in a freshwater–seawater mixing zone in permeable sediments along the coast of Southern Brazil, Mar. Chem., 83(3-4), 121-130, doi: 10.1016/s0304-4203(03)00106-3.

Winter, T. C. (1977), Classification of the hydrologic settings of lakes in the north central United States, Water Resour. Res., 13(4), 753-767, doi: 10.1029/WR013i004p00753.

Winter, T. C. (1986), Effect of ground-water recharge on configuration of the water table beneath sand dunes and on seepage in lakes in the sandhills of Nebraska, U.S.A, J. Hydrol., 86(3-4), 221-237.

Winter, T. C., and H. O. Pfannkuch (1984), Effect of anisotropy and groundwater system geometry on seepage through lakebeds: 2. Numerical simulation analysis, J. Hydrol., 75(1-4), 239-253, doi: 10.1016/0022-1694(84)90052-0.

Wood, B. L., and R. F. Hay (1970), Geology of the Cook Islands, 103 pp., Consolidated Press Holdings Limited, Wellington, New Zealand.

Worthington, S. R. H. (2007), Groundwater residence times in unconfined carbonate aquifers, Journal of Cave and Karst Studies, 69(1), 94-102.

Wright, L. D., and A. D. Short (1984), Morphodynamic variability of surf zones and beaches: A synthesis, Mar. Geol., 56(1–4), 93-118, doi: 10.1016/0025-3227(84)90008-2.

Xie, P., and P. A. Arkin (1997), Global Precipitation: A 17-Year Monthly Analysis Based on Gauge Observations, Satellite Estimates, and Numerical Model Outputs, Bull. Am. Meteorol. Soc., 78(11), 2539-2558, doi: 10.1175/1520-0477(1997)078<2539:GPAYMA>2.0.CO;2.

Xin, P., C. Robinson, L. Li, D. A. Barry, and R. Bakhtyar (2010), Effects of wave forcing on a subterranean estuary, Water Resour. Res., 46(12), W12505, doi: 10.1029/2010wr009632.

Zarroca, M., J. Bach, R. Linares, and X. M. Pellicer (2011), Electrical methods (VES and ERT) for identifying, mapping and monitoring different saline domains in a coastal plain region (Alt Empordà, Northern Spain), J. Hydrol., 409(1–2), 407-422, doi: 10.1016/j.jhydrol.2011.08.052.

Zienkiewicz, O. C., C. Emson, and P. Bettess (1983), A novel boundary infinite element, Int. J. Numer. Meth. Eng., 19(3), 393-404, doi: 10.1002/nme.1620190307.

Zipperle, A., and K. Reise (2005), Freshwater springs on intertidal sand flats cause a switch in dominance among polychaete worms, J. Sea Res., 54(2), 143-150, doi: 10.1016/j.seares.2005.01.003.

Zlotnik, V. A., F. Olaguera, and J. B. Ong (2009), An approach to assessment of flow regimes of groundwater-dominated lakes in arid environments, J. Hydrol., 371(1-4), 22-30, doi: 10.1016/j.jhydrol.2009.03.012.

Zlotnik, V. A., N. I. Robinson, and C. T. Simmons (2010), Salinity dynamics of discharge lakes in dune environments: Conceptual model, Water Resour. Res., 46(11), W11548, doi: 10.1029/2009wr008999.

Zlotnik, V. A., J. B. Ong, J. D. Lenters, J. Schmieder, and S. C. Fritz (2012), Quantification of salt dust pathways from a groundwater-fed lake: Implications for solute budgets and dust emission rates, Journal of Geophysical Research: Earth Surface, 117(F2), F02014, doi: 10.1029/2011JF002107.

Zohdy, A., and D. Jackson (1969), Application of deep electrical soundings for groundwater exploration in Hawaii, Geophysics, 34(4), 584-600, doi: doi:10.1190/1.1440033.

Zongyu, C., N. Zhenlong, Z. Zhaoji, Q. Jixiang, and N. Yunju (2005), Isotopes and Sustainability of Ground Water Resources, North China Plain, Ground Water, 43(4), 485-493, doi: 10.1111/j.1745-6584.2005.0038.x.